The Role of Fully Coupled Ice Sheet Basal Processes in Quaternary Glacial Cycles

by

© Matthew Drew

A thesis submitted to the
School of Graduate Studies
in partial fulfilment of the
requirements for the degree of
Doctor of Philosophy

Department of Physics & Physical Oceanography
Memorial University of Newfoundland

May 2023

St. John's Newfoundland

ABSTRACT

Bed conditions such as meltwater pressurization and unconsolidated sediment cover (soft versus hard bedded) strongly impact ice sheet sliding velocities. How the dynamical processes governing these conditions affect glacial cycle scale ice sheet evolution has been little studied. The influence of subglacial hydrology and glacial sediment production and transport is therefore largely unknown. Here I present a glaciological model Glacial Systems Model (GSM) with the to-date most complete representations of fully coupled subglacial hydrology and sediment production and transport for the glacial cycle continental scale context. I compare the influence of of several types of subglacial hydrology drainage systems on millennial scale variability and examine the role dynamical sediment processes potentially played in the mid-Pleistocene Transition (MPT) from 41 to 100 kyr glacial cycles.

Subglacial hydrology has long been inferred to play a role in glacial dynamics at decadal and shorter scales. However, it remains unclear whether subglacial hydrology has a critical role in ice sheet evolution on greater than centennial time-scales. It is also unclear which drainage system is most appropriate for the continental/glacial cycle scale. Here I compare the dynamical role of three subglacial hydrology systems most dominant in the literature in the context of surge behaviour for an idealized Hudson Strait scale ice stream. I find that subglacial hydrology is an important system inductance for realistic ice stream surging and that the three formulations all exhibit similar surge behaviour. Even a detail as fundamental as mass conserving transport of subglacial water is not necessary for simulating a full range of surge frequency and amplitude. However, one difference is apparent: the combined positive and negative feedbacks of the linked-cavity system yields longer duration surges and a broader range of effective pressures than its poro-elastic and leaky-bucket counterparts.

The MPT from 41 kyr to 100 kyr glacial cycles was one of the largest changes in the Earth system over the past million years. A change from a low to high friction base under the North American Ice Complex through the removal of pre-glacial regolith has been hypothesized to play a critical role in the transition to longer and stronger glaciations. However, this hypothesis requires constraint on pre-glacial regolith cover as well as mechanistic constraints on whether the appropriate amount of regolith can be removed from the required regions to enable MPT occurrence at the right time. This is the first study to test the regolith hypothesis for a realistic 3D North American ice sheet that treats regolith removal as a system internal process instead of a forced soft to hard transition.

The fully coupled climate, ice, subglacial hydrology, and sediment physics capture the progression of Pleistocene glacial cycles within parametric and observational uncertainty. Incorporating the constraint from estimates for the present day sediment distribution, Quaternary erosion, and Atlantic Quaternary sediment volume suggests the mean Pliocene regolith thickness was 40 m or less. Given this constraint, I compare the simulated soft to hard bed transitions with the timing inferred for the MPT. The combined constraint, bedrock erosion, and sediment transport poses a challenge to the Regolith Hypothesis: denudation occurs well in advance of the MPT and the hard bedded area stays largely constant by 1.5 Ma. Furthermore, I examine the sensitivity of glacial cycle evolution to the initial thickness of the regolith in the absence of erosion. Surprisingly, thicker regolith does not delay the transition but produces large glacial cycles in the early Pleistocene even extending the length of some. This is due to the effect from higher topography on ice sheet mass balance. Therefore, I suggest that the regolith removal mechanism is not singularly responsible for the MPT, but that the MPT results from changes in many aspects of the systems. One of these aspects which remains under-studied in the literature is the long term evolution of glacierized beds over the Pleistocene.

Dedication

For Laura, Charlie, Joseph, and Ada.

"If I had a brontosaurus
I would name him Morris or Horace;
But if suddenly one day he had a lot of little brontosauri
I would change his name to Laurie."

— Shel Silverstein

Acknowledgments

Thank you to my thesis supervisor, scientific mentor, and fearless Glacial Dynamics Group leader Lev Tarasov for generously giving time, ideas, and candid feedback. I am grateful to have joined the Glacial Dynamics Group – a wonderful bunch for bouncing ideas around (in chronological order): Kevin Le Morzedac (who familiarized me with the GSM), Benoit Lecavalier (who familiarized me with ice dynamics and paleoclimate science more broadly), Ryan Love (who elevated my nix, coding, and hardware proficiency), Heather Andres (a wonderful scientific and science communication mentor), Marilena Geng (who helped me with large scale climate systems thinking and communication), Kevin Hank (who delved into thermo, numerical, and ice dynamical issues with me), Audrey Parnell (who always has a finger to the pulse and is ready with a coffee and a WaPo article), Alexis Goffin (who is a great source of commaraderie and ice sheet interest), and April Dalton (who is a marvelous glacial geology reference).

I am appreciative to Art Dyke, John Gosse, and Sophie Norris, for the long walks, till fabrics, hunts for Gossian Boulders, and erosion discussions. The PAGES working group QUIGS provided support for joining meetings which shaped my thinking and was a needed source of motivation and inspiration. Financial support for this work was provided through Lev Tarasov's NSERC Discovery Grant, Memorial University, and the PalMod German Climate Modelling Initiative. Computational resources were provided by the Canadian Foundation for Innovation (CFI) and ACEnet – a regional partner of the Digital Research Alliance of Canada. The free and open source software community is an important enabler of science and this work would not have been possible without them.

Thank you to my parents – who never hesitate to jump on a plane at a moments notice – for being the very best mom and dad. Thank you to Daphne and Charlie for showing me which end of the hammer to use and for constantly, perpetually, and tirelessly being there. Thank you Laura for the support, perspective, sanity,

wee hours, and the Grand Adventure. Thank you Ada, Charlie, and Joseph for the giggles, the tears, and making my heart happy.

Co-Authorship Statement

Lev Tarasov initially conceived of and secured funding for the broad project which was then refined by Matthew Drew. The introductory material in chap. 1, 2,and 3 was written by Matthew Drew with editorial input by Lev Tarasov, Marilena Geng, and Kevin Hank.

Lev Tarasov maintains the GSM and coded and coupled the climate and solid earth models. Matthew Drew performed subglacial hydrology model development (detailed in chap. 3) and verification (chap. 4), sediment model development (detailed in chap. 2) and verification (chap. 5), and basal drag coupling to each of these models (chap. 3 and 5)

Matthew Drew designed and carried out the methods (experiments and analysis) and wrote the manuscripts for chap. 4, 5, and 6. Lev Tarasov advised on methodological design and provided editorial input for these chapters.

Matthew Drew wrote chap. 7 with editorial input from Lev Tarasov and Audrey Parnell.

Editorial contributions to the thesis by coauthors and colleagues did not extend to providing substantive writing for any component. Editorial contributions amounted to assisting in clarifying language to enhance readability and suggestions for contextual content.

List of Figures

List of Tables

Abbreviations

pe poro-elastic

lc linked-cavity

lb leaky-bucket

nh no hydrology

gsm Glacial Systems Model

mpt mid-Pleistocene Transition

ep early Pleistocene

lp late Pleistocene

epica European Project for Ice Coring in Antarctica

sicopolis SImulation COde for POLythermal Ice Sheets

naic North American Ice Complex

lr04 Lisiecki and Raymo (2005) benthic stack

ird ice rafted debris

thc thermohaline circulation

lgm last glacial maximum

ebm energy balance model

eof empirical orthogonal function

cia chemical index of alteration

r-channel Röthlisberger channel

brahms Basal Hydrology Model

gcm general circulation model

emics earth systems models of intermediate complexity

ppt Plio-Pleistocene Transition

gia glacial isostatic adjustment

dem digital elevation map

Contents

Chapter 1

Pleistocene Glacial Cycles

"When we try to pick out anything by itself, we find it hitched to everything else in the Universe."

— John Muir, My First Summer in the Sierra (1911)

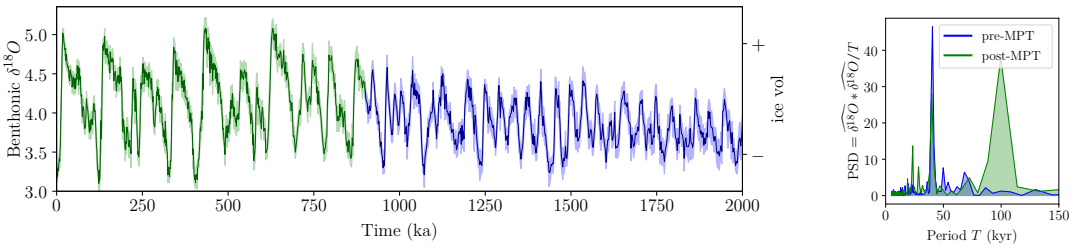

(a) Lisiecki and Raymo (2005) benthic stack (LR04) stack

(b) Power of LR04

Figure 1: a) Pleistocene ice volume proxy from LR04 with 2σ error, b) power spectral density of LR04 showing shift from 41 kyr mode to dominant 100 kyr.

The Pleistocene Ice Ages (2.6-0.01 Ma) are characterized by periodic growth and decay of large ice sheets that were paced by seasonal and latitudinal insolation changes from Earth's orbital variations on $10^4 - 10^5$ yr timescales, commonly known as the Milankovitch astronomical theory of ice ages (Hays, Imbrie, and N. J. Shackleton, 1976). Interactions and feedbacks among Earth system components such as ice sheets, carbon cycle, land cover, oceans, and atmosphere transformed these insolation changes into global surface temperature changes of 4-6°C (N. Shackleton, 1967). Understanding the response of the Earth system to a well-known (orbital) radiative forcing can significantly facilitate constraint of its response to anthropogenic radiative forcing. Given the possibility for tipping point transitions,

there is potentially much value in the analysis of paleoclimate dynamics at a time when the Earth system configuration was significantly different from the pre-industrial time period.

Although Milankovitch's theory of orbital forcing of global climate and sea-level change is well supported by paleoclimate data, three aspects of Pleistocene climate variability response to orbital forcing are unresolved. These aspects are:

1. the dominance of 41 kyr cycles in the early Pleistocene (EP, 2.6-1.2 Ma) climate and sea-level variability – corresponding to the obliquity frequency – despite summer insolation being dominated by the 23-kyr precessional frequency (Raymo and Nisancioglu, 2003);

2. the mid Pleistocene transition (MPT, 1.2-0.7 Ma) from low-amplitude 41-kyr variability to higher-amplitude 100-kyr variability in the absence of any change in orbital forcing (Pisias and Moore, 1981);

3. the continued dominance of high-amplitude 100-kyr cycles over the last 0.7 Myr (the 100-kyr world) despite virtually no forcing from the 100-kyr eccentricity cycle (Imbrie et al., 1993).

Three observations define the mid-Pleistocene Transition (MPT) problem. The first is that well-dated geological evidence demonstrates that EP ice sheets extended at least several times as far south as 39°N (Balco and Rovey, 2010), thus contradicting the hypothesis that EP ice sheets restricted to obliquity response were restricted to high latitudes ($>$ 60°N Huybers and Tziperman, 2008). The second is the smaller volume of EP ice sheets relative to those of the late Pleistocene (LP), largely inferred from benthic δ^{18}O records (Rohling, Foster, Gernon, et al., 2022). Finally the EP glacial cycles were largely symmetric whereas the LP cycles where asymmetric – deglaciating much more quickly than the process of inception and build to maximum size (Clark, Archer, et al., 2006).

To understand the MPT and the evolution of Pleistocene glacial cycles, it is useful to consider potential major changes in the structure of the Earth system from the EP to the LP. There have been a broad range of such changes hypothesized in the literature. For example, Pisias and Moore (1981) proposed that Hudson Bay only developed through long-term ice-sheet erosion, leading to a change from a terrestrial-based to marine-based Laurentide Ice Sheet. England (1987) suggested the Canadian Arctic Archipelago was a contiguous landmass and was glacially incised. Clark and Pollard (1998) hypothesized that EP ice sheets developed on a low-friction regolith substrate, with subsequent glacial removal of the regolith exposing a high-friction bedrock substrate inducing the MPT. Berger and Loutre (2010) showed that a secular decline in CO_2 over the course of the Pleistocene could cause a MPT like transition. Willeit, Ganopolski, Calov, and Brovkin (2019) proposed that a combination of the regolith removal and long-term cooling contributed to the MPT.

Of these conjectured changes, a continental scale change in basal friction of the North American Ice Complex (NAIC) via the removal of unconsolidated sediment – the Regolith Hypothesis of Clark and Pollard (1998) – is a favoured hypothesis for the MPT. To date modelling studies of the contribution of regolith to the MPT have forced a soft/hard transition, whether such a transition is consistent with the processes of glacial dynamics *and* sedimentation has not been properly assessed. This work treats regolith removal as a system internal dynamic process and accounts for the full effect of both changing friction and landscape.

1.1 PLIOCENE-PLEISTOCENE TRANSITION

The evolution of Pleistocene glacial cycles began with the onset of glaciation in the Pliocene and the intensification of Northern Hemispheric glaciation across the Pliocene-Pleistocene Transition. There is marine evidence of a major glaciation

in North America around 3.3 Ma (Mudelsee and Raymo, 2005; De Schepper et al., 2014) and terrestrial evidence from preserved till that glaciation around this time may have extended as far south as 52°50‘ N (Gao et al., 2012). This glaciation was followed by the mid-Pliocene Warm Period (MPWP) ca. 3.3-3.0 Ma (Brigham-Grette et al., 2013).

As these major climatic events were occurring, the Northern reaches of North America in the Canadian Arctic Archipelago underwent significant change. Now a polar tundra landscape, this area was once inhabited by Arctic camels (Rybczynski et al., 2013), beavers (Mitchell et al., 2016), and 12 different tree taxa (Gosse et al., 2017). The climate was likely much warmer than present day (Feng et al., 2017). The pre-Pleistocene Canadian Arctic may not have been an archipelago but instead contiguous with the rest of continental North America (England, 1987; Blakey, 2021; Stashin, 2021). The channels dividing the region may have been incised through glacial activity (Medvedev, Hartz, and Faleide, 2018). For example, paleo-flow indicators on Northern Banks Island do not point toward M’Clure Strait as one would expect if a trough existed there at the time (see fig. 2), but instead flow west directly to the Beaufort Sea (personal communication John Gosse). Additionally, the on-shore exposures of the Beaufort formation (3.8-2.6 Ma) is a ribbon-like deposit stretching along the west side of the archipelago from Banks Island to Meighan Island (fig. 2) raising the possibility of post-depositional incision.

Following sporadic glaciation during the mid-Pliocene, the intensification of Northern hemisphere glaciation (ca. 2.7 Maslin et al., 1995) occurred soon before the Pliocene-Pleistocene boundary (2.58 Ma Head and Gibbard, 2015). While the specific timing of NHG may be due to a variety of factors, it occurred during a declining trend in global temperature and atmospheric CO_2 concentration (Rae et al., 2021). The magnitude of change in climate proxies (e.g. for temperature, CO_2 and ice volume)was significant enough to motivate the definition of a Pliocene-Pleistocene geologic boundary (Head and Gibbard, 2015).

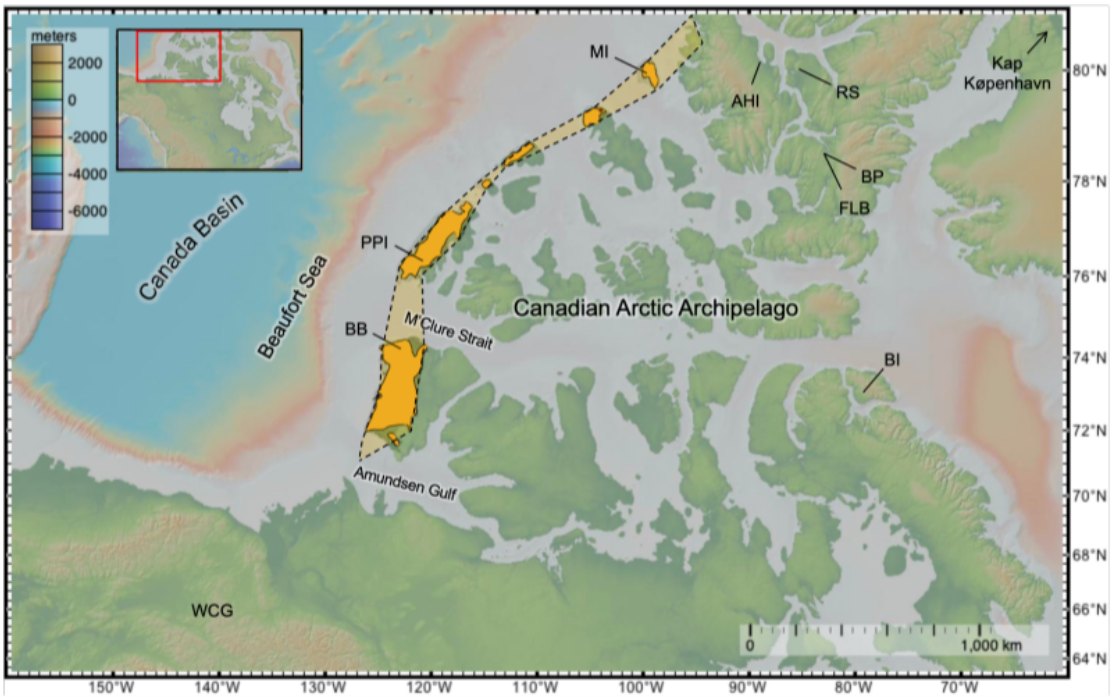

Figure 2: Map showing the onshore distribution of the Beaufort Formation along the west side of the Canadian Arctic Archipelago (from Stashin, 2021). BB Indicates Banks, PPi is Prince Patrick Island, and MI indicates Meighen Island.

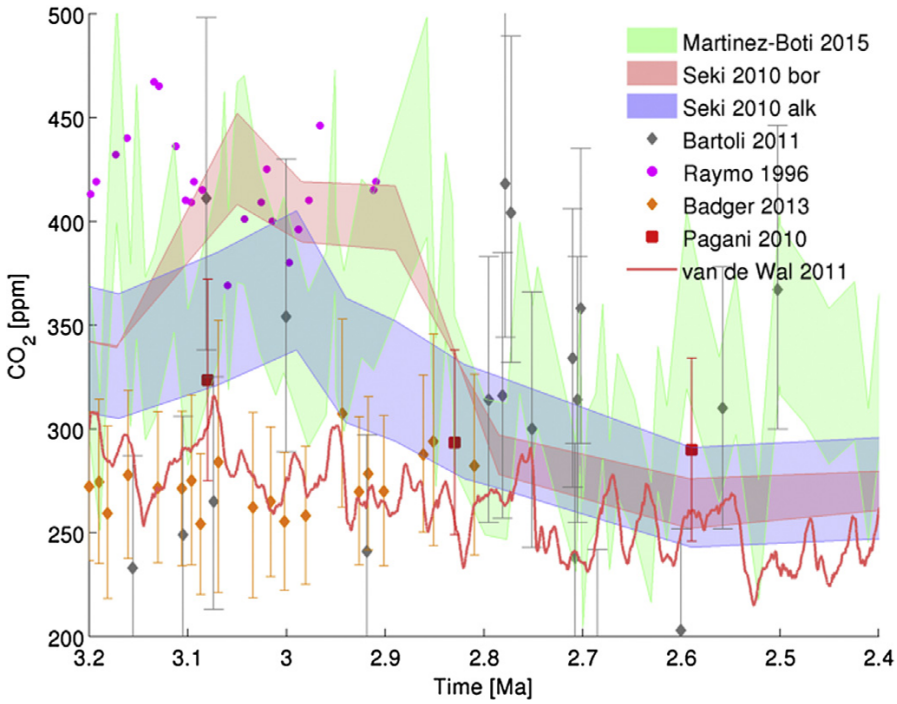

Figure 3: Estimates of Carbon Dioxide decline across the Pliocene-Pleistocene Transition (from Willeit, Ganopolski, Calov, Robinson, et al., 2015).

The PPT may have occurred at different times in different areas. Barendregt and Duk-Rodkin (2004) and N. J. Shackleton, Backman, et al. (1984) presented early evidence for the timing of the intensification of northern hemispheric glaciation in piston-cored sediments in the North Atlantic. These sediments show a marked rise in δ^{18}O from benthic foraminifera indicating an increase in terrestrial ice and cooler temperatures. Additionally, this core shows the onset of ice rafted debris (IRD) in the North Atlantic at 2.4 Ma (revised to 2.55 Ma by N. J. Shackleton, Berger, and Peltier, 1990). This contrasts with evidence of glaciation in Pacific cores. Maslin et al. (1995) find the onset of IRD in the Pacific at 2.75 Ma as indicated by an increase in magnetic susceptibility at site 882.

The ultimate cause for the PPT is not fully understood. Willeit, Ganopolski, Calov, Robinson, et al. (2015) have summarized multiple proxies all showing a decline in CO_2 from Pliocene to Pleistocene, but the absolute value of atmospheric concentration is highly uncertain. Garzione, 2008 summarizes the evidence that uplift of the Himalaya and Tibetan Plateau and resultant draw-down of CO_2 via increased chemical weathering were responsible for a global cooling trend. Maslin et al. (1995) suggests an increase in obliquity variation giving periods of lower obliquity and thus colder Northern Hemisphere summers. Haug et al. (2005) points out that a moisture source is necessary in addition to cold temperatures. Through proxy and model evidence, they demonstrate a rise in Northern Pacific SST providing a moisture source for growth of Northern Hemisphere ice. Barendregt and Duk-Rodkin (2004) suggest that moisture transport into the continent evolved with time as the Cordilleran ice sheet changed the orography of Western Canada and Alaska. It has been suggested that the closure of the Central American Seaway may have produced the northward moisture transport necessary for Laurentide inception (Bartoli et al., 2005) but later review of the timing of seaway changes around North America seems to make this unlikely (Molnar, 2008). The Bering Strait was open during the high-stands sea level of the interglacial state by 4.8

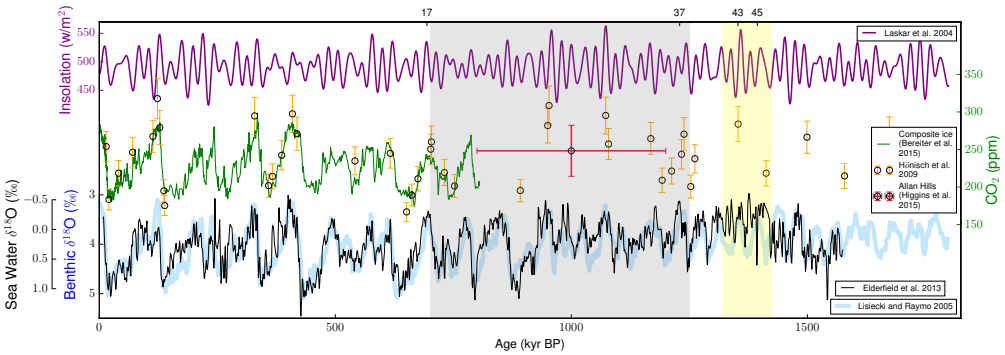

Figure 4: Summary of data presented at the QUIGS 2017 workshop on MPT in Molyvos, Greece (Chalk, Capron, et al., 2017)

Ma (Marincovich and Gladenkov, 1999). The Central American Seaway was likely closed around 13-15 Ma (Montes et al., 2015).

1.2 THE MID-PLEISTOCENE TRANSITION

Estimates of timing and abruptness vary, but around 1 Ma the volume of terrestrial ice during glaciation on the planet grew along with a transition from 41 kyr to approximate 100 kyr periodicity in the mid-Pleistocene Transition (MPT) (Clark, Archer, et al., 2006). The MPT represents a major shift in the climate. The EP (≈2.6 Ma - 0.9 Ma) was characterized by:

- smaller ice sheets by volume,
- a dominant 41 kyr period glacial cycle,
- symmetric glaciation and deglaciation time,
- and ice sheets extending as far south as LP ice sheets at least several times during the EP.

The LP (≈0.9 Ma to PD) was characterized by:

- larger ice sheets,
- a dominant 100 kyr period glacial cycle,

- and asymmetric glaciation/deglaciation times with slow accumulation (≈90 kyr) and rapid ablation (≈10 kyr).

There are two views of the MPT as measured in marine cores: a change in power spectral density of climate oscillations and a change in glacial state resilience. Whereas Berger and Loutre (2010) approaches the MPT problem as a frequency modulation – a non-linear response to the eccentricity or precessional beat frequencies, Tzedakis et al. (2017) approaches it as a process of interglacial skipping. This difference in approach leads Tzedakis et al. (2017) to quantify the resilience of glacial states after the MPT. Higher resilience enabled a skip of obliquity-paced insolation (caloric summer half year) maxima. This measure formed the basis of an interglacial prediction framework. Within this framework, the threshold insolation for triggering an interglacial goes up. As these glacial states persist, they accumulate instabilities (*e.g.* arising from large ice sheets) which lowers the threshold over time so that a subsequent obliquity maximum results in a more rapid deglaciation than during the EP. The timing and pace of the MPT is debated. This disagreement may depend on the underlying processes of the proxies used to infer timing. Using the ramp up in resilience as the transition itself, Tzedakis et al. (2017) suggests the transition took place from 1.25-.65 Ma, which is similar to N. J. Shackleton, Berger, and Peltier (1990) who find that the 100 kyr cycle disappears before 640 ka in the ODP677 δ^{18}O record. Berger and Loutre (2010) lists several earlier marine proxy studies during the 70's and 80's giving a 900-1100 ka start date for the transition, and finishing by 400-600 ka. On the basis of a proxy for ocean circulation (εNd), Pena and Goldstein (2014) hypothesizes the MPT to be correlated with an inferred decrease in the glacial thermohaline circulation (THC) at 950-850 ka. Chalk, Hain, et al. (2017) find an increase in glacial-interglacial CO_2 amplitude from 1200-800 ka indicating the MPT occurred during this period. The δ^{18}O sea water signal calculated by Elderfield et al. (2012) shows large 100

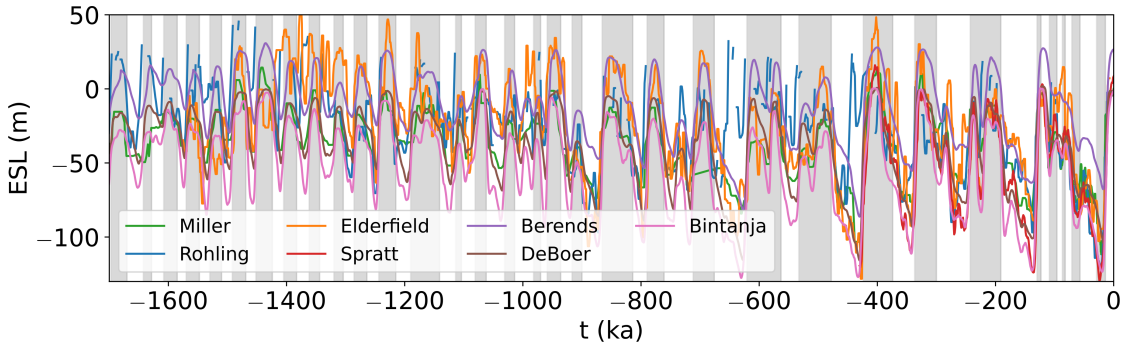

Figure 5: Multiple sea level reconstructions spanning the MPT showing the uncertainty in early to mid-Pleistocene sea level changes. Miller is from K. G. Miller et al. (2020), Rohling from Rohling, Foster, Grant, et al. (2014), Elderfield from Elderfield et al. (2012), Spratt from Spratt and Lisiecki (2016), Berends from Berends, de Boer, and R. S. W. van de Wal (2021), DeBoer from de Boer, Lourens, and R. S. van de Wal (2014), and Bintanja from Bintanja and R. S. W. van de Wal (2008). The vertical grey and white bars indicate alternating marine isotope stages.

kyr glacial cycles starting ≈900 ka. The above variance in estimates may indicate that some processes transitioned more abruptly while others more slowly.

Clark, Archer, et al. (2006) estimate that average glacial maximum ice volume gradually increased by ≈50 m sea level after the MPT versus before. Sea level reconstructions, however vary quite considerably and uncertainties remain large. Fig. 5 presents multiple sea level reconstructions. Even for the most recent glaciation, for which we have the best records, sea level estimates lie within a 30 m range for most of the reconstructions. Earlier in the Pleistocene this range grows to ≈75 m. The amount of ice sheet volume increase in the LP relative to the EP remains unconstrained. Further review of methodology and records is available from Rohling, Foster, Gernon, et al. (2022).

Similarly, prior to European Project for Ice Coring in Antarctica (EPICA) ice core coverage (≈ 800 to 0 ka Bereiter et al., 2015), CO_2 levels are not well resolved. The best proxy data we have for CO_2 are from the ^{11}B isotope record of sea surface pH (Dyez, Hönisch, and Schmidt, 2018). Fig. 6 shows the spread between the model-based reconstructions of Stap et al. (2016), Willeit, Ganopolski, Calov, and Brovkin (2019), and Berends, de Boer, and R. S. W. van de Wal (2021), the ^{11}B isotope-based reconstructions of Chalk, Hain, et al. (2017) and Dyez, Hönisch, and

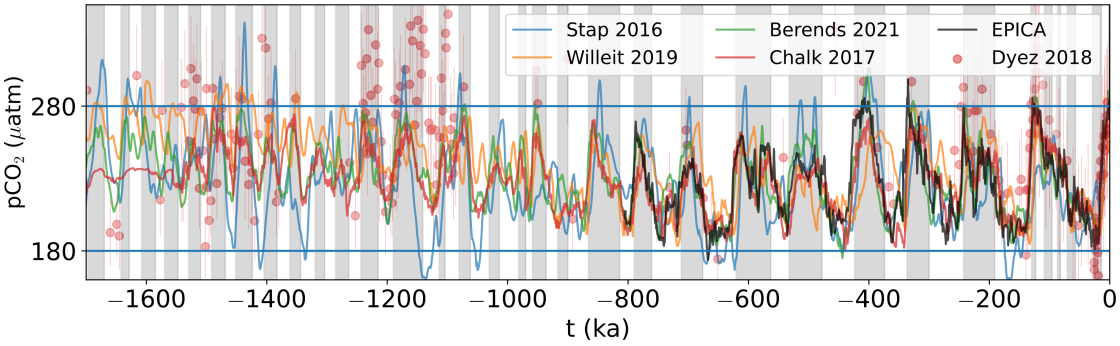

Figure 6: Multiple CO_2 reconstructions spanning the MPT showing the uncertainty in early to mid-Pleistocene greenhouse gas concentration. Stap 2016 is from Stap et al. (2016), Willeit 2019 is from Willeit, Ganopolski, Calov, and Brovkin (2019), Berends 2021 is from Berends, de Boer, and R. S. W. van de Wal (2021), Chalk 2017 is from Chalk, Hain, et al. (2017), Dyez 2018 is from Dyez, Hönisch, and Schmidt (2018). Grey and white bars indicate alternating marine isotope stages.

Schmidt (2018), and the EPICA ice core CO_2 record. The Chalk, Hain, et al. (2017) reconstruction is a ^{11}B isotope inversion incorporating their new data orbitally resolving the time period 1100 to 1250 ka. The data included in Dyez, Hönisch, and Schmidt (2018) incorporates the ^{11}B isotope data of Chalk, Hain, et al. (2017) along with a reanalysis of those of Hönisch et al. (2009). Notably, the model-based reconstructions all vary by tens of ppmv in places and are occasionally anti-phase with the ^{11}B isotope inversion. Meanwhile the spread on the ^{11}B isotope-based CO_2 estimates themselves have wide uncertainties.

1.2.1 *Drivers of the MPT*

The mid-Pleistocene transition occurred while the Earth's orbital configuration was unchanged (Berger and Loutre, 1991; Laskar, Robutel, et al., 2004; Laskar, Fienga, et al., 2011). The standard reconstructions of the Earth's orbital history by Berger and Loutre (1991), Laskar, Robutel, et al. (2004), and Laskar, Fienga, et al. (2011) have been validated back to 54 Ma through comparison of astronomically calibrated chronology and isotopic dating ($^{40}Ar/^{39}Ar$ and U/Pb ages) of tephra standards (Westerhold, Röhl, and Laskar, 2012), finding agreement.

The absence of a change in orbital forcing of the climate and low power in the eccentricity band hints at an internal mechanism for the onset of the 100 kyr glacial cycles (Berger and Loutre, 2010). Furthermore, the eccentricity component of the orbital signal declines over the late Pleistocene while strengthening in the records (Berger and Loutre, 2010). Hypothesized mechanisms fall into two camps: ice sheet dynamic changes and atmospheric/oceanic changes.

The CO_2 Mechanism

A downward trend in CO_2 would make ice sheets more resilient (e.g. Berger and Loutre, 2010). Assessing this contribution is made difficult by the uncertainty around the Pleistocene trend in CO_2 stemming from the lack of an orbitally resolved CO_2 record or proxy covering the full Pleistocene. Any suggested Pleistocene trend has reversed since the start of the EPICA ice core record (800 ka, seen in fig. 4) (Clark, Archer, et al., 2006). Chalk, Hain, et al. (2017) present an inversion of boron isotope data from 0-1.5 Ma which shows the importance of this greenhouse gas as a contributor to glacial cycle intensification. While their results do not indicate a decline in interglacial CO_2, the glacial levels do show a marked decline. Their proposed mechanism is CO_2 draw down during dust-driven (iron fertilized) increases in Southern Ocean bio-productivity from exposed continental shelves resulting from lower sea levels. This mechanism enhances any CO_2 independent increase in ice volume across the MPT driven by an internal process such as a stabilization from an increase in NAIC basal friction.

The Regolith Mechanism

In places this covering is made up of material originating through rock-weathering or plant growth in situ. In other instances it is of fragmental and more or less decomposed matter drifted by wind, water, or ice from other sources. This entire mantle of ***unconsolidated material****, whatever its nature or origin, it is proposed*

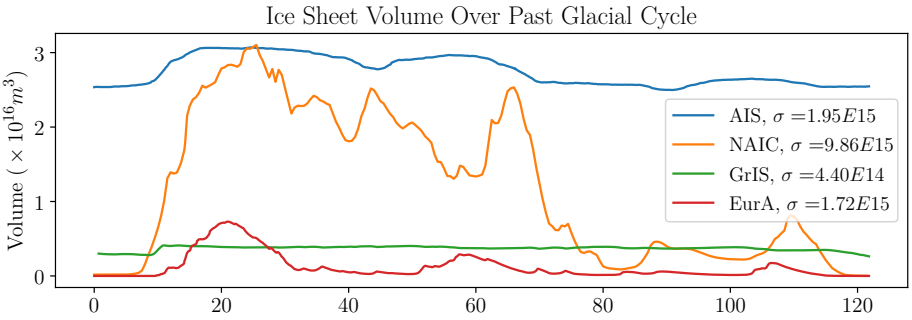

Figure 7: GLAC1-D ice volume since last interglacial simulated with the Glacial Systems Model (GSM) (personal communication Lev Tarasov)

to call the regolith, from the Greek words ρηγοσ, meaning a blanket, and λιθοσ, a stone.

—Merrill (1897)

During the warmer, wetter climate of the Pliocene, a fast rate of chemical weathering likely generated a mantle of unconsolidated sediment. The NAIC was the largest ice sheet during last glacial maximum (LGM) and most variable across the last glacial cycle (fig. 7), a shift in North American ice dynamics would have a profound effect globally. The regolith hypothesis proposes a mechanism for such a shift: successive glaciations gradually removed sediment cover over North America increasing basal drag on the ice sheet (Clark and Pollard, 1998). Slower sliding velocity from an increase in basal drag would result in large ice sheets as, to first order (under the shallow ice sheet approximation), the ice sheet surface slope is proportional to the basal drag. This hypothesis explains the increase in ice volume through the slower flux into the southern ablation zone and overall thicker ice. In turn, longer periods arise due to stabilization from a larger ice volume. Asymmetry of the glacial cycle growth/decay can the be ascribed to the accumulation of instabilities during a longer period (e.g. greater marine instability from deeper GIA). but also accounts for the similar extent reached by some EP ice sheets as LP ones due to the faster sliding velocities before versus after the transition. This additional factor is not accounted for in CO_2/ocean dynamical mechanisms.

There is a growing consensus that no one mechanism is responsible, but that changes in the CO_2 cycle may have further amplified deeper glacial cycles induced by a change in ice dynamics (Willeit, Ganopolski, Calov, and Brovkin, 2019; Chalk, Hain, et al., 2017; Tabor and Poulsen, 2016). Furthermore, there is a CO_2 feedback due to glacial erosion: freshly unroofed crust weathers more quickly, sequestering more CO_2. $^{87}Sr/^{86}Sr$ ratios in sea water can act as a record for this weathering and do support an increase in chemical weathering (Clark, Archer, et al., 2006). This work will use the CO_2 from the EPICA ice core back to 800 ka (Bereiter et al., 2015; Siegenthaler et al., 2005; Lüthi et al., 2008). Prior to EPICA coverage, several linear transforms of $\delta^{18}O$ are tested, based on regression of EPICA against the updated global benthic stack, ProbStack (Ahn et al., 2017; Lisiecki and Raymo, 2005). This will not comprise a test of the CO_2 contribution to any greater degree than others have done (testing multiple scenarios of CO_2 levels). The main goal in this work is to test the contribution of regolith removal to the MPT.

There are some geochemical observations supporting the Regolith Hypothesis. Multiple tills spanning Pliocene onset through LGM – dated with paleomagnetism and tephrachronology – in the mid continent tills overlying Nebraska, Iowa, Missouri, and Kansas provide the opportunity to study the character of the source material for these tills. Roy, Clark, Raisbeck, et al. (2004) studied these tills and concluded that those dating to Pliocene and early Pleistocene were depleted in soluble elements. This indicates prolonged exposure to chemical weathering: these tills were comprised of early Pleistocene regolith developed in bedrock exposed to chemical weathering. Tills dating to mid/late Pleistocene had chemical indices of alteration more similar to fresh crystalline rock, inferred to be basement rock exhumed by the NAIC likely where there was minimal regolith cover. Tills transported and deposited earlier had higher cosmogenic ^{10}Be concentrations versus tills deposited more recently, indicating earlier tills were sub-aerially exposed whereas the later tills were produced from bedrock covered by regolith (not exposed to either cosmic rays or chemical

weathering). Ensuring these differences were not due to a change in provenance Roy, Clark, Duncan, et al. (2007) used $^{40}Ar/^{39}Ar$ dating to show that the early and late till material stemmed from the same cratonic source rock. Refsnider and G. H. Miller (2013) followed a similar workflow for tills on Baffin island mapping out chemical index of alteration and ages for glacial deposits around the island. They found a similar trend: early Pleistocene tills transported from weathered regolith, late Pleistocene tills eroded from crystalline bedrock.

1.3 MODELLING THE MPT

To date modelling efforts to simulate the MPT have been simplistic and limited in scope. These efforts have largely been aimed at 0 order test of viable mechanisms for a 100 kyr glacial cycle. These mechanisms include: glacial isostatic adjustment destabilizing a larger ice sheet, lower atmospheric CO_2 concentration, or a change in ice/substrate interaction. Each test of a mechanism has assumed pre-MPT or post-MPT conditions (*e.g.* full regolith cover or PD regolith cover). Most of these studies do not test how the conditions themselves arise.

Paillard (1998) showed with a simple three state model, the collection of glacial and interglacial states during the LP (900 to PD) can be captured. This model used normalized insolation thresholds to trigger the jump from interglacial to moderate glacial and full glacial states back to the interglacial state. In contrast to the modelling of Tzedakis et al. (2017), the model transitions to a full glacial once enough time has elapsed that a sufficiently large ice volume could accumulate and surpass a proscribed threshold (the model does not directly simulate ice volume, only this elapsed time). The model does not however allow for failed glacials/interglacials as does Tzedakis et al. (2017). Paillard (1998) then extends this model to allow for dynamically calculated ice volume from a simple one-dimensional differential equation. As before this model captures the timing of interglacials for the last

900 kyr. However, this second model is also able to capture the transition to 100 kyr glacial cycles by implementing a linearly increasing ice volume threshold for transitioning to a full glacial state and adding a linear trend to the radiative forcing to simulate cooling over the Pleistocene. Tzedakis et al. (2017) are able to capture the full suite of Pleistocene interglacials using a simple statistical model similar to that of Paillard (1998) but for deglaciation. The system remains in a glacial state until a threshold of caloric summer half-year insolation is achieved, a threshold which lowers with the amount of time elapsed since the previous interglacial, representing an accumulation of instability in the system. Tzedakis et al. (2017) empirically derive an increase in this activation energy which begins at 1500 ka, reaching a maximum at 600 ka. This period defines their MPT estimate.

Using an approximate process-based model to simulate the MPT, Clark and Pollard (1998) model 1-D ice flow using the shallow ice approximation (non-linear diffusion) with sediment transported through shear deformation from sliding. They implemented a simple delay in isostatic rebound for the solid earth response. These mechanisms produced the transition from smaller 41 kyr ice sheets to larger volume 100 kyr ice sheets with similar areal extent. This seminal paper on the Regolith Hypothesis also showed that the build up of ice could produce bedrock subsidence which would make for greater marine incursion at the margin and rapid ablation when the ablation (melt) zone engulfs a greater proportion of the ice sheet than during a previous “failed” interglacial.

Another low complexity process-based simulation by Berger and Loutre (2010) assumes a gradual linear trend in CO2 from 320 at 3 Ma to 200 ppmv at present. This trend is an assumed continuation of the long term trend during the Eocene/Oligocene, and they allow that it may not hold for the Pleistocene in particular. Berger and Loutre, 2010 advocate a fully coupled climate system with as many components as possible with long run times in order to test climate

cycle response to insolation changes and atmospheric CO_2 changes. As such these components were simplified and applied to the Northern Hemisphere:

- prescribed linearly decreasing atmospheric CO_2 (from 320 to 200 ppmv),
- zonal/altitudinal ocean/atmosphere with mixed layer,
- zonal belts divided into ocean/continent types classified as ice covered or not,
- zonally-averaged quasi-geostrophic atmospheric dynamics,
- mixed layer upper ocean model with meridional heat convergence,
- non-linear diffusion of ice thickness with a parabolic lateral profile,
- GIA based on diffusion,
- and no dynamic CO_2 coupling.

The climate is spun up to quasi-equilibrium and asynchronously coupled to the ice-sheet with zonal averaged insolation. Their modelling captured the transition from mostly symmetric glacial/interglacials pre-MPT to asymmetric post-MPT and from dominant 41 kyr to 100 kyr glacial cycles across the MPT. They do not however examine the post-MPT asymmetry, the causes thereof, nor the constancy of ice areal extent. From this work they concluded that a decline in CO_2 was sufficient for a MPT.

Several studies have built on the earlier work of Clark and Pollard (1998) to simulate the effect of North American regolith removal of glacial cycles, also comparing this to the effect from a secular CO_2 decline as in Berger and Loutre (2010). These models treat the regolith removal process as a forcing instead of a system-internal process. Ganopolski and Calov, 2011 modelled the pre-MPT cycles with a comprehensive earth systems model of intermediate complexity: CLIMBER-2 has a 3D polythermal ice sheet model, SImulation COde for POLythermal Ice Sheets (SICOPOLIS), coupled to the climate model via a surface energy and

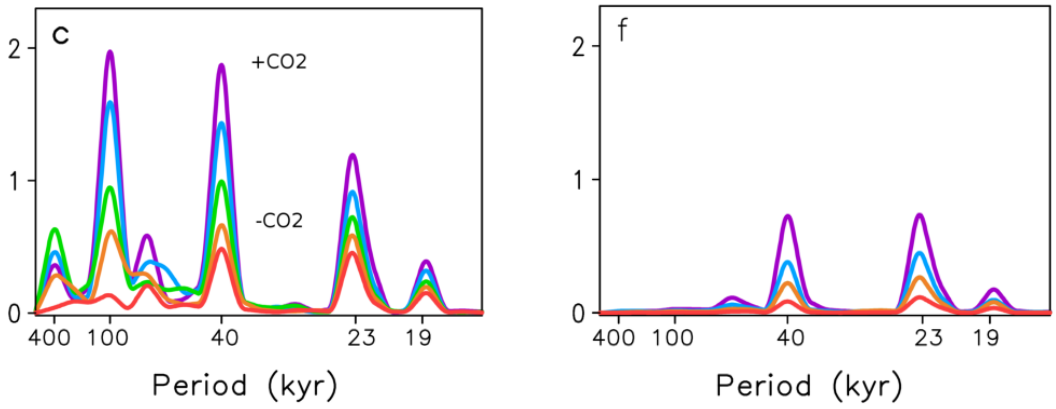

Figure 8: From Ganopolski and Calov, 2011. Power spectra of simulated ice sheet volume for decreasing CO_2 levels (red – 280, orange – 260, green – 240, blue – 220, purple – 220 ppm). Panel C is for PD sediment distribution and constant CO_2 levels, panel f is for thick sediment cover and constant CO_2 levels.

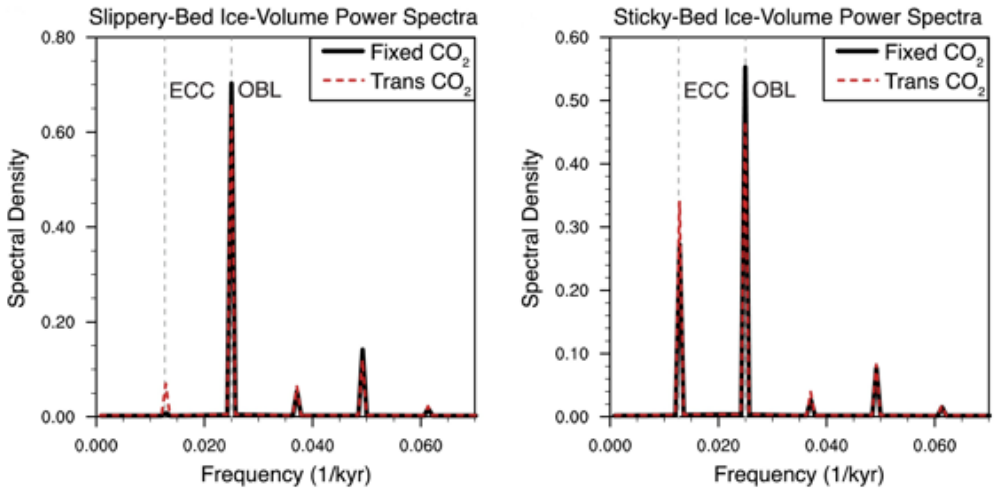

Figure 9: From Tabor and Poulsen, 2016. Power spectra of simulated ice sheet volume for soft bedded (left) and hard bedded (right) scenarios. Fixed and transient CO_2 shown in each case.

mass balance interface. The coupled model also had a dust deposition model for modifying ice albedo, vegetation model for CO_2 cycle and albedo. A suite of scenarios using a leave one out strategy (holding a given input constant/modified) tested sensitivity to input: GHG concentrations from EPICA ice cores vs constant CO_2, modified weighting of orbital parameters (constant obliquity/eccentricity), and PD sediment vs omnipresent regolith distribution. Interestingly, they have shown that for constant CO_2 lower than 260 ppm the presence of a thick sediment mask kills the 100 kyr cycle whereas present day sediment distribution gives a peak at 100 kyr (in addition to the ever present 19, 23, and 41 kyr peaks) (see fig. 8).

Tabor and Poulsen (2016) used an atmospheric GCM, land surface, vegetation, and 3D thermomechanically coupled ice sheet model to show the effect on glacial cycles from regolith cover. Sliding was parameterized from basal temperature and a hard bedded/soft bedded parameter to represent the effect of sedimentology and hydrology. Although basal processes were oversimplified and insolation cycles were not Milankovitch (80, 40, 20 kyr), they showed more power in the eccentricity band of ice sheet volume spectra for the hard bedded simulation than for the soft bedded (see fig. 9).

Willeit, Ganopolski, Calov, and Brovkin (2019) built on the work of Ganopolski and Calov (2011), also using CLIMBER-2 coupled to the ice sheet model SICOPOLIS to simulate the effect of varied regolith and CO_2 scenarios on glacial cycle evolution. Willeit, Ganopolski, Calov, and Brovkin (2019), however, simulated the full Pleistocene sequence of glacial cycles in a sequence of overlapping simulations, forcing multiple regolith area cover and prescribed CO_2 pathways justified with removal of regolith by glacial sedimentary processes and volcanic outgassing mechanisms respectively. These simulations were best correlated (lowest RMSE) to the benthic $\delta^{18}O$ record and capture the MPT, when regolith removal began around 1.5 Ma, being mostly complete by 0.5 Ma and the decline in CO_2 occurred between 2 and 1 Ma.

Berends, de Boer, and R. S. W. van de Wal (2021) used the hybrid ice sheet model ANICE driven by GCM snapshots (selected based on modelled CO_2 and ice sheets). Throughout the simulation, atmospheric CO_2 concentration is modified based on the misfit between observed (LR04, Lisiecki and Raymo, 2005) and modelled benthic $\delta^{18}O$. Through this adjustment of CO_2, they obtain a fit against EPICA with a RMSE of 13.5 ppmv, and capture the change in cyclicity and increased amplitude of $\delta^{18}O$.

1.4 PROJECT DESCRIPTION AND RESEARCH QUESTIONS

MPT modelling efforts to date have tested the plausibility that a change in basal friction might induce a change in climate cyclicity but these models have forced the different frictional basal boundary conditions. A further requirement of the Regolith Hypothesis is that the NAIC could plausibly affect this change in friction on itself. Assessing this plausibility requires bounding the timing of regolith removal by quantifying the contributing glacial sedimentary processes (production,entrainment, transport, deposition).

The Regolith Hypothesis not only relies on the progressive cycles of the NAIC removing a significant portion of the pre-existing regolith by the MPT, but also relies on a thick enough regolith mantle having developed before the Pleistocene to blanket the North American topography and produce a predominantly soft bed. Estimates of bedrock erosion and total volume of Quaternary sediment deposition do exist for select sectors of the NAIC. However, these estimates have unconstrained uncertainty bounds. We can gain confidence in the hypothesis through failure to assert the contrapositive – if a transition from soft to hard bed at the MPT is inconsistent with the sedimentary record then the Regolith Hypothesis is implausible.

The main objective of this research is to assess the self consistency of the Regolith Hypothesis. Given a model which reproduces the total Pleistocene sediment transport to the North American Atlantic Sector (M. Bell and Laine, 1985), the broad present day distribution of sediment (Taylor, 2023; Shangguan et al., 2017; Pelletier et al., 2016), and basin scale or larger estimates for bedrock erosion depth (Naylor et al., 2021; Ehlers et al., 2006), this work answers:

- are the consequent likely bounds on regolith thickness consistent with a predominantly soft bedded early Pleistocene NAIC and a subsequent transition to more hard bedded NAIC within the timing inferred for the MPT (1250-600 ka)?

- Furthermore, what is the combined effect on Pleistocene glacial cycle evolution from the frictional and topographic change due to sedimentary processes?

The relevant glacial sedimentary processes are driven not only by ice dynamical changes but by the state of the subglacial hydrologic system – water pressure controls the stress state at the bed. This stress state affects not only the sedimentary processes but also the large scale dynamics of the ice sheet and has been inferred to play a role in speeding up fast flowing regions of ice. Several formulations of the subglacial hydrologic system have been proposed but their applicability at the scales relevant to continental ice sheets and therefore the choices ice sheet modellers should make is poorly understood. In order to address the main objectives of this research and incorporate subglacial hydrology appropriately, this work assesses how the various structural choices of subglacial hydrology affect ice sheet dynamics at centennial and longer time scales.

1.4.1 *Shopping List*

Answering these questions around the Pliocene regolith layer and its removal by the end of the MPT requires a model which incorporates all of the relevant processes. These processes include:

- a climate which is feasibly simulated for multi-million year time frames with minimal forcing (orbital insolation and greenhouse gas only),
- ice sheet dynamics with sufficiently complete stress balance for realistic ice streaming and self-consistent thermo-mechanics to enable realistic simulation of the basal boundary (*i.e.*, temperature and effective pressure).
- a solid earth system capable of realistically simulating topographic deflection due to surface load changes from all sources (ice, water bedrock and sediment),
- Mass conserving sediment production and transport which can capture the full sediment budget, simulating bedrock erosion and sediment movement in line with the current best understanding of glacial sedimentary processes,
- and a subglacial hydrological model which simulates basal effective pressure which abrasion, quarrying, entrainment, viscoplastic soft sediment deformation, and ice sheet basal sliding velocity all depend.

Many of these components were previously available in the GSM, those that were not have been implemented and/or improved upon in this project. Given the timescales involved, it is not possible to force this system with a climatology-based on the Greenland ice core record. A new climate coupling based on a parameterized weighting of temperature and precipitation fields from two components has been implemented by Lev Tarasov in the GSM. The first is an energy balance model (EBM) with 2D geography, non-linear snow and ice albedo feedbacks, and a slab ocean. The second is a glacial indexing of a set of empirical orthogonal

functions (EOFs) extracted from the PMIP II and III modelling results. These modelling projects used 3 ice sheet boundary conditions – ICE4G, Glac1D, and ANU. Of these, ICE4G did not have a major Keewatin Ice Dome while Glac1D did. The glacial indexing (interpolation between present day and last glacial maximum conditions) of the EOFs relies both on the height of the simulated Keewatin ice dome from the ice dynamical model and the temperature of the North Atlantic from the EBM slab ocean model. This model is tuned here to reproduce characteristics of both the Early and Late Pleistocene based on the available evidence (see chap. 5 and 6).

The coupling of the solid earth model to changing bed load was done by Lev Tarasov with advice on the design by myself for the purposes of this project and tested and applied by myself. The sediment model sliding velocity coupling was performed by myself and uses an empirical relationship between soft bed coverage and subglacial sediment thickness simulated by the sediment model. Updates to the sediment model of Melanson, T. Bell, and Tarasov (2013) implemented in this project are details in § 2.2.6. Verification and sensitivity analysis of this model are detailed in § 5.2.4 and 5.2.5

Due to the array of subglacial hydrologic structural choices ice sheet modellers must make, several were incorporated into the GSM. In the first version of this model, Kavanagh and Tarasov (2018) incorporated the poro-elastic hydrology. Following this first version the model is extended here to include the highly non-linear linked-cavity system and the simplest case leaky-bucket (0-dimensional, non-mass conserving) system.

1.4.2 *Project Layout*

Simulation of regolith removal requires reliable simulation of water pressure in the subglacial hydrologic system and a tested sediment model coupled in an earth

systems model with the processes laid out above. Further, bounds on Pliocene regolith thickness are necessary for establishing initial conditions for simulations of regolith removal and the MPT. In order to reliably simulate the effective pressure at the base of the ice sheet, three subglacial hydrology systems are explored in the subglacial hydrology model. This required the implementation and testing of those systems. To determine which system is most applicable at the continental ice sheet scale all three are compared and contrasted under the lens of ice stream surging (chap. 4).

In order to determine reasonable bounds on Pliocene regolith thickness for the purpose of testing the regolith hypothesis, the GSM was applied to the North American and Eurasian contexts to gauge what mean Pliocene regolith thickness best matches the available evidence in chap. 5. The contribution from regolith removal and topographic change to the MPT in particular and Pleistocene glacial cycle evolution more generally is then presented in chap. 6. This work is summarized in chap. 7. The relevant processes – glacial sedimentary processes and subglacial hydrology – are reviewed the next two chapters (chap. 2 and 3).

REFERENCES

Ahn, S., D. Khider, L. E. Lisiecki, and C. E. Lawrence (2017). "A probabilistic Pliocene–Pleistocene stack of benthic δ^{18}O using a profile hidden Markov model". In: *Dynamics and Statistics of the Climate System* 2.1. ISSN: 2059-6987. DOI: 10.1093/climsys/dzx002. URL: http://dx.doi.org/10.1093/climsys/dzx002.

Balco, G. and C. W. Rovey (Sept. 2010). "Absolute chronology for major Pleistocene advances of the Laurentide Ice Sheet". In: *Geology* 38.9, pp. 795–798. ISSN: 0091-7613. DOI: 10.1130/g30946.1. URL: http://dx.doi.org/10.1130/G30946.1.

Barendregt, R. W. and A. Duk-Rodkin (2004). "Chronology and extent of Late Cenozoic ice sheets in North America: A magnetostratigraphic assessment". In: *Developments in Quaternary Sciences*, pp. 1–7. ISSN: 1571-0866. DOI: 10.1016/s1571-0866(04)80181-7. URL: http://dx.doi.org/10.1016/S1571-0866(04)80181-7.

Bartoli, G., M. Sarnthein, M. Weinelt, H. Erlenkeuser, D. Garbe-Schönberg, and D. Lea (Aug. 2005). "Final closure of Panama and the onset of northern hemisphere glaciation". In: *Earth and Planetary Science Letters* 237.1-2, pp. 33–44. ISSN: 0012-821X. DOI: 10.1016/j.epsl.2005.06.020. URL: http://dx.doi.org/10.1016/j.epsl.2005.06.020.

Bell, M. and E. P. Laine (Mar. 1985). "Erosion of the Laurentide Region of North America by Glacial and Glaciofluvial Processes". In: *Quaternary Research* 23.02, pp. 154–174. ISSN: 1096-0287. DOI: 10.1016/0033-5894(85)90026-2. URL: http://dx.doi.org/10.1016/0033-5894(85)90026-2.

Bereiter, B., S. Eggleston, J. Schmitt, C. Nehrbass-Ahles, T. F. Stocker, H. Fischer, S. Kipfstuhl, and J. Chappellaz (Jan. 2015). "Revision of the EPICA Dome C CO2 record from 800 to 600 kyr before present". In: *Geophysical Research Letters* 42.2, pp. 542–549. ISSN: 0094-8276. DOI: 10.1002/2014gl061957. URL: http://dx.doi.org/10.1002/2014GL061957.

Berends, C. J., B. de Boer, and R. S. W. van de Wal (Feb. 2021). "Reconstructing the evolution of ice sheets, sea level, and atmospheric CO_2 during the past 3.6 million years". In: *Climate of the Past* 17.1, pp. 361–377. ISSN: 1814-9332. DOI: 10.5194/cp-17-361-2021. URL: http://dx.doi.org/10.5194/cp-17-361-2021.

Berger, A. and M. Loutre (Jan. 1991). "Insolation values for the climate of the last 10 million years". In: *Quaternary Science Reviews* 10.4, pp. 297–317. ISSN: 0277-3791. DOI: 10.1016/0277-3791(91)90033-q. URL: http://dx.doi.org/10.1016/0277-3791(91)90033-Q.

— (July 2010). "Modeling the 100-kyr glacial–interglacial cycles". In: *Global and Planetary Change* 72.4, pp. 275–281. ISSN: 0921-8181. DOI: 10.1016/j.gloplacha.2010.01.003. URL: http://dx.doi.org/10.1016/j.gloplacha.2010.01.003.

Bintanja, R. and R. S. W. van de Wal (Aug. 2008). "North American ice-sheet dynamics and the onset of 100,000-year glacial cycles". In: *Nature* 454.7206, pp. 869–872. ISSN: 1476-4687. DOI: 10.1038/nature07158. URL: http://dx.doi.org/10.1038/nature07158.

Blakey, R. (Jan. 2021). "Paleotectonic and paleogeographic history of the Arctic region". In: *Atlantic Geology* 57, pp. 007–039. ISSN: 0843-5561. DOI: 10.4138/atlgeol.2021.002. URL: http://dx.doi.org/10.4138/atlgeol.2021.002.

Brigham-Grette, J., M. Melles, P. Minyuk, A. Andreev, P. Tarasov, R. DeConto, S. Koenig, N. Nowaczyk, V. Wennrich, P. Rosen, and et al. (May 2013). "Pliocene Warmth, Polar Amplification, and Stepped Pleistocene Cooling Recorded in NE Arctic Russia". In: *Science* 340.6139, pp. 1421–1427. ISSN: 1095-9203. DOI: 10.1126/science.1233137. URL: http://dx.doi.org/10.1126/science.1233137.

Bueler, E. and W. van Pelt (June 2015). "Mass-conserving subglacial hydrology in the Parallel Ice Sheet Model version 0.6". In: *Geoscientific Model Development* 8.6, pp. 1613–1635. ISSN: 1991-9603. DOI: 10.5194/gmd-8-1613-2015. URL: http://dx.doi.org/10.5194/gmd-8-1613-2015.

Chalk, T. B., E. Capron, M. Drew, and K. Panagiotopoulos (Dec. 2017). "Interglacials of the 41 ka-world and the Mid-Pleistocene Transition". In: *Past Global Changes Magazine* 25.3, pp. 155–155. ISSN: 2411-9180. DOI: 10.22498/pages.25.3.155. URL: http://dx.doi.org/10.22498/pages.25.3.155.

Chalk, T. B., M. P. Hain, G. L. Foster, E. J. Rohling, P. F. Sexton, M. P. S. Badger, S. G. Cherry, A. P. Hasenfratz, G. H. Haug, S. L. Jaccard, and et al. (Nov. 2017). "Causes of ice age intensification across the Mid-Pleistocene Transition".

In: *Proceedings of the National Academy of Sciences* 114.50, pp. 13114–13119. ISSN: 1091-6490. DOI: 10.1073/pnas.1702143114. URL: http://dx.doi.org/10.1073/pnas.1702143114.

Clark, P. U., D. Archer, D. Pollard, J. D. Blum, J. A. Rial, V. Brovkin, A. C. Mix, N. G. Pisias, and M. Roy (Dec. 2006). "The middle Pleistocene transition: characteristics, mechanisms, and implications for long-term changes in atmospheric pCO2". In: *Quaternary Science Reviews* 25.23-24, pp. 3150–3184. ISSN: 0277-3791. DOI: 10.1016/j.quascirev.2006.07.008. URL: http://dx.doi.org/10.1016/j.quascirev.2006.07.008.

Clark, P. U. and D. Pollard (Feb. 1998). "Origin of the Middle Pleistocene Transition by ice sheet erosion of regolith". In: *Paleoceanography* 13.1, pp. 1–9. ISSN: 0883-8305. DOI: 10.1029/97pa02660. URL: http://dx.doi.org/10.1029/97PA02660.

Dalton, A. S., M. Margold, C. R. Stokes, L. Tarasov, A. S. Dyke, R. S. Adams, S. Allard, H. E. Arends, N. Atkinson, J. W. Attig, P. J. Barnett, R. L. Barnett, M. Batterson, P. Bernatchez, H. W. Borns, A. Breckenridge, J. P. Briner, E. Brouard, J. E. Campbell, A. E. Carlson, J. J. Clague, B. B. Curry, R.-A. Daigneault, H. Dubé-Loubert, D. J. Easterbrook, D. A. Franzi, H. G. Friedrich, S. Funder, M. S. Gauthier, A. S. Gowan, K. L. Harris, B. Hétu, T. S. Hooyer, C. E. Jennings, M. D. Johnson, A. E. Kehew, S. E. Kelley, D. Kerr, E. L. King, K. K. Kjeldsen, A. R. Knaeble, P. Lajeunesse, T. R. Lakeman, M. Lamothe, P. Larson, M. Lavoie, H. M. Loope, T. V. Lowell, B. A. Lusardi, L. Manz, I. McMartin, F. C. Nixon, S. Occhietti, M. A. Parkhill, D. J. Piper, A. G. Pronk, P. J. Richard, J. C. Ridge, M. Ross, M. Roy, A. Seaman, J. Shaw, R. R. Stea, J. T. Teller, W. B. Thompson, L. H. Thorleifson, D. J. Utting, J. J. Veillette, B. C. Ward, T. K. Weddle, and H. E. Wright (Apr. 2020). "An updated radiocarbon-based ice margin chronology for the last deglaciation of the North American Ice Sheet Complex". In: *Quaternary Science Reviews* 234,

p. 106223. ISSN: 0277-3791. DOI: 10.1016/j.quascirev.2020.106223. URL: http://dx.doi.org/10.1016/j.quascirev.2020.106223.

de Boer, B., L. J. Lourens, and R. S. van de Wal (Jan. 2014). "Persistent 400,000-year variability of Antarctic ice volume and the carbon cycle is revealed throughout the Plio-Pleistocene". In: *Nature Communications* 5.1. ISSN: 2041-1723. DOI: 10.1038/ncomms3999. URL: http://dx.doi.org/10.1038/ncomms3999.

De Schepper, S., P. L. Gibbard, U. Salzmann, and J. Ehlers (Aug. 2014). "A global synthesis of the marine and terrestrial evidence for glaciation during the Pliocene Epoch". In: *Earth-Science Reviews* 135, pp. 83–102. ISSN: 0012-8252. DOI: 10.1016/j.earscirev.2014.04.003. URL: http://dx.doi.org/10.1016/j.earscirev.2014.04.003.

Dyez, K. A., B. Hönisch, and G. A. Schmidt (Nov. 2018). "Early Pleistocene Obliquity-Scale pCO 2 Variability at 1.5 Million Years Ago". In: *Paleoceanography and Paleoclimatology* 33.11, pp. 1270–1291. ISSN: 2572-4525. DOI: 10.1029/2018pa003349. URL: http://dx.doi.org/10.1029/2018PA003349.

Ehlers, T. A., K. A. Farley, M. E. Rusmore, and G. J. Woodsworth (2006). "Apatite (U-Th)/He signal of large-magnitude accelerated glacial erosion, southwest British Columbia". In: *Geology* 34.9, p. 765. ISSN: 0091-7613. DOI: 10.1130/g22507.1. URL: http://dx.doi.org/10.1130/G22507.1.

Elderfield, H., P. Ferretti, M. Greaves, S. Crowhurst, I. N. McCave, D. Hodell, and A. M. Piotrowski (Aug. 2012). "Evolution of Ocean Temperature and Ice Volume Through the Mid-Pleistocene Climate Transition". In: *Science* 337.6095, pp. 704–709. ISSN: 1095-9203. DOI: 10.1126/science.1221294. URL: http://dx.doi.org/10.1126/science.1221294.

England, J. (1987). "Glaciation and the evolution of the Canadian high arctic landscape". In: *Geology* 15.5, p. 419. ISSN: 0091-7613. DOI: 10.1130/0091-7613(1987)15<419:gateot>2.0.co;2. URL: http://dx.doi.org/10.1130/0091-7613(1987)15%3C419:GATEOT%3E2.0.CO;2.

Feng, R., B. L. Otto-Bliesner, T. L. Fletcher, C. R. Tabor, A. P. Ballantyne, and E. C. Brady (May 2017). "Amplified Late Pliocene terrestrial warmth in northern high latitudes from greater radiative forcing and closed Arctic Ocean gateways". In: *Earth and Planetary Science Letters* 466, pp. 129–138. ISSN: 0012-821X. DOI: 10.1016/j.epsl.2017.03.006. URL: http://dx.doi.org/10.1016/j.epsl.2017.03.006.

Flowers, G. (Nov. 2000). "A Multicomponent Coupled Model of Glacier Hydrology". PhD thesis. Department of Earth, Ocean and Atmospheric Sciences Faculty of Science 2020 – 2207 Main Mall Vancouver, BC Canada V6T 1Z4: University of British Columbia.

Ganopolski, A. and R. Calov (Dec. 2011). "The Role of Orbital Forcing, Carbon Dioxide and Regolith in 100 kyr Glacial Cycles". In: *Climate of the Past* 7, pp. 1415–1425.

Gao, C., J. H. McAndrews, X. Wang, J. Menzies, C. L. Turton, B. D. Wood, J. Pei, and C. Kodors (Nov. 2012). "Glaciation of North America in the James Bay Lowland, Canada, 3.5 Ma". In: *Geology* 40.11, pp. 975–978. ISSN: 0091-7613. DOI: 10.1130/g33092.1. URL: http://dx.doi.org/10.1130/G33092.1.

Garzione, C. N. (2008). "Surface uplift of Tibet and Cenozoic global cooling". In: *Geology* 36.12, pp. 1003–1004. ISSN: 0091-7613. DOI: 10.1130/focus122008.1. URL: http://dx.doi.org/10.1130/focus122008.1.

Gosse, J. C., A. P. Ballantyne, J. D. Barker, A. Z. Csank, T. L. Fletcher, G. W. Grant, D. R. Greenwood, R. D. MacPhee, and N. Rybczynski (Apr. 2017). "PoLAR-FIT: Pliocene Landscapes and Arctic Remains—Frozen in Time". In: *Geoscience Canada* 44.1, p. 47. ISSN: 0315-0941. DOI: 10.12789/geocanj.2017.44.116. URL: http://dx.doi.org/10.12789/geocanj.2017.44.116.

Haug, G. H., A. Ganopolski, D. M. Sigman, A. Rosell-Mele, G. E. A. Swann, R. Tiedemann, S. L. Jaccard, J. Bollmann, M. A. Maslin, M. J. Leng, and G. Eglinton (Feb. 2005). "North Pacific seasonality and the glaciation of North

America 2.7 million years ago". In: *Nature* 433.7028, pp. 821–825. ISSN: 1476-4687. DOI: 10.1038/nature03332. URL: http://dx.doi.org/10.1038/nature03332.

Hays, J. D., J. Imbrie, and N. J. Shackleton (Dec. 1976). "Variations in the Earth's Orbit: Pacemaker of the Ice Ages". In: *Science* 194.4270, pp. 1121–1132. ISSN: 1095-9203. DOI: 10.1126/science.194.4270.1121. URL: http://dx.doi.org/10.1126/science.194.4270.1121.

Head, M. J. and P. L. Gibbard (Oct. 2015). "Formal subdivision of the Quaternary System/Period: Past, present, and future". In: *Quaternary International* 383, pp. 4–35. ISSN: 1040-6182. DOI: 10.1016/j.quaint.2015.06.039. URL: http://dx.doi.org/10.1016/j.quaint.2015.06.039.

Hönisch, B., N. G. Hemming, D. Archer, M. Siddall, and J. F. McManus (June 2009). "Atmospheric Carbon Dioxide Concentration Across the Mid-Pleistocene Transition". In: *Science* 324.5934, pp. 1551–1554. ISSN: 1095-9203. DOI: 10.1126/science.1171477. URL: http://dx.doi.org/10.1126/science.1171477.

Huybers, P. and E. Tziperman (Feb. 2008). "Integrated summer insolation forcing and 40,000-year glacial cycles: The perspective from an ice-sheet/energy-balance model". In: *Paleoceanography* 23.1, n/a–n/a. ISSN: 0883-8305. DOI: 10.1029/2007pa001463. URL: http://dx.doi.org/10.1029/2007PA001463.

Imbrie, J., A. Berger, E. A. Boyle, S. C. Clemens, A. Duffy, W. R. Howard, G. Kukla, J. Kutzbach, D. G. Martinson, A. McIntyre, A. C. Mix, B. Molfino, J. J. Morley, L. C. Peterson, N. G. Pisias, W. L. Prell, M. E. Raymo, N. J. Shackleton, and J. R. Toggweiler (Dec. 1993). "On the structure and origin of major glaciation cycles 2. The 100,000-year cycle". In: *Paleoceanography* 8.6, pp. 699–735. ISSN: 0883-8305. DOI: 10.1029/93pa02751. URL: http://dx.doi.org/10.1029/93PA02751.

Kageyama, M., S. P. Harrison, M.-L. Kapsch, M. Lofverstrom, J. M. Lora, U. Mikolajewicz, S. Sherriff-Tadano, T. Vadsaria, A. Abe-Ouchi, N. Bouttes, and

et al. (May 2021). "The PMIP4 Last Glacial Maximum experiments: preliminary results and comparison with the PMIP3 simulations". In: *Climate of the Past* 17.3, pp. 1065–1089. ISSN: 1814-9332. DOI: 10.5194/cp-17-1065-2021. URL: http://dx.doi.org/10.5194/cp-17-1065-2021.

Kavanagh, M. and L. Tarasov (Aug. 2018). "BrAHMs V1.0: a fast, physically based subglacial hydrology model for continental-scale application". In: *Geoscientific Model Development* 11.8, pp. 3497–3513. ISSN: 1991-9603. DOI: 10.5194/gmd-11-3497-2018. URL: http://dx.doi.org/10.5194/gmd-11-3497-2018.

Laskar, J., A. Fienga, M. Gastineau, and H. Manche (July 2011). "La2010: a new orbital solution for the long-term motion of the Earth". In: *Astronomy & Astrophysics* 532, A89. ISSN: 1432-0746. DOI: 10.1051/0004-6361/201116836. URL: http://dx.doi.org/10.1051/0004-6361/201116836.

Laskar, J., P. Robutel, F. Joutel, M. Gastineau, A. C. M. Correia, and B. Levrard (Nov. 2004). "A long-term numerical solution for the insolation quantities of the Earth". In: *Astronomy & Astrophysics* 428.1, pp. 261–285. ISSN: 1432-0746. DOI: 10.1051/0004-6361:20041335. URL: http://dx.doi.org/10.1051/0004-6361:20041335.

Laske, G., G. Masters, Z. Ma, and M. E. Pasyanos (2013). "Update on CRUST1.0: a 1-degree Global Model of Earth's Crust". In: *Geophysical Research Abstracts*. Vol. 15. European Geosciences Union General Assembly 2013 2658. European Geosciences Union. Vienna,Austria.

Lisiecki, L. E. and M. E. Raymo (Jan. 2005). "A Pliocene-Pleistocene stack of 57 globally distributed benthic δ^{18}O records". In: *Paleoceanography* 20.1, n/a–n/a. ISSN: 0883-8305. DOI: 10.1029/2004pa001071. URL: http://dx.doi.org/10.1029/2004PA001071.

Lüthi, D., M. Le Floch, B. Bereiter, T. Blunier, J.-M. Barnola, U. Siegenthaler, D. Raynaud, J. Jouzel, H. Fischer, K. Kawamura, and T. F. Stocker (May 2008). "High-resolution carbon dioxide concentration record 650,000-800,000

years before present". In: *Nature* 453.7193, pp. 379–382. ISSN: 1476-4687. DOI: 10.1038/nature06949. URL: http://dx.doi.org/10.1038/nature06949.

Marincovich, L. and A. Y. Gladenkov (Jan. 1999). "Evidence for an early opening of the Bering Strait". In: *Nature* 397.6715, pp. 149–151. ISSN: 1476-4687. DOI: 10.1038/16446. URL: http://dx.doi.org/10.1038/16446.

Maslin, M., G. Haug, M. Sarnthein, R. Tiedemann, H. Erlenkeuser, and R. Stax (Nov. 1995). "Northwest Pacific Site 882: The Initiation of Northern Hemisphere Glaciation". In: *Proceedings of the Ocean Drilling Program*. DOI: 10.2973/odp.proc.sr.145.119.1995. URL: http://dx.doi.org/10.2973/odp.proc.sr.145.119.1995.

Medvedev, S., E. H. Hartz, and J. I. Faleide (Sept. 2018). "Erosion-driven vertical motions of the circum Arctic: Comparative analysis of modern topography". In: *Journal of Geodynamics* 119, pp. 62–81. ISSN: 0264-3707. DOI: 10.1016/j.jog.2018.04.003. URL: http://dx.doi.org/10.1016/j.jog.2018.04.003.

Melanson, A., T. Bell, and L. Tarasov (May 2013). "Numerical modelling of subglacial erosion and sediment transport and its application to the North American ice sheets over the Last Glacial cycle". In: *Quaternary Science Reviews* 68, pp. 154–174. ISSN: 0277-3791. DOI: 10.1016/j.quascirev.2013.02.017. URL: http://dx.doi.org/10.1016/j.quascirev.2013.02.017.

Merrill, G. P. (1897). "A treatise on rocks, rock-weathering and soils;" in: DOI: 10.5962/bhl.title.66971. URL: http://dx.doi.org/10.5962/bhl.title.66971.

Miller, K. G., J. V. Browning, W. J. Schmelz, R. E. Kopp, G. S. Mountain, and J. D. Wright (May 2020). "Cenozoic sea-level and cryospheric evolution from deep-sea geochemical and continental margin records". In: *Science Advances* 6.20. ISSN: 2375-2548. DOI: 10.1126/sciadv.aaz1346. URL: http://dx.doi.org/10.1126/sciadv.aaz1346.

Mitchell, W. T., N. Rybczynski, C. Schröder-Adams, P. B. Hamilton, R. Smith, and M. Douglas (June 2016). "Stratigraphic and Paleoenvironmental Reconstruction of a Mid-Pliocene Fossil Site in the High Arctic (Ellesmere Island, Nunavut): Evidence of an Ancient Peatland with Beaver Activity". In: *ARCTIC* 69.2. ISSN: 0004-0843. DOI: 10.14430/arctic4567. URL: http://dx.doi.org/10.14430/arctic4567.

Molnar, P. (Apr. 2008). "Closing of the Central American Seaway and the Ice Age: A critical review". In: *Paleoceanography* 23.2, n/a–n/a. ISSN: 0883-8305. DOI: 10.1029/2007pa001574. URL: http://dx.doi.org/10.1029/2007PA001574.

Montes, C., A. Cardona, C. Jaramillo, A. Pardo, J. C. Silva, V. Valencia, C. Ayala, L. C. Pérez-Angel, L. A. Rodriguez-Parra, V. Ramirez, and H. Niño (Apr. 2015). "Middle Miocene closure of the Central American Seaway". In: *Science* 348.6231, pp. 226–229. ISSN: 1095-9203. DOI: 10.1126/science.aaa2815. URL: http://dx.doi.org/10.1126/science.aaa2815.

Mudelsee, M. and M. E. Raymo (Dec. 2005). "Slow dynamics of the Northern Hemisphere glaciation". In: *Paleoceanography* 20.4, n/a–n/a. ISSN: 0883-8305. DOI: 10.1029/2005pa001153. URL: http://dx.doi.org/10.1029/2005PA001153.

Naylor, S., A. D. Wickert, D. A. Edmonds, and B. J. Yanites (Nov. 2021). "Landscape evolution under the southern Laurentide Ice Sheet". In: *Science Advances* 7.48. ISSN: 2375-2548. DOI: 10.1126/sciadv.abj2938. URL: http://dx.doi.org/10.1126/sciadv.abj2938.

Paillard, D. (Jan. 1998). "The timing of Pleistocene glaciations from a simple multiple-state climate model". In: *Nature* 391.6665, pp. 378–381. ISSN: 1476-4687. DOI: 10.1038/34891. URL: http://dx.doi.org/10.1038/34891.

Parent, M., M. Ross, D. Howlett, and K. Bédard (2021). "3D model of the Quaternary sediments in the St. Lawrence valley and adjacent regions, southern Quebec and eastern Ontario". In: DOI: 10.4095/329082. URL: http://dx.doi.org/10.4095/329082.

Pelletier, J. D., P. D. Broxton, P. Hazenberg, X. Zeng, P. A. Troch, G.-Y. Niu, Z. Williams, M. A. Brunke, and D. Gochis (Jan. 2016). "A gridded global data set of soil, intact regolith, and sedimentary deposit thicknesses for regional and global land surface modeling". In: *Journal of Advances in Modeling Earth Systems* 8.1, pp. 41–65. ISSN: 1942-2466. DOI: 10.1002/2015ms000526. URL: http://dx.doi.org/10.1002/2015MS000526.

Pena, L. D. and S. L. Goldstein (June 2014). "Thermohaline circulation crisis and impacts during the mid-Pleistocene transition". In: *Science* 345.6194, pp. 318–322. ISSN: 1095-9203. DOI: 10.1126/science.1249770. URL: http://dx.doi.org/10.1126/science.1249770.

Pianosi, F. and T. Wagener (May 2015). "A simple and efficient method for global sensitivity analysis based on cumulative distribution functions". In: *Environmental Modelling & Software* 67, pp. 1–11. ISSN: 1364-8152. DOI: 10.1016/j.envsoft.2015.01.004. URL: http://dx.doi.org/10.1016/j.envsoft.2015.01.004.

Pisias, N. and T. Moore (Feb. 1981). "The evolution of Pleistocene climate: A time series approach". In: *Earth and Planetary Science Letters* 52.2, pp. 450–458. ISSN: 0012-821X. DOI: 10.1016/0012-821x(81)90197-7. URL: http://dx.doi.org/10.1016/0012-821X(81)90197-7.

Rae, J. W., Y. G. Zhang, X. Liu, G. L. Foster, H. M. Stoll, and R. D. Whiteford (May 2021). "Atmospheric CO2 over the Past 66 Million Years from Marine Archives". In: *Annual Review of Earth and Planetary Sciences* 49.1, pp. 609–641. ISSN: 1545-4495. DOI: 10.1146/annurev-earth-082420-063026. URL: http://dx.doi.org/10.1146/annurev-earth-082420-063026.

Raymo, M. E. and K. H. Nisancioglu (Mar. 2003). "The 41 kyr world: Milankovitch's other unsolved mystery". In: *Paleoceanography* 18.1, n/a–n/a. ISSN: 0883-8305. DOI: 10.1029/2002pa000791. URL: http://dx.doi.org/10.1029/2002PA000791.

Refsnider, K. A. and G. H. Miller (May 2013). "Ice-sheet erosion and the stripping of Tertiary regolith from Baffin Island, eastern Canadian Arctic". In: *Quaternary Science Reviews* 67, pp. 176–189. ISSN: 0277-3791. DOI: 10.1016/j.quascirev.2013.01.010. URL: http://dx.doi.org/10.1016/j.quascirev.2013.01.010.

Rohling, E. J., G. L. Foster, K. M. Grant, G. Marino, A. P. Roberts, M. E. Tamisiea, and F. Williams (Apr. 2014). "Sea-level and deep-sea-temperature variability over the past 5.3 million years". In: *Nature* 508.7497, pp. 477–482. ISSN: 1476-4687. DOI: 10.1038/nature13230. URL: http://dx.doi.org/10.1038/nature13230.

Rohling, E. J., G. L. Foster, T. M. Gernon, K. M. Grant, D. Heslop, F. D. Hibbert, A. P. Roberts, and J. Yu (Nov. 2022). "Comparison and Synthesis of Sea-Level and Deep-Sea Temperature Variations Over the Past 40 Million Years". In: *Reviews of Geophysics* 60.4. ISSN: 1944-9208. DOI: 10.1029/2022rg000775. URL: http://dx.doi.org/10.1029/2022RG000775.

Roy, M., P. U. Clark, R. A. Duncan, and S. R. Hemming (Sept. 2007). "Insights into the late Cenozoic configuration of the Laurentide Ice Sheet from 40Ar/39Ar dating of glacially transported minerals in midcontinent tills". In: *Geochemistry, Geophysics, Geosystems* 8.9, n/a–n/a. ISSN: 1525-2027. DOI: 10.1029/2006gc001572. URL: http://dx.doi.org/10.1029/2006GC001572.

Roy, M., P. U. Clark, G. M. Raisbeck, and F. Yiou (Nov. 2004). "Geochemical constraints on the regolith hypothesis for the middle Pleistocene transition". In: *Earth and Planetary Science Letters* 227.3-4, pp. 281–296. ISSN: 0012-821X. DOI: 10.1016/j.epsl.2004.09.001. URL: http://dx.doi.org/10.1016/j.epsl.2004.09.001.

Russell, H., N. Atkinson, A. Bajc, B. Brodaric, G. Keller, K. Lo, M. Parent, M. Pyne, R. Smith, and B. Todd (2017). "A 3-D framework of surficial geology for Canada". In: *Joint Annual Meeting, Programs with Abstracts* 40. URL:

https://geoscan.nrcan.gc.ca/starweb/geoscan/servlet.starweb?path=geoscan/fulle.web&search1=R=327036.

Rybczynski, N., J. C. Gosse, C. Richard Harington, R. A. Wogelius, A. J. Hidy, and M. Buckley (Mar. 2013). "Mid-Pliocene warm-period deposits in the High Arctic yield insight into camel evolution". In: *Nature Communications* 4.1. ISSN: 2041-1723. DOI: 10.1038/ncomms2516. URL: http://dx.doi.org/10.1038/ncomms2516.

Saltelli, A., M. Ratto, T. Andres, F. Campolongo, J. Cariboni, D. Gatelli, M. Saisana, and S. Tarantola (2008). *Global Sensitivity Analysis. The Primer*. 1st ed. The Atrium, Southern Gate, Chichester,West Sussex PO19 8SQ, England: John Wiley & Sons, Ltd. ISBN: 978-0-470-05997-5.

Schoof, C. (Dec. 2010). "Ice-sheet acceleration driven by melt supply variability". In: *Nature* 468.7325, pp. 803–806. ISSN: 1476-4687. DOI: 10.1038/nature09618. URL: http://dx.doi.org/10.1038/nature09618.

Setterholm, D. R. and G. B. Morey (1995). In: DOI: 10.3133/b1989h. URL: http://dx.doi.org/10.3133/b1989H.

Shackleton, N. J., J. Backman, H. Zimmerman, D. V. Kent, M. A. Hall, D. G. Roberts, D. Schnitker, J. G. Baldauf, A. Desprairies, R. Homrighausen, and et al. (Feb. 1984). "Oxygen isotope calibration of the onset of ice-rafting and history of glaciation in the North Atlantic region". In: *Nature* 307.5952, pp. 620–623. ISSN: 1476-4687. DOI: 10.1038/307620a0. URL: http://dx.doi.org/10.1038/307620a0.

Shackleton, N. J., A. Berger, and W. R. Peltier (1990). "An alternative astronomical calibration of the lower Pleistocene timescale based on ODP Site 677". In: *Transactions of the Royal Society of Edinburgh: Earth Sciences* 81.04, pp. 251–261. ISSN: 1473-7116. DOI: 10.1017/s0263593300020782. URL: http://dx.doi.org/10.1017/S0263593300020782.

Shackleton, N. (July 1967). "Oxygen Isotope Analyses and Pleistocene Temperatures Re-assessed". In: *Nature* 215.5096, pp. 15–17. ISSN: 1476-4687. DOI: 10.1038/215015a0. URL: http://dx.doi.org/10.1038/215015a0.

Shangguan, W., T. Hengl, J. Mendes de Jesus, H. Yuan, and Y. Dai (Jan. 2017). "Mapping the global depth to bedrock for land surface modeling". In: *Journal of Advances in Modeling Earth Systems* 9.1, pp. 65–88. ISSN: 1942-2466. DOI: 10.1002/2016ms000686. URL: http://dx.doi.org/10.1002/2016MS000686.

Siegenthaler, U., T. F. Stocker, E. Monnin, D. Lüthi, J. Schwander, B. Stauffer, D. Raynaud, J.-M. Barnola, H. Fischer, V. Masson-Delmotte, and J. Jouzel (Nov. 2005). "Stable Carbon Cycle–Climate Relationship During the Late Pleistocene". In: *Science* 310.5752, pp. 1313–1317. ISSN: 1095-9203. DOI: 10.1126/science.1120130. URL: http://dx.doi.org/10.1126/science.1120130.

Smith, I. R. and K. Lesk-Winfield (2010). "Drift isopach, till isopach, and till facies reconstructions for Northwest Territories and northern Yukon". In: DOI: 10.4095/261783. URL: http://dx.doi.org/10.4095/261783.

Soller, D. R. and C. P. Garrity (2018). "Quaternary sediment thickness and bedrock topography of the glaciated United States east of the Rocky Mountains". In: *Scientific Investigations Map*. ISSN: 2329-132X. DOI: 10.3133/sim3392. URL: http://dx.doi.org/10.3133/sim3392.

Spratt, R. M. and L. E. Lisiecki (Apr. 2016). "A Late Pleistocene sea level stack". In: *Climate of the Past* 12.4, pp. 1079–1092. ISSN: 1814-9332. DOI: 10.5194/cp-12-1079-2016. URL: http://dx.doi.org/10.5194/cp-12-1079-2016.

Stap, L. B., B. de Boer, M. Ziegler, R. Bintanja, L. J. Lourens, and R. S. van de Wal (Apr. 2016). "CO_2 over the past 5 million years: Continuous simulation and new δ^{11} B-based proxy data". In: *Earth and Planetary Science Letters* 439, pp. 1–10. ISSN: 0012-821X. DOI: 10.1016/j.epsl.2016.01.022. URL: http://dx.doi.org/10.1016/j.epsl.2016.01.022.

Stashin, S. (2021). “Late Cenozoic Basin Evolution of the western Canadian Arctic Archipelago: The Beaufort Formation and Iperk Sequence”. Masters Thesis. Dalhousie University. URL: http://hdl.handle.net/10222/80367.

Straume, E. O., C. Gaina, S. Medvedev, K. Hochmuth, K. Gohl, J. M. Whittaker, R. Abdul Fattah, J. C. Doornenbal, and J. R. Hopper (Apr. 2019). “GlobSed: Updated Total Sediment Thickness in the World’s Oceans”. In: *Geochemistry, Geophysics, Geosystems* 20.4, pp. 1756–1772. ISSN: 1525-2027. DOI: 10.1029/2018gc008115. URL: http://dx.doi.org/10.1029/2018GC008115.

Tabor, C. R. and C. J. Poulsen (2016). “Simulating the Mid-Pleistocene Transition Through Regolith Removal”. In: *Earth and Planetary Science Letters* 434, pp. 231–240.

Taylor, A. (Mar. 2023). “Sediment thickness map of continental Canada and Canada-U.S. transboundary watersheds”. In.

Tzedakis, P. C., M. Crucifix, T. Mitsui, and E. W. Wolff (Feb. 2017). “A simple rule to determine which insolation cycles lead to interglacials”. In: *Nature* 542.7642, pp. 427–432. ISSN: 1476-4687. DOI: 10.1038/nature21364. URL: http://dx.doi.org/10.1038/nature21364.

Werder, M. A., I. J. Hewitt, C. G. Schoof, and G. E. Flowers (Oct. 2013). “Modeling channelized and distributed subglacial drainage in two dimensions”. In: *Journal of Geophysical Research: Earth Surface* 118.4, pp. 2140–2158. ISSN: 2169-9003. DOI: 10.1002/jgrf.20146. URL: http://dx.doi.org/10.1002/jgrf.20146.

Westerhold, T., U. Röhl, and J. Laskar (June 2012). “Time scale controversy: Accurate orbital calibration of the early Paleogene”. In: *Geochemistry, Geophysics, Geosystems* 13.6, n/a–n/a. ISSN: 1525-2027. DOI: 10.1029/2012gc004096. URL: http://dx.doi.org/10.1029/2012GC004096.

Willeit, M., A. Ganopolski, R. Calov, and V. Brovkin (Apr. 2019). “Mid-Pleistocene transition in glacial cycles explained by declining CO2 and regolith removal”.

In: *Science Advances* 5.4, eaav7337. ISSN: 2375-2548. DOI: 10.1126/sciadv.aav7337. URL: http://dx.doi.org/10.1126/sciadv.aav7337.

Willeit, M., A. Ganopolski, R. Calov, A. Robinson, and M. Maslin (July 2015). "The role of CO2 decline for the onset of Northern Hemisphere glaciation". In: *Quaternary Science Reviews* 119, pp. 22–34. ISSN: 0277-3791. DOI: 10.1016/j.quascirev.2015.04.015. URL: http://dx.doi.org/10.1016/j.quascirev.2015.04.015.

Chapter 2

Sedimentary Processes in Glacial Systems

"The ruins of an older world, are visible in the present structure of our planet; and the strata which now compose our continents have been once beneath the Sea, and were formed out of the waste of pre-existing continents. The same forces are still destroying, by chemical decomposition or mechanical violence, even the hardest rocks, and transporting the materials to the sea, where they are spread out, and form strata analogous to those of more ancient date. Although loosely deposited along the bottom of the ocean, they become afterwards altered and consolidated by volcanic heat, and then heaved up, fractured, and contorted."

— Charles Lyell, summarizing James Hutton's views in Principles of Geology (Lyell, 1837).

2.1 Background: glacial sediment production & transport

Accurate estimation of regolith removal and range of pre-Pleistocene sediment distributions requires a comprehensive model of the important process components. Ice sheets erode the surface of the solid earth by four processes: subglacial fluvial erosion, dissolution, abrasion, and quarrying (Hallet, 1996). The principal erosion

processes (Melanson, 2012), abrasion and quarrying, are implemented in the Glacial Systems Model (GSM).

2.1.1 *Modes of sediment production in the cryosphere*

There are many modes of sediment production relevant to glacial processes. These include surficial processes which occurred prior to glaciation but which weakened surficial material enough to be susceptible to transport (e.g. chemical weathering), periglacial processes such as frost and glaciofluvial processes, and glacial processes such as glacial abrasion and quarrying.

Chemical weathering occurs as rain absorbs atmospheric carbon dioxide, forming carbonic acid. This carbonic acid then modbilizes the most easily dissolved ions (Na^{+1}, K^{+1}, Fe^{+2}, Mg^{+2}, Al^{+3}, and Ca^{+2}) in fresh crystalline rock, e.g. granite and gneiss (Ruddiman, 2008):

$$H_2O_{(\text{rain})} + CO_{2(\text{atm})} \longrightarrow H_2CO_3 \tag{1}$$

$$CaSiO_3{}^{+}H_2CO_3 \longrightarrow CaCO_3{}^{+}SiCO_3{}^{+}SiO_2{}^{+}H_2O \tag{2}$$

This process of chemical weathering produces a vertical sequence of progressively more weathered products toward the surface. From the bottom these are: slightly weathered bedrock, saprock (altered but still firm), saprolith (easily crumbled but retains structure of the parent rock), and clay at the top; 184 m thick layers of saprolith have been found south of the glaciated region of North America (Setterholm and Morey, 1995). This process is in part responsible for the generation of regolith which forms a part of the Regolith Hypothesis for the mid-Pleistocene transition (e.g. Braun et al., 2016).

Frost processes can propagate fracture networks within the top 1-4 m of rock (Hales and Roering, 2007). This has been argued to occur either through volumetric

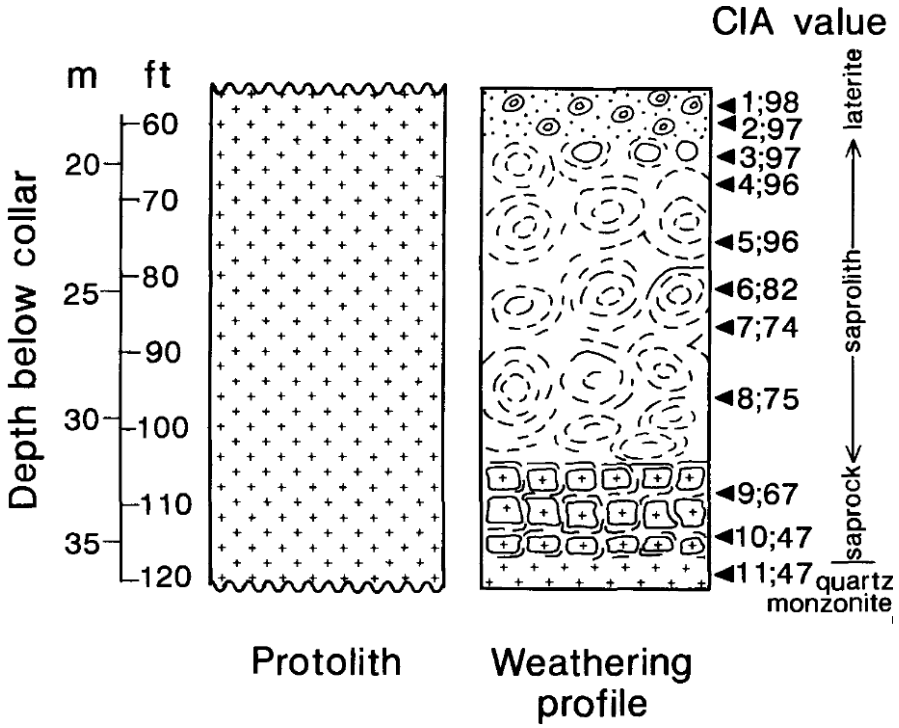

Figure 10: An example chemical weathering profile taken from Setterholm and Morey (1995) showing the progression from bedrock to saprock, saprolith, and laterite clay. The chemical index of alteration (CIA) progresses from high values at the bottom, indicating most of the easily mobilized cations are retained, to low at the top, indicating most of these ions have been leached.

expansion of water in the pore-space –freeze/thaw cycling – or through a mechanism in which van der Waals and electrostatic forces generate stress (Hales and Roering, 2007). Similar to frost processes, thermal expansion is thought to exfoliate rock surfaces through diurnal and seasonal temperature changes inducing rock falls (Collins and Stock, 2016).

Similar to fluvial processes, glaciofluvial erosion likely occurs through bed load transport and grain saltation over the bed (Scheingross et al., 2014). These systems produce Nye-Channels and tunnel valleys (Benn and Evans, 2010), transport sediment much the same as fluvial environments, and are responsible for esker formation (Beaud, Flowers, and Venditti, 2018). Koppes and Montgomery (2009) present erosion rates for mountain glaciers. They show rates are highly variable across timescales with large increases during deglacial periods (10-1000 mm/yr erosion at 10-100 yr timescales, 0.1-10 mm/yr at 1-10 Myr timescales). Fluvial erosion on the other hand is consistent at all time scales. It is most sensitive to how

tectonically active its drainage basin is. Erosion rates in the most stable regions (for example the North American craton) are low: 0.001-0.1 mm/yr across 10^1-10^8 yr time scales.

The two glacial processes considered most important are abrasion and quarrying, which are examined in more detail in § 2.2.1 and 2.2.2.

2.1.2 *Modes of sediment transport in glacial systems*

While glacio-fluvial sediment transport remains a largely under-studied factor of in the glacial sediment transport system, it is difficult to disentangle from other mechanisms. Glacial action would have mobilized the pre-glacial regolith (M. Bell and Laine, 1985), facilitating the processes of glacio-fluvial and fluvial transport. Furthermore, the same sediment packages could have been transported by a combination of glacial, glaciofluvial, and fluvial systems. Fluvial denudation is most effective where sediment is disturbed such as tectonically and glaciologically active areas (Koppes and Montgomery, 2009).

Stress from the overbearing ice sheet causes unconsolidated sediment to deform – this deformation plays an essential role in basal motion of both ice sheets and glaciers (Cuffey and Paterson, 2010). The deformation response of subglacial till to stress is affected by pore pressure, hydraulic properties, till lithology, grain size distribution, and strain history. N. R. Iverson, Baker, and Hooyer (1997) found that clay content is a primary control on the constitutive relationship of subglacial sediment (e.g. R. M. Iverson, 1985). Clay content affects sediment compaction, hydraulic permeability, and controls localization of strain within the sediment – thereby modifying the bulk rheology of the layer.

The entrainment of sediment into the basal layers of glacial ice has intrigued glaciologists for a long time (e.g. Chamberlin, 1894). It is currently accepted that entrainment occurs through regelation: pressure melting occurs at the top of a

grain and meltwater refreezes at the bottom of the grain (Benn and Evans, 2010). N. R. Iverson and Semmens (1995) developed a theory of entrainment whereby the rate of entrainment is proportional to the overburden pressure. They tested this theory by applying a force to a block of ice, pressing it onto an array of ceramic spheres, quartz sand, or till, varying their sizes and the amount of overburden pressure. The entrainment theory of N. R. Iverson and Semmens (1995) agreed within a factor of 2 with the experimental evidence arising from this variety of factors. This entrainment mechanism is effective: debris entrained in this way has been observed in basal ice with more than 75% by volume concentration (Benn and Evans, 2010).

Sediment are also transported long distances through ice rafting. These ice rafted debris occur in large swaths of the North Atlantic deposited in periodic events during at least the last glacial cycle, termed Heinrich Events (Hemming, 2004).

2.2 MODEL OF SEDIMENT PRODUCTION & TRANSPORT

The sediment model applied in the GSM is designed after that of D. H. D. Hildes (2001). Both employ separate descriptions of abrasion and quarrying for the erosive part, although Melanson (2012) also provides an optional empirical erosion as well as a choice between Boulton and Hallet style erosion whereas D. H. D. Hildes (2001) uses only Hallet. D. H. D. Hildes (2001) input a map of substrate lithology and track the distribution of clast lithology within a given cell, calculating the relative hardness of substrate and abrasive. Abrasion is switched off when clast hardness is lower than the substrate, whereas Melanson (2012) neglects the clast-substrate hardness differential. D. H. D. Hildes (2001) also uses lithology dependent quarrying rate factors, although the accuracy of this is questionable as quarrying primarily relies on the density of pre-existing joints and weaknesses in the substrate (Hooyer,

Cohen, and N. R. Iverson, 2012; N. R. Iverson, 2012). Joint and fracture density is not easily quantified at the relevant scales and is highly variable within the dimension of a grid cell (e.g. km to 100's km). D. H. Hildes et al. (2004) and Melanson (2012) both use estimates of cavitation (from basal water pressure) in the lee side of basal protrusions to estimate stress regimes and thus quarrying rates. Both models give englacial transport rates through advection, however, D. H. D. Hildes (2001) omits subglacial transport.

2.2.1 *Abrasion Law*

Abrasion occurs from contact between two surfaces either through polishing or through striation (Benn and Evans, 2010). Polishing is the process by which the abrading surface removes protrusions in the bed reducing its roughness. Striation is the process by which stress caused by asperities in the abrading surface generate fracture sets which accumulate as linear troughs behind the asperity. Abrasion in the GSM is given by (Melanson, T. Bell, and Tarasov, 2013):

$$\dot{A} = \exp\left(-h_{sed}/\tilde{h}^{\star}_{sed}\right)\frac{k_{abr}}{HV^{\star}}\sum_{R} C_b\left(R\right)F_N\left(R\right)\left|v_{par}\left(R\right)\right| \tag{3}$$

The exponential represents a shielding coefficient – decreased contact between the abrading surface and the substrate as sediment accumulates. h_{sed} is the sediment layer thickness and $\tilde{h}^{\star}_{sed}$ is a characteristic thickness for shielding (shielding factor). This shielding factor is taken by D. H. D. Hildes (2001) to represent the areal fraction of the rough bed within a given cell which is covered by sediment. D. H. D. Hildes (2001) calculates this as

$$\tilde{h}^{\star}_{sed} = \tilde{d}_1\theta_{mean} + \tilde{d}_0 \tag{4}$$

where $\tilde{d}_1 = 10.0$m and $\tilde{d}_0 = 2.0$m and bed dip $\theta_{mean} \in [0, 0.45]$ (deg) so that $\tilde{h}^{\star}_{sed}\epsilon\,[2.0, 6.5]$. Here, since this range of bed dips was defined using coarser resolution digital elevation maps (30-1000 m horizontal resolution, § 2.1 in D. H. D. Hildes, 2001), the assumed a priori range of $\tilde{h}^{\star}_{sed}$ is widened to $[2.0, 20.0]$ as higher resolution could pick up steeper (rougher) beds. The abrasion coefficient $C^{\star}_{abr}$ is a tuning parameter defined as

$$C^{\star}_{abr} = k_{abr}\,/\,HV^{\star}. \tag{5}$$

The abrasion wear coefficient, k_{abr}, is shown in D. H. D. Hildes (2001) to vary over 2 orders of magnitude from $[0.002, 0.3]$ on the basis of reference to the literature. $HV^{\star}$ is the Vickers hardness. Since the substrate hardness does not appear here it is implicitly assumed that the substrate is softer than the abrading material. From review of the literature, D. H. D. Hildes (2001) gives a range of Vickers hardness values of $HV^{\star} \in \left[0.3 \times 10^{-9}, 12 \times 10^{-9}\right]$ Pa. This gives the range of abrasion coefficient: $C_{abr} \in \left[1.7 \times 10^{5}, 1.0 \times 10^{9}\right]$. Experiments by N. R. Iverson (1990) (granitic fragments frozen into ice and pressed into a sliding marble substrate) found that abrasion in their experiments more closely resembled the abrasion law of Hallet (1979) than that of Boulton (1979).

C_b is entrained debris concentration at a range of sediment radii (R), calculated from the englacial sediment concentration at the bottom (first) layer, C^{1}_{eng} (see § 2.2.4) assuming volume concentration is equal to areal concentration:

$$C_b(R) = \frac{C^{1}_{eng} \exp\left\{-\left(\log_{10}(R) - \log_{10}(\mathrm{E}[R])\right)^2 / \left(2 \log_{10} \mathrm{Var}[R]\right)\right\}}{\pi R^2 \sum \exp\left\{-\left(\log_{10}(R) - \log_{10}(\mathrm{E}[R])\right)^2 / \left(2 \log_{10} \mathrm{Var}[R]\right)\right\}} \tag{6}$$

F_N is the normal force between bed and abrading particle, v_{par} is the speed of the abrasive across the bed. These last two factors are calculated according to two different models of subglacial abrasion: the Boulton model assumes the normal

force is proportional to the effective pressure N_{eff} while particle velocity is reduced by a particle size, effective pressure, and ice flow dependent drag terms.

$$F_N = A_e P_e \tag{7}$$

$$v_{par}(R) = |v_s| - 2B_g^\star R \left(\frac{\mu^\star P_e A_e}{A_r} \right)^3 - \frac{P_m P_e A_e}{2 L_{fus} \rho_i A_r R} \tag{8}$$

Conversely, the Hallet model assumes the normal force is proportional to particle size and normal velocity (from normal component ice velocity due to subgrid bed undulation and basal melt rate). Hallet's particle velocity also assumes a slow down from bed contact, assuming equilibrium between friction with the bed and "drag" from the ice.

$$F_N(R) = f_{bed}^N \frac{4\pi\eta R^3}{\tilde{R}^2 + R^2} v_n \tag{9}$$

$$v_{par} = |v_s| \left(1 - \frac{\mu^\star f_{bed}^N \sin\theta}{f_{bed}^T} \right) - \frac{\mu^\star f_{bed}^N}{f_{bed}^T} \dot{b}_{melt} \tag{10}$$

Abrasion is turned off when abrading particle velocity reaches zero, ice becomes cold-bedded, or N_{eff} reaches zero (flotation).

2.2.2 *Quarrying Law*

Quarrying is also an erosive process like abrasion, but produces larger ($> 1\,\text{cm}$) fragments of rock, taking advantage of joints (weaknesses in the rock Benn and Evans, 2010) as seen in the control of quarried surface orientation toward pre-existing joint and fracture sets over sliding direction (Hooyer, Cohen, and N. R. Iverson, 2012). Stress gradients due to cavity growth concentrate force on bedrock steps where these forces can exceed 50% higher than ambient ice-bed pressures

(N. R. Iverson, 1991). Separation pressure, P_s, is given in Melanson, T. Bell, and Tarasov (2013) and Cuffey and Paterson (2010) as:

$$P_s = P_{ice} - \frac{\tau_b}{\pi \zeta^\star} \tag{11}$$

where P_{ice} is ice overburden, τ_b is basal shear stress (assumed to be driving stress), and $\zeta^\star$ is basal roughness (protrusion height over distance between).

$\zeta^\star$ is similar to the basal roughness h_r in the linked-cavity hydrology formulation. Additionally, Melanson (2012) assumes the grid-scale cavity extent (important for quarrying rate) is proportional to the residual pressure (difference between water pressure and separation pressure). However cavity extent is given in linked-cavity hydrology directly by the grid-scale subglacial water thickness h_{wb}. Because of this dependence on cavity formation, where quarrying rates are large, linked-cavity drainage may be dominant.

The quarrying rate in Melanson, T. Bell, and Tarasov (2013) is given by:

$$\dot{Q} = \exp\left(-h_{sed}/\tilde{h}^\star_{sed}\right) C^\star_{quar} \left(\frac{P_w - P_s}{\tilde{P}_r}\right)^{n^\star_p} \tag{12}$$

with $C^\star_{quar}$ the quarrying coefficient, $n^\star_p$ an exponent controlling residual pressure contribution, $\tilde{P}_r$ the characteristic residual pressure ($\approx 18kPa$)

2.2.3 *Empirical Erosion Law*

The empirical erosion rate used in the GSM is (Melanson, T. Bell, and Tarasov, 2013)

$$\dot{E}_{emp} = \exp\left(-h_{sed}/\tilde{h}^\star_{sed}\right) C^\star_{emp} |\tau_b||v_s| \tag{13}$$

with $C^\star_{emp}$ a coefficient and v_s the sliding velocity.

2.2.4 *Englacial Transport: Entrainment, Mixing, and Advection*

Englacial transport in the GSM is (Melanson, T. Bell, and Tarasov, 2013)

$$\frac{\partial C}{\partial t} = -\nabla \cdot C\vec{v}_i - \frac{\partial (C\dot{V}_{net})}{\partial z} + V_{mix} \tag{14}$$

The lateral velocities v_i are a function of lateral and vertical position. The entrainment/deposition rate V_{net} is a function of lateral position. The vertical mixing rate V_{mix} is diffusion of sediment concentration between layers which varies laterally and vertically. Within the GSM, vertical diffusion and lateral advection are treated separately with lateral advection calculated first for a given time step. A tri-diagonal matrix solver is used to calculate the sediment concentrations due to vertical diffusion. Vertical mixing is given by:

$$V_{mix} = \frac{\partial}{\partial z}\left(D\frac{\partial C}{\partial z}\right) \tag{15}$$

$$D = \tilde{D}^{\star}\left(\frac{|v_s|}{\tilde{v}_s}\right) e^{-z/\tilde{z}^{\star}} e^{-h_{sed}/\tilde{h}^{\star}} \tag{16}$$

Where $\tilde{D}^{\star}$, $\tilde{z}^{\star}$, and $\tilde{h}^{\star}$ are scale factor parameters and $\tilde{v}_s$ is a scale factor based on typical sliding velocities. Vertical diffusion decreases with increased sediment cover because where there is more soft sediment there will be less folding within the basal ice and thus less vertical (eddy) diffusion. This is because basal stress is balanced by viscous or plastic forces within the soft-deformation layer instead of by the process of folding in basal ice.

Sediment is entrained within the ice by regelation (N. R. Iverson and Semmens, 1995). The rate of regelation of ice into the sediment is given by:

$$v_r = K_s \frac{N_{eff}}{l_a} \tag{17}$$

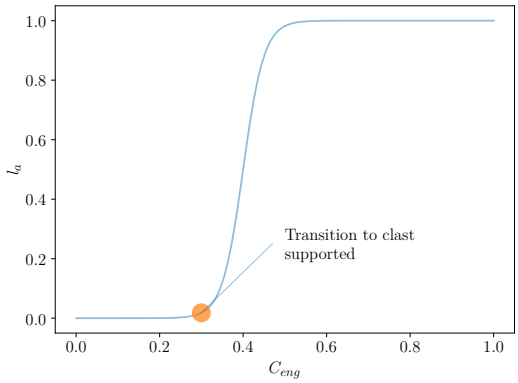

Figure 11: Array thickness modifier in eqn. 19

where K_s is the conductivity of ice into the sediment layer (defined in D. H. D. Hildes (2001, eqn. 4.4 and 4.5)) and l_a is the englacial sediment array thickness. This array thickness acts to limit sediment entrainment as the medium transitions from ice supported to clast supported and the medium can no longer regelate around sediment grains. The effective array depth is the series of smoothed step functions of sediment thickness within each basal grid layer:

$$l_a = \sum_{k_z} l_{mod}\left(k_z\right) \Delta z\left(k_z\right) \tag{18}$$

$$l_{mod}(z) = 0.5\left\{\tanh\left[20\left(C(z) - C^{\star}_{crit}\right)\right] + 1\right\} \tag{19}$$

V_{net} term calculated as the net of entrainment (due to regelation) and deposition (due to basal melt), giving:

$$V_{net} = v_r - \frac{\dot{b}_{melt} C(z=0)}{1-\phi^{\star}} \tag{20}$$

where the sediment concentration in the bottom layer is deposited with porosity $\phi^{\star}$ when melting ($\dot{b}_{melt}$) occurs. This implies recently entrained sediment has concentration $C(z=0) = 1-\phi^{\star}$. Entrainment rate is capped at value $v^{\star}_{max}$ and layer concentration is capped at $C^{\star}_{max}$.

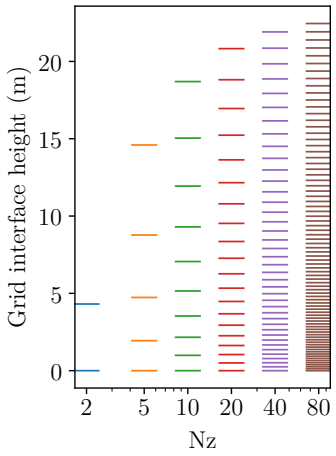

Figure 12: Depiction of the vertical englacial sediment grid for various resolutions.

Englacial Grid

Discretization above the ice-sediment interface used for modelling entrainment, mixing, and advection of sediment in the ice uses an exponential grid. This exponential grid concentrates resolution in the most dynamic basal layers where mixing/entrainment velocities are highest. The ice-sediment interface moves up as sediment is deposited and down as bedrock is eroded or denuded. The grid is chosen uniform in ξ and transformed using:

$$z_{ice} = \frac{z_{max}}{\sum \left[e^{\xi / z_0} \right]} e^{\xi / z_0} \tag{21}$$

where $z_0 = 15$ is the exponential grid spacing parameter and $z_{max} = 23$ is the full height of the entrainment grid in the ice. This grid is depicted in fig. 12.

2.2.5 *Subglacial Transport Law*

Basal sediment transport is governed by the sediment continuity relationship given in Melanson, T. Bell, and Tarasov (2013):

$$\frac{\partial h_{sed}}{\partial t} = -\nabla \cdot \vec{Q}_s + \dot{E} - V_{net} \tag{22}$$

where sediment thickness through time is given as the sum of the convergence of subglacial transport through deformation, erosion rate $\dot{E}$ (empirical or process), and entrainment rate. This acts with englacial transport in eqn. 106 to give the total sediment transport and production.

Subglacial transport from soft sediment deformation occurs as basal shear stress from the overbearing ice sheet is applied to a layer of unconsolidated till assumed to behave as a Coulomb plastic in the manner of R. M. Iverson (1985). The constitutive relationship presented therein is between the deformation rate tensor ($\mathbf{D}$) and the stress deviator tensor ($\mathbf{T}$):

$$\mathbf{D} = \begin{bmatrix} \frac{\partial v_x}{\partial x} & \frac{1}{2}\left(\frac{\partial v_x}{\partial y} + \frac{\partial v_y}{\partial x}\right) & \frac{1}{2}\left(\frac{\partial v_x}{\partial z} + \frac{\partial v_z}{\partial x}\right) \\ \frac{1}{2}\left(\frac{\partial v_y}{\partial x} + \frac{\partial v_x}{\partial y}\right) & \frac{\partial v_y}{\partial y} & \frac{1}{2}\left(\frac{\partial v_y}{\partial z} + \frac{\partial v_z}{\partial y}\right) \\ \frac{1}{2}\left(\frac{\partial v_z}{\partial x} + \frac{\partial v_x}{\partial z}\right) & \frac{1}{2}\left(\frac{\partial v_z}{\partial y} + \frac{\partial v_y}{\partial z}\right) & \frac{\partial v_z}{\partial z} \end{bmatrix} \tag{23a}$$

$$\mathbf{T} = \begin{bmatrix} \tau_{xx} + p & \tau_{xy} & \tau_{xz} \\ \tau_{yx} & \tau_{yy} + p & \tau_{yz} \\ \tau_{zx} & \tau_{zy} & \tau_{zz} + p \end{bmatrix} \tag{23b}$$

where v_i is the i^{th} component of velocity, τ_{ij} are the components of deviator stress, and $p = -\frac{1}{3}\left(\tau_{xx} + \tau_{yy} + \tau_{zz}\right)$. R. M. Iverson (1985) then uses a generalization of

the Coulomb criterion for plastic yield, the extended Von Mises (Von Mises, 1913) criterion — Drucker and Prager (1952, eqn. 2):

$$II_T^{1/2} = k + \alpha p \tag{24}$$

where II_T is the second invariant of the stress deviator tensor, k is the cohesion and α is the tangent of the angle of internal friction. This is

$$II_T = \frac{1}{2}\left[\operatorname{tr} T^2 - \operatorname{tr} T^2\right] \tag{25}$$

$$= \frac{1}{2}\left[(\tau_{xx}+p)^2 + (\tau_{yy}+p)^2 + (\tau_{zz}+p)^2 + 2\left(\tau_{xy}^2 + \tau_{yz}^2 + \tau_{zx}^2\right)\right]. \tag{26}$$

R. M. Iverson (1985) then works out his constitutive equation:

$$\mathbf{T} = 2\mu\mathbf{D} + \frac{k+\alpha p}{II_D^{1/2}}\mathbf{D} \tag{27}$$

where

$$II_D^{1/2} = \begin{cases} \frac{1}{2\mu}\left[II_T^{1/2} - (k+\alpha p)\right] & II_T^{1/2} > k + \alpha p \\ 0 & II_T^{1/2} \leq k + \alpha p \end{cases}. \tag{28}$$

In the context of the shallow ice approximation (no lateral or longitudinal shear components) and assuming no vertical transport (vertical length scales are much shorter than lateral when comparing the horizontal dimensions of ice sheets against vertical dimensions of till beds), the deformation and stress tensors become:

$$\mathbf{D} = \begin{bmatrix} 0 & 0 & \frac{1}{2}\left(\frac{\partial v_x}{\partial z} + \right) \\ 0 & 0 & \frac{1}{2}\left(\frac{\partial v_y}{\partial z}\right) \\ \frac{1}{2}\left(\frac{\partial v_x}{\partial z}\right) & \frac{1}{2}\left(\frac{\partial v_y}{\partial z}\right) & 0 \end{bmatrix} \tag{29a}$$

$$\mathbf{T} = \begin{bmatrix} 0 & 0 & \tau_{xz} \\ 0 & 0 & \tau_{yz} \\ \tau_{zx} & \tau_{zy} & 0 \end{bmatrix} \tag{29b}$$

, this also assumes incompressible shear such that $\tau_{xx} = \tau_{yy} = \tau_{zz} = -p$. This p is the effective pressure with sediment overburden, $N_{eff} + \Delta\rho g z$. Using a similar model of subglacial deformation, Pollard and Deconto (2009) assumes $N_{eff} = 0$ so that the normal stress is only applied by the sediment overburden. The model in the GSM follows Jenson et al. (1995) and take the normal stress as $N_{eff} + (\rho_s - \rho_w)gz$ with z the depth into sediment. Jenson et al. (1995) then shows that the independent lateral components are:

$$\tau_{xz} = (2D_0)^{(n_s-1)/n_s} \mu_0 \left(\frac{dv_x}{dz}\right)^{1/n_s} + c + (N_{eff} + \Delta\rho g z)\tan\phi^\star \tag{30a}$$

$$\tau_{yz} = (2D_0)^{(n_s-1)/n_s} \mu_0 \left(\frac{dv_y}{dz}\right)^{1/n_s} + c + (N_{eff} + \Delta\rho g z)\tan\phi^\star \tag{30b}$$

τ_{xz} and τ_{yz} are the x/y components of ice basal shear stress. Rearranging for v_i (i^{th} component of sediment velocity) gives:

$$v_i = \int \left[\frac{\tau_{iz} - c - (N_{eff} + \Delta\rho g z)\tan\phi^\star}{(2D_0)^{\frac{n_s-1}{n_s}} \mu_0}\right]^{n_s} dz \tag{31}$$

$$= \frac{\left[\tau_{iz} - (c + N_{eff}\tan\phi^\star + \Delta\rho g z \tan\phi^\star)\right]^{n_s+1} / (n_s+1)}{\left[(2D_0)^{\frac{n_s-1}{n_s}} \mu_0\right]^{n_s} \Delta\rho g \tan\phi^\star} + \gamma_1 \tag{32}$$

Where γ_1 is the constant of integration. Assuming a reference frame of zero background flow of sediment, this constant is $\gamma_1 = 0$. At the ice-sediment interface, $z = 0$,

$$v_i = \frac{\left[\tau_{iz} - c - N_{eff}\tan\phi^\star\right]^{n_s+1}}{(n_s+1)(2D_0)^{n_s-1} \mu_0^{n_s} \Delta\rho g \tan\phi^\star} \tag{33}$$

Deformation thickness is found by solving for $v_i\,(z = z_d) = 0$:

$$0 = \tau_{iz} - c - N_{eff}\tan\phi^\star - \Delta\rho g z_d \tan\phi^\star \tag{34}$$

$$\Rightarrow z_d = \frac{\tau_{iz} - c - N_{eff}\tan\phi^\star}{\Delta\rho g \tan\phi^\star} \tag{35}$$

Integrating once more to get flux over the deformation thickness,

$$Q_i = \int_{z_d}^{0} v_i dz = -\int_{z_d}^{0} \frac{\left[\tau_{iz} - c - N_{eff}\tan\phi^\star - \Delta\rho g z \tan\phi^\star\right]^{n_s+1}}{\left[(2D_0)^{\frac{n_s-1}{n_s}}\mu_0\right]^{n_s}\Delta\rho g\tan\phi^\star\left(n_s+1\right)}dz \tag{36}$$

$$= \frac{\left(\Delta\rho g\tan\phi^\star\right)^{n_s}\left(\right)^{n_s+1}}{\left[(2D_0)^{\frac{n_s-1}{n_s}}\mu_0\right]^{n_s}\left(\Delta\rho g\tan\phi^\star\right)^2\left(n_s+1\right)\left(n_s+2\right)} \tag{37}$$

$$Q_{sx} = \begin{cases} 0 & \text{ice floating}||\text{freezing}||H \leq 0. \end{cases}$$

$$Q_s = \begin{cases} h_{sed} \leq z_p & \frac{\left[\frac{-\left(\tau - c_{cohe} - N_{eff} + (\rho_s-\rho_w)g\tan\phi h_{sed}\right)^{n_s+2}}{(n_s+2)(\rho_s-\rho_w)g\tan\phi} - \left(\tau - c_{cohe} - N_{eff}\tan\phi\right)^{n_s+2} - \left[\tau - c_{cohe} - \left(N_{eff} + (\rho_s-\rho_w)gh_{sed}\right)\tan\phi\right]^{n_s+1}h_{sed}\right]}{(n_s+1)(2D_0)^{n_s-1} * \mu_0^{n_s}(\rho_s-\rho_w)g*\tan\phi} \\ h_{sed} > z_p & \frac{-1}{(n_s+1)(n_s+2)(2D_0)^{n_s-1}\mu_0^{n_s}[(\rho_s-\rho_w)g\tan\phi]^2}\left[(-\tau - c_{cohe} - N_{eff}\tan\phi)^{n_s+2}\right] \end{cases}$$

2.2.6 *Sediment Model Update*

The sediment model formulated in the GSM uses physical process laws to calculate erosion (in the form of abrasion and quarrying, as well as an optional empirical erosion law) while modelling sediment transport via subglacial (soft deformation) and englacial (advection within ice matrix). Melanson (2012) could not conclude which form of erosion was more accurate than the others (empirical vs. quarrying with two modes of abrasion, giving three forms) and so included all.

This project updated several aspects of the sediment model in the GSM: closer coupling with the GSM, numerical aspects, and technical debt reduction. This was done through extensive model testing, code examination, and static code analysis. Code performance was improved by adjusting the size of subgrid arrays which had greatly increased run time: englacial levels (15 lowered to 10), clast size distribution (10 stayed at 10), and bed dip distribution (97 lowered to 10). Array and loop indices were adjusted to take advantage of vectorization. Confusing nomenclature was changed and values repeatedly hard coded throughout the code were named for reuse. Sensitive model parameters were changed to being read in instead of hard coded in include files.

In the previous version of the sediment model each model component was assumed constant throughout the subroutine call. This meant that the the erosion rate was held constant even though sediment shielding could change within a subroutine call (one to five years). This also meant that the entrainment/deposition rate was out of sync between the subglacial and englacial transport models – where sediment became thin it was more likely that sediment would not be conserved. This time stepping has since been adjusted such that each process is called in turn within a single time loop. This transition improved mass conservation during testing.

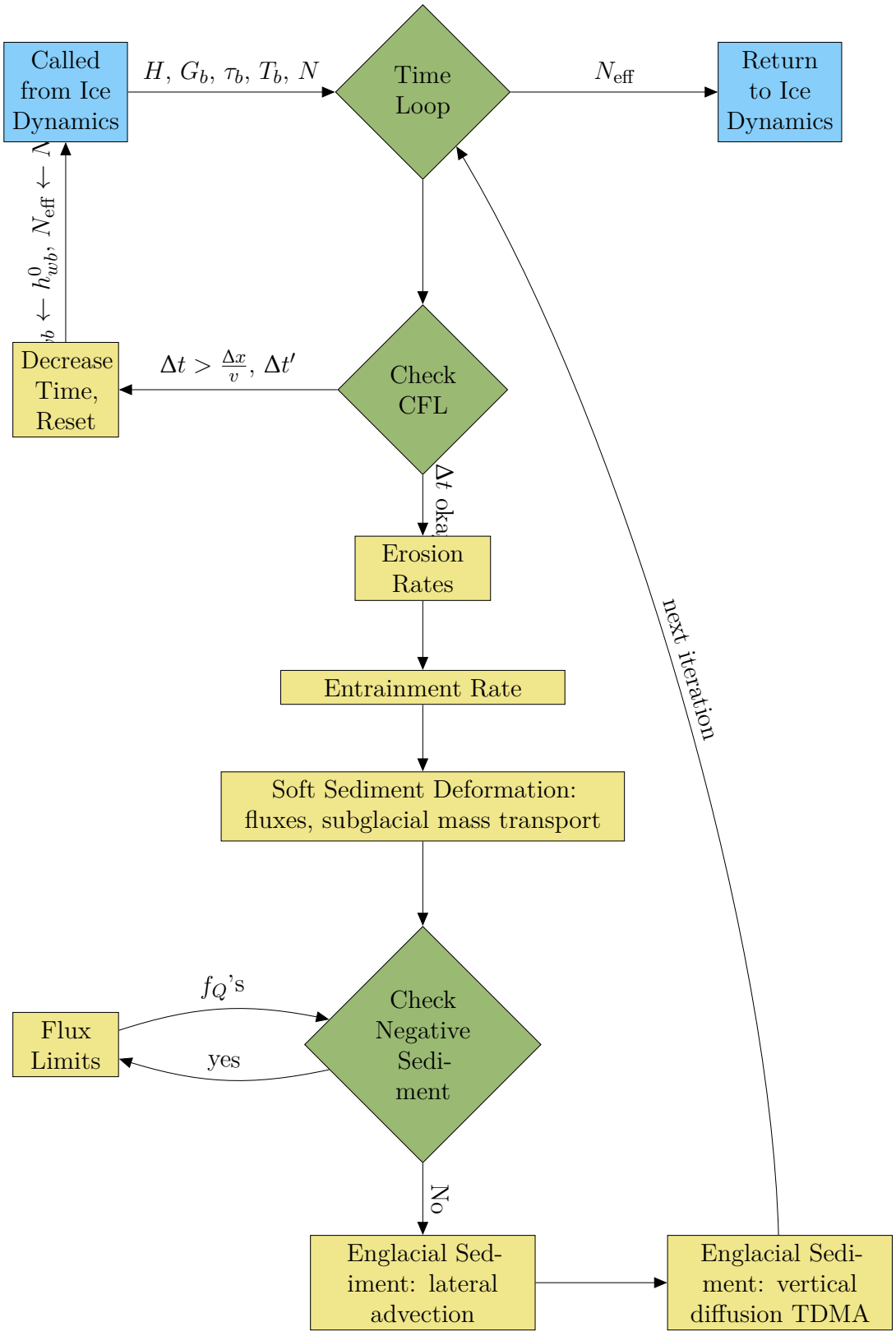

Figure 13: Flow chart of sediment model algorithm execution

Model grid was converted from a lat/lon grid to the generalized GSM grid. Additionally, the model was moved to an Arkawa C grid instead of a centered difference derivative scheme and some boundary conditions were adjusted (e.g. when ice melts all sediment is dumped to bed).

The sediment model was also coupled to the ice dynamics through dynamically calculated soft bed fraction used to calculate sliding velocity. The sediment model was also coupled to the solid earth isostatic adjustment model via changing bedrock elevation and sediment load.

As subglacial sediment processes depending on the basal water pressure, the processes of subglacial hydrology are reviewed in the next chapter (chap. 3) and the design choices of the subglacial hydrology model are laid out.

REFERENCES

Beaud, F., G. E. Flowers, and J. G. Venditti (Dec. 2018). "Modeling Sediment Transport in Ice-Walled Subglacial Channels and Its Implications for Esker Formation and Proglacial Sediment Yields". In: *Journal of Geophysical Research: Earth Surface* 123.12, pp. 3206–3227. ISSN: 2169-9003. DOI: 10.1029/2018jf004779. URL: http://dx.doi.org/10.1029/2018JF004779.

Bell, M. and E. P. Laine (Mar. 1985). "Erosion of the Laurentide Region of North America by Glacial and Glaciofluvial Processes". In: *Quaternary Research* 23.02, pp. 154–174. ISSN: 1096-0287. DOI: 10.1016/0033-5894(85)90026-2. URL: http://dx.doi.org/10.1016/0033-5894(85)90026-2.

Benn, D. I. and D. J. A. Evans (2010). *Glaciers & Glaciation*. 2nd ed. 338 Euston Road, London NW1 3BH: Hodder Education, An Hachette UK Company.

Boulton, G. (1979). "Processes of Glacier Erosion on Different Substrata". In: *Journal of Glaciology* 23.89, pp. 15–38. ISSN: 1727-5652. DOI: 10.3189/s0022143000029713. URL: http://dx.doi.org/10.3189/S0022143000029713.

Braun, J., J. Mercier, F. Guillocheau, and C. Robin (Nov. 2016). "A simple model for regolith formation by chemical weathering". In: *Journal of Geophysical Research: Earth Surface* 121.11, pp. 2140–2171. ISSN: 2169-9003. DOI: 10.1002/2016jf003914. URL: http://dx.doi.org/10.1002/2016JF003914.

Chamberlin, T. C. (Jan. 1894). "Recent Glacial Studies in Greenland". In: *Geological Society of America Bulletin* 6.1, pp. 199–220. ISSN: 1943-2674. DOI: 10.1130/gsab-6-199. URL: http://dx.doi.org/10.1130/GSAB-6-199.

Collins, B. D. and G. M. Stock (Mar. 2016). "Rockfall triggering by cyclic thermal stressing of exfoliation fractures". In: *Nature Geoscience* 9.5, pp. 395–400. ISSN: 1752-0908. DOI: 10.1038/ngeo2686. URL: http://dx.doi.org/10.1038/ngeo2686.

Cuffey, K. and W. S. B. Paterson (2010). *The Physics of Glaciers*. 4th ed. Academic Press.

Drucker, D. C. and W. Prager (July 1952). "Soil mechanics and plastic analysis or limit design". In: *Quarterly of Applied Mathematics* 10.2, pp. 157–165. ISSN: 1552-4485. DOI: 10.1090/qam/48291. URL: http://dx.doi.org/10.1090/qam/48291.

Hales, T. C. and J. J. Roering (June 2007). "Climatic controls on frost cracking and implications for the evolution of bedrock landscapes". In: *Journal of Geophysical Research* 112.F2. ISSN: 0148-0227. DOI: 10.1029/2006jf000616. URL: http://dx.doi.org/10.1029/2006JF000616.

Hallet, B. (1996). "Glacial quarrying: a simple theoretical model". In: *Annals of Glaciology* 22, pp. 1–8. ISSN: 1727-5644. DOI: 10.3189/1996aog22-1-1-8. URL: http://dx.doi.org/10.3189/1996AoG22-1-1-8.

Hallet, B. (1979). "Subglacial Regelation Water Film". In: *Journal of Glaciology* 23.89, pp. 321–334. ISSN: 1727-5652. DOI: 10.1017/s0022143000029932. URL: http://dx.doi.org/10.1017/S0022143000029932.

Hemming, S. R. (Mar. 2004). "Heinrich events: Massive late Pleistocene detritus layers of the North Atlantic and their global climate imprint". In: *Reviews of Geophysics* 42.1. ISSN: 8755-1209. DOI: 10.1029/2003rg000128. URL: http://dx.doi.org/10.1029/2003RG000128.

Hildes, D. H. D. (Dec. 2001). "Modelling subglacial erosion and englacial sediment transport of the North American ice sheets". PhD thesis. Department of Earth, Ocean and Atmospheric Sciences Faculty of Science 2020 – 2207 Main Mall Vancouver, BC Canada V6T 1Z4: University of British Columbia. DOI: 10.14288/1.0052346. URL: http://hdl.handle.net/2429/13111.

Hildes, D. H., G. K. Clarke, G. E. Flowers, and S. J. Marshall (Feb. 2004). "Subglacial erosion and englacial sediment transport modelled for North American ice sheets". In: *Quaternary Science Reviews* 23.3-4, pp. 409–430. ISSN: 0277-3791. DOI: 10.1016/j.quascirev.2003.06.005. URL: http://dx.doi.org/10.1016/j.quascirev.2003.06.005.

Hooyer, T. S., D. Cohen, and N. R. Iverson (June 2012). "Control of glacial quarrying by bedrock joints". In: *Geomorphology* 153–154, pp. 91–101. ISSN: 0169-555X. DOI: 10.1016/j.geomorph.2012.02.012. URL: http://dx.doi.org/10.1016/j.geomorph.2012.02.012.

Iverson, N. R. (1990). "Laboratory Simulations Of Glacial Abrasion: Comparison With Theory". In: *Journal of Glaciology* 36.124, pp. 304–314. ISSN: 1727-5652. DOI: 10.3189/002214390793701264. URL: http://dx.doi.org/10.3189/002214390793701264.

— (1991). "Potential effects of subglacial water-pressure fluctuations on quarrying". In: *Journal of Glaciology* 37.125, pp. 27–36. ISSN: 1727-5652. DOI: 10.3189/s0022143000042763. URL: http://dx.doi.org/10.3189/S0022143000042763.

— (Aug. 2012). "A theory of glacial quarrying for landscape evolution models". In: *Geology* 40.8, pp. 679–682. ISSN: 0091-7613. DOI: 10.1130/g33079.1. URL: http://dx.doi.org/10.1130/g33079.1.

Iverson, N. R., R. W. Baker, and T. S. Hooyer (Jan. 1997). "A ring-shear device for the study of till deformation: Tests on tills with contrasting clay contents". In: *Quaternary Science Reviews* 16.9, pp. 1057–1066. ISSN: 0277-3791. DOI: 10.1016/s0277-3791(97)00036-x. URL: http://dx.doi.org/10.1016/S0277-3791(97)00036-X.

Iverson, N. R. and D. J. Semmens (June 1995). "Intrusion of ice into porous media by regelation: A mechanism of sediment entrainment by glaciers". In: *Journal of Geophysical Research: Solid Earth* 100.B6, pp. 10219–10230. ISSN: 0148-0227. DOI: 10.1029/95jb00043. URL: http://dx.doi.org/10.1029/95JB00043.

Iverson, R. M. (Mar. 1985). "A Constitutive Equation for Mass-Movement Behavior". In: *The Journal of Geology* 93.2, pp. 143–160. ISSN: 1537-5269. DOI: 10.1086/628937. URL: http://dx.doi.org/10.1086/628937.

Jenson, J. W., P. U. Clark, D. R. MacAyeal, C. Ho, and J. C. Vela (Nov. 1995). "Numerical modeling of advective transport of saturated deforming sediment beneath the Lake Michigan Lobe, Laurentide Ice Sheet". In: *Geomorphology* 14.2, pp. 157–166. ISSN: 0169-555X. DOI: 10.1016/0169-555x(95)00056-0. URL: http://dx.doi.org/10.1016/0169-555X(95)00056-0.

Koppes, M. N. and D. R. Montgomery (Aug. 2009). "The relative efficacy of fluvial and glacial erosion over modern to orogenic timescales". In: *Nature Geoscience* 2.9, pp. 644–647. ISSN: 1752-0908. DOI: 10.1038/ngeo616. URL: http://dx.doi.org/10.1038/NGEO616.

Lyell, C. (1837). "Principles of geology". In: DOI: 10.5962/bhl.title.50199. URL: http://dx.doi.org/10.5962/bhl.title.50199.

Melanson, A. (2012). "Numerical modelling of subglacial erosion and sediment transport and its application to the North American ice sheets over the last glacial cycle". Includes bibliographical references (leaves 76-87). URL: https://research.library.mun.ca/2370/.

Melanson, A., T. Bell, and L. Tarasov (May 2013). "Numerical modelling of subglacial erosion and sediment transport and its application to the North American ice sheets over the Last Glacial cycle". In: *Quaternary Science Reviews* 68, pp. 154–174. ISSN: 0277-3791. DOI: 10.1016/j.quascirev.2013.02.017. URL: http://dx.doi.org/10.1016/j.quascirev.2013.02.017.

Pollard, D. and R. M. Deconto (Mar. 2009). "A Coupled Ice-Sheet/Ice-Shelf/Sediment Model Applied to a Marine-Margin Flowline: Forced and Unforced Variations". In: *Glacial Sedimentary Processes and Products*, pp. 37–52. DOI: 10.1002/9781444304435.ch4. URL: http://dx.doi.org/10.1002/9781444304435.ch4.

Ruddiman, W. F. (2008). *Earth's Climate. Past and Future*. 2nd ed. 41 Madison Avenue,New York,NY 10010, Houndmills,Basingstoke RG21 6XS,England: W. H. Freeman and Company. ISBN: 978-0-7167-8490-6.

Scheingross, J. S., F. Brun, D. Y. Lo, K. Omerdin, and M. P. Lamb (June 2014). "Experimental evidence for fluvial bedrock incision by suspended and bedload sediment". In: *Geology* 42.6, pp. 523–526. ISSN: 0091-7613. DOI: 10.1130/g35432.1. URL: http://dx.doi.org/10.1130/G35432.1.

Setterholm, D. R. and G. B. Morey (1995). In: DOI: 10.3133/b1989h. URL: http://dx.doi.org/10.3133/b1989H.

Von Mises, R. (1913). "Mechanik der festen Körper im plastisch- deformablen Zustand". In: *Nachrichten von der Gesellschaft der Wissenschaften zu Göttingen, Mathematisch-Physikalische Klasse* 1913, pp. 582–592. URL: http://eudml.org/doc/58894.

Chapter 3

Subglacial Hydrology

Liquid water is an important factor in the glacial system. Mass leaves the glacial system either through sublimation at surface, calving icebergs at the margin, through drainage in its liquid state generally regarded to occur supraglacially or subglacially. Water is transported in the supraglacial hydrologic system via sheet flows or through incised channels and is stored in the supraglacial system in lakes and firn aquifers (Benn and Evans, 2010). Instead of running off to the margin, some water in this supraglacial drainage system enters the englacial system via moulins (shafts melted through the ice extending to the base) and crevasses (cracks opening in the ice due to strain) (Clason et al., 2012). Water filling pre-existing crevasses can jack them open, weakening the ice mass and increasing calving rates which in turn increases crevassing due to reduced buttressing and ice acceleration, resulting in a positive feedback (Gagliardini and Werder, 2018). Water in this englacial system can reach the base of the ice sheet and supply meltwater in addition to that produced locally from basal melting (Zwally et al., 2002). Water pressure at the base of the ice can be sufficient to lift the ice off its substrate, inducing high velocity ice streaming (Iken, Röthlisberger, et al., 1983; Iken and Bindschadler, 1986).

Subglacial drainage systems can be categorized by their relationship between flux and pressure as either efficient or inefficient with the same area of the bed switching between categories over time (G. E. Flowers, 2015). In an efficient

drainage system the system capacity can adapt to increasing melt water supply such that flux and pressure are negatively correlated where increasing water flux lowers the basal water pressure (Schoof, 2010). In inefficient systems the system capacity is externally determined (*e.g.* the size of the aquifer pore-space is largely fixed) such that flux and water pressure are positively correlated as forcing more water through the system requires higher pressure gradients (*e.g.* Darcy flow).

Water flows through inefficient subglacial hydrologic systems in 3 ways: thin water films, porous flows, and linked-cavity flows (G. E. Flowers, 2015). In permeable till beds at the base of the glacier, water can drain through the sediment pore-space. In beds with immobile protrusions, ice sliding over protrusions can form cavities on the lee side (Kamb, 1987). As cavities become more numerous they form a network linked through smaller orifices giving a tortuous drainage network. As flux through the subglacial drainage system increases, heating by viscous dissipation melts channels into the base of the ice, so called Röthlisberger channels (Röthlisberger, 1972). These channels form a far more efficient drainage mode than the others and typically result in a drop in basal water pressure.

Linked cavities open by ice sliding over substrate highs and wall melting by heat dissipation at the ice-water interface. They close due to ice creep from overburden pressure (Schoof, 2010). For smaller cavities with lower flux (proportional to water pressure) than channels, ice sliding over bedrock highs dominates the opening. J. Walder and Hallet (1979) mapped one such system by examining bedrock evidence of cavities (depressions on the lee side of bedrock protuberances without ice-contact features) in the same deglaciated area as Hallet (1979). The mapped cavities were around 0.1-1.5 m high, elongated transverse to flow as described in the linked-cavity model by Kamb (1987).

Water Flux in the efficient system occurs in subglacial tunnels incised through overbearing ice, subglacial sediments, or hard bedrock. Channels eroded into bedrock remain in the same place through time while those formed into ice or

sediment can open, move and close depending on overbearing ice and hydrologic conditions. Nye channels, those engraved in hard bedrock, are less common and less important on a continental scale. J. Walder and Hallet (1979) mapped channels incised into the rock (Nye channels, or N-channels) 50-250 mm deep, 100-200 mm wide, and 2-5 m long running approximately parallel to ice flow features. Whereas N-channel are for channels incised into a hard bed, canals are channels excised into soft till J. S. Walder and Fowler (1994). These differ dynamically in that the floor of canals can close in on the conduit via soft-sediment deformation. The most common efficient system is the Röthlisberger channel (R-channel). Dendritic subglacial tunnels open up into the ice from the base by wall melting due to frictional heat from the contact between ice and flowing water (Röthlisberger, 1972) – the faster the water, the larger the channel. Counter to the inefficient regime, water pressure and flux are inversely proportional (Schoof, 2010; G. E. Flowers, 2015).

If water percolating through the inefficient system flows quickly enough to give significant wall melting, the system becomes unstable and quickly transitions to a channelized system (Schoof, 2010). At high fluxes, frictional melting of the tunnel ice wall from fast flowing water becomes a run away effect opening a R-channel into the ice. Canals likely also open due to high flux in the subglacial system, where energetic water mobilizes sediment along its path (Alley, 1992; J. S. Walder and Fowler, 1994). J. S. Walder and Fowler (1994) describes a continuum between two end member ephemeral tunnels systems – R-channels and canals– whereby wall melting into the ice is prevalent at high effective pressures and sediment removal at low pressures. The switch between efficient and inefficient drainage is controlled by water flux.

3.1 MODELLING SUBGLACIAL HYDROLOGY

In general, the flux through a subglacial hydrologic drainage element is (G. E. Flowers, 2015):

$$Q = -kh^{\alpha}|\psi|^{\beta-2}\psi \tag{38}$$

where

$$\psi = \nabla \left[P_{water} + \rho_w g z_b\right]. \tag{39}$$

$\alpha = 1$ and $\beta = 2$, gives Darcy flow for laminar flow through porous media. $\alpha = 5/4$ and $\beta = 3/2$ gives the Darcy-Weisbach relation for turbulent flow through conduits in eqn. 38. These flow and potential equations are combined with a relationship between basal water thickness and pressure (through assumptions about the drainage system) to get the formulations in § 3.1.1 and 4.2.1.

Treating water as an incompressible fluid, the continuity equation is:

$$-c\frac{\partial N}{\partial t} + \frac{\partial h}{\partial t} + \vec{\nabla} q = m \tag{40}$$

This elastic accommodation space term ($c\frac{\partial N}{\partial t}$) in eqn. 40 is neglected for longer time scales giving:

$$\frac{\partial h}{\partial t} + \vec{\nabla} q = m \tag{41}$$

Many hydrology models employ physics intended for single glacier scale and diurnal meltwater fluxes (I. Hewitt, 2013; Werder et al., 2013; Fleurian et al., 2014). Fewer hydrology models are intended for continental and glacial cycle scale application. These large scales require simplifying assumptions to render the problem computationally feasible. Some make the simplifying assumption that a thin water film is ubiquitous at the base and effective pressure is therefore zero.

Others make the assumption that at longer timescales the hydraulic potential follows the ice sheet topography and basal topography (eqn. 42),

$$\phi = \rho_w g z_b + \rho_i g H. \tag{42}$$

Using this simplification water can be distributed at the bed using a down-gradient routing scheme assuming steady state water thickness, $\frac{\partial h_{wb}}{\partial t} = 0$, instead of solving a transport equation and setting water pressure equal to overburden instead of assuming a pressure closure. Roberts, Payne, and Valdes (2016) used such a model intended for continental scale hydrology with sheet flow, calculating basal water thickness on the basis of hydraulic potential and flux from up-gradient,

$$\frac{h_{wb}^3 \phi}{12\mu} = \frac{q_{in} + \dot{m} r^2}{l}$$

with ϕ the hydraulic potential from ice sheet thickness and topography, μ the viscosity of water, q_{in} the flux into the cell, $\dot{m}$ the basal melt rate, and r, l grid cell dimensions. q_{in} is given by the flux routing scheme from Budd and Warner (1996) (which assumes flux divergence equivalent to accumulation, $A = \nabla \cdot (VZ)$ for accumulation A, average velocity V and thickness Z). Gudlaugsson et al. (2017) applied a nearly identical model to show the sensitivity of EAIS to subglacial hydrology. Calov et al. (2018) also implements this model, with an added modification to the hydraulic gradient in depressions or flat cells to ensure seaward drainage. Their hydrology model is coupled with ice sheet dynamics via basal sliding, simulating future GrIS change. The full model was tuned to present day observations for ice sheet topography and surface velocities.

Bueler and van Pelt (2015) implements a versatile version of a linked cavity transport layer with an underlying till reservoir (for calculating sliding velocities). They tested a variety of numerical schemes settling on an up-winding scheme as in this work. This model does not implement an efficient drainage scheme.

Interestingly, they also implement a routing scheme for comparison ($P_w = P_{ice}$, $N_{\text{eff}} = 0$) and find an appreciable difference, indicating that including a "pressure-determining closure" in place of this assumption may be worthwhile at the ice sheet scale.

3.1.1 *G. Flowers (2000) Poro-elastic Model*

The poro-elastic drainage formulation was developed by G. Flowers (2000). The main components are 3 equations:

- relationship between height of water column in elastic pore-space and water pressure in that pore-space
- mass conservation: fluxes in, fluxes out
- Darcy flow law describing flux as a function of hydraulic head

The Darcy flow law is given in eqn 43. This is eqn. 38 with $\alpha = 1$, $\beta = 2$

$$Q = -Kh\psi. \tag{43}$$

Water pressure in the elastic pore-space is given by eqn: 44

$$P_{water} = P_{ice}\left(\frac{h}{h_c}\right)^{7/2}. \tag{44}$$

3.1.2 *Schoof (2010) Linked-Cavity Model*

The main components are 3 equations:

- Opening/Closing relationship for cavity size
- Mass conservation

- Darcy-Weisbach flow law describing flux as a function of hydraulic head

Water transport is given in eqn. 41: The Darcy-Weisbach flow law is given in eqn. 45. This is eqn. 38 with $\alpha = 5/4$ and $\beta = 3/2$ and the hydraulic potential in eqn. 39

$$Q = -Kh^{5/4}|\psi|^{-1/2}\psi \tag{45}$$

k in eqn. 45 can represent various parameters such as tortuosity, orifice hydraulic head gradient, cavity density, etc. h is water sheet thickness, a continuum property used to describe the average amount of water in a grid cell. ψ is the same hydraulic potential in eqn. 39 with $P_{water} = P_{ice} - N_{eff}$ the hydraulic gradient is:

$$\psi = \nabla \left[\rho_w g z_b + (P_{ice} - N_{eff})\right] \tag{46}$$

N_{eff} is formulated in the following section (§ 3.1.2).

Effective Pressure

The opening closing relationship for cavity cross sectional area with respect to time is given by eqn. 47 which has three parts:

- wall melting term ($\propto Q\psi$)
- opening from sliding over bed protrusions ($\propto u_b h_r$)
- closing due to overburden pressure (creep) ($\propto N_{eff}^n S$)

$$\frac{\partial S}{\partial t} = c_1 Q\psi + u_b h_r - c_2 N_{eff}^n S \tag{47}$$

where S is the cavity size, c_1 and c_2 are constants, Q is flux, u_b is basal sliding velocity, h_r is bed protrusion height, $N_{eff} = P_{ice} - P_{water}$, and n is a coefficient from Glen's flow law (Schoof, 2010; Werder et al., 2013). These three actions act to increase/decrease cavity area. Schoof (2010) shows that the wall melting term is not important until a critical value is reached and the run away effect opens

tunnels (see assumption 1). As such the wall melting term is assumed zero until tunnelling is triggered.

$$\frac{\partial S}{\partial t} = u_b h_r - c_2 N_{eff}^n S \tag{48}$$

The efficient drainage system has been handled in various ways before, however no study to date has modelled a dynamic efficient drainage system at glacial-cycle continental scale. Kessler (2004) model the efficient drainage system as a single centerline channel which exchanges subglacial water with adjacent linked cavity system over a model domain two by fifteen kilometres over a time period of 100 days. G. E. Flowers et al. (2004) use a one-dimensional subglacial hydrology model integrated in the cross flowline direction with coupled dynamic efficient (channel) and inefficient (sheet) flow – this model is applied to a ($\approx$) 50 km domain over a 50 hour timeframe. Schoof (2010), Schoof, I. J. Hewitt, and Werder (2012), and Werder et al. (2013) formulate similar subglacial hydrology models coupling dynamically evolving linked-cavity and channel systems. Each are applied to domains on the order of tens of kilometres in length over time scales of less than 500 days. The largest scale application of dynamic efficient and inefficient subglacial hydrology to date is that of Dow et al. (2022) who applies the model of Werder et al. (2013) to 3 Antarctic glaciers, the largest study area of which has a domain of about 300 by 400 km, to steady state (though modelled timeframe is not given). Sommers, Rajaram, and Morlighem (2018) run their subglacial hydrology model which smoothly transitions between dynamical inefficient and efficient systems for 365 days on a two by ten kilometre domain, the study by Felden, Martin, and Ng (2023) details a similar model applied to a similar scale.

There are a few studies which do simulate the subglacial hydrological system for multi-millennial-continental ice sheet scales but these do not include a dynamical efficient system. Arnold and Sharp (2002) use an upstream contributing area flow integration and routing algorithm to calculate a non-dynamical effective pressure. Similarly, (Johnson and Fastook, 2002) also use a routing algorithm and assume the

simplify the hydraulic potential by assuming the effective pressure is proportional to the ratio of basal drag to basal water thickness. Bueler and van Pelt (2015) implement a mass conserving linked-cavity hydrology applied to the Greenland ice sheet with steady state forcing and one-way hydrology coupling for 50 ka but do not include an efficient regime. (Gudlaugsson et al., 2017) use a mass conserving, lateral flux routing algorithm similar to (Le Brocq et al., 2009), assuming zero effective pressure, steady state basal water thickness, and inefficient drainage only. Gandy et al. (2019) use a leaky-bucket hydrology (a zeroth order, non-conservative hydrology as laid out in our manuscript) coupled to BISICLES for their British-Irish ice sheet simulations. Though Bueler and van Pelt (2015) implemented a dynamical inefficient subglacial hydrology model coupled to PISM, Albrecht, Winkelmann, and Levermann (2020) use a non-mass conserving model similar to the leaky-bucket without an efficient system for their glacial cycle Antarctic ice sheet simulations.

3.2 THIS HYDROLOGY MODEL: BRAHMSV1

V1 of the Basal Hydrology Model (BrAHMs) is described in Kavanagh and Tarasov (2018). This model is an implementation of the subglacial hydrology model of G. Flowers (2000) for the inefficient system with an added down-gradient tunnel solver for the efficient system. The model uses a mass conserving transport equation with Darcy flux law and empirical pressure closure. When a flux threshold is reached, the tunnel solver is called and water is routed to a local minimum in potential gradient or exits the sheet.

While dynamically modelling flux through an efficient system might be ideal, the CFL criterion would impose prohibitively long run times for our context. Given a lower bound water velocity of 1 m/s in the channel system as measured by Chandler et al. (2013) and our (coarse) resolution of 50 km, a time step of 0.00158 model years is required. Our down-gradient routing, drainage solver is not subject

to timestep limitations imposed by the CFL criterion. The time step depends only on the inefficient system for our setup. This typically lies in the range of 0.5 to 0.25 model years (lower bound time step of 0.0625 yr). Directly modelling the efficient system would increase BrAHMs runtime anywhere from 150 to >300 fold rendering simulation of millennial scale variability unfeasible.

3.2.1 *Hydraulic Conductivity Calculation*

The range of values appropriate for hydraulic conductivity arise according to whether the drainage system is assumed to be poro-elastic or linked cavity or whether the flux is assumed laminar (Darcian) or turbulent (Darcy-Weisbach). Hydraulic conductivity in both the poro-elastic and linked cavity formulations is defined at the cell centres and is a function of temperature relative to pressure melt point. Since temperature is averaged over a cell, portions of the cell will be cold based and warm based. The transition from fully cold based (frozen) to fully warm based (thawed) marks the relative proportion of these areas between temperatures $[\mathrm{T_{froz}}, 0.0]$ °C.

$$hK^{i,j} = (K_{cond} - hK_f) * \left(1 - \exp\left\{\left[3\lceil min\left(0.0, Tbp^{i,j}\right), T_{froz}\rceil / T_{froz} - 1\right]\right\}\right) + hK_f \tag{49}$$

Interface conductivity values are calculated as the harmonic mean of the adjacent cell centred conductivities:

$$K_{we}^{ij} = \frac{2hK^{i-1j} hK^{i,j}}{hK^{i-1j} + hK^{ij}} \tag{50}$$

where i indicates the indices increasing west to east and j indicates indices increasing north to south.

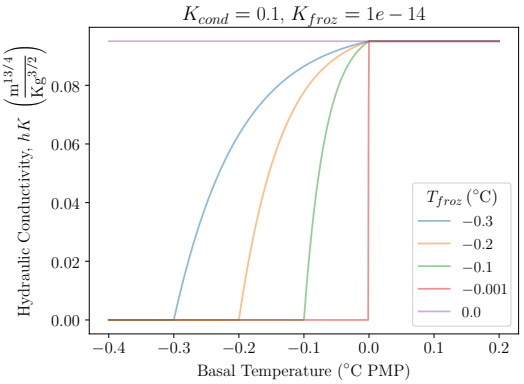

(a) Function of conductivity with cell averaged temperature showing transition from fully to partially cold based and on to full warm based as in eqn. 67

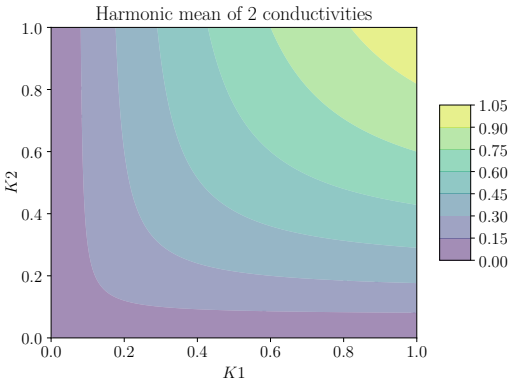

(b) Harmonic mean conductivity as in eqn. 68

3.2.2 *Hydrology Model Numerics Summary*

The conservative flux equation – transport equation (eqn. 41) is solved using a combination of explicit and semi-implicit methods. Time integration is done with a leap-frog trapezoidal predictor corrector method and Heun's method (Euler with trapezoidal integration) is used for the initial time step. conditions, followed by leapfrogging with trapezoidal integration. A detailed discretization for this numerical scheme is shown in § 8.1.

3.3 UPDATES TO BRAHMS IN V2

The updates to BrAHMsV1 undertaken as part of this work extend functionality and reduce the technical debt. This was done through extensive model testing (e.g. § 4.12), code examination, and static code analysis. These updates are four fold: physical, numerical, performance and coupling. Physical changes include the addition of linked-cavity and leaky-bucket hydrology. Numerical changes include updated time stepping, flux limiter calculation, and convergence criterion.

Performance changes include removing unused variables and calculations, moving repeated calculations to subroutines and functions, specifying proper intent

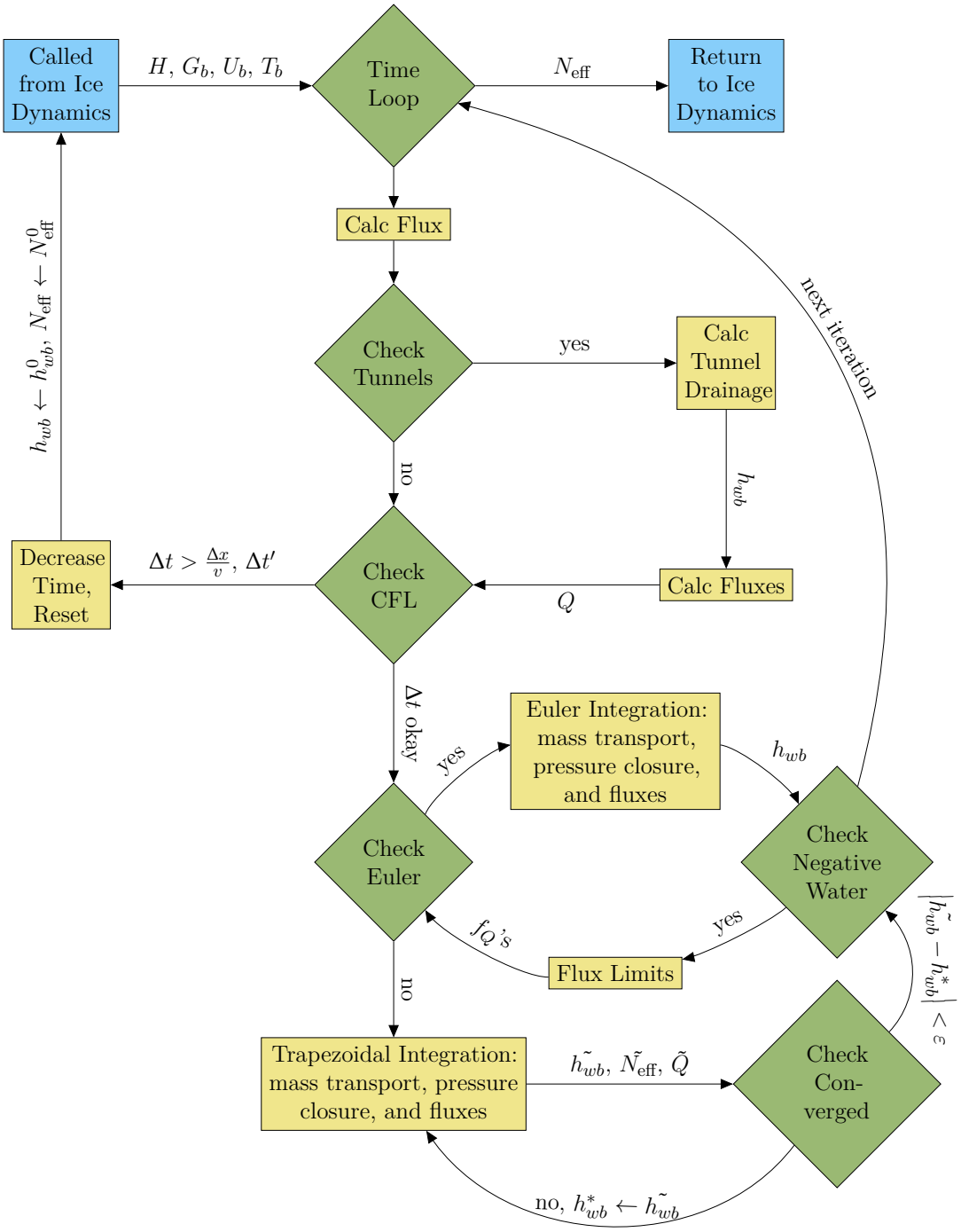

Figure 15: Updated flow chart of hydrology model algorithm execution, *cf.* V1 in Kavanagh and Tarasov (2018).

and interface error checking to ensure against segmentation faults and bounds overstepping errors, reordering array dimensions to take advantage of vectorization, and bringing the code up to Fortran 90 standard.

Coupling changes include using the effective pressure calculation in the basal sliding coefficient calculation. Improvements to the interface between BrAHMs and the Glacial Systems Model (GSM) were made as well – parameters read in via subroutine allowed for probing parametric uncertainty instead of hard coded parameter values in .inc.f files and fortran include statements, discretization change to use generalized grid terms for locations, widths, and derivative coefficients to take advantage of multiple GSM grids (*i.e.*, square grid, lat/lon, and Southern Polar Stereographic). Flags for standalone version to be used with f2py for specifying boundary ice sheet thickness, basal melt, and temperature for example were included to enable testing with SHMIP scenarios and large scale parameter probing. Boundary conditions were modified to use fields calculated elsewhere in the GSM (for example with ice is grounded or not) rather than re-calculating those terms and risking bugs.

Numerical changes include a switch to average and maximum discrepancy between predictor $\left(\tilde{h_{wb}}\right)$ and corrector (h^*_{wb}) basal water thickness solution in the trapezoidal integration loop:

$$\Delta h_{wb} = \frac{\left|\tilde{h_{wb}} - h^*_{wb}\right|}{h^*_{wb}}, \quad max\left(\Delta h_{wb}\right) \leq 0.02 \wedge mean\left(\Delta h_{wb}\right) \leq 0.001 \tag{51}$$

Prior to these updates, the criterion was based on conservation of mass traced throughout the code making it difficult to verify mass conservation in the model and adding a cumbersome additional layer of calculation. As time splitting can be a problem with the leap-frog trapezoidal methods (where even and odd iterations get out of sync with each other), a check to perform an Euler integration every n-iterations (default n=10) was implemented. The hydraulic potential also needed

to be modified following calls to the down-gradient tunnel solver as this generated large changes in basal water thickness such that the mass transport equation was suddenly rendered incorrect, generating potential instabilities.

The physical updates to this model extended the simulated systems to include a more complex, non-linear linked-cavity and a simplest case non-mass-transporting leaky-bucket hydrology in addition to the original Darcy, poro-elastic hydrology. These updates have also been described in chapter 4 where extensive model testing is also presented. This update implements the generalized flux calculation of eqn. 38 whereby Darcy or Darcy-Weisbach flux is determined by setting the flux exponents. The leaky-bucket hydrology does not transport water laterally but instead has a parameterized time-independent subglacial water removal rate similar to that of Gandy et al. (2019):

$$\frac{\partial h_{wb}}{\partial t} = s_{melt} - s_{drain} \tag{52}$$

with s_{melt} is the meltwater input and s_{drain} is the constant removal. The leaky-bucket and poro-elastic systems both use the original pressure closure from V1 as laid out in eqn. 44, while the linked-cavity system uses a new dynamic pressure closure the same as that of Werder et al. (2013) and Bueler and van Pelt (2015). The switch to efficient drainage in a cell is calculated as a flux condition whereby the same drainage solver is called as that of V1 with a few minor bug fixes. Including the linked-cavity physics required the addition of a dynamical pressure closure in eqn. 65 in place of the previous diagnostic pressure calculation in eqn. 44

ASSUMPTIONS The physics of the linked cavity system is highly non-linear. As such, a set of simplifying assumptions is required to make numerical modelling of this framework feasible. These assumptions are as follows:

1. Wall melting is not a control on cavity size until tunnels are opened, drainage systems switch from inefficient to efficient for a given value of flux.

2. At time scales of continental scale ice sheets, tunnels drain a fraction of water instantaneously.

3. Cavities are filled with water.

ASSUMPTION 1 Schoof (2010) showed the evolution of the subglacial drainage system (given eqn. 47) gives a bifurcation between cavity style and tunnel style drainage networks. Given effective pressure, the cavity opening speed is dominated by basal sliding below a certain flux and by the run away wall melting term above it.

ASSUMPTION 2 This assumption alleviates CFL violations from fast tunnel flux which would render modelling on the long time scales of glacial cycles infeasible. The time scale of drainage through subglacial tunnels is less than a single melt season, much shorter than the glacial cycle aim for application of this model. Any error introduced as a result of this assumption can be controlled through an adjustment factor of the tunnel switching criterion.

ASSUMPTION 3 This assumption (filled cavities) is justified by scale analysis of eqn. 47. Get 1 year time scale for creep term with 1 bar effective pressure, and 10^5s for opening from sliding with $u_b = 30\text{m/yr}$. Effective pressure will be far higher if the cavity is not filled and closure due to creep will be faster

3.3.1 *Modifications to the Linked-Cavity system of Schoof (2010)*

In this model the cavities are described as a continuum: height of a cavity averaged over protrusions separation (l_r) is given as $h = \frac{s}{l_r}$,

$$\frac{\partial (h \cdot l_r)}{\partial t} = u_b h_r - c_2 N_{eff}^n h \cdot l_r.$$

The wall melting term is dropped from eqn. 47 The opening term is modified to drop as cavity thickness rises over the bed protrusion $u_b\,(h_r - h)$.

The time varying water pressure calculation of Bueler and van Pelt (2015) turns this into a dynamical pressure closure. The rational summarized here is shown by Bueler (2014). Here the subglacial and englacial hydrologic systems are assumed in perfect communication and their co-evolution is described. The englacial hydrologic system is analogized to a rigid "pore-space" (comprised of crevasses, moulins, englacial channels, and intergranular porosity). The **tot**al volume of water is the sum of **eng**lacial and **sub**glacial water:

$$V_{tot} = V_{eng} + V_{sub} \tag{53}$$

and the mass balance for incompressible water is

$$\frac{\partial V_{tot}}{\partial t} = Q_{out} - Q_{in} + \frac{m}{\rho_w} \tag{54}$$

from total flux in and out of a control section of the system plus any sources (volume water, $\frac{m}{\rho_w}$) within that section. This section is of area $\Delta x X \Delta y$ and pressure in the connected englacial-subglacial system is given by the hydrostatic head in the englacial part:

$$P_w = \frac{\rho_w g}{\Delta x \Delta y \phi_{eng}} V_{eng}. \tag{55}$$

The effective englacial porosity (connected englacial void space) is ϕ_{eng}. Cavity volume within an area of bed with roughness wavelength l_r and height h_r is:

$$V_{sub} = n_{cav} w_{cav} S_{cav} = \frac{\Delta x \Delta y}{{l_r}^2} w_{cav} S_{cav} \tag{56}$$

where n_{cav} is the number of cavities in the given bed section, w_{cav} is the average width of those cavities, and S_{cav} is their average cross sectional area. Differentiating this gives the change in pressure with time:

$$\begin{aligned}\frac{\partial P_w}{\partial t} =& \frac{\rho_w g}{\Delta x \Delta y \phi_{eng}} \frac{\partial V_{eng}}{\partial t} \\ =& \frac{\rho_w g}{\Delta x \Delta y \phi_{eng}} \frac{\partial V_{tot} - V_{sub}}{\partial t} \\ =& \frac{\rho_w g}{\Delta x \Delta y \phi_{eng}} \left\{ Q_{in} - Qout + \frac{m}{\rho_w} - \frac{\Delta x \Delta y}{{l_r}^2} w_{cav} \frac{\partial S_{cav}}{\partial t} \right\}\end{aligned}$$

The $\frac{\partial S_{cav}}{\partial t}$ derivative is given by the opening and closing balance in eqn. 63,

$$\begin{aligned}\frac{\partial P_w}{\partial t} &= \frac{\rho_w g}{\Delta x \Delta y \phi_{eng}} \left\{ Q_{in} - Qout + \frac{m}{\rho_w} - \frac{\Delta x \Delta y}{{l_r}^2} w_{cav} \left(u_b h_r - c_2 [P_{ice} - P_w]^n \right) \right\} \\ &= \frac{\rho_w g}{\phi_{eng}} \left\{ \frac{Q_{in} - Qout + \frac{m}{\rho_w}}{\Delta x \Delta y} - \frac{w_{cav}}{{l_r}^2} \left(u_b h_r - c_2 [P_{ice} - P_w]^n \right) \right\}.\end{aligned}$$

Here opening due to wall melting has been omitted (see Assumption 1) relative to what is shown by Bueler (2014). As $\Delta x \to 0$ and $\Delta y \to 0$ the difference of the fluxes in versus out of the control section goes to the divergence of the fluxes within it.

$$\frac{\partial P_w}{\partial t} = \frac{\rho_w g}{\phi_{eng}} \left\{ \nabla \cdot \mathbf{Q} + m_t - \frac{w_{cav}}{{l_r}^2} \left(u_b h_r - c_2 [P_{ice} - P_w]^n \right) \right\}. \tag{57}$$

with m_t the source of water in thickness per unit time. Water is assumed to only travel laterally through the subglacial system and so all fluxes are through the linked cavities.

The dynamical subglacial hydrology models implemented here are the state of the art for the intended large scale application. The breadth of structural choices available in BrAHMsV2 are representative of those most commonly made in the literature. These choices are examined in chap. 4 along with a 0th order leaky-bucket hydrology. The surge cycling response of a Hudson Strait scale ice stream to the different formulations of subglacial hydrology is compared, drawing

the conclusion that the details of subglacial hydrology physics largely do not matter in this context. As such the new and most physically self consistent system, linked-cavity drainage, is coupled with the sediment model in chap. 5 and 6.

REFERENCES

Albrecht, T., R. Winkelmann, and A. Levermann (Feb. 2020). "Glacial-cycle simulations of the Antarctic Ice Sheet with the Parallel Ice Sheet Model (PISM) – Part 1: Boundary conditions and climatic forcing". In: *The Cryosphere* 14.2, pp. 599–632. ISSN: 1994-0424. DOI: 10.5194/tc-14-599-2020. URL: http://dx.doi.org/10.5194/tc-14-599-2020.

Alley, R. B. (1992). "How can low-pressure channels and deforming tills coexist subglacially?" In: *Journal of Glaciology* 38.128, pp. 200–207. ISSN: 1727-5652. DOI: 10.3189/s0022143000009734. URL: http://dx.doi.org/10.3189/S0022143000009734.

Arnold, N. and M. Sharp (Feb. 2002). "Flow variability in the Scandinavian ice sheet: modelling the coupling between ice sheet flow and hydrology". In: *Quaternary Science Reviews* 21.4–6, pp. 485–502. ISSN: 0277-3791. DOI: 10.1016/s0277-3791(01)00059-2. URL: http://dx.doi.org/10.1016/S0277-3791(01)00059-2.

Benn, D. I. and D. J. A. Evans (2010). *Glaciers & Glaciation*. 2nd ed. 338 Euston Road, London NW1 3BH: Hodder Education, An Hachette UK Company.

Budd, W. F. and R. C. Warner (1996). "A computer scheme for rapid calculations of balance-flux distributions". In: *Annals of Glaciology* 23, pp. 21–27. ISSN: 1727-5644. DOI: 10.3189/s0260305500013215. URL: http://dx.doi.org/10.3189/S0260305500013215.

Bueler, E. and W. van Pelt (June 2015). "Mass-conserving subglacial hydrology in the Parallel Ice Sheet Model version 0.6". In: *Geoscientific Model Development*

8.6, pp. 1613–1635. ISSN: 1991-9603. DOI: 10.5194/gmd-8-1613-2015. URL: http://dx.doi.org/10.5194/gmd-8-1613-2015.

Bueler, E. (2014). "Extending the lumped subglacial–englacial hydrology model of Bartholomaus and others (2011)". In: *Journal of Glaciology* 60.222, pp. 808–810. ISSN: 1727-5652. DOI: 10.3189/2014jog14j075. URL: http://dx.doi.org/10.3189/2014JoG14J075.

Calov, R., S. Beyer, R. Greve, J. Beckmann, M. Willeit, T. Kleiner, M. Rückamp, A. Humbert, and A. Ganopolski (Mar. 2018). "Simulation of the future sea level contribution of Greenland with a new glacial system model". In: *The Cryosphere Discussions*, pp. 1–37. ISSN: 1994-0440. DOI: 10.5194/tc-2018-23. URL: http://dx.doi.org/10.5194/tc-2018-23.

Chandler, D. M., J. L. Wadham, G. P. Lis, T. Cowton, A. Sole, I. Bartholomew, J. Telling, P. Nienow, E. B. Bagshaw, D. Mair, and et al. (Feb. 2013). "Evolution of the subglacial drainage system beneath the Greenland Ice Sheet revealed by tracers". In: *Nature Geoscience* 6.3, pp. 195–198. ISSN: 1752-0908. DOI: 10.1038/ngeo1737. URL: http://dx.doi.org/10.1038/NGEO1737.

Clason, C., D. W. Mair, D. O. Burgess, and P. W. Nienow (2012). "Modelling the delivery of supraglacial meltwater to the ice/bed interface: application to southwest Devon Ice Cap, Nunavut, Canada". In: *Journal of Glaciology* 58.208, pp. 361–374. ISSN: 1727-5652. DOI: 10.3189/2012jog11j129. URL: http://dx.doi.org/10.3189/2012JoG11J129.

Dow, C. F., N. Ross, H. Jeofry, K. Siu, and M. J. Siegert (Oct. 2022). "Antarctic basal environment shaped by high-pressure flow through a subglacial river system". In: *Nature Geoscience* 15.11, pp. 892–898. ISSN: 1752-0908. DOI: 10.1038/s41561-022-01059-1. URL: http://dx.doi.org/10.1038/s41561-022-01059-1.

Felden, A. M., D. F. Martin, and E. G. Ng (Jan. 2023). "SUHMO: an adaptive mesh refinement SUbglacial Hydrology MOdel v1.0". In: *Geoscientific Model*

Development 16.1, pp. 407–425. ISSN: 1991-9603. DOI: 10.5194/gmd-16-407-2023. URL: http://dx.doi.org/10.5194/gmd-16-407-2023.

Fleurian, B. de, O. Gagliardini, T. Zwinger, G. Durand, E. Le Meur, D. Mair, and P. Råback (Jan. 2014). "A double continuum hydrological model for glacier applications". In: *The Cryosphere* 8.1, pp. 137–153. ISSN: 1994-0424. DOI: 10.5194/tc-8-137-2014. URL: http://dx.doi.org/10.5194/tc-8-137-2014.

Flowers, G. E. (Mar. 2015). "Modelling water flow under glaciers and ice sheets". In: *Proceedings of the Royal Society A: Mathematical, Physical and Engineering Sciences* 471.2176, pp. 1–41. ISSN: 1471-2946. DOI: 10.1098/rspa.2014.0907. URL: http://dx.doi.org/10.1098/rspa.2014.0907.

Flowers, G. (Nov. 2000). "A Multicomponent Coupled Model of Glacier Hydrology". PhD thesis. Department of Earth, Ocean and Atmospheric Sciences Faculty of Science 2020 – 2207 Main Mall Vancouver, BC Canada V6T 1Z4: University of British Columbia.

Flowers, G. E., H. Björnsson, F. Pálsson, and G. K. C. Clarke (Mar. 2004). "A coupled sheet-conduit mechanism for jökulhlaup propagation". In: *Geophysical Research Letters* 31.5, n/a–n/a. ISSN: 0094-8276. DOI: 10.1029/2003gl019088. URL: http://dx.doi.org/10.1029/2003GL019088.

Gagliardini, O. and M. A. Werder (Aug. 2018). "Influence of increasing surface melt over decadal timescales on land-terminating Greenland-type outlet glaciers". In: *Journal of Glaciology*, pp. 1–11. ISSN: 1727-5652. DOI: 10.1017/jog.2018.59. URL: http://dx.doi.org/10.1017/jog.2018.59.

Gandy, N., L. J. Gregoire, J. C. Ely, S. L. Cornford, C. D. Clark, and D. M. Hodgson (Nov. 2019). "Exploring the ingredients required to successfully model the placement, generation, and evolution of ice streams in the British-Irish Ice Sheet". In: *Quaternary Science Reviews* 223, p. 105915. ISSN: 0277-3791. DOI: 10.1016/j.quascirev.2019.105915. URL: http://dx.doi.org/10.1016/j.quascirev.2019.105915.

Gudlaugsson, E., A. Humbert, K. Andreassen, C. C. Clason, T. Kleiner, and S. Beyer (Apr. 2017). "Eurasian ice-sheet dynamics and sensitivity to subglacial hydrology". In: *Journal of Glaciology* 63.239, pp. 556–564. ISSN: 1727-5652. DOI: 10.1017/jog.2017.21. URL: http://dx.doi.org/10.1017/jog.2017.21.

Hallet, B. (1979). "Subglacial Regelation Water Film". In: *Journal of Glaciology* 23.89, pp. 321–334. ISSN: 1727-5652. DOI: 10.1017/s0022143000029932. URL: http://dx.doi.org/10.1017/S0022143000029932.

Hewitt, I. (June 2013). "Seasonal changes in ice sheet motion due to melt water lubrication". In: *Earth and Planetary Science Letters* 371-372, pp. 16–25. ISSN: 0012-821X. DOI: 10.1016/j.epsl.2013.04.022. URL: http://dx.doi.org/10.1016/j.epsl.2013.04.022.

Iken, A., H. Röthlisberger, A. Flotron, and W. Haeberli (1983). "The Uplift of Unteraargletscher at the Beginning of the Melt Season—A Consequence of Water Storage at the Bed?" In: *Journal of Glaciology* 29.101, pp. 28–47. ISSN: 1727-5652. DOI: 10.3189/s0022143000005128. URL: http://dx.doi.org/10.3189/S0022143000005128.

Iken, A. and R. A. Bindschadler (1986). "Combined measurements of Subglacial Water Pressure and Surface Velocity of Findelengletscher, Switzerland: Conclusions about Drainage System and Sliding Mechanism". In: *Journal of Glaciology* 32.110, pp. 101–119. ISSN: 1727-5652. DOI: 10.3189/s0022143000006936. URL: http://dx.doi.org/10.3189/S0022143000006936.

Johnson, J. and J. L. Fastook (Sept. 2002). "Northern Hemisphere glaciation and its sensitivity to basal melt water". In: *Quaternary International* 95–96, pp. 65–74. ISSN: 1040-6182. DOI: 10.1016/s1040-6182(02)00028-9. URL: http://dx.doi.org/10.1016/S1040-6182(02)00028-9.

Kamb, B. (1987). "Glacier surge mechanism based on linked cavity configuration of the basal water conduit system". In: *Journal of Geophysical Research* 92.B9,

pp. 9083–9100. ISSN: 0148-0227. DOI: 10.1029/jb092ib09p09083. URL: http://dx.doi.org/10.1029/JB092iB09p09083.

Kavanagh, M. and L. Tarasov (Aug. 2018). "BrAHMs V1.0: a fast, physically based subglacial hydrology model for continental-scale application". In: *Geoscientific Model Development* 11.8, pp. 3497–3513. ISSN: 1991-9603. DOI: 10.5194/gmd-11-3497-2018. URL: http://dx.doi.org/10.5194/gmd-11-3497-2018.

Kessler, M. A. (2004). "Testing a numerical glacial hydrological model using spring speed-up events and outburst floods". In: *Geophysical Research Letters* 31.18. ISSN: 0094-8276. DOI: 10.1029/2004gl020622. URL: http://dx.doi.org/10.1029/2004GL020622.

Le Brocq, A., A. Payne, M. Siegert, and R. Alley (2009). "A subglacial water-flow model for West Antarctica". In: *Journal of Glaciology* 55.193, pp. 879–888. ISSN: 1727-5652. DOI: 10.3189/002214309790152564. URL: http://dx.doi.org/10.3189/002214309790152564.

Roberts, W. H. G., A. J. Payne, and P. J. Valdes (Aug. 2016). "The role of basal hydrology in the surging of the Laurentide Ice Sheet". In: *Climate of the Past* 12.8, pp. 1601–1617. ISSN: 1814-9332. DOI: 10.5194/cp-12-1601-2016. URL: http://dx.doi.org/10.5194/cp-12-1601-2016.

Röthlisberger, H. (1972). "Water Pressure in Intra- and Subglacial Channels". In: *Journal of Glaciology* 11.62, pp. 177–203. ISSN: 1727-5652. DOI: 10.3189/s0022143000022188. URL: http://dx.doi.org/10.3189/S0022143000022188.

Schoof, C. (Dec. 2010). "Ice-sheet acceleration driven by melt supply variability". In: *Nature* 468.7325, pp. 803–806. ISSN: 1476-4687. DOI: 10.1038/nature09618. URL: http://dx.doi.org/10.1038/nature09618.

Schoof, C., I. J. Hewitt, and M. A. Werder (May 2012). "Flotation and free surface flow in a model for subglacial drainage. Part 1. Distributed drainage". In: *Journal of Fluid Mechanics* 702, pp. 126–156. ISSN: 1469-7645. DOI: 10.1017/jfm.2012.165. URL: http://dx.doi.org/10.1017/jfm.2012.165.

Sommers, A., H. Rajaram, and M. Morlighem (July 2018). "SHAKTI: Subglacial Hydrology and Kinetic, Transient Interactions v1.0". In: *Geoscientific Model Development* 11.7, pp. 2955–2974. ISSN: 1991-9603. DOI: 10.5194/gmd-11-2955-2018. URL: http://dx.doi.org/10.5194/gmd-11-2955-2018.

Walder, J. and B. Hallet (1979). "Geometry of Former Subglacial Water Channels and Cavities". In: *Journal of Glaciology* 23.89, pp. 335–346. ISSN: 1727-5652. DOI: 10.1017/s0022143000029944. URL: http://dx.doi.org/10.1017/S0022143000029944.

Walder, J. S. and A. Fowler (1994). "Channelized subglacial drainage over a deformable bed". In: *Journal of Glaciology* 40.134, pp. 3–15. ISSN: 1727-5652. DOI: 10.3189/s0022143000003750. URL: http://dx.doi.org/10.3189/S0022143000003750.

Werder, M. A., I. J. Hewitt, C. G. Schoof, and G. E. Flowers (Oct. 2013). "Modeling channelized and distributed subglacial drainage in two dimensions". In: *Journal of Geophysical Research: Earth Surface* 118.4, pp. 2140–2158. ISSN: 2169-9003. DOI: 10.1002/jgrf.20146. URL: http://dx.doi.org/10.1002/jgrf.20146.

Zwally, H. J., W. Abdalati, T. Herring, K. Larson, J. Saba, and K. Steffen (July 2002). "Surface Melt-Induced Acceleration of Greenland Ice-Sheet Flow". In: *Science* 297.5579, pp. 218–222. ISSN: 1095-9203. DOI: 10.1126/science.1072708. URL: http://dx.doi.org/10.1126/science.1072708.

Preface to Chapter 4, "Surging of a Hudson Strait Scale Ice Stream: Subglacial hydrology matters but the process details mostly don't"

This chapter is in review at The Cryosphere (Drew and Tarasov, 2022). The results and conclusions herein support the coupled climate-ice-basal process modelling techniques employed in chap. 5 and 6. This chapter applies the concept and model developed in chap. 3 to assess the contribution from subglacial hydrology to surging of a large scale ice stream and compare the contribution from three drainage systems.

Chapter 4

Surging of a Hudson Strait Scale Ice Stream: Subglacial hydrology matters but the process details mostly don't

ABSTRACT

While subglacial hydrology is known to play a role in glacial dynamics on sub-annual to decadal scales, it remains unclear whether subglacial hydrology plays a critical role in ice sheet evolution on centennial or longer time-scales. Furthermore, several drainage systems have been inferred but it is unclear which is most applicable at the continental/glacial scale. More fundamentally, it is even unclear if the structural choice of subglacial hydrology truly matters for this context.

Here we compare the contribution to the surge behaviour of an idealized Hudson Strait like ice stream from three subglacial hydrology systems. We use the newly updated **BA**sal **H**ydrology **M**odel BrAHMs2.0 and provide model verification tests. BrAHMs2.0 incorporates two process-based representations of inefficient drainage dominant in the literature (linked-cavity and poro-elastic) and a non-mass

conserving zero-dimensional form (herein termed leaky-bucket) coupled to an ice sheet systems model (the **G**lacial **S**ystems **M**odel ,GSM). The linked-cavity and poro-elastic configurations include an efficient drainage scheme while the leaky-bucket does not. All three systems have a positive feedback on ice velocity whereby faster basal velocities increase melt supply. The poro-elastic and leaky-bucket systems have diagnostic effective pressure relationships – only the linked-cavity system has an additional negative feedback whereby faster basal ice velocities increase the dynamical effective pressure due to higher cavity opening rates. We examine the contribution of mass transport, efficient drainage, and the linked-cavity negative feedback to surging. We also assess the likely bounds on poorly constrained subglacial hydrology parameters and adopt an ensemble approach to study their impact and interactions within those bounds.

We find that subglacial hydrology is an important system inductance for realistic ice stream surging but that the three formulations all exhibit similar surge behaviour within parametric uncertainties. Even a detail as fundamental as mass conserving transport of subglacial water is not necessary for simulating a full range of surge frequency and amplitude. However, one difference is apparent: the combined positive and negative feedbacks of the linked-cavity system yields longer duration surges and a broader range of effective pressures than its poro-elastic and leaky-bucket counterparts.

4.1 INTRODUCTION

The role of subglacial hydrology at time scales longer than multiple decades and at ice sheet spatial scales is unclear. Previous studies have inferred subglacial hydrology to play a strong role in internally (e.g. Siegfried et al., 2016) and externally (e.g. Joughin et al., 1996; Cook, Christoffersen, and Todd, 2021) driven ice sheet variability on sub-annual to multi-decadal time scales (Retzlaff and Bentley, 1993;

R. B. Alley et al., 1994; Ou, 2021; Bennett, 2003). Observations beyond these time scales do not exist.

Several subglacial hydrologic systems have been conceptualized (G. E. Flowers, 2015). Constraint of the role of hydrological systems is further challenged by the large parametric uncertainties for all choices of drainage system. For example, the bounds of hydraulic conductivity vary over several orders of magnitude and according to the particular system (Werder et al., 2013). These uncertainties hinder widespread adoption of subglacial hydrology models in earth systems models in general and glacial cycle scale ice sheet modelling in particular (G. E. Flowers, 2018). As such, what is needed to adequately incorporate the subglacial hydrologic system into glacial cycle simulations is not understood.

We ask a basic question: does subglacial hydrology matter on longer than decadal time-scales? And if so, to what extent are the structural details of the hydrological system important for this context, especially given the rest of the system uncertainties? Taking a modelling approach, we focus these broad questions to the following: Is subglacial hydrology needed to capture Hudson Strait scale ice stream cyclicity? If so, should effective pressure be dynamically determined – based on fully mass conserving lateral drainage? Or does a zero-dimensional meltwater volume balance with a diagnostic pressure closure suffice? Turning to the parametric uncertainties, which are most important?

Previous model-based tests of Hudson Strait ice stream surging (e.g. Calov et al., 2010; Payne, Huybrechts, et al., 2000; Payne and Dongelmans, 1997; MacAyeal, 1993) have focused on thermomechanical feedbacks but omitted the contribution from the subglacial hydrological system. While these studies capture surges in their simulations based on these limited feedbacks, all models except one (model (d), Calov et al., 2010) implemented an abrupt transition at the frozen-temperate thermal boundary, suddenly initiating large scale sliding within a grid cell. This abrupt thermal transition is physically unrealistic at the scales of ice sheet modelling:

a region equivalent to a glacial cycle scale ice sheet model grid cell ($100 - 2500$ km^2) does not become instantly warm based with wholesale transition to basal slide. Instead, the streaming portions of ice sheets transition to faster sliding velocities as their coupling to the bed (effective pressure) decreases. Subglacial hydrology is a potentially critical piece of the binge-purge conceptual model of internal oscillations (MacAyeal, 1993) as heat production from sliding and deformation work generates meltwater.

Here we examine the contribution to ice sheet internal oscillations from the three most dominant forms of distributed subglacial hydrology – linked cavity (Schoof, 2010), poro-elastic (G. Flowers, 2000), and non-mass transporting leaky-bucket (Gandy et al., 2019) – relative to each other and to no hydrology at all. In each case, the frozen to temperate transition is smoothed following the work of Hank, Tarasov, and Mantelli (2023). We couple these processes to an ice sheet systems model, the **G**lacial **S**ystems **M**odel GSM Tarasov, Dyke, et al., 2012.

Simple configurations make system behaviours more interpretable (e.g. Calov et al., 2010; Payne, Huybrechts, et al., 2000). With a realistic bed and actual climate, spatio-temporal variations in model solutions are largely due to the variation in boundary conditions. We therefore model these coupled systems for a simplified North American analogue setup which implements a square bed and flat topography with soft beds in the southern latitudes and in the Hudson Strait/Bay area. The ice sheet is forced with a steady climate and first order feedbacks: Northward cooling temperature trend, vertical lapse rate, and thermodynamic moisture control. The numerical model retains important processes while still being feasible to run large ensembles over a glacial cycle on continental scales to probe parametric uncertainties.

Below, we first test the **BA**sal **H**ydrology **M**odel BrAHMs. This includes demonstration of mass conservation, convergence, and symmetry of BrAHMs2.0 and verification of its solutions against another prominent model, GlaDS (Werder

et al., 2013). Next we show the sensitivity of ice sheet geometry to subglacial hydrologic parameters in comparison with climate and ice sheet parameters. Finally, we compare results from a set of 4 large ensembles (between 11 and 20 thousand members each) using no hydrology, linked-cavity, poro-elastic, and leaky-bucket hydrology.

4.2 SUBGLACIAL HYDROLOGY

In the context of continental scale ice sheet modelling, resolving individual drainage elements and multiple topologies present within the domain is not computationally feasible. In this section we briefly overview some structural choices made by others and present the options compared in this study, beginning with the current understanding of subglacial hydrology and progressing to increasingly approximate representations of it.

Water in the subglacial system flows either through inefficient drainage systems (pressure $\propto$ flux) or efficient drainage systems (pressure $\propto$ flux^{-1} G. E. Flowers, 2015). Inefficient distributed networks are widespread under temperate areas of ice sheets, whereas efficient channel networks are discrete, localized elements. Each class evolves to the other and the change is controlled by system throughput, i.e. water flux. When the flux in an inefficient system rises above a threshold, the system transitions to efficient drainage. When the efficient system flux falls through different lower flux threshold, the system transitions to inefficient drainage, resulting in hysteresis Schoof, 2010. Any mass transporting hydrology model should have three main components: mass conservation describing transport, a flow law describing flux as a function of hydraulic gradient and subglacial water thickness, and a pressure closure relationship.

4.2.1 *Inefficient flow*

In the inefficient drainage regime, flux and water pressure rise together. Several inefficient drainage systems have been theorized: thin film, poro-elastic media, and linked-cavities. Of these, poro-elastic and linked-cavity (e.g. G. Flowers, 2000; J. S. Walder, 1986) dominate recently published models (G. E. Flowers, 2015; de Fleurian et al., 2018) and as such these are the two systems we model and contrast herein.

In the poro-elastic formulation, water can drain through the pore space of some permeable surficial material (e.g. till). Increasing subglacial water pressures expand the pore-space and modify the permeability of the porous medium to flowing water. The conceptual basis for this system is examined in greater detail by G. E. Flowers and Clarke (2002). The pressure closure has no theoretical basis and is based on a power law with empirically constrained parameters (G. Flowers, 2000).

In the linked-cavity system, cavities within the base of the ice open up as basal ice flows over and around bed protrusions – fast flow and larger objects beget larger cavities (Kamb, 1987). As cavities grow larger and numerous they form a connected network linked through smaller orifices giving a tortuous drainage network.

The substrate type that controls which inefficient system dominates – i.e. till cover and roughness – is variable (Pelletier et al., 2016; Brubaker et al., 2013). Conceivably, while poro-elastic drainage requires a porous ice sheet substrate, the cavities can form in any environment with bed protrusions which are less mobile than ice flow. A soft bedded cavity has been seen at the base of a borehole in ice stream C (Carsey et al., 2002) and the theoretical basis for these cavities (Schoof, 2007) is motivated by drumlin formation (A. C. Fowler, 2009). However, cavities can only drain water once they grow enough to join and form a connected network (Rada and Schoof, 2018).

The contrast between the order kilometre or larger model scales and the order metre or smaller process scales permits inefficient flow to be described as a continuum at the macro scale. On the macro scale, flux is related to water thickness and hydraulic gradient as (G. E. Flowers, 2015):

$$\vec{Q} = -k{h_{wb}}^{\alpha}|\vec{\psi}|^{\beta-2}\vec{\psi} \tag{58}$$

with flux $\vec{Q}$, hydraulic conductivity k, and subglacial (basal) water thickness h_{wb}. The gradient of the hydraulic potential is given by

$$\vec{\psi} = \vec{\nabla}\left[P_{water} + \rho_w g z_b\right] \tag{59}$$

with subglacial water pressure P_{water}, density of freshwater ρ_w, gravitational acceleration g, and basal topographic elevation z_b. The exponents in eqn. 58 set laminar or turbulent flow. $\alpha = 1$ and $\beta = 2$ gives Darcy's law for laminar flow through porous media (Darcy, 1856; Muskat, 1934). $\alpha = 5/4$ and $\beta = 3/2$ gives the Darcy-Weisbach relation for turbulent flow through conduits (Clarke, 1996; Weisbach, 1855). Eqn. 59 and 58 are combined with a water pressure closure relationship given by the underlying physical system to get the formulations in § 4.2.1 and 4.2.1.

Water sheet thickness is a continuum property used to describe the average amount of water in a grid cell. Changes in water thickness is given by the fluxes and the aggregate of sources and sinks, m, in the water transport eqn. 60

$$\frac{\partial h_{wb}}{\partial t} + \vec{\nabla}\cdot\vec{Q} = m \tag{60}$$

cell, $\vec{Q}$ is the subglacial water flux and m is the aggregate of sources and sinks.

Poro-Elastic System

Pressurized subglacial water flows through the pore-space of a layer between ice and bedrock, conceptualized as the interstitial space between till grains. As water pressure increases, permeability of the porous medium rises. Water pressure is related to subglacial water thickness by a non-linear function using pore-space saturation (61). This poro-elastic drainage formulation is laid out in G. Flowers (2000). The flow law is Darcy's law describing laminar flux as a function of hydraulic gradient and subglacial water thickness. The pressure closure is an empirical relationship between the water column height in the elastic pore-space and subglacial water pressure.

The Darcy flow law is eqn. 58 with $\alpha = 1$, $\beta = 2$ Water pressure in the elastic pore-space is set by eqn. 61 (G. Flowers, 2000):

$$P_{water} = P_{ice} \left(\frac{h_{wb}}{h_c} \right)^{7/2} \tag{61}$$

where P_{ice} is the pressure due to the weight of overbearing ice and h_c is the water thickness scalar interpreted as thickness of the pore-space accommodating water.

Linked-Cavity System

As ice flows over protrusions in the bed, cavities open in the lee side. The faster ice flows and the higher the protrusion, the greater the opening rate. The weight of the overbearing ice acts to close the void through viscous creep. The trade off between these two rates determines the net cavity size change rate. These cavities link through smaller connections and form a drainage network whose throughput is controlled by orifice size and system tortuosity. As water flows more quickly in the drainage network, wall melting due to frictional heating at the ice/water interface further opens cavities and the interconnecting orifices, forming a more efficient system. The Darcy-Weisbach flow law for turbulent flux depends on the

hydraulic gradient and subglacial water thickness. The pressure closure is based on cavity opening and closing velocities and mass balance. The Darcy-Weisbach flow law is eqn. 58 with $\alpha = 5/4$ and $\beta = 3/2$ with $P_{water} = P_{ice} - N_{eff}$. For the linked-cavity system, $k = k_{lc}$ in eqn. 58 aggregates quantities such as tortuosity, hydraulic gradient across the orifice, cavity density, etc. Completing the set of equations, the effective pressure, N_{eff}, is given by the opening/closing relationship for cavity cross-sectional area with respect to time in eqn. 62. This has three parts:

- wall melting term ($\propto \vec{Q} \cdot \vec{\psi}|$)
- opening from sliding over bed protrusions ($\propto u_b h_r$)
- closing due to overburden pressure (creep) ($\propto N_{eff}^n S$)

$$\frac{\partial S}{\partial t} = c_1 \vec{Q} \cdot \vec{\psi} + u_b h_r - c_2 N_{eff}^n S \tag{62}$$

where S is the cavity size, c_1 and c_2 are constants, $\vec{Q}$ is flux, u_b is basal sliding velocity, h_r is bed protrusion height, and n is the exponent from Glen's flow law (Schoof, 2010; Werder et al., 2013). These three terms act to increase or decrease cavity area.

4.2.2 *Efficient flow*

In the efficient drainage regime, flux and water pressure are inversely related. Flux in the efficient system occurs in subglacial tunnels incised into overbearing ice (Röthlisberger, 1972), down into subglacial sediments (J. S. Walder and A. Fowler, 1994), or hard bedrock (R. Alley, 1989). Channels eroded into bedrock remain in the same place through time while those formed into ice or sediment can open, move and close depending on overbearing ice and hydrologic conditions. The most commonly modelled efficient system is the Röthlisberger channel (R-channel) carved up into the overbearing ice (de Fleurian et al., 2018). Dendritic subglacial tunnels

Name	Description	Range	Drainage
k_{lc}	Hydraulic conductivity of cavities	1.00e-06 1.00e+01	LC
h_r	Vertical basal roughness height	1.00e-02 2.00e+01	LC, Tunnel
R_{ratio}	Roughness height:wavelength (h_r/l_r)	1. 20.	LC
Q_{scale}	Tunnel switch criterion scaler	1.00e-03 1.00e+00	Tunnel
$F_{N_{eff}}$	N_{eff} normalization in sliding	1.0e4 1.0e6	LC, PE, LB
T_{froz}	Freeze point, hydrology system	-1.00e-00 0.00e+00	LC, PE, LB
k_{max}	Max hydraulic conductivity	1.00e-06 1.00e+01	PE
k_{ratio}	Max:min hydraulic conductivity	1.00e+00 1.00e+02	PE
h_c	h_{wb} quotient, water pressure	1.00e-01 5.00e+01	PE, LB
s_{drain}	Drainage rate	1.00e-03 1.00e-02	LB

Table 1: Table of parameter names, descriptions, their numerical ranges, and the subglacial hydrologic system they parameterize used in the ensembles for this study. LC corresponds to the linked-cavity system, PE the poro-elastic system, and LB the leaky bucket system.

open up into the ice from the base by wall melting due to frictional heat from the contact between ice and flowing water (Röthlisberger, 1972) – the faster the water, the larger the channel. Counter to the inefficient regime, water pressure and flux are inversely proportional (Schoof, 2010; G. E. Flowers, 2015). As water percolating through the inefficient system flows quickly enough to give significant wall melting, the system becomes unstable and quickly transitions to a channelized system (Schoof, 2010). Schoof (2010) showed that eqn. 62 bifurcates into the inefficient linked-cavity system and the efficient R-channel system, the switch between the two controlled by flux in the subglacial system. At high fluxes, frictional melting of the tunnel ice wall from fast flowing water becomes a run away effect opening a R-channel into the ice. Canals likely open due to high flux as well in the subglacial system, where energetic water mobilizes sediment along its path (R. B. Alley, 1992; J. S. Walder and A. Fowler, 1994).

The conceptual basis for the efficient flow model herein is the R-channel which evolves out of the inefficient system based on high fluxes.

Configuration	Drainage	Efficient Drainage	N_{eff}
LC	Darcy-Weisbach	yes	Dynamic, u_b two way feedback, Bueler and van Pelt (e.g. 2015)
PE	Darcy	yes	Diagnostic, (e.g. G. Flowers, 2000)
LB	None	no	Diagnostic, (e.g. G. Flowers, 2000)
NH	N/A	N/A	N/A

Table 2: Table of subglacial hydrology configurations showing the drainage law used, whether the efficient drainage system is coupled in, and what effective pressure is used. LC corresponds to the linked-cavity system, PE the poro-elastic system, and LB the leaky bucket system.

4.3 MODEL DESCRIPTION

The model used here is a fully coupled system of hybrid SIA/SSA ice physics (Pollard and DeConto, 2012) and 3D ice thermodynamics and 1D bed thermodynamics (Tarasov and W. R. Peltier, 2007). The climate forcing imposes a background surface temperature trend and elevation dependencies for temperature and precipitation. The subglacial hydrology model includes a choice of linked-cavity, poro-elastic, or leaky-bucket inefficient drainage, of whicgh the linked-cavity and poro-elastic can be coupled to the efficient drainage tunnel solver. The transition from frozen to temperate is smoothed to more realistically capture the transition to sliding (as in model (d) of Calov et al. (2010)) following the work of Hank, Tarasov, and Mantelli (2023). A more detailed description of the GSM is forthcoming Tarasov et al. (in prep.).

4.3.1 *Subglacial Hydrology Model*

The subglacial hydrology model – BrAHMs2.0 – is an extensive update to version 1.0 (Kavanagh and Tarasov, 2018). The update includes: the addition of linked-cavity and leaky bucket systems, an updated generalized grid, modified convergence

criteria, modified flux limiter, and code restructuring. This model uses a finite volume discretization with a staggered Arakawa C grid (fluxes at interfaces Arakawa and Lamb, 1977). In the case of the 2D mass transporting hydrology setups (poro-elastic and linked cavity), we implement the generalized flux calculation in eqn. 58 with a choice of either the pressure-determining closure of G. Flowers (2000) or a modified version of Schoof (2010) as in that of Werder et al. (2013) and Bueler and van Pelt (2015) whereby the cavity opening rate is proportional to the difference in bed roughness and subglacial water sheet thickness. Schoof (2010) shows that the wall melting term in eqn. 62 is unimportant until a critical value is reached and the run away effect opens tunnels (see assumption 1 below). As such, the wall melting term is assumed zero until tunnelling is triggered.

$$\frac{\partial S}{\partial t} = u_b h_r - c_2 N_{eff}^n S \tag{63}$$

In this model the cavities are described as a continuum: height of a cavity averaged over protrusion spacing (l_r) is given as $h_{cav} = \frac{S}{l_r}$,

$$\frac{\partial \left(h_{cav} \cdot l_r\right)}{\partial t} = u_b h_r - c_2 N_{eff}^n h_{cav} \cdot l_r. \tag{64}$$

The opening term is modified to drop as average cavity thickness rises over the bed protrusion $u_b \left(h_r - h_{cav}\right)$ as in (e.g.) Werder et al. (2013), and cavities are assumed filled by subglacial water ($h_{cav} = h_{wb}$, see assumption 3). This leads to the relationship for water pressure evolution:

$$\frac{\partial P_w}{\partial t} = \frac{\rho_w g}{\phi_{eng}} \left(-\vec{\nabla} \cdot \vec{Q} + m_t - u_b \left(h_r - h_{wb}\right) / l_r + c_2 [P_{ice} - P_w]^n\right) \tag{65}$$

where ϕ_{eng} is the englacial porosity and m_t Eqn. 65 is derived in apdx. 4.13.1 following Bueler (2014) and is similar to that used in Werder et al. (2013), Hewitt (2013), and Bueler and van Pelt (2015).

While in the linked-cavity model the hydraulic conductivity is a single parameter, in the poro-elastic model G. Flowers (2000) uses a meltwater thickness dependent arctan function for hydraulic conductivity to capture a transition from low to high permeability during expansion of the pore-space:

$$\log(k) = \frac{1}{\pi}\left[\log(k_{max}) - \log\left(k_{min}\right)\right] \arctan\left[k_a\left(\frac{h_{wb}}{h_c} - k_b\right)\right] + \frac{1}{2}\left[\log(k_{max}) + \log\left(k_{min}\right)\right]. \tag{66}$$

Where k is the poro-elastic hydraulic conductivity, k_{max} is the maximum conductivity, $k_{min} = k_{max}/k_{ratio}$ is the minimum conductivity, h_c is the critical water thickness in the pore-space (h_c in tbl. 2), and k_a and k_b control the transition between the maximum and minimum conductivity.

Numerically, hydraulic conductivity in both the poro-elastic and linked cavity formulations is defined at the cell centres and is a function of cell temperature relative to pressure melt point (T_{bp}). To account for the transition from fully cold based (frozen) to fully warm based (thawed), the bed is assumed to be fully frozen below T_{froz} and the hydraulic conductivity is given the following dependence on basal temperature relative to pressure melt point (T_{bp}):

$$k^{i,j}_{therm} = (k - k_f) * \left(1 - \exp\left\{\left[3\lceil min\left(0.0, T^{i,j}_{bp}\right), T_{froz}\rceil / T_{froz} - 1\right]\right\}\right) + k_f \tag{67}$$

where k_f is the hydraulic conductivity of frozen till (effectively zero). As the flux should be a function of the potential difference across the interface, the harmonic mean of the adjacent cell centred conductivities gives the most appropriate interface conductivity (Patankar, 1980).

$$k^{ij}_{we} = \frac{2k^{i-1j}_{therm}k^{i,j}_{therm}}{k^{i-1j}_{therm} + k^{ij}_{therm}} \tag{68}$$

In order to assess the importance of transport vs pressure determination in surging, we implement a non-mass conserving zero$^{\text{th}}$ order "leaky bucket" scheme:

a constant drainage rate (s_{drain}) counters the melt rate (s_{melt}) to give basal water thickness in that cell following Gandy et al. (eqn. 3, 2019):

$$\frac{\partial h_{wb}}{\partial t} = s_{melt} - s_{drain} \tag{69}$$

The leaky-bucket scheme uses the empirical pressure-determining closure of G. Flowers (2000) shown in eqn 61. with basal water thickness limited between zero and the critical thickness of the pressure closure (h_c in eqn. 61).

Fully modelling the process of efficient drainage of water through the channel system would require very short time steps due to CFL (Courant, Friedrichs, and Lewy, 1928) restrictions and consequently prohibitively long run times. Given the disparity in time scale between efficient drainage (sub-annual) and the dynamical behaviour examined here (centennial to millenial scale surging), it is unlikely that dynamically versus diagnostically modelling the efficient drainage will have an effect on the longer time scale surging, though as the model is non-linear there is potential for propagation across time scales. As such an alternate scheme is used under the assumption that drainage happens far quicker than in the inefficient system (assumption 2), which should especially hold for ice sheet modelling contexts. If flux at a cell face exceeds the bifurcation threshold or "critical discharge" of Schoof (2010), water is routed down the background hydraulic gradient (i.e. from topography and ice sheet overburden), filling in potential lows along the way until routed water is depleted or exits the ice sheet. This subglacial meltwater routing scheme is a slight modification of the down slope surface meltwater routing scheme of Tarasov and W. Peltier (2006) (i.e. with a modified hydraulic gradient). This routing scheme is further discussed in Kavanagh and Tarasov (2018).

For details on the numerical solver used here, readers are invited to read appendix 4.10. Assumptions used in the design of this model are examined

in appendix 4.11. The verification of the model implementation presented in appendix 4.12 shows that the model:

1. gives symmetric solutions given symmetric boundary conditions

2. converges under increasing spatial and temporal resolution at a rate commensurate with the discretization schemes

3. conserves mass

4. gives similar solutions to another model using similar physics (GlaDS Werder et al., 2013)

4.3.2 *Basal Drag Coupling*

The basal velocity is from either a hard or soft bed sliding rule. For the hard bed the basal sliding rule is a fourth power Weertman sliding law (Cuffey and Paterson, 2010):

$$u_b^{hard} = \frac{c_{hard} c_{fslid} F_{N_{eff}} |\tau_b|^3 \tau_b}{N_{eff}} \tag{70}$$

where c_{hard} is a parmeterized sliding coefficient which includes a parameterization for basal roughness, $F_{N_{eff}}$ is the effective pressure normalization factor, N_{eff} is the effective pressure given by the subglacial hydrology model, and τ_b is the basal drag. The basal velocity for soft bedded sliding is similarly a Weertman type sliding law with integer exponent values between one and seven.

$$u_b^{soft} = \frac{c_{soft} c_{rmu} F_{N_{eff}} |\tau_b|^{b_{till}-1} \tau_b}{N_{eff}} \tag{71}$$

with separately parametrized soft sliding coefficient c_{soft} (which also includes a parameterization for basal roughness).

4.4 LISSQ EXPERIMENTAL DESIGN

Using a simple setup without externally driven variability from topography, complex land-sea mask, and an unsteady climate, system behaviour is due to the initial transient response and internal feedbacks. Our **L**aurentide **I**ce **S**heet **sq**uare (LISsq) setup includes broad features of the North American bed (fig. 16) and computationally cheap first order diagnostic climate imposed as a steady forcing with ice sheet thickness feedbacks. The simple climate allows a free southern margin determined by the background temperature and feedbacks giving a dynamically determined ice sheet geometry at 50 km horizontal resolution. Next we present the design choices of this setup in three categories: bed, climate, and glacial systems.

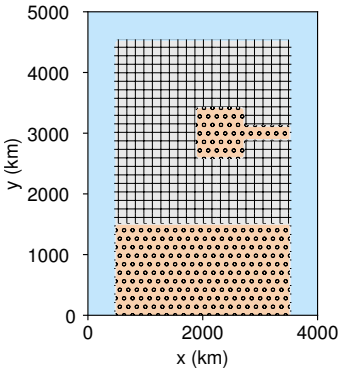

Figure 16: This map of the LISsq bed configuration shows the extent of the domain and the position of the Hudson Bay/Strait and Southern soft beds. Grey hatched regions are hard bedded, beige dotted regions are soft bedded, and blue represents water where ice is ablated.

4.4.1 *Bed*

LISsq aims to probe the effect of large scale hard to soft bed transitions characteristic of North America. This simplified setup allows separating out the internal feedbacks from the externally forced elements (e.g. variability from real topography and land-sea mask and unsteady, spatially varying climate). The shorter run times of this setup also allow larger ensembles, giving a better probe of the parameter space.

The simplicity helps with model verification as any variability in the model stems purely from the encoded physical processes.

The majority of the inferred late-Pleistocene Laurentide substrate has been hard bedded (Clark et al., 2006), with unconsolidated sediment cover at the south and in the Hudson Bay/Strait. The HEINO experiments were conducted over similar length scale hard beds with the same soft bedded Hudson Bay/Strait at the centre of the hard bed (Calov et al., 2010). HEINO differed in that it included a circular continental configuration bounded by a highly ablating ocean – the ice sheet geometry was largely set. Here we wish to examine surge behaviour for a variety of ice sheet geometries within the roughly approximate range of the Laurentide length scales and bed. As such, a rectangular bed geometry is set with the boundary of the soft bedded south at a constant latitude and an equilibrium line which is free to evolve with a changing ice sheet.

4.4.2 *Climate*

The LISsq climate prescribes a linear background temperature trend with lapse rate feedback. The annually averaged surface temperature, T_{surf} is:

$$T_{surf} = T_{north} + [\![0, T_{grad}\,(5000 - y)]\!] - LH \tag{72}$$

where T_{north} is the ground level temperature at northern end in °C, T_{grad} is the latitudinal warming rate in °C/km, L is the slope temperature lapse rate (°C/km), and H is ice sheet thickness (m, recall the bed is at constant elevation and glacial isostatic adjustment is not included). The brackets, $[\![\ ]\!]$, denote max.

These temperatures are then used together with a positive degree day scheme (PDD) to simulate net seasonal contribution to accumulation and ablation for an annual average temperature. The positive degree day sum assumes 100 day melt

season length with temperatures 10 °C warmer than the annual mean, T_{surf}, and melt coefficient in m/PDD. Ablation is then

$$\dot{b}_{melt} = C_{pdd} \left[\!\left[0.0, 100 \left(T_{surf} + 10 \right) \right]\!\right] \tag{73}$$

where b_{melt} is ablation in m/a and T_{surf} is surface temperature in °C. Accumulation incorporates the thermodynamic effect on atmospheric moisture content using the August-Roche-Magnus approximation for the Clausius-Clapeyron relationship (Lawrence, 2005) with parameter ranges adjusted for under saturated air. Accumulation, b_{accum}, is zero where $T_{surf} \geq 0$°C:

$$\dot{b}_{accum} = p_{ref} \; e^{h_{pre} T_{surf}} \tag{74}$$

where the reference precipitation rate, p_{ref}, and precipitation pre-exponential factor, h_{pre}, are ensemble parameters.

4.4.3 *Glacial systems*

We use a subset of the full featured GSM for this setup. Here we omit glacial isostatic adjustment, surface meltwater drainage, sediment transport and production, and ice shelves with grounding-line flux and calving model. This is in order to clearly show the effect of hydrology feedbacks on ice flow and ice thermomechanics.

4.4.4 *Parameter Range Estimation*

In this section we justify chosen parameter ranges based on physical and heuristic arguments and current understanding in the literature.

4.4.5 *Hydraulic Conductivity Parametrization*

The range of values appropriate for hydraulic conductivity varies according to whether the drainage system is assumed to be poro-elastic or linked cavity or whether the flux is assumed laminar (Darcian) or turbulent (Darcy-Weisbach). Hydraulic conductivity is not truly known at the continuum-level macro-scale. Here we use a range based on bounding subglacial hydrologic flow velocities, typical hydraulic gradients, and subglacial water thicknesses.

The velocity of water flow in the subglacial channel end-member imposes an upper bound on the linked-cavity end-member flow velocity in the bifurcated channel-linked-cavity system (Schoof, 2010). Chandler et al. (2013) used dye tracing experiments at a land terminating West Greenland catchment to measure maximum velocities between moulin injection site and the margin. Their slowest first arrival time gave 1.00 m/s in the efficient drainage regime.

Fast ice velocities (e.g. ≈1 km/a) give a loose lower bound on water flow speeds. Whereas the viscosities differ by many orders of magnitude (10^{14}Pa*s for ice versus 10^{-3}Pa*s for water, Cuffey and Paterson, 2010), the pressure gradient forces are less dissimilar. Assuming the hydraulic gradient is approximately equivalent to that imposed by ice sheet and bed topography (i.e. no contribution from basal water pressure) – around 1000 m/56 km (Chandler et al., 2013) ice sheet surface gradient contribution and 500 m/56 km for bed contribution (Morlighem et al., 2013) – gives a hydraulic gradient of $\psi \approx 240$ Pa/m. Assuming further ranges of 1 mm to 10 m of basal water thickness and Darcy-Weisbach flow speeds between 3×10^{-4} and 1×10^{0} m/s, gives a range of linked-cavity hydraulic conductivity (k_{cond}, tbl. 2) between 1×10^{-5} and 1×10^{-1} $m^{5/4}/Pa^{1/2}s$. To ensure complete bounding, we probe a wider range of 1×10^{-6} and $1 \times 10^{+1}$ $m^{5/4}/Pa^{1/2}s$. This range encapsulates values suggested by Hager et al. (2022) and Werder et al. (2013). G. Flowers (2000) assessed the range of hydraulic conductivities to be $k_{max} = 1m/s$

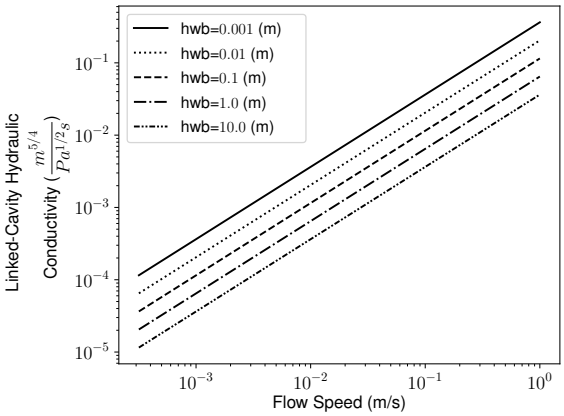

Figure 17: Range of linked-cavity hydraulic conductivities based on basal water flow speed, hydraulic gradient, and basal water thickness ranges in the text – using $k = \frac{v}{\psi^{1/2} h^{1/4}}$.

and $k_{min} = 10e-7 m/s$. The hydraulic coductivity transitions from k_{max} to k_{min} according to eqn. 66.

4.4.6 *Basal roughness*

The height of bedrock protrusions relevant to subglacial cavity formation and its spatial variation lacks assessment in the literature and justified values are difficult to come by. The height of these protrusions, or terrain roughness, affects several basal processes in glaciated regions, including heat generation in basal ice, sliding, subglacial cavity opening, and bedrock quarrying. Length scales relevant to subglacial cavity formation have been estimated from chemical alteration of bedrock (deposition of calcium carbonate precipitates) (J. Walder and Hallet, 1979). These cavity outlines form during sliding-associated-regelation when water refreezes at the glacier substrate in the lee side of bedrock highs, precipitating dissolved carbonates. The deposits in this study indicate cavities 0.1-0.15 m high. Several studies then use a value in this range (e.g. Werder et al., 2013). Kingslake and Ng (2013) refers to J. S. Walder (1986) for this value, but J. S. Walder (1986) does not provide any justification for it in their table 2 and do not refer explicitly to the earlier work of (J. Walder and Hallet, 1979).

In deglaciated areas with bed access, quantifying roughness at the ice sheet scale is a non-unique problem and measures abound. For example: standard deviation of elevation, power spectral density of elevation, and local bed slope. These are relative measures which do not identify the typical prominence of roughness features in a domain. What is needed for modelling linked-cavities is the average height of bedrock protrusions relevant to the cavity scale (itself uncertain) at given wavelengths. How these heights vary spatially for previously glaciated regions has not been assessed. Identifying this as a gap in the current glaciological literature, we adopt similar scale values and probe a wide range in order to capture ice sheet sensitivity to the scale of cavity-forming-bump-height. As stated above, Werder et al. (2013) and Kingslake and Ng (2013) both use $h_r = 0.1$ with the latter referring to J. S. Walder (1986) who gives a range of 0.01 to 0.5 m for the relevant bump height. Iverson (2012) show cavities and quarrying are intrinsically linked. As such, the step size of quarried surfaces may indicate a scale for cavity growth. Anderson et al. (1982) mapped cavities forming along 1 m high steps at the base of Grinnell Glacier in Montana, United States. Following the same reasoning, the size of quarried boulders also gives an estimate of the upper bound for length scales. 20 m boulders, though less common, can be found (though if transported debris were comminuted in transit, the original size distribution would have been larger). As such, we use a range of $h_r \in [0.01, 20.0]$m and a range for the roughness wavelength as a function of roughness, $l_r \in [1.0, 20.0] \times h_r$.

4.4.7 *Hydrology Temperate Transition*

This parameter is used to interpolate between a conducting (at 0°C) and non-conducting (at a lower bound temperature) hydrologic system with a logic similar to the temperature ramp reasoning. Thus, the range is based on Hank, Tarasov,

and Mantelli (2023) and the lower bound of the interpolation is probed in the range of $[-1.0, 0.0]$.

4.4.8 *Tunnel Switching Scalar*

The flux threshold switch from inefficient to efficient drainage is given by the ratio of cavity opening due to sliding versus wall melting from viscous heating (Schoof, 2010):

$$Q_{crit} = Q_{scale} \frac{u_b h_r / l_r}{c_1(\alpha - 1)\psi} \tag{75}$$

where u_b is the velocity, h_r/l_r the basal roughness ratio, c_1 a scalar, α the Darcy Weisbach water thickness exponent, ψ the hydraulic gradient. Q_{scale} is a scale factor adjusting for subgrid uncertainty – small scale fluctuations in flux may trigger a run-away tunnelling positive feedback affecting the larger scale.

4.4.9 *Effective Pressure Normalization*

This is the value used to normalize the effective pressure in the basal sliding velocity calculation and is set based on typical effective pressures. Effective pressures greater than this parameter values should slow sliding and less than should hasten sliding. We set this range to $[10kPa, 1MPa]$ based on the typical effective pressure values seen in fig. 25. The effective pressure and normalization ($F_{N_{eff}}$) is incorporated into the hard and soft basal sliding velocities in eqn. 92 and 93.

4.4.10 *Basal Sliding Parameters*

The soft and hard sliding factors used in eqn. 92 and 93 were set to wide bounds somewhat outside the recommended range for the GSM (Tarasov et al. in prep.),

the power for soft bedded sliding was kept within the typical range. These ranges were $c_{rmu} \in [0.01, 4.0]$ (set such that sliding speed is ≈ 3 km/a for $(30 \text{ kPa})^{b_{till}}$ kPa of basal drag), $c_{fslid} \in [0.0, 5.0]$ (set such that sliding speed is ≈ 200 m/a for 100 kPa of basal drag), and $b_{till} \in [1, 7]$.

4.4.11 *Climate parameters*

A range of $[5, 10]^{\circ}$C/km is used for slope lapse rate on the basis of PMIP2 Greenland model simulations in Erokhina et al. (2017). The range for T_{north} was obtained from PMIP4 ensemble mean distribution of northern ($> 75^{\circ}$) latitude temperatures at LGM in Kageyama et al. (2021) shown in fig. 18a. The precipitation parameter ranges in eqn. 74 were adjusted to bound the range of precipitation and temperatures below freezing in Kageyama et al. (2021), as shown in fig. 18b.

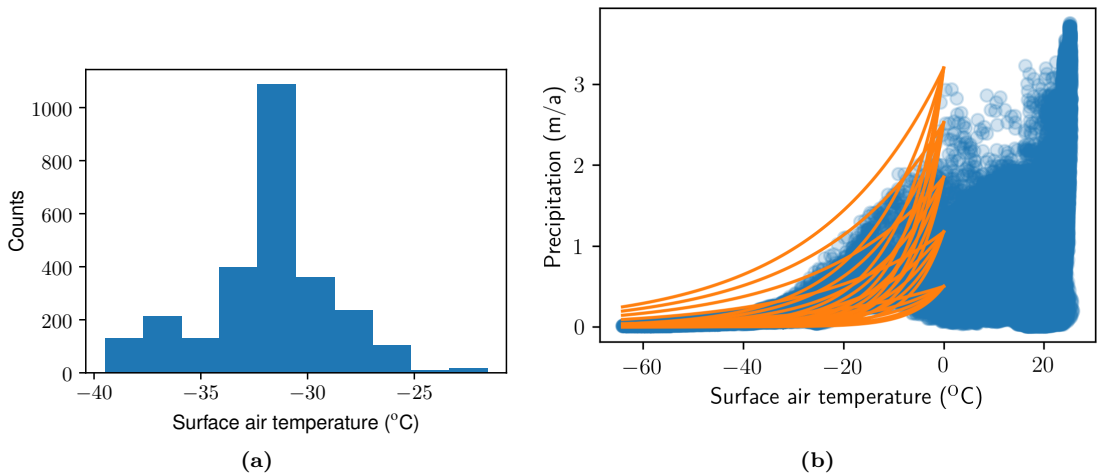

Figure 18: Precipitation and temperature values extracted from PMIP4 (Kageyama et al., 2021) ensemble mean fields at LGM. A histogram of surface air temperatures (count of points north of 75°N with temperature in the given bin) is shown in a). A scatter plot of precipitation and surface air temperature with overlain precipitation temperature relationships showing the range of parametrizations used is presented in b).

4.4.12 *Ensemble Design and Parameter Sensitivity*

To understand the effect of hydrology, ensembles for different model configurations are compared: Linked-cavity (LC), poro-elastic (PE), Leaky-Bucket (LB), and no hydrology (NH) – 18816, 19992, 15288, and 11760 runs in each ensemble respectively. Each ensemble varied the hydrology, ice sheet, and climate parameters simultaneously in order to capture parameter interactions and the number of runs was scaled with the number of parameters in each setup (15 in LC, 16 in PE, 12 in LB and 9 in NH, shown in tbl. 2). The parameter space is sampled with the quasi-random-low-discrepancy Saltelli extension of the Sobol sequence (Saltelli, 2002) as implemented in SALib (Herman and Usher, 2017) with second order terms enabled. Parameters are sampled with a log uniform distribution for parameter values which vary over orders of magnitude. Each run proceeded for 100 kyr with the first 50 kyr taken as spin up (from no ice, initial accumulation given by the background temperature from T_{north} and T_{grad}). Ensembles were run on a heterogenous linux cluster with 24-32 Gb RAM and 8-24 xeon or opteron cores per node, clock speeds ranging 2.4-2.7 GHz and a total of 652 cores. Runtimes averaged about 3 hours.

Ice sheet geometries vary widely among runs for all model configurations. Maximum ice thickness ranges from 0 to $\sim$ 6000 m while maximum North-South extent ranges from 0 to 4500 km. Here we study surge behaviour at scale similar to the Laurentide ice sheet by sieving (discarding runs outside the target metric ranges) the ensembles according to maximum ice sheet thickness and North-South extent. At **L**ast **G**lacial **M**aximum (LGM, 22 ka) the maximum ice thickness was plausibly around 4000 m (Tarasov, Dyke, et al., 2012). We use this estimate with a lower bound of 3000 m for the sieve in the main study and examined additional sieves with bounds $[2500, 3500]$ and $[3500, 4500]$ in appendices (§ 4.9). LGM North-South

extent was ≈4000 km, while the last margin to fully encircle the Hudson Bay and Strait (11.50 ka) extended ≈2500 km North to South (Dalton et al., 2020).

The importance of hydrology parameters to determining ice sheet geometry can be probed with sensitivity analysis. Local sensitivity analysis methods neglect interaction terms important for studying feedbacks in coupled models and so are not applicable here (Saltelli et al., 2008). Meanwhile variance based (Sobol, 2001) methods require assumptions about the sampling structure of the underlying inputs. The trouble with coupled models is they can be unstable, as such there are incomplete runs which render sampling structure assumptions moot. There are other non-parametric sensivity methods which do not require assumptions about the input sample distibution but these require sample sizes even larger than those presented here in order to converge (e.g. Borgonovo, 2007; Pianosi and Wagener, 2015).

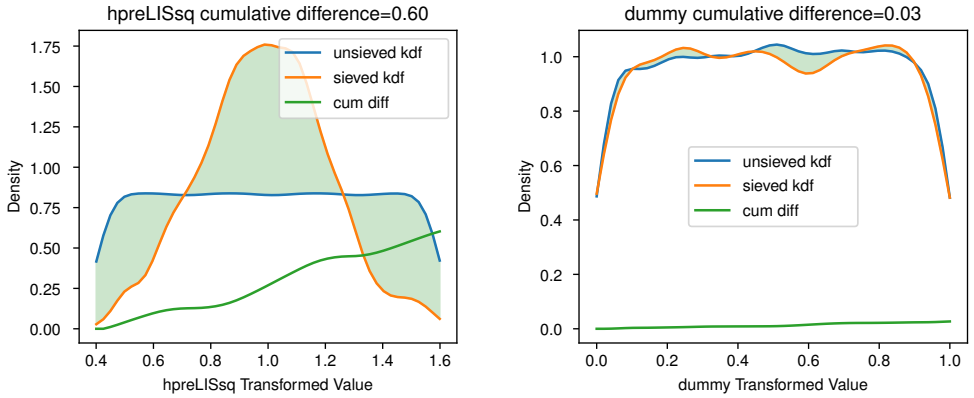

(a) (b)

Figure 19: Cumulative kernel density function difference sensitivity metric for the most sensitive parameter, hpre (a) and least sensitive parameter, dummy (b) for the LC setup ice sheet geometry sieve. The parameter values are transformed for input to the GSM. The blue line shows the ensemble total parameter value distribution, orange shows the distribution after sieving the ensemble for geometry, and the green line shows the cumulative (integrated) absolute difference of blue and orange up to that value. The total cumulative difference gives the sensitivity measure, shaded in green.

We develop a novel non-parametric method to measure sensitivity: we assess ice sheet geometry sensitivity to parameters by comparing the original uniform input parameter distribution with the parameter distribution corresponding to the sieved geometries (limiting the ensemble to those within geometric bounds). The non-

parametric nature alleviates the need to make assumptions about the underlying parametric distribution class (e.g. variance is a normal distribution parameter). Using the impact of a sieve on parameter distribution to measure sensitivity means that assumptions about the sampling methodology are not required and that successive sieves can be applied to the ensembles to measure different aspects of model sensitivities. For example, in § 4.5.1 we measure the sensitivity of surge frequency for those ensemble members which pass the geometry sieve by further sieving on surge frequency. Parameters which are not controlling the ice sheet geometry will have a similar distribution after selecting for that geometry range as the original input sample distribution. The more modified the distribution, the more sensitive the parameter. More precisely, each distribution is approximated with a kernel density function (KDF) normalized to unit area under the KDF. The sensitivity metric is then the integral of the absolute difference between the sieved and unsieved KDFs, i.e. the measure of how much the sieve modifies each parameter's KDF. For example, the maximum KDF difference would stem from a narrow spike on the sieved distribution, which would mean that parameter strongly controls the model output, e.g. the more limited range indicated for hpre in fig. 19a. We add a uniformly sampled dummy parameter not used by the model to set a threshold of accuracy of the sensitivity metric in each case. This dummy parameter has a very similar input and sieved distribution (with minor difference due to the essential random sampling from sieving), for example that for the LC geometry sieving in fig. 19b.

The sensitivity metrics for all parameters in fig. 20 rise above the baseline significance level set by the dummy parameter in each ensemble. The temperature coefficient in the August-Roche-Magnus relation (h_{pre},), North-South temperature gradient and intercept (T_{grad} and T_{north},eqn. 72), and lapse rate are the top four geometry controlling parameters in all cases except LB (though lapse rate is close

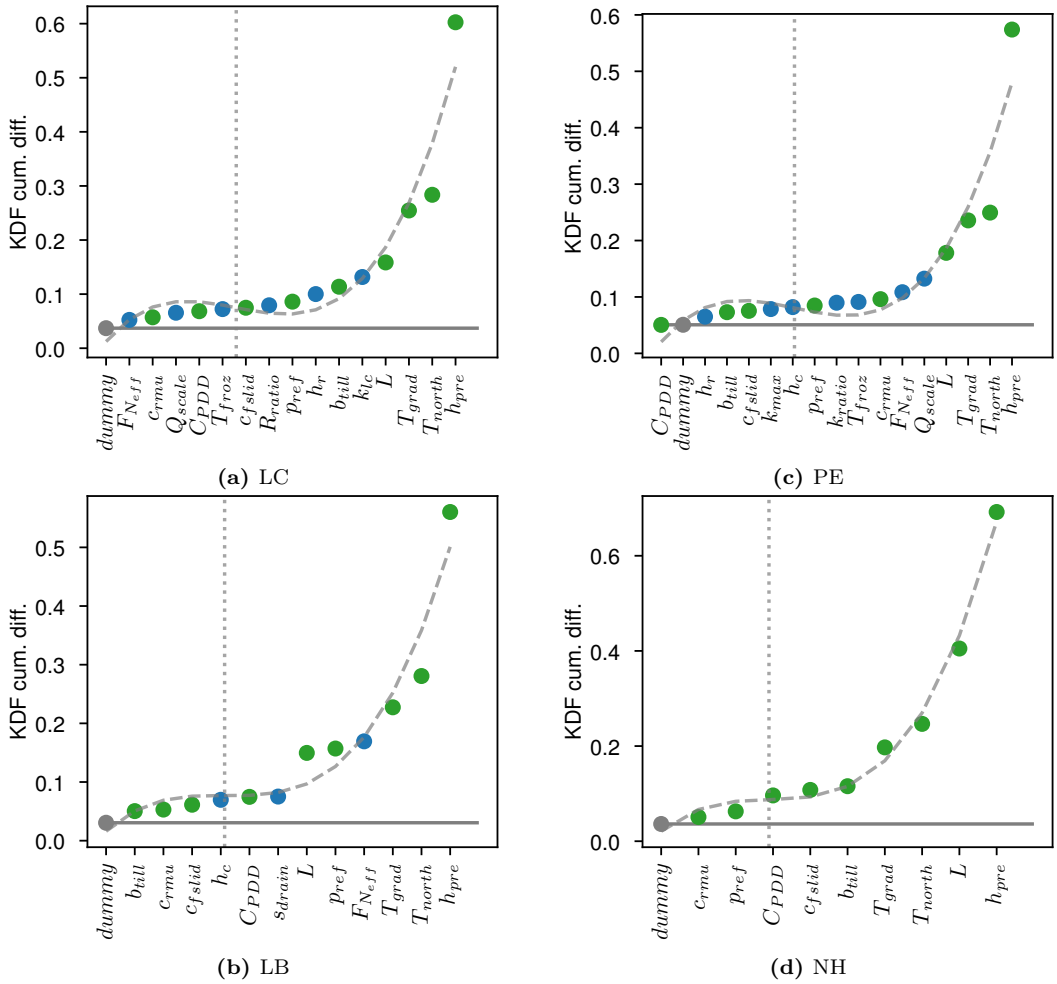

Figure 20: Parameters ranked by relative sensitivity by sieving for geometry ($\mathcal{S}^0_{geom}$, tbl. 3) relative to input parameter distribution for each model setup: LC (a), LB (b), PE (c), and NH (d). Blue dots represent subglacial hydrology parameters, green dots the climate parameters, and the gray dot is the dummy parameter. The vertical dotted line indicates the inflection point in the sorted sensitivities used to approximate a transition from diminishingly sensitive to increasingly sensitive parameters. The dashed gray curve shows the fitted third order polynomial used to calculate the inflection point. The horizontal solid gray line indicates the sensitive threshold of the sensitivity analysis technique given by an unused, random dummy variable.

for this ensemble as well). In the hydrology enabled setups, hydrology parameters rank in the top 5.

The ranked parameter sensitivity for each model in fig. 20 exhibits an inflection point in parametric sensitivity which we use to determine the number of controlling parameters. This inflection point is an approximate indication of the diminishing sensitivities in the model setup. As such, parameters to the right of this point are taken as sensitive and those to the left are considered insensitive and could be fixed for the purposes of geometry. Around two-thirds of parameters fall on the right

hand side of the inflection in each ensemble. For those hydrology bearing model configurations, half or more of the hydrology parameters lie in the sensitive zone. This shows that subglacial hydrology is even important at the scale of whole ice sheet geometry.

The most influential hydrology parameter in the LC setup is hydraulic conductivity which controls the dynamic effective pressure, while in LB and PE the geometry is quite sensitive to the normalization of the effective pressure in basal drag (though PE is more sensitive to the tunnelling tendency, Q_{scale}). In the LC case, the ice sheet geometry is most sensitive to those parameters which control the dynamics of effective pressure themselves (k_{cond} and h_r). In the PE case, the parameters controlling the transition to efficient drainage (Q_{scale}) and effective pressure normalization are most important hydrology parameters. These parameters are both diagnostic controls on subglacial water balance and sliding velocity. Similar to PE, the most important subglacial hydrology parameter for LB is the effective pressure normalization.

4.4.13 *Surge metric definition*

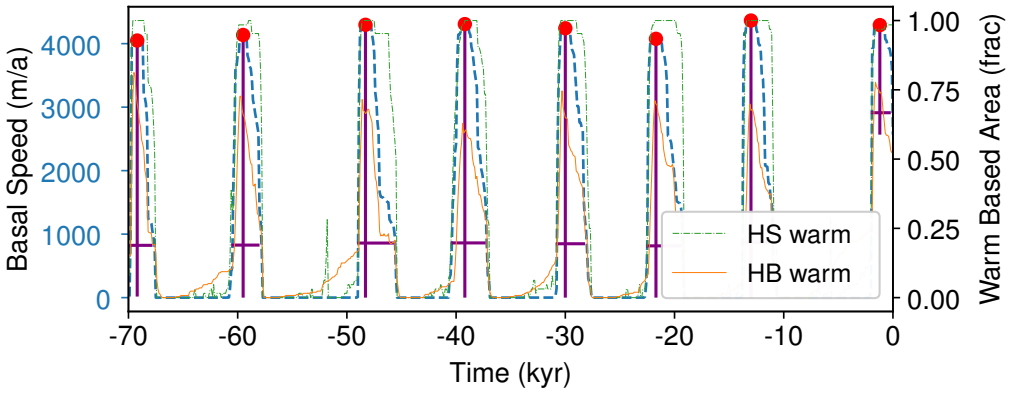

Figure 21: Evolution of the ice sheet and idealized Hudson Strait ice stream showing repeated surge events and how metrics are extracted from a sample run. HS basal speed is shown as dashed blue line – which is used to pick surge peaks and estimate prominences – along with the area fraction of warm based ice within the HS (dash-dotted green line) and its Hudson Bay source region (solid orange line). The red dots show picked event peaks, the vertical purple lines give their "strength" (prominence) and horizontal purple lines show the event duration.

The two most obvious measures of internal oscillation are amplitude and period. This highly non-linear system does not exhibit sinusoidal behaviour, but we can pick surge metrics which approximate these measures. To this end, each surge type was evaluated in two ways – number of surge events (an indication of periodicity, the number of red dots in fig. 21) and strength (or speed increase, height of vertical purple bars in fig. 21) of surge events (i.e. amplitude).

The background sliding speed of the actual HSIS in the non-surging state is unknown. While this study does not aim to replicate the actual HS, we are studying the behaviour of an ice stream and sheet with similar dimensions to the HS and Laurentide. As such, labelling and measuring the strength of a surge event needs to be agnostic of quiescent-phase conditions between events. Ice stream acceleration at scales comparable to the HS has not been observed in the modern period. Though significantly smaller than the HSIS and its catchment, the Vavilov ice cap did accelerate from 12 m/a to 75 m/a between 1998 and 2011 CE (Willis et al., 2018). Satellite observations of the North East Greenland Ice Stream (NEGIS) combine with modelling to show acceleration greater than 1 m/a^2 in places between 1985 to 2018 CE (Grinsted et al., 2022). Therefore we define a surge event in this setup as a large increase in spatially averaged HS basal sliding speed ($>$ 1000 m/a over a given 25-100 year acceleration period) over the background, quiescent-phase speed. Velocity can also change during a surge as portions of ice within the HS accelerate over others. Ice stream shear margins can be regions of the fastest velocity changes and ice stream geometry can change over time (Grinsted et al., 2022). As such, we do not define adjacent short lived changes in velocity as separate surge events.

A typical run with surge events and which passes the $\mathcal{S}^0_{geom}$ sieve is shown in fig. 21. In order to label surge events (red dots in fig. 21), we use peak prominence (Virtanen et al., 2020) – drawn from the concept of topographic prominence (height of local max above adjacent local minima) – to estimate surge events from the basal velocity time series (1 year sample rate) for each run. This allowed surged metrics

Label	Subset	Use
$\mathcal{S}^0_{geom}$	$\{H_{max} \in [3000, 4000]$ m$\} \bigcap \{\Delta y \in [2500, 4000]$ km$\}$	Main geometry sieve
$\mathcal{S}^{high}_{geom}$	$\{H_{max} \in [3500, 4500]$ m$\} \bigcap \{\Delta y \in [2500, 4000]$ km$\}$	Additional geometry sieve used in apdx. 4.9 to assess thicker ice sheet effect on duration sensitivity
$\mathcal{S}^{low}_{geom}$	$\{H_{max} \in [2500, 3500]$ m$\} \bigcap \{\Delta y \in [2500, 4000]$ km$\}$	Additional geometry sieve used in apdx. 4.9 to assess thinner ice sheet effect on duration sensitivity
$\mathcal{S}_{surge}$	$\mathcal{S}^0_{geom} \bigcap \{$Surge Count $\in [3, 12]\}$	Sieve used to asses subglacial hydrology parameter contribution to surge frequency

Table 3: Sieves used to select runs from each ensemble for analysis.

to be agnostic of any background value. In order to minimize spurious peaks picked on variations in velocity during a single event, a 401 year median filter was applied. This means that abrupt velocity changes lasting ∼200 years or less will not get picked as events. This is less than the lower bound on HSIS surge duration inferred from IRD by Dowdeswell et al. (1995) who estimate that those surges most likely lasted between 250 and 1250 yr on the basis of Heinrich Events interpreted in 50 North Atlantic drill cores. A comprehensive review of Heinrich Events and IRD age intervals available in the literature by Hemming (tbl. 3, 2004) infers a mean duration of 495 years where the lowest estimate is 208 years.The duration for these modelled surge events is calculated as full width at 80% maximum prominence (height above adjacent local minima).

4.5 HS SURGING RESULTS

The sieves used for sensitivity analysis are shown in tbl. 3. Sieving the data by ice sheet geometry ($\mathcal{S}^0_{geom}$) cuts the ensemble size to ≈1/6 to 1/9: Poro-elastic (PE) has 3154/19992 (15.8%), linked-cavity (LC) 3566/18816 (19.0%), leaky-bucket

(LB) 2721/15288 (17.8%), and no hydrology (NH) 1382/11760 (11.8%)runs. The histograms in fig. 22 show the frequency of surge events and strength of speed up of those events in the last 50 kyr of each simulation. The lower bound of HSIS surge frequency inferred from the Heinrich Event record (Hemming, 2004; Naafs, Hefter, and Stein, 2013) is 3 in 50 kyr. The rate of runs with three to twelve surge events in the sieved results is: 423/3154 (13.4%) for PE, 504/3566 (14.1%) for LC, 836/2721 (30.7%) for LB, and 75/1382 (5.4%) for NH. The distribution of the frequency of surge events stemming from each hydrology setup is not significantly different from the others (though LB does have more surges in the 4-7/50 kyr frequency range), nor is the magnitude of ice stream speed up. The no hydrology case, however does differ from those three: the rate of runs with surge events is significantly lower and the frequency and strength of events per run are also lower.

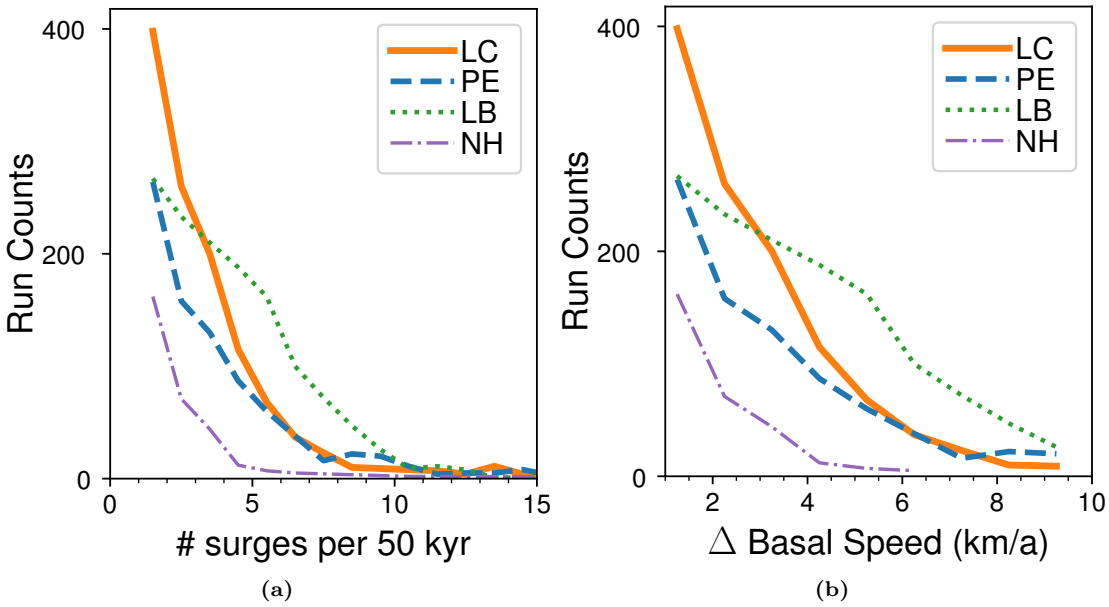

Figure 22: Surge event metric distribution across parametrizations by model configuration for runs in the main geometry sieve ($\mathcal{S}^0_{geom}$, tbl. 3). The linked-cavity ensemble is shown by the solid orange line, poro-elastic by the dashed blue line, leaky-bucket by the dotted green line, and no hydrology ensemble by the dash-dotted purple line. The number of runs with a given number of surge events in a 50 kyr time frame (referred to here as frequency) is shown in a). Similarly, the distribution of runs with a given surge strength (peak prominence of spatial mean HS velocity over adjacent local minima) is shown in b).

The duration of HS surge events highlights a difference between the three hydrologies: The linked cavity system yields longer duration events and the trend

in duration with increasing event frequency diverges between linked cavity and the other two hydrology systems. As the duration of surge events necessarily depends on the frequency of those events (having more events in a time period decreases the maximum possible duration of those events), we examine surge duration as a function of the number of events (as shown by the horizontal purple lines in fig. 21). In fig. 23 we extract the median surge duration by selecting runs with a given number of events and comparing the duration-frequency trends between the four setups. Frequency levels with ten or fewer runs passing the sieve are omitted as trends degrade around this level of membership.

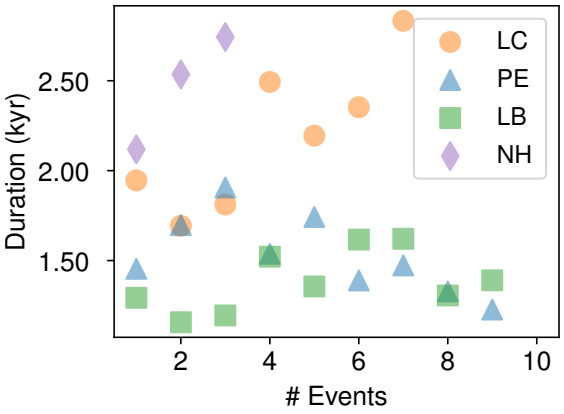

Figure 23: Surge event duration at different frequencies. The scatterplot and histogram in (a) shows trends in median duration with increasing number of surges in a run. The overlying histogram shows the number of runs in each frequency sieve with the 10 run cutoff level shown by the horizontal gray line. The no-hydrology setup falls below this level after the three event bin, and the linked-cavity setup shows a divergence from the other two at this point. (b) and (c) show the kernel density functions of surge duration for runs with one to three and five to seven events respectively.

As the frequency of surge events in each run increases, the median duration of surges in those runs stays largely flat, perhaps decreasing slightly for both the poro-elastic and leaky-bucket hydrologies. Not so for linked cavity, the duration of surges increases up to the seven surge level where it roughly doubles that of the poro-elastic and leaky-bucket hydrologies. This relationship is stronger still when selecting thinner ice sheets with mean maximum thickness between $[2500, 3500]$ m as shown in fig. 27. In this geometry range, the surge duration decreases at first, reaching a minimum at 3 surges before steadily increasing in duration until

it more than doubles the leaky-bucket surge duration (PE run counts are below the significance threshold). For thicker geometries no differences between the three hydrologies are apparent (fig. 29).

4.5.1 *Sensitivity of Surge Frequency*

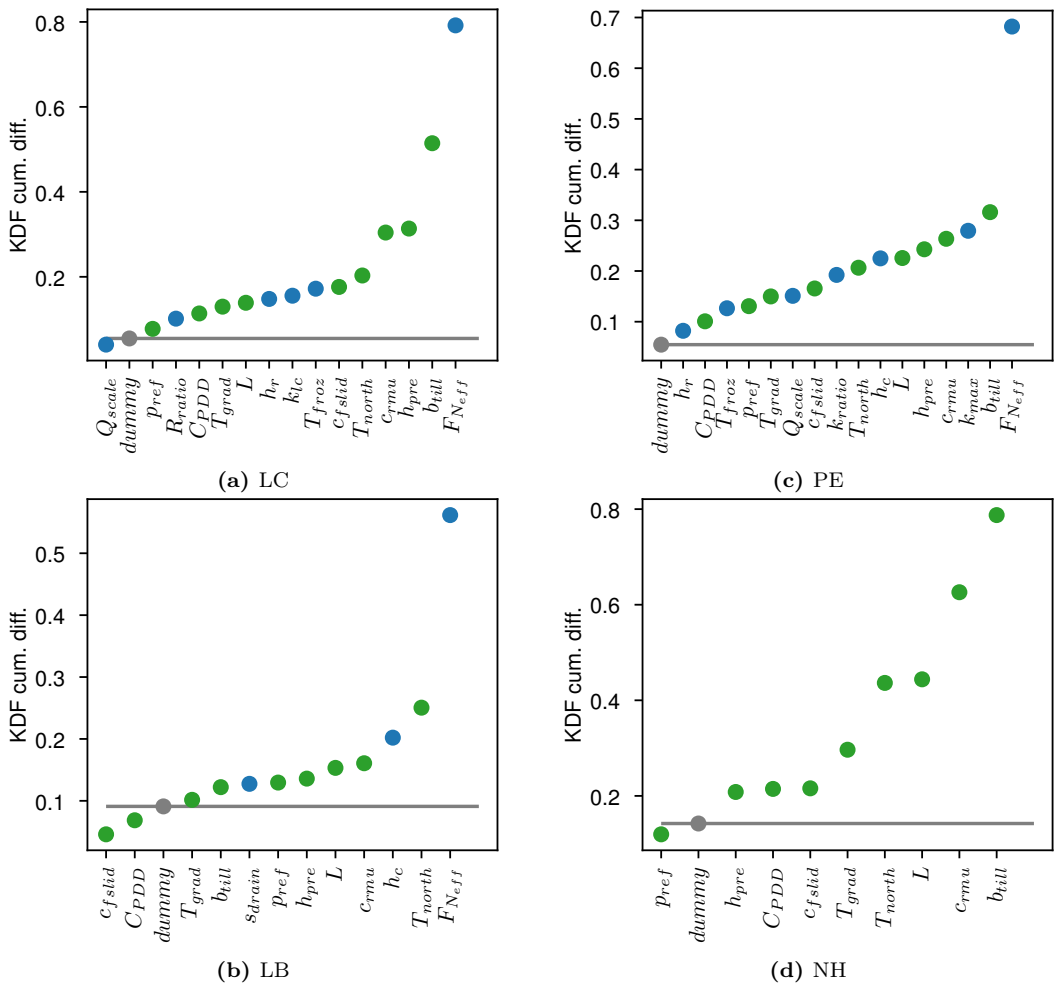

Figure 24: Surge frequency sensitivity to model parameters. Parameters are ranked by relative sensitivity by sieving for surge frequencies (three to twelve events) relative to the geometry sieve ($\mathcal{S}_{surge}$ relative to $\mathcal{S}^0_{geom}$, tbl. 3) for each model setup. The horizontal solid gray line indicates the sensitive threshold of the sensitivity analysis technique given by an unused, random dummy variable. Inflection is weak in each case and so is not used to delineate between sensitive and insensitive parameters (cf. fig. 20).

Applying a sieve on surge frequency in addition to the geometry sieve ($\mathcal{S}_{surge}$ in tbl. 3) highlights the system sensitivity to subglacial hydrology. Fig. 23 shows

the result from selecting those runs with between three and twelve surge events which is consistent with the minimum number of Hudson Strait surges inferred from the Heinrich Event record and the maximum number of events in the figure. The sensitivity ranking in fig. 24 is insensitive to whether the sieve upper bound is eight or forty events, likely due to the fact that most runs have eight or fewer surge events. For all of the hydrology ensembles, the effective pressure normalization exerts the most control on surge frequency (fig. 24) . In the case of the PE and LB ensembles, hydrology parameters give the first and third highest sensitivities – $F_{N_{eff}}$ in both cases, k_{max} is third for PE and h_c is third for LB. For LC, the next hydrology parameters do not appear until seventh and eighth place. This may be due to the dual role $F_{N_{eff}}$ plays in the linked-cavity system: it exerts influence on the sliding velocity which in turn controls the cavity opening rate which is proportional to effective pressure. In the NH case, soft bed sliding parameters c_{rmu} (soft bed sliding coefficient) and POWbtill (soft bed sliding law power) are the most important for surge frequency. POWbtill is also the second most important parameter in both the LC and PE cases.

4.5.2 *Relationship Between Effective Pressure and Sliding Velocity*

In fig: 25, all warm based points in the ensemble (across the parameter-space-time domain) for each hydrology configuration were cross-plotted in $log\,(N_{eff})$ - $log\,(u_b)$ space in order to check for any systematic differences in velocity between the four configurations. If the configurations with subglacial hydrology had increased basal velocities at the ensemble level relative to the no hydrology case then the conclusion that subglacial hydrology produces a wider distribution of surge characteristics would have much less confidence.

The increased incidence of surge behaviour in the hydrology cases is not due to increased sliding – the no hydrology ensemble exhibits higher basal velocities

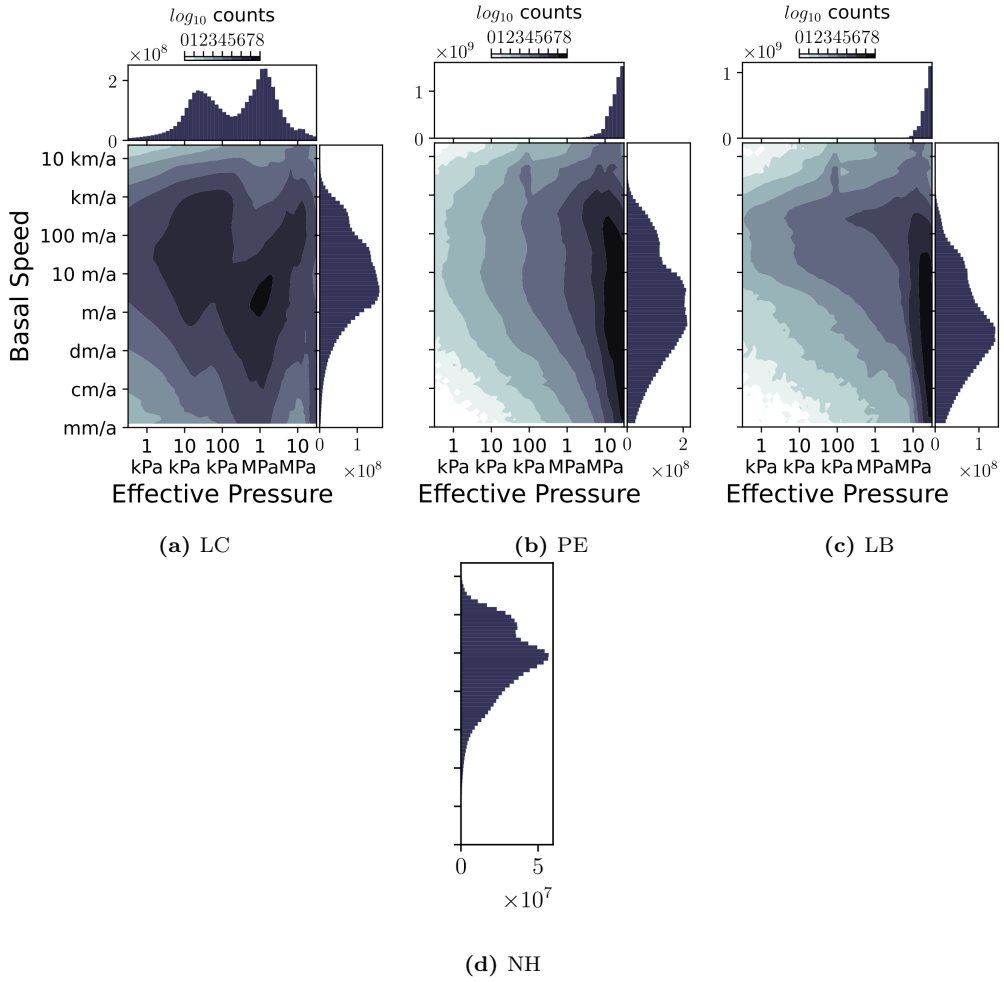

(a) LC **(b)** PE **(c)** LB

(d) NH

Figure 25: Two dimensional logarithmic histogram of effective pressure and velocity solutions for all warm based points across the parameter-space-time domain. Fields are output every 100 years. Marginalized distribution for effective pressure and velocity shown along side, sharing the respective axes.

than the three hydrology ensembles in fig. 25. This check allowed for an interesting overall comparison between the hydrology configurations. The three hydrology formulations do exhibit differences in $log\,(N_{eff})$ - $log\,(u_b)$ space (fig. 25). Linked-cavity hydrology produces a bimodal clustering at lower velocities/ higher effective pressures and higher velocities/lower effective pressures. This is a stark difference from the other two hydrologies whose effective pressure distribution simply decays toward lower values. This bifurcation of the effective pressures from a linked-cavity system show that it can sustain lower effective pressures than its poro-elastic and leaky-bucket counterparts.

4.6 DISCUSSION OF SURGE CONTRIBUTION

As we show above through sensitivity analysis and ensemble comparison of surge frequency and amplitude, subglacial hydrology is an important process that contributes to the feedbacks which govern Hudson Strait scale ice stream surging. While the process as a whole matters, the details matter less so – though it does depend on the aspects of ice stream surging under scrutiny. Across the three hydrology setups, the same range of HS basal velocity increase occurs: the magnitude of ice stream speed up is not dependent on the form of the subglacial hydrologic system and the three models can attain the same velocities within parametric uncertainty. This means that for model experiments looking to realistically capture ice stream surges, a leaky-bucket hydrology (the computationally cheapest of the three) is sufficient. Additionally, the range of frequency of HS surge occurrences is quite similar across the three hydrologies. However, the no hydrology case falls short of covering the range inferred for actual Heinrich Events attributed to HS surging (Naafs, Hefter, and Stein, 2013). This indicates that inclusion of some form of coupled subglacial hydrology is important for modelling large scale surge periodicities on geologic time scales. Once again, however, the exact form of the subglacial hydrology does not matter for the periodicity of the surge onsets.

Plausibly, one might expect that simply increasing the sliding coefficient in the no hydrology case would generate more surges. We therefore compared the basal velocity distributions between the configurations (§ 4.5.2). The velocity distributions (min, mode, max) in the hydrology ensembles were slower relative to the no hydrology configuration in fig. 25. The range of soft bed sliding coefficient covered in each ensemble approaches the bounds of plausibility – $c_{rmu} \in [0.01, 4.0]$, where c_{rmu} is scaled to give a 3 km/a sliding velocity for 30 kPa basal drag. HS surge behaviour cannot be captured by increasing the sliding coefficient.

Increasing the lapse rate to non-physical bounds can increase the incidence of HS surge events in the no hydrology case. In the main experiments, the lapse rate is limited to the range $[5, 10]$ °C/km. However, increasing the lapse rates to $[10, 20]$ °C/km, increases the rate of surge events. This is because decreasing the surface temperature of ice in the Hudson Bay and Strait both increases the vertical heat diffusion and decreases the temperature of ice advected to the base during a surge event. This enables a stronger thermomechanical surge termination mechanism.

Surge initiation at peak velocity for Hudson Strait scale ice streams as soon as the pressure melt point is reached is physically implausible. Basal velocity increases after ice becomes warm based and the effective pressure decreases. Inclusion of subglacial hydrology in the coupled system accomplishes this. The accommodation of increasing amounts of basal meltwater and pressurization (in the case that channelization does not occur) acts as a system inductance and the ice stream continues to speed up after becoming warm based. This inductance does not require the lateral transport of meltwater – only the balance of meltwater and a pressure closure dependence on subglacial water thickness.

Though periodicity and strength of surges are similar between the three hydrology bearing experiments, an interesting distinction occurs when examining the duration of events at varied frequencies. The stabilizing negative feedback of increasing effective pressure at higher basal velocities in the linked-cavity pressure closure gives surge durations longer (up to double, depending on frequency) than those of the diagnostic pressure closure of the poro-elastic and leaky-bucket hydrologies. This feedback also results in a bimodal effective pressure distribution (i.e. fig. 25). When studying ice stream surge behaviour, any of the hydrologies may give the same surge response in terms of frequency and strength of surges. If the study requires a more granular understanding of how long the surge was active, for example when studying the surge timing of multiple ice streams in a catchment (e.g.

Payne, 1998; Anandakrishnan and R. B. Alley, 1997) or the lifespan of palaeo-ice streams, our results suggest that accounting for the appropriate hydrology system is required.

It is not possible to simulate fully dynamic channelized drainage at the scale studied here – the CFL criterion (Courant, Friedrichs, and Lewy, 1928) would impose prohibitively long run times for our context. For illustration, Chandler et al. (2013) measured a lower bound water velocity of 1 m/s in the channel system. At this speed with our (coarse) resolution of 50 km, a time step of 0.00158 model years is required. The down gradient routing scheme representing the efficient drainage system is not restricted by CFL and so the time step depends only on the inefficient system which is typically in the range of 0.5 to 0.25 model years. A dynamic model of the efficient system would increase BrAHMs runtime anywhere from 150 to >300 fold rendering simulation of millenial scale variability infeasible.

Dynamical changes in flow through the efficient system occur on diurnal to seasonal time scales while the time scales of system features examined here are centennial to millenial. This separation in scale by several orders of magnitude makes it unlikely that dynamical changes in the efficient system (requiring a dynamic model) would be a significant control on the longer scale variability. However, in a non-linear system, such a control across scales cannot be fully ruled out.

While the treatment of efficient drainage in the model makes it more difficult to closely examine its role in the overall surging system, it is possible to evaluate its role at the ensemble level. At this level it is apparent efficient drainage does not play a significant role in surging at this scale. Three points bring this to light:

1. The impact on effective pressure from the down gradient tunnel routing scheme is exagerated as its modification of the basal water distribution is immediate instead of smooth. This modifies the effective pressure field in both the poro-elastic and linked-cavity systems through the h_{wb}/h_c term in eqn. 61 and the cavity opening rate term in eqn. 65 respectively.

2. The tunnel switching criterion is well established from a physical mechanistic standpoint (Schoof, 2010). Here we have included a tunnel switching subgrid uncertainty factor (§ 4.4.8). Sensitivity analysis shows this parameter, which varies by three orders of magnitude, plays little role in surge generation (fig. 24) where the parameter ranks last in the linked-cavity model and sixth from last in the poro-elastic model. The role of efficient drainage may be greater in the poro-elastic system than the linked-cavity system, suggested by its higher ranking in both the surge sensitivity (fig. 24) and geometry sensitivity (fig. 20). This difference in sensitivity may result because whereas in the linked cavity system the rate of change in effective pressure is proportional to the basal water thickness, in the poro-elastic system the effective pressure is directly proportional to the basal water thickness.

3. Though the efficient system is not included in the leaky-bucket configuration, there is little difference in the range of surge frequency and amplitude with respect to the other two systems. The distinction in surge duration stems from the dynamic pressure closure of the linked-cavity system and its direct two way feed back with sliding velocity.

4.7 CONCLUSIONS

The model presented herein passes multiple verification tests and as such is dependable for comparing the effects of structural choices of subglacial hydrology. The sensitivity analysis and ensemble comparison shows subglacial hydrology is an important control on both ice sheet geometry and on surging of major ice streams similar in scale to the Hudson Strait Ice Stream. However, depending on the characteristics of interest, the process details do not matter within current parametric uncertainties. The details do not matter for surge periodicity nor strength, but when studying the surge duration the hydrologic details are essential.

Surge behaviours can be produced in the absence of modelling a subglacial hydrology system but this requires unrealistic assumptions: pushing lapse rates to unrealistic ranges or implementing an un-physical sudden thaw in a large grid cell when the temperature reaches the pressure melt point. Subglacial hydrology provides a system inductance necessary for realistic ice speed up at the temperate transition. The critical components are the accommodation of meltwater and a meltwater pressure closure, not the mass conserving meltwater transport itself.

4.8 APPENDIX

4.9 SURGING WITH THINNER & THICKER ICE SHEETS

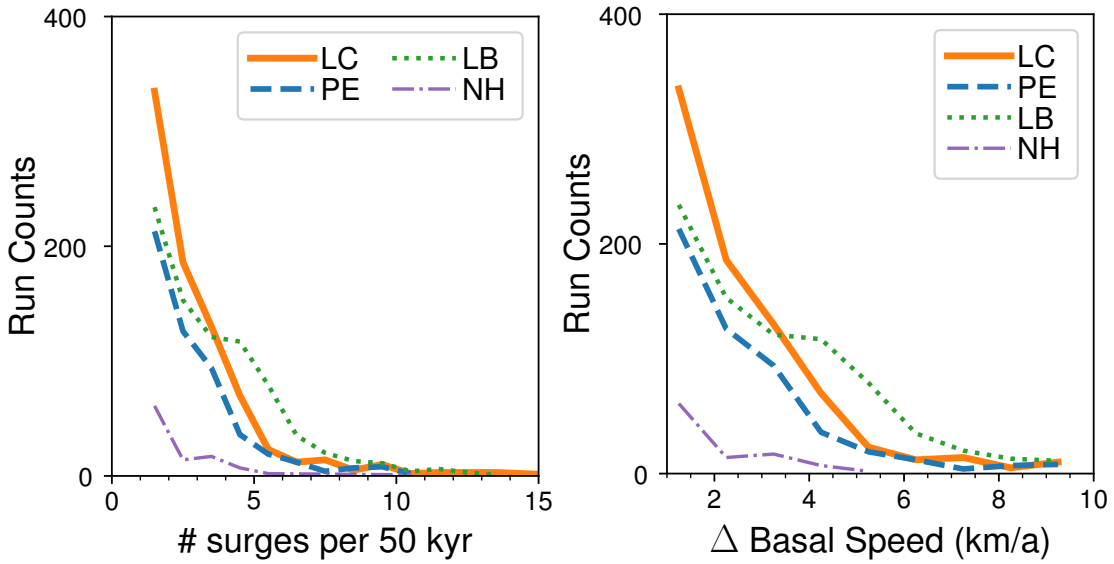

Figure 26: Surge event metric distribution across parametrizations by model configuration for runs in the thinner geometry sieve ($\mathcal{S}^{low}_{geom}$, tbl. 3). The linked-cavity ensemble is shown by the solid orange line, poro-elastic by the dashed blue line, leaky-bucket by the dotted green line, and no hydrology ensemble by the dash-dotted purple line. The number of runs with a given number of surge events in a 50 kyr time frame (referred to here as frequency) is shown in a). Similarly, the distribution of runs with a given surge strength (peak prominence of spatial mean HS velocity over adjacent local minima) is shown in b).

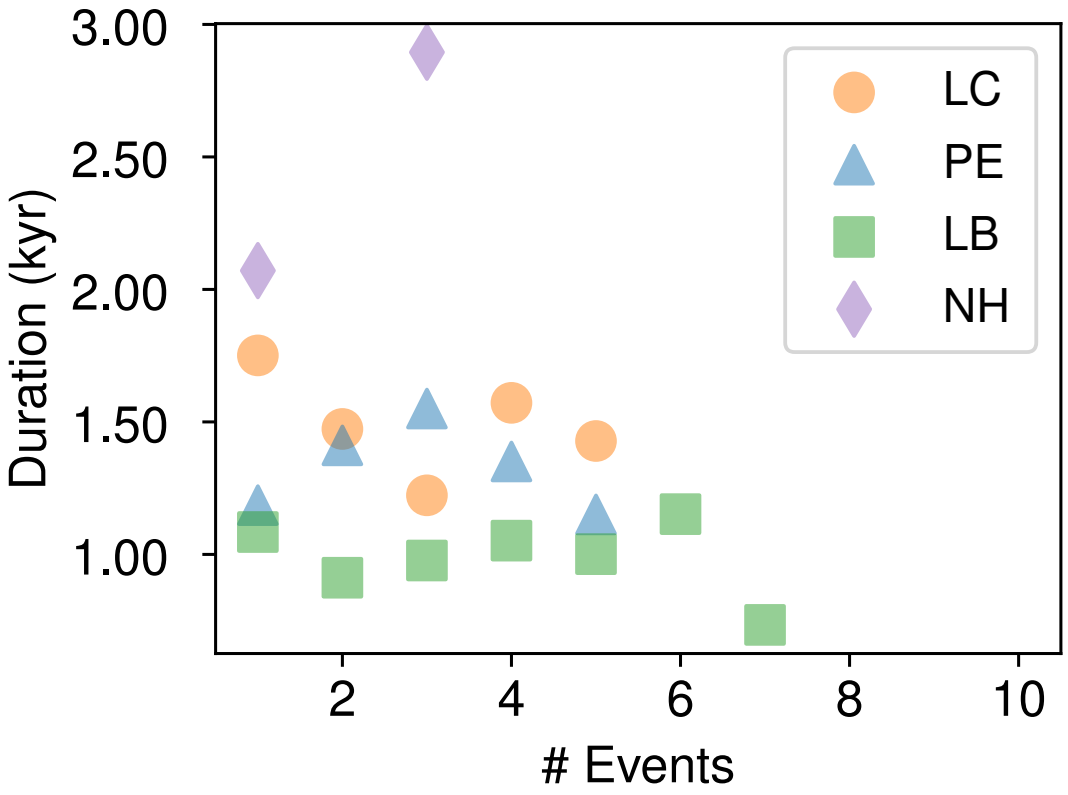

Figure 27

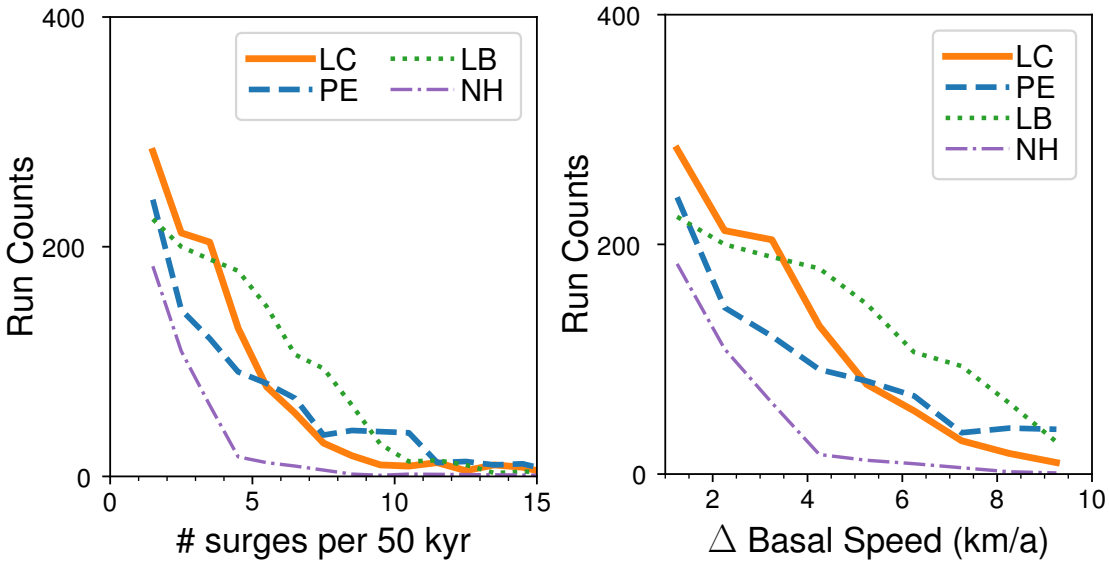

(a) **(b)**

Figure 28: Surge event metric distribution across parametrizations by model configuration for runs in the thicker geometry sieve ($\mathcal{S}^{high}_{geom}$, tbl. 3). The linked-cavity ensemble is shown by the solid orange line, poro-elastic by the dashed blue line, leaky-bucket by the dotted green line, and no hydrology ensemble by the dash-dotted purple line. The number of runs with a given number of surge events in a 50 kyr time frame (referred to here as frequency) is shown in a). Similarly, the distribution of runs with a given surge strength (peak prominence of spatial mean HS velocity over adjacent local minima) is shown in b).

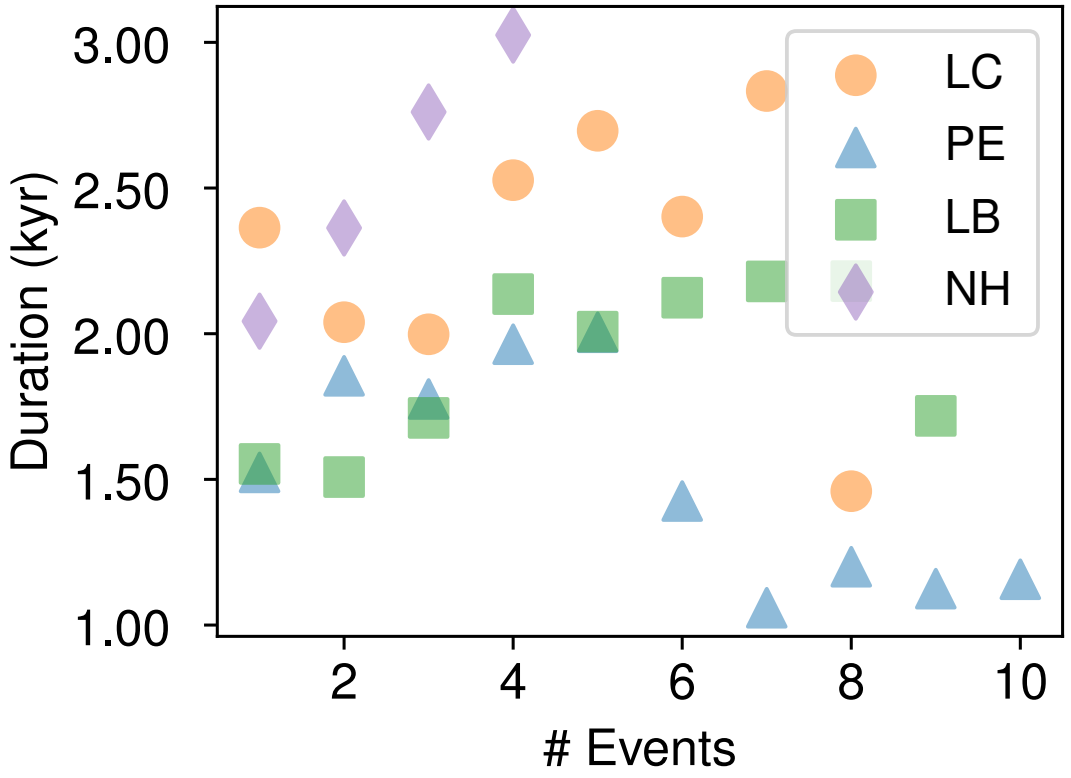

Figure 29

Figure 30: Surge event duration at different frequencies for thicker ice sheet sieve ($\mathcal{S}^{high}_{geom}$), $[3500, 4500]$ m. The scatterplot in shows trends in median duration with increasing number of surges in a run. The no-hydrology setup falls below this level after the three event bin, and the linked-cavity setup shows a divergence from the other two at this point. (b) and (c) show the kernel density functions of surge duration for runs with one to three and five to seven events respectively.

4.10 SUBGLACIAL HYDROLOGY MODEL SOLVER

BrAHMs2.0 solves the conservative transport equation for distribution of subglacial water (eqn. 60) and effective pressure evolution equation (eqn. 65) using combined explicit and semi-implicit methods. Time integration is done first with Heun's method for the initial time step followed by a leap-frog trapezoidal predictor corrector method (Kavanagh and Tarasov, 2018). To avoid time splitting, Heun's method is called after every 10 leap frog steps (varying the number of leap frog steps had little effect on the solution in tests).

The verification of this scheme and its implementation is presented in § 4.12 with a four pronged approach. The model is shown to give spatially symmetric solutions given symmetric boundary conditions. The convergence is examined for the spatial and temporal discretizations and found to approximately match the expected rate for each scheme: the first order upstream finite volume implementation spatially converges at a linear rate, while the second order leapfrog-trapezoidal implementation temporally converges nearly quadratically. The associated partial differential equations, however, are non-linear, coupled, and likely to have non-local responses. As such assessing the expected convergence rate of this system is not straightforward (Tadmor, 2012). In appendix 4.12 the model is shown to also conserve mass and match the solution of another numerical model with similar physics (Werder et al., 2013).

4.11 SUBGLACIAL HYDROLOGY MODEL ASSUMPTIONS

The physics of the linked cavity system is highly non-linear. As such, a set of simplifying assumptions is required to make numerical modelling of this framework feasible:

1. Wall melting is not a control on cavity size until tunnels are opened. Drainage systems switch from inefficient to efficient for a given value of flux. Schoof (2010) showed the evolution of the subglacial drainage system (described in eqn. 62) gives a bifurcation between cavity style and tunnel style drainage networks. Given effective pressure, the cavity opening speed is dominated by basal sliding below a certain flux and by run away wall melting above it.

2. At time scales of continental scale ice sheets, tunnels drain water instantaneously. The time scale of drainage through subglacial tunnels is less than a single melt season, much shorter than the centennial to millennial scale changes this model is applied to. This assumption alleviates CFL violations from fast tunnel flux which would render modelling on the long time scales of glacial cycles infeasible.

3. Cavities are filled with water. Consider the time scale for closure of a recently drained cavity given various combinations of ice sheet overburden (thickness, m) and sliding velocities. This time scale for closure (from eqn. 63) is given by:

$$T = \frac{S}{u_b h_r - c_2 N^3 S} \tag{76}$$

The range of time scales, assuming speed in range 1-1000 m/a and ice overburden thickness greater than 200 m is shown in fig. 31 where the maximum time for closure is around two weeks, less than the minimum time step of 0.125 yr in the hydrology model.

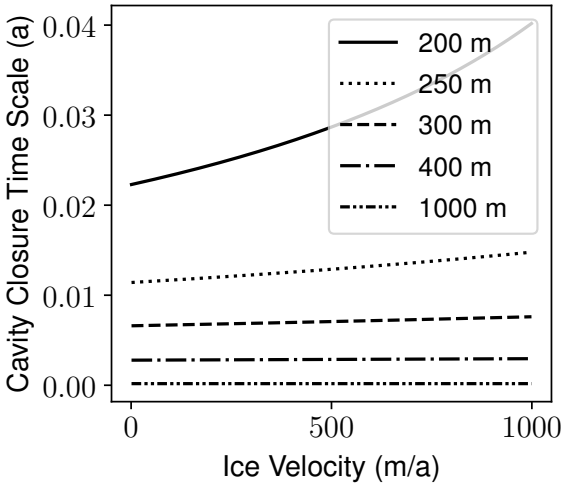

Figure 31: Cavity closure times at varied ice sheet thickness and sliding speeds.

4.12 SUBGLACIAL HYDROLOGY MODEL VERIFICATION

Oreskes, Shrader-Frechette, and Belitz (1994) describe model verification in general as the task of demonstrating model veracity, correctly asserting that no model can ever be proven – only disproven. However, this problem is not unique to computational model testing, this is a more philosophical epistemological problem. As Sornette et al. (2007) identifies, we do not prove models, we simply build our trust in them through a series of failed attempts to disprove them. In this section, we document performance on some simple tests which every model should pass before any amount of confidence can be conferred.

Following others (e.g. Sornette et al. (2007)), we take model verification to be more pedestrian than validation: a test that the computational model actually solves the model equations as intended. Or, as Roache (1997) defines, "solving the equations right." Meanwhile, we take validation as the converse from Roache (1997), "solving the right equations." Validation-wise, in this work we are showing not that the right equations were solved, but that it seems to be of low consequence.

The results presented in this section were done in effort to expose errors in the models, the lowest hanging fruit in gaining confidence in the model solutions. The verification strategy in this section is to satisfy:

1. model solutions are symmetric given symmetric input
2. model solutions converge under increasing spatial and temporal resolution
3. mass is conserved
4. models using similar physics should have similar solutions

Using simplified setups, expected behaviours are straightforward and in some cases may be calculated by hand (though hand calculations are not shown here). By using a progression of most simple to increasingly complex model setups for

testing, model behaviour can be verified against expected behaviour and shown capable of simulating increasingly realistic environments. Here we demonstrate that the model correctly solves the equations. A progression of forcings and couplings were used – of which the transient, two way coupled solutions from the least stable parameters (while still physical) are shown.

Parabolic surface topographies haven been used to approximate non-streaming ice sheet topographies (e.g. Mathews, 1974). The **S**ubglacial **H**ydrology **M**odel **I**ntercomparison **P**roject (SHMIP) (de Fleurian et al., 2018) uses such an ice sheet surface (depicted in fig. 34) and provides solutions to models using similar physics as the model herein. This therefore provides an appropriate test bed. This *SQRT_TOPO* surface is given by:

$$z_s = 6.0 \left(\sqrt{x + 5000.} - \sqrt{5000.} \right) + 10. \tag{77}$$

and flat base, $z_b = 0$.

Testing of the linked cavity system with Darcy-Weisbach flux model configuration (eqn. 65 and 58) is presented here as this is the most non-linear form and a new addition to the model.

The basal sliding velocity is determined by the effective pressure from eqn. 65:

$$u = k_{slide} \frac{\tau_b}{N_{eff}} \tag{78}$$

where $k_{slide} = 5.0 \times 10^1 m/s$ is a scaling constant, an effective pressure regularization 10 Pa is applied for numerical stability, and basal shear stress (τ_b) is calculated from the constant driving stress (τ_d):

$$\tau_b = \tau_d = \rho_{ice} g H \frac{\partial H}{\partial x}. \tag{79}$$

4.12.1 *Symmetry Test*

Spatial symmetry at each spatial resolution was calculated as the sum of the difference between the two ice sheet halves across the divide. This difference is zero for all fields showing perfect symmetry.

4.12.2 *Temporal Resolution Test*

Here we test the effect of changing the length of the time step in the basal hydrology on model solution using the SHMIP *SQRT_TOPO* setup (depicted in fig. 34). The per run discrepancy with respect to the shortest time step shown in fig. 32 is calculated as:

$$ERR\left(\Delta t_i\right) = \sum_{k}^{N_y} \sum_{j}^{N_x} \left| N_{eff}^{jk}\left(\Delta t_i\right) - N_{eff}^{jk}\left(\Delta t_{-1}\right) \right|. \tag{80}$$

As a first test of convergence under increasing temporal resolution (decreasing time step length) the hydrology model was run to steady state under SHMIP scenario A (constant 2.5 mm/a). Seeing convergence at shorter time steps for the steady forcing, an unsteady sinusoidal meltwater forcing was applied (50 year period, 3.5 mm/yr amplitude). The convergence for the unsteady case is shown in fig. 32 with the error metric of eqn. 80. The rate of convergence is approximately quadratic as expected for the $\mathcal{O}\left(\Delta t^2\right)$ leap-frog trapezoidal scheme.

4.12.3 *Spatial resolution test*

Here we show the effect of varying spatial resolution on the model solution. The model was run to steady state with prescribed melt and basal velocity (1.75 m/a ice and 2.0 m/a respectively). For this test, the SHMIP setup was used as shown

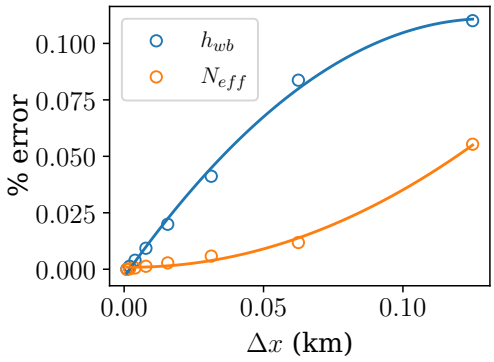

Figure 32: Convergence with decreasing time step. Each field is normalized with the normalization factor shown in the legend (max). The points are fitted with a degree 2 polynomial to show the approximately quadratic rate of convergence.

in fig. 34. The *SQRT_TOPO* flowline length from divide to toe was set to 2500 km and the number of grid cells was adjusted: $\{n_i = 2i + 1\}$ for $i \in [11, 121]$, $i \in \mathbb{N}$ and $\Delta x_i = 2500 \text{ km}/n_i$, so that the highest resolution was $\Delta x_i = 22.66$ km. The model solution at each resolution was linearly interpolated to the highest resolution grid and the sum of the element-wise difference with the highest resolution used for the (L1 norm) error metric, in keeping with eqn. 80:

$$ERR\left(\Delta x_i\right) = \sum_{k}^{N_y} \sum_{j}^{N_x} \left| \Lambda^{jk}\left(\Delta x_i\right) - \Lambda^{jk}\left(\Delta x_{-1}\right) \right|. \tag{81}$$

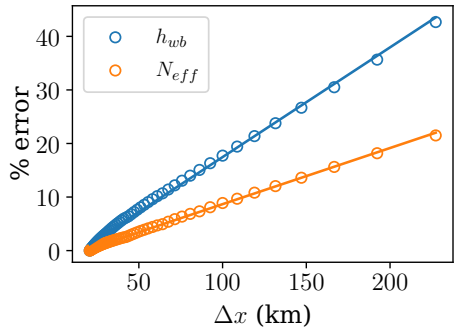

Figure 33: Difference in mean flowline solutions for unsteady SHMIP sqrt ice sheet topography at increasing spatial resolution, at end of 10 kyr run. The points are fitted with a line to demonstrate the match with the order of the numerical scheme.

Fig. 33 shows the convergence of model solutions (same set as § 4.12.2) at increasing spatial resolution (shorter cell width). The numerical order of the

upwind and finite volume schemes used here is $\mathcal{O}(\Delta x)$. The approximately linear rate of convergence in fig. 33 matches this numerical order.

4.12.4 *Mass conservation*

Mass conservation is demonstrated by comparing flux at the margin to source rates of water or sediment within the ice sheet: the integral of the melt rate over ice sheet less the total flux through the margin will give the change in basal water volume over time. Integrating this change up to each time step will give the basal water volume at each time step – which can be compared to model calculated basal water volume in order to assess mass conservation.

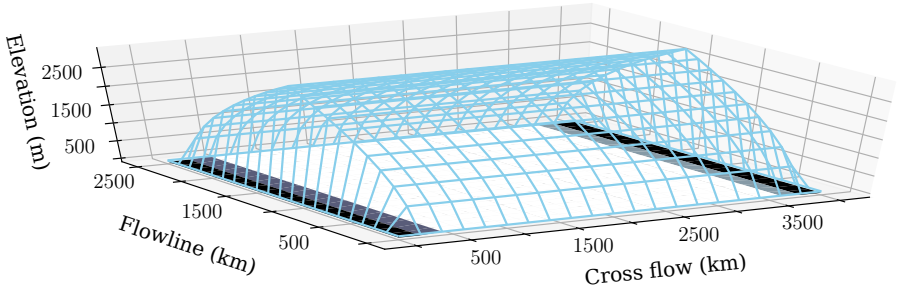

Figure 34: Ice sheet configuration used in SHMIP with basal temperature (black=-40,white=0.01)

To test mass conservation with unsteady input, we applied a sinusoidal meltwater forcing

$$m_t^{jk} = \frac{melt}{2}\sin\frac{2\pi}{T}t + \frac{melt}{2} + \frac{melt}{4}\sin 12\frac{2\pi}{T}t + \frac{melt}{4} + \frac{melt}{8}\sin 25\frac{2\pi}{T}t + \frac{melt}{8} \tag{82}$$

(where $T = 50$ kyr is the longest and highest amplitude period and $melt = 3.5$ mm/yr) to the *SQRT_TOPO* setup (depicted in fig. 34) and calculated basal sliding velocity dynamically as in eqn. 78. Here we assume incompressibility of water such that volume is scaled mass.

A net volume of basal water time series was calculated by time-integrating the net of input and output, $net_{hyd}^{t_i}$, up to each time step t_i:

$$net_{hyd}^{t_i} = \int_0^{t_i} \left(\int_{\mathcal{A}} m_t da - \oint_{\mathcal{S}} \vec{Q} \cdot \hat{n} dS \right) d\tau. \tag{83}$$

where $\mathcal{A}$ is the area covered by ice, m_t is the melt at the ice sheet base (eqn. 82), $\mathcal{S}$ is the ice margin (interface beyond which ice thickness is zero), $\vec{Q} \cdot \hat{n}$ is the flux through the margin, The $net_{hyd}^{t_i}$ time series was then compared against modelled total water volume ($V_{hyd}^{t_i}$) to calculate mass conservation error (ERR^{t_i}):

$$ERR_{hyd}^{t_i} = \frac{|net_{hyd}^{t_i} - V_{hyd}^{t_i}|}{V_{hyd}^{t_i}} \tag{84}$$

where V_{hyd} is the volume of water under the ice sheet.

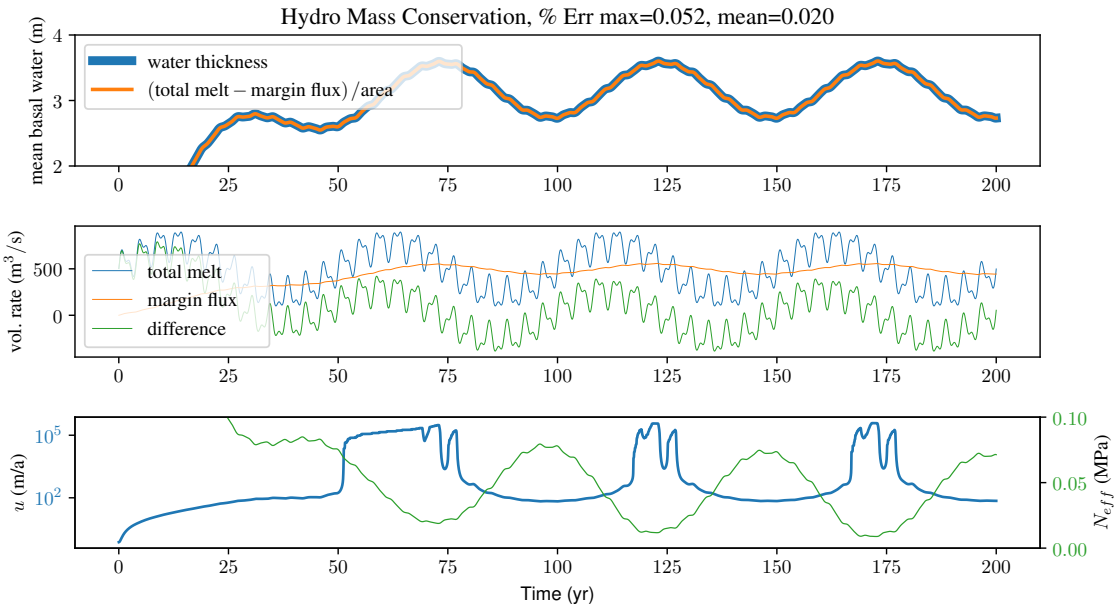

Figure 35: Assessment of mass conservation for subglacial hydrology model given steady square root ice sheet topography, flat basal topography, and sinusoidal ice sheet basal meltwater generation (m/a) given in eqn. 82, The basal sliding velocity calculated from driving stress and effective pressure (eqn. 79) over a 200 year modelled time period. The model solution for basal water thickness is compared with the time integrated difference of basal melt and flux out of the margin (eqn. 83) in the top panel (near complete visual overlap). For an illustration of model input and response, the centre panel shows the basal meltwater, flux out of the margin and the difference between the two over time. The bottom panel shows dynamically calculated, two way coupled basal velocity in blue and effective pressure in green.

The dynamic model outputs from this test are summarized in fig. 35. This mass conservation test shows a maximum error of 0.052% between the model output and the calculation in eqn. 83 (given in eqn. 112).

4.12.5 *Comparison with Werder et al. (2013) results for SHMIP*

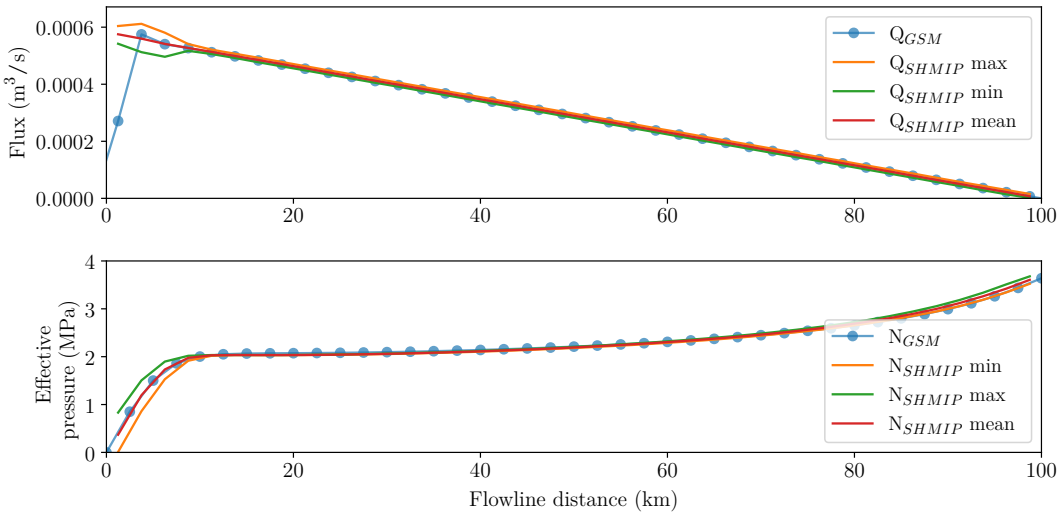

Figure 36: Comparison of our model solution with the SHMIP tuning set which used output from the model of Werder et al. (2013) which uses similar physics to BrAHMs2.0 in the linked-cavity configuration.

Results for this model are compared with output of the Glacier Drainage System model (GlaDS, Werder et al. (2013)) employing the same physics: a continuum representation of a linked-cavity system with Darcy-Weisbach flux shown in fig. 36. While their model is similar to this one, there are noteworthy differences. Werder et al. (2013) uses an unstructured mesh and finite element discretization, the channel elements are always active (with water exchanged between the channels at the edges and the distributed system at the subdomains). This is in contrast to BrAHMs2.0 in which the channel system switches on in a particular cell given a flux criterion (and uses finite volume discretization with a regular Cartesian grid). We therefore use the SHMIP scenario in which the least amount of channelized flux

is active in order to get the most structurally consistent comparison between the two models. BrAHMs2.0 closely reproduces the flux and effective pressure solutions for this scenario, concluding our verification that we solved the equations "right."

4.13 DISCRETIZATION

4.13.1 *Pressure Closure of Bueler and van Pelt (2015)*

Here we use the time varying water pressure calculation of Bueler and van Pelt (2015). The rationale summarized here is shown by Bueler (2014). Here the subglacial and englacial hydrologic systems are assumed in perfect communication and their co-evolution is described. The englacial hydrologic system is analogized to a rigid "pore-space" (comprised of crevasses, moulins, englacial channels, and inter-granular porosity). The **tot**al volume of water is the sum of **eng**lacial and **sub**glacial water:

$$V_{tot} = V_{eng} + V_{sub} \tag{85}$$

and the mass balance for incompressible water is

$$\frac{\partial V_{tot}}{\partial t} = -Q_{out} + Q_{in} + \frac{m}{\rho_w} \tag{86}$$

from total flux in and out of a control section of the system plus any sources (volume water, $\frac{m}{\rho_w}$) within that section. This section is of area Δx by Δy and pressure in the connected englacial-subglacial system is given by the hydrostatic head in the englacial part:

$$P_w = \frac{\rho_w g}{\Delta x \Delta y \phi_{eng}} V_{eng}. \tag{87}$$

The effective englacial porosity (ice volume relative proportion of connected englacial void space) is ϕ_{eng}. Cavity volume within an area of bed with roughness wavelength l_r (cavity generating obstacle spacing) is:

$$V_{sub} = n_{cav} V_{cav} = \frac{\Delta x \Delta y}{{l_r}^2} V_{cav} \tag{88}$$

where n_{cav} is the number of cavities in the given bed section and V_{cav} is their average volume. Differentiating this gives the change in pressure with time:

$$\begin{aligned}\frac{\partial P_w}{\partial t} =& \frac{\rho_w g}{\Delta x \Delta y \phi_{eng}} \frac{\partial V_{eng}}{\partial t} \\ =& \frac{\rho_w g}{\Delta x \Delta y \phi_{eng}} \frac{\partial V_{tot} - V_{sub}}{\partial t} \\ =& \frac{\rho_w g}{\Delta x \Delta y \phi_{eng}} \left\{ Q_{in} - Qout + \frac{m}{\rho_w} - \frac{\Delta x \Delta y}{{l_r}^2} \frac{\partial V_{cav}}{\partial t} \right\}\end{aligned}$$

The $\left(1/l_r^2\right) \frac{\partial V_{cav}}{\partial t} = \frac{\partial h_{cav}}{\partial t}$ derivative is given by the opening and closing balance in eqn. 64,

$$\frac{\partial P_w}{\partial t} = \frac{\rho_w g}{\phi_{eng}} \left\{ \frac{Q_{in} - Q_{out} + \frac{m}{\rho_w}}{\Delta x \Delta y} - u_b \left(h_r - h_{wb}\right) / l_r + c_2 [P_{ice} - P_w]^n \right\}.$$

Here opening due to wall melting has been omitted (see Assumption 1) relative to what is shown by Bueler (2014). As $\Delta x \to 0$ and $\Delta y \to 0$ the difference of the fluxes in versus out of the control section goes to the divergence of the fluxes within it.

$$\frac{\partial P_w}{\partial t} = \frac{\rho_w g}{\phi_{eng}} \left\{ -\nabla \cdot \mathbf{Q} + m_t - u_b \left(h_r - h_{wb}\right) / l_r - c_2 [P_{ice} - P_w]^n \right\}. \tag{89}$$

with m_t the source of water in thickness per unit time. we assume that water only travels laterally through the subglacial system and so all fluxes are through the linked cavities.

REFERENCES

Alley, R. B., S. Anandakrishnan, C. R. Bentley, and N. Lord (1994). "A water-piracy hypothesis for the stagnation of Ice Stream C, Antarctica". In: *Annals of Glaciology* 20, pp. 187–194. ISSN: 1727-5644. DOI: 10.3189/1994aog20-1-187-194. URL: http://dx.doi.org/10.3189/1994AoG20-1-187-194.

Alley, R. (1989). "Water-Pressure Coupling of Sliding and Bed Deformation: I. Water System". In: *Journal of Glaciology* 35.119, pp. 108–118. ISSN: 1727-5652. DOI: 10.3189/002214389793701527. URL: http://dx.doi.org/10.3189/002214389793701527.

Alley, R. B. (1992). "How can low-pressure channels and deforming tills coexist subglacially?" In: *Journal of Glaciology* 38.128, pp. 200–207. ISSN: 1727-5652. DOI: 10.3189/s0022143000009734. URL: http://dx.doi.org/10.3189/S0022143000009734.

Anandakrishnan, S. and R. B. Alley (Feb. 1997). "Stagnation of Ice Stream C, West Antarctica by water piracy". In: *Geophysical Research Letters* 24.3, pp. 265–268. ISSN: 0094-8276. DOI: 10.1029/96gl04016. URL: http://dx.doi.org/10.1029/96GL04016.

Anderson, R. S., B. Hallet, J. Walder, and B. F. Aubry (Jan. 1982). "Observations in a cavity beneath grinnell glacier". In: *Earth Surface Processes and Landforms* 7.1, pp. 63–70. ISSN: 1096-9837. DOI: 10.1002/esp.3290070108. URL: http://dx.doi.org/10.1002/esp.3290070108.

Arakawa, A. and V. R. Lamb (1977). "Computational design of the basic dynamical processes of the UCLA general circulation model". In: *General circulation models of the atmosphere* 17.Supplement C, pp. 173–265.

Bennett, M. R. (June 2003). "Ice streams as the arteries of an ice sheet: their mechanics, stability and significance". In: *Earth-Science Reviews* 61.3-4, pp. 309–

339. ISSN: 0012-8252. DOI: 10.1016/s0012-8252(02)00130-7. URL: http://dx.doi.org/10.1016/S0012-8252(02)00130-7.

Borgonovo, E. (June 2007). "A new uncertainty importance measure". In: *Reliability Engineering & System Safety* 92.6, pp. 771–784. ISSN: 0951-8320. DOI: 10.1016/j.ress.2006.04.015. URL: http://dx.doi.org/10.1016/j.ress.2006.04.015.

Brubaker, K. M., W. L. Myers, P. J. Drohan, D. A. Miller, and E. W. Boyer (2013). "The Use of LiDAR Terrain Data in Characterizing Surface Roughness and Microtopography". In: *Applied and Environmental Soil Science* 2013, pp. 1–13. ISSN: 1687-7675. DOI: 10.1155/2013/891534. URL: http://dx.doi.org/10.1155/2013/891534.

Bueler, E. and W. van Pelt (June 2015). "Mass-conserving subglacial hydrology in the Parallel Ice Sheet Model version 0.6". In: *Geoscientific Model Development* 8.6, pp. 1613–1635. ISSN: 1991-9603. DOI: 10.5194/gmd-8-1613-2015. URL: http://dx.doi.org/10.5194/gmd-8-1613-2015.

Bueler, E. (2014). "Extending the lumped subglacial–englacial hydrology model of Bartholomaus and others (2011)". In: *Journal of Glaciology* 60.222, pp. 808–810. ISSN: 1727-5652. DOI: 10.3189/2014jog14j075. URL: http://dx.doi.org/10.3189/2014JoG14J075.

Calov, R., R. Greve, A. Abe-Ouchi, E. Bueler, P. Huybrechts, J. V. Johnson, F. Pattyn, D. Pollard, C. Ritz, F. Saito, and et al. (2010). "Results from the Ice-Sheet Model Intercomparison Project–Heinrich Event Intercomparison (ISMIP HEINO)". In: *Journal of Glaciology* 56.197, pp. 371–383. ISSN: 1727-5652. DOI: 10.3189/002214310792447789. URL: http://dx.doi.org/10.3189/002214310792447789.

Carsey, F., A. Behar, A. Lonne Lane, V. Realmuto, and H. Engelhardt (2002). "A borehole camera system for imaging the deep interior of ice sheets". In:

Journal of Glaciology 48.163, pp. 622–628. ISSN: 1727-5652. DOI: 10.3189/172756502781831124. URL: http://dx.doi.org/10.3189/172756502781831124.

Chandler, D. M., J. L. Wadham, G. P. Lis, T. Cowton, A. Sole, I. Bartholomew, J. Telling, P. Nienow, E. B. Bagshaw, D. Mair, and et al. (Feb. 2013). "Evolution of the subglacial drainage system beneath the Greenland Ice Sheet revealed by tracers". In: *Nature Geoscience* 6.3, pp. 195–198. ISSN: 1752-0908. DOI: 10.1038/ngeo1737. URL: http://dx.doi.org/10.1038/NGEO1737.

Clark, P. U., D. Archer, D. Pollard, J. D. Blum, J. A. Rial, V. Brovkin, A. C. Mix, N. G. Pisias, and M. Roy (Dec. 2006). "The middle Pleistocene transition: characteristics, mechanisms, and implications for long-term changes in atmospheric pCO2". In: *Quaternary Science Reviews* 25.23-24, pp. 3150–3184. ISSN: 0277-3791. DOI: 10.1016/j.quascirev.2006.07.008. URL: http://dx.doi.org/10.1016/j.quascirev.2006.07.008.

Clarke, G. K. C. (Aug. 1996). "Lumped-element analysis of subglacial hydraulic circuits". In: *Journal of Geophysical Research: Solid Earth* 101.B8, pp. 17547–17559. ISSN: 0148-0227. DOI: 10.1029/96jb01508. URL: http://dx.doi.org/10.1029/96JB01508.

Cook, S. J., P. Christoffersen, and J. Todd (Oct. 2021). "A fully-coupled 3D model of a large Greenlandic outlet glacier with evolving subglacial hydrology, frontal plume melting and calving". In: *Journal of Glaciology* 68.269, pp. 486–502. ISSN: 1727-5652. DOI: 10.1017/jog.2021.109. URL: http://dx.doi.org/10.1017/jog.2021.109.

Courant, R., K. Friedrichs, and H. Lewy (Dec. 1928). "Über die partiellen Differenzengleichungen der mathematischen Physik". In: *Mathematische Annalen* 100.1, pp. 32–74. ISSN: 1432-1807. DOI: 10.1007/bf01448839. URL: http://dx.doi.org/10.1007/bf01448839.

Cuffey, K. and W. S. B. Paterson (2010). *The Physics of Glaciers*. 4th ed. Academic Press.

Dalton, A. S., M. Margold, C. R. Stokes, L. Tarasov, A. S. Dyke, R. S. Adams, S. Allard, H. E. Arends, N. Atkinson, J. W. Attig, P. J. Barnett, R. L. Barnett, M. Batterson, P. Bernatchez, H. W. Borns, A. Breckenridge, J. P. Briner, E. Brouard, J. E. Campbell, A. E. Carlson, J. J. Clague, B. B. Curry, R.-A. Daigneault, H. Dubé-Loubert, D. J. Easterbrook, D. A. Franzi, H. G. Friedrich, S. Funder, M. S. Gauthier, A. S. Gowan, K. L. Harris, B. Hétu, T. S. Hooyer, C. E. Jennings, M. D. Johnson, A. E. Kehew, S. E. Kelley, D. Kerr, E. L. King, K. K. Kjeldsen, A. R. Knaeble, P. Lajeunesse, T. R. Lakeman, M. Lamothe, P. Larson, M. Lavoie, H. M. Loope, T. V. Lowell, B. A. Lusardi, L. Manz, I. McMartin, F. C. Nixon, S. Occhietti, M. A. Parkhill, D. J. Piper, A. G. Pronk, P. J. Richard, J. C. Ridge, M. Ross, M. Roy, A. Seaman, J. Shaw, R. R. Stea, J. T. Teller, W. B. Thompson, L. H. Thorleifson, D. J. Utting, J. J. Veillette, B. C. Ward, T. K. Weddle, and H. E. Wright (Apr. 2020). "An updated radiocarbon-based ice margin chronology for the last deglaciation of the North American Ice Sheet Complex". In: *Quaternary Science Reviews* 234, p. 106223. ISSN: 0277-3791. DOI: 10.1016/j.quascirev.2020.106223. URL: http://dx.doi.org/10.1016/j.quascirev.2020.106223.

Darcy, H. (1856). *Les Fontaines Publiques De La Ville De Dijon: Exposition Et Application Des Principes A Suivre Et Des Formules A Employer Dans Les Questions De Distribution D'eau*. Ed. by V. Dalmont. 1st ed. 49 Quai des Augustins, Paris, France: Libraire des corps impériaux des ponts et chaussées et des mines.

de Fleurian, B., M. A. Werder, S. Beyer, D. J. Brinkerhoff, I. Delaney, C. F. Dow, J. Downs, O. Gagliardini, M. J. Hoffman, R. L. Hooke, J. Seguinot, and A. N. Sommers (Oct. 2018). "SHMIP The subglacial hydrology model intercomparison Project". In: *Journal of Glaciology* 64.248, pp. 897–916. ISSN: 1727-5652. DOI: 10.1017/jog.2018.78. URL: http://dx.doi.org/10.1017/jog.2018.78.

Dowdeswell, J. A., M. A. Maslin, J. T. Andrews, and I. N. McCave (1995). "Iceberg production, debris rafting, and the extent and thickness of Heinrich layers (H-1, H-2) in North Atlantic sediments". In: *Geology* 23.4, p. 301. ISSN: 0091-7613. DOI: 10.1130/0091-7613(1995)023<0297:ipdrat>2.3.co;2. URL: http://dx.doi.org/10.1130/0091-7613(1995)023%3C0297:IPDRAT%3E2.3.CO;2.

Erokhina, O., I. Rogozhina, M. Prange, P. Bakker, J. Bernales, A. Paul, and M. Schulz (Apr. 2017). "Dependence of slope lapse rate over the Greenland ice sheet on background climate". In: *Journal of Glaciology* 63.239, pp. 568–572. ISSN: 1727-5652. DOI: 10.1017/jog.2017.10. URL: http://dx.doi.org/10.1017/jog.2017.10.

Flowers, G. E. (Mar. 2015). "Modelling water flow under glaciers and ice sheets". In: *Proceedings of the Royal Society A: Mathematical, Physical and Engineering Sciences* 471.2176, pp. 1–41. ISSN: 1471-2946. DOI: 10.1098/rspa.2014.0907. URL: http://dx.doi.org/10.1098/rspa.2014.0907.

Flowers, G. (Nov. 2000). "A Multicomponent Coupled Model of Glacier Hydrology". PhD thesis. Department of Earth, Ocean and Atmospheric Sciences Faculty of Science 2020 – 2207 Main Mall Vancouver, BC Canada V6T 1Z4: University of British Columbia.

Flowers, G. E. (July 2018). "Hydrology and the future of the Greenland Ice Sheet". In: *Nature Communications* 9.1. ISSN: 2041-1723. DOI: 10.1038/s41467-018-05002-0. URL: http://dx.doi.org/10.1038/s41467-018-05002-0.

Flowers, G. E. and G. K. C. Clarke (Nov. 2002). "A multicomponent coupled model of glacier hydrology 1. Theory and synthetic examples". In: *Journal of Geophysical Research: Solid Earth* 107.B11, ECV 9-1-ECV 9–17. ISSN: 0148-0227. DOI: 10.1029/2001jb001122. URL: http://dx.doi.org/10.1029/2001JB001122.

Fowler, A. C. (June 2009). "Instability modelling of drumlin formation incorporating lee-side cavity growth". In: *Proceedings of the Royal Society A: Mathematical,*

Physical and Engineering Sciences 465.2109, pp. 2681–2702. ISSN: 1471-2946. DOI: 10.1098/rspa.2008.0490. URL: http://dx.doi.org/10.1098/rspa.2008.0490.

Gandy, N., L. J. Gregoire, J. C. Ely, S. L. Cornford, C. D. Clark, and D. M. Hodgson (Nov. 2019). "Exploring the ingredients required to successfully model the placement, generation, and evolution of ice streams in the British-Irish Ice Sheet". In: *Quaternary Science Reviews* 223, p. 105915. ISSN: 0277-3791. DOI: 10.1016/j.quascirev.2019.105915. URL: http://dx.doi.org/10.1016/j.quascirev.2019.105915.

Grinsted, A., C. S. Hvidberg, D. A. Lilien, N. M. Rathmann, N. B. Karlsson, T. Gerber, H. A. Kjær, P. Vallelonga, and D. Dahl-Jensen (Sept. 2022). "Accelerating ice flow at the onset of the Northeast Greenland Ice Stream". In: *Nature Communications* 13.1. ISSN: 2041-1723. DOI: 10.1038/s41467-022-32999-2. URL: http://dx.doi.org/10.1038/s41467-022-32999-2.

Hager, A. O., M. J. Hoffman, S. F. Price, and D. M. Schroeder (Sept. 2022). "Persistent, extensive channelized drainage modeled beneath Thwaites Glacier, West Antarctica". In: *The Cryosphere* 16.9, pp. 3575–3599. ISSN: 1994-0424. DOI: 10.5194/tc-16-3575-2022. URL: http://dx.doi.org/10.5194/tc-16-3575-2022.

Hank, K., L. Tarasov, and E. Mantelli (Feb. 2023). "Numerical issues in modeling ice sheet instabilities such as binge-purge type cyclic ice stream surging". In: DOI: 10.5194/egusphere-2023-81. URL: http://dx.doi.org/10.5194/egusphere-2023-81.

Hemming, S. R. (Mar. 2004). "Heinrich events: Massive late Pleistocene detritus layers of the North Atlantic and their global climate imprint". In: *Reviews of Geophysics* 42.1. ISSN: 8755-1209. DOI: 10.1029/2003rg000128. URL: http://dx.doi.org/10.1029/2003RG000128.

Herman, J. and W. Usher (Jan. 2017). "SALib: An open-source Python library for Sensitivity Analysis". In: *The Journal of Open Source Software* 2.9, p. 97. ISSN: 2475-9066. DOI: 10.21105/joss.00097. URL: http://dx.doi.org/10.21105/joss.00097.

Hewitt, I. (June 2013). "Seasonal changes in ice sheet motion due to melt water lubrication". In: *Earth and Planetary Science Letters* 371-372, pp. 16–25. ISSN: 0012-821X. DOI: 10.1016/j.epsl.2013.04.022. URL: http://dx.doi.org/10.1016/j.epsl.2013.04.022.

Iverson, N. R. (Aug. 2012). "A theory of glacial quarrying for landscape evolution models". In: *Geology* 40.8, pp. 679–682. ISSN: 0091-7613. DOI: 10.1130/g33079.1. URL: http://dx.doi.org/10.1130/g33079.1.

Joughin, I., S. Tulaczyk, M. Fahnestock, and R. Kwok (Oct. 1996). "A Mini-Surge on the Ryder Glacier, Greenland, Observed by Satellite Radar Interferometry". In: *Science* 274.5285, pp. 228–230. ISSN: 1095-9203. DOI: 10.1126/science.274.5285.228. URL: http://dx.doi.org/10.1126/science.274.5285.228.

Kageyama, M., S. P. Harrison, M.-L. Kapsch, M. Lofverstrom, J. M. Lora, U. Mikolajewicz, S. Sherriff-Tadano, T. Vadsaria, A. Abe-Ouchi, N. Bouttes, and et al. (May 2021). "The PMIP4 Last Glacial Maximum experiments: preliminary results and comparison with the PMIP3 simulations". In: *Climate of the Past* 17.3, pp. 1065–1089. ISSN: 1814-9332. DOI: 10.5194/cp-17-1065-2021. URL: http://dx.doi.org/10.5194/cp-17-1065-2021.

Kamb, B. (1987). "Glacier surge mechanism based on linked cavity configuration of the basal water conduit system". In: *Journal of Geophysical Research* 92.B9, pp. 9083–9100. ISSN: 0148-0227. DOI: 10.1029/jb092ib09p09083. URL: http://dx.doi.org/10.1029/JB092iB09p09083.

Kavanagh, M. and L. Tarasov (Aug. 2018). "BrAHMs V1.0: a fast, physically based subglacial hydrology model for continental-scale application". In: *Geoscientific*

Model Development 11.8, pp. 3497–3513. ISSN: 1991-9603. DOI: 10.5194/gmd-11-3497-2018. URL: http://dx.doi.org/10.5194/gmd-11-3497-2018.

Kingslake, J. and F. Ng (2013). "Modelling the coupling of flood discharge with glacier flow during jökulhlaups". In: *Annals of Glaciology* 54.63, pp. 25–31. ISSN: 1727-5644. DOI: 10.3189/2013aog63a331. URL: http://dx.doi.org/10.3189/2013AoG63A331.

Lawrence, M. G. (Feb. 2005). "The Relationship between Relative Humidity and the Dewpoint Temperature in Moist Air: A Simple Conversion and Applications". In: *Bulletin of the American Meteorological Society* 86.2, pp. 225–234. ISSN: 1520-0477. DOI: 10.1175/bams-86-2-225. URL: http://dx.doi.org/10.1175/BAMS-86-2-225.

MacAyeal, D. R. (Dec. 1993). "Binge/purge oscillations of the Laurentide Ice Sheet as a cause of the North Atlantic's Heinrich events". In: *Paleoceanography* 8.6, pp. 775–784. ISSN: 0883-8305. DOI: 10.1029/93pa02200. URL: http://dx.doi.org/10.1029/93PA02200.

Mathews, W. H. (1974). "Surface profiles of the laurentide ice sheet in its marginal areas". In: *Journal of Glaciology* 13.67, pp. 37–43. ISSN: 1727-5652. DOI: 10.1017/s0022143000023352. URL: http://dx.doi.org/10.1017/s0022143000023352.

Morlighem, M., E. Rignot, J. Mouginot, X. Wu, H. Seroussi, E. Larour, and J. Paden (2013). "High-resolution bed topography mapping of Russell Glacier, Greenland, inferred from Operation IceBridge data". In: *Journal of Glaciology* 59.218, pp. 1015–1023. ISSN: 1727-5652. DOI: 10.3189/2013jog12j235. URL: http://dx.doi.org/10.3189/2013JoG12J235.

Muskat, M. (Mar. 1934). "The Flow of Compressible Fluids Through Porous Media and Some Problems in Heat Conduction". In: *Physics* 5.3, pp. 71–94. ISSN: 2163-5102. DOI: 10.1063/1.1745233. URL: http://dx.doi.org/10.1063/1.1745233.

Naafs, B., J. Hefter, and R. Stein (Nov. 2013). "Millennial-scale ice rafting events and Hudson Strait Heinrich(-like) Events during the late Pliocene and Pleistocene: a review". In: *Quaternary Science Reviews* 80, pp. 1–28. ISSN: 0277-3791. DOI: 10.1016/j.quascirev.2013.08.014. URL: http://dx.doi.org/10.1016/j.quascirev.2013.08.014.

Oreskes, N., K. Shrader-Frechette, and K. Belitz (Feb. 1994). "Verification, Validation, and Confirmation of Numerical Models in the Earth Sciences". In: *Science* 263.5147, pp. 641–646. ISSN: 1095-9203. DOI: 10.1126/science.263.5147.641. URL: http://dx.doi.org/10.1126/science.263.5147.641.

Ou, H.-W. (Mar. 2021). "A theory of glacier dynamics and instabilities Part 1: Topographically confined glaciers". In: *Journal of Glaciology*, pp. 1–12. ISSN: 1727-5652. DOI: 10.1017/jog.2021.20. URL: http://dx.doi.org/10.1017/jog.2021.20.

Patankar, S. V. (1980). *Numerical Heat Transfer and Fluid Flow*. 1st ed. 1221 Avenue of the Americas, New York, New York, USA: McGraw-Hill Book Company.

Payne, A. J. (Aug. 1998). "Dynamics of the Siple Coast ice streams, west Antarctica: Results from a thermomechanical ice sheet model". In: *Geophysical Research Letters* 25.16, pp. 3173–3176. ISSN: 0094-8276. DOI: 10.1029/98gl52327. URL: http://dx.doi.org/10.1029/98GL52327.

Payne, A. J. and P. W. Dongelmans (June 1997). "Self-organization in the thermomechanical flow of ice sheets". In: *Journal of Geophysical Research: Solid Earth* 102.B6, pp. 12219–12233. ISSN: 0148-0227. DOI: 10.1029/97jb00513. URL: http://dx.doi.org/10.1029/97JB00513.

Payne, A. J., P. Huybrechts, A. Abe-Ouchi, R. Calov, J. L. Fastook, R. Greve, S. J. Marshall, I. Marsiat, C. Ritz, L. Tarasov, and et al. (2000). "Results from the EISMINT model intercomparison: the effects of thermomechanical coupling". In: *Journal of Glaciology* 46.153, pp. 227–238. ISSN: 1727-5652.

DOI: 10.3189/172756500781832891. URL: http://dx.doi.org/10.3189/172756500781832891.

Pelletier, J. D., P. D. Broxton, P. Hazenberg, X. Zeng, P. A. Troch, G.-Y. Niu, Z. Williams, M. A. Brunke, and D. Gochis (Jan. 2016). "A gridded global data set of soil, intact regolith, and sedimentary deposit thicknesses for regional and global land surface modeling". In: *Journal of Advances in Modeling Earth Systems* 8.1, pp. 41–65. ISSN: 1942-2466. DOI: 10.1002/2015ms000526. URL: http://dx.doi.org/10.1002/2015MS000526.

Pianosi, F. and T. Wagener (May 2015). "A simple and efficient method for global sensitivity analysis based on cumulative distribution functions". In: *Environmental Modelling & Software* 67, pp. 1–11. ISSN: 1364-8152. DOI: 10.1016/j.envsoft.2015.01.004. URL: http://dx.doi.org/10.1016/j.envsoft.2015.01.004.

Pollard, D. and R. M. DeConto (Sept. 2012). "A simple inverse method for the distribution of basal sliding coefficients under ice sheets, applied to Antarctica". In: *The Cryosphere* 6.5, pp. 953–971. ISSN: 1994-0424. DOI: 10.5194/tc-6-953-2012. URL: http://dx.doi.org/10.5194/tc-6-953-2012.

Rada, C. and C. Schoof (Aug. 2018). "Channelized, distributed, and disconnected: subglacial drainage under a valley glacier in the Yukon". In: *The Cryosphere* 12.8, pp. 2609–2636. ISSN: 1994-0424. DOI: 10.5194/tc-12-2609-2018. URL: http://dx.doi.org/10.5194/tc-12-2609-2018.

Retzlaff, R. and C. R. Bentley (1993). "Timing of stagnation of Ice Stream C, West Antarctica, from short-pulse radar studies of buried surface crevasses". In: *Journal of Glaciology* 39.133, pp. 553–561. ISSN: 1727-5652. DOI: 10.3189/s0022143000016440. URL: http://dx.doi.org/10.3189/S0022143000016440.

Roache, P. J. (Jan. 1997). "QUANTIFICATION OF UNCERTAINTY IN COMPUTATIONAL FLUID DYNAMICS". In: *Annual Review of Fluid Mechanics*

29.1, pp. 123–160. ISSN: 1545-4479. DOI: 10.1146/annurev.fluid.29.1.123. URL: http://dx.doi.org/10.1146/annurev.fluid.29.1.123.

Röthlisberger, H. (1972). "Water Pressure in Intra- and Subglacial Channels". In: *Journal of Glaciology* 11.62, pp. 177–203. ISSN: 1727-5652. DOI: 10.3189/s0022143000022188. URL: http://dx.doi.org/10.3189/S0022143000022188.

Saltelli, A. (May 2002). "Making best use of model evaluations to compute sensitivity indices". In: *Computer Physics Communications* 145.2, pp. 280–297. ISSN: 0010-4655. DOI: 10.1016/s0010-4655(02)00280-1. URL: http://dx.doi.org/10.1016/S0010-4655(02)00280-1.

Saltelli, A., M. Ratto, T. Andres, F. Campolongo, J. Cariboni, D. Gatelli, M. Saisana, and S. Tarantola (2008). *Global Sensitivity Analysis. The Primer*. 1st ed. The Atrium, Southern Gate, Chichester,West Sussex PO19 8SQ, England: John Wiley & Sons, Ltd. ISBN: 978-0-470-05997-5.

Schoof, C. (Jan. 2007). "Cavitation on Deformable Glacier Beds". In: *SIAM Journal on Applied Mathematics* 67.6, pp. 1633–1653. ISSN: 1095-712X. DOI: 10.1137/050646470. URL: http://dx.doi.org/10.1137/050646470.

— (Dec. 2010). "Ice-sheet acceleration driven by melt supply variability". In: *Nature* 468.7325, pp. 803–806. ISSN: 1476-4687. DOI: 10.1038/nature09618. URL: http://dx.doi.org/10.1038/nature09618.

Siegfried, M. R., H. A. Fricker, S. P. Carter, and S. Tulaczyk (Mar. 2016). "Episodic ice velocity fluctuations triggered by a subglacial flood in West Antarctica". In: *Geophysical Research Letters* 43.6, pp. 2640–2648. ISSN: 1944-8007. DOI: 10.1002/2016gl067758. URL: http://dx.doi.org/10.1002/2016GL067758.

Sobol, I. (Feb. 2001). "Global sensitivity indices for nonlinear mathematical models and their Monte Carlo estimates". In: *Mathematics and Computers in Simulation* 55.1-3, pp. 271–280. ISSN: 0378-4754. DOI: 10.1016/s0378-4754(00)00270-6. URL: http://dx.doi.org/10.1016/S0378-4754(00)00270-6.

Sornette, D., A. B. Davis, K. Ide, K. R. Vixie, V. Pisarenko, and J. R. Kamm (Apr. 2007). "Algorithm for model validation: Theory and applications". In: *Proceedings of the National Academy of Sciences* 104.16, pp. 6562–6567. ISSN: 1091-6490. DOI: 10.1073/pnas.0611677104. URL: http://dx.doi.org/10.1073/pnas.0611677104.

Tadmor, E. (2012). "A review of numerical methods for nonlinear partial differential equations". In: *Bulletin of the American Mathematical Society* 49.4, pp. 507–554. ISSN: 1088-9485. DOI: 10.1090/s0273-0979-2012-01379-4. URL: http://dx.doi.org/10.1090/s0273-0979-2012-01379-4.

Tarasov, L., A. S. Dyke, R. M. Neal, and W. Peltier (Jan. 2012). "A data-calibrated distribution of deglacial chronologies for the North American ice complex from glaciological modeling". In: *Earth and Planetary Science Letters* 315-316, pp. 30–40. ISSN: 0012-821X. DOI: 10.1016/j.epsl.2011.09.010. URL: http://dx.doi.org/10.1016/j.epsl.2011.09.010.

Tarasov, L. and W. R. Peltier (June 2007). "Coevolution of continental ice cover and permafrost extent over the last glacial-interglacial cycle in North America". In: *Journal of Geophysical Research* 112.F2. ISSN: 0148-0227. DOI: 10.1029/2006jf000661. URL: http://dx.doi.org/10.1029/2006JF000661.

— (Apr. 2006). "A calibrated deglacial drainage chronology for the North American continent: evidence of an Arctic trigger for the Younger Dryas". In: *Quaternary Science Reviews* 25.7–8, pp. 659–688. ISSN: 0277-3791. DOI: 10.1016/j.quascirev.2005.12.006. URL: http://dx.doi.org/10.1016/j.quascirev.2005.12.006.

Virtanen, P., R. Gommers, T. E. Oliphant, M. Haberland, T. Reddy, D. Cournapeau, E. Burovski, P. Peterson, W. Weckesser, J. Bright, S. J. van der Walt, M. Brett, J. Wilson, K. J. Millman, N. Mayorov, A. R. J. Nelson, E. Jones, R. Kern, E. Larson, C. J. Carey, İ. Polat, Y. Feng, E. W. Moore, J. VanderPlas, D. Laxalde, J. Perktold, R. Cimrman, I. Henriksen, E. A. Quintero, C. R. Harris,

A. M. Archibald, A. H. Ribeiro, F. Pedregosa, P. van Mulbregt, and SciPy 1.0 Contributors (2020). "SciPy 1.0: Fundamental Algorithms for Scientific Computing in Python". In: *Nature Methods* 17, pp. 261–272. DOI: 10.1038/s41592-019-0686-2.

Walder, J. and B. Hallet (1979). "Geometry of Former Subglacial Water Channels and Cavities". In: *Journal of Glaciology* 23.89, pp. 335–346. ISSN: 1727-5652. DOI: 10.1017/s0022143000029944. URL: http://dx.doi.org/10.1017/S0022143000029944.

Walder, J. S. (1986). "Hydraulics of Subglacial Cavities". In: *Journal of Glaciology* 32.112, pp. 439–445. ISSN: 1727-5652. DOI: 10.3189/s0022143000012156. URL: http://dx.doi.org/10.3189/S0022143000012156.

Walder, J. S. and A. Fowler (1994). "Channelized subglacial drainage over a deformable bed". In: *Journal of Glaciology* 40.134, pp. 3–15. ISSN: 1727-5652. DOI: 10.3189/s0022143000003750. URL: http://dx.doi.org/10.3189/S0022143000003750.

Weisbach, J. (1855). *Lehrbuch der ingenieur- und maschinen-mechanik*. 1st ed. Vieweg, Braunschweig, Germany. URL: https://babel.hathitrust.org/cgi/pt?id=wu.89088908009&view=1up&seq=8.

Werder, M. A., I. J. Hewitt, C. G. Schoof, and G. E. Flowers (Oct. 2013). "Modeling channelized and distributed subglacial drainage in two dimensions". In: *Journal of Geophysical Research: Earth Surface* 118.4, pp. 2140–2158. ISSN: 2169-9003. DOI: 10.1002/jgrf.20146. URL: http://dx.doi.org/10.1002/jgrf.20146.

Willis, M. J., W. Zheng, W. J. Durkin, M. E. Pritchard, J. M. Ramage, J. A. Dowdeswell, T. J. Benham, R. P. Bassford, L. A. Stearns, A. F. Glazovsky, Y. Y. Macheret, and C. C. Porter (Nov. 2018). "Massive destabilization of an Arctic ice cap". In: *Earth and Planetary Science Letters* 502, pp. 146–155. ISSN: 0012-821X. DOI: 10.1016/j.epsl.2018.08.049. URL: http://dx.doi.org/10.1016/j.epsl.2018.08.049.

Preface to Chapter 5, "Sediment Production & Transport by the North American Ice Complex Throughout the Pleistocene"

This manuscript is intended for submission to Climate of the Past. This chapter couples the sediment model which was presented in chap. 2 to the subglacial hydrology model presented in chap. 3 and assessed within the context of surging of a large ice stream in chap. 4. The constraints on Pliocene regolith thickness inferred herein support the conclusions in chap. 6.

Chapter 5

Sediment Production & Transport by the North American Ice Complex Throughout the Pleistocene

ABSTRACT

Landscape evolution is typically neglected at large scale when considering the basal boundary condition for ice sheet and climate modelling over past glacial cycles. The appropriate sediment/bedrock mask, bed elevation, and land sea mask to use during time frames prior to last glacial maximum is often not given any consideration.

To address the above context, we present an updated sediment production and transport model with dynamically calculated soft sediment mask, isostatic adjustment to dynamical sediment load and bedrock erosion, and a new subglacial hydrology model coupled to the Glacial Systems Model. The coupled model is capable of multi-million year integrations driven only by greenhouse gas concentration and insolation. The model passes a set of verification tests and conserves mass. We assess parametric sensitivity of the erosion rates and sediment transport.

We quantify the differences in the spatial distribution of abrasion and quarrying rates given by the Hallet and Hildes models of erosion. Finally we compare the final sediment solutions in an ensemble of whole-Pleistocene simulations for a range of initial (Pliocene) regolith thicknesses and erosion rates against multiple estimates for present day drift thickness, Quaternary sediment volume in the Atlantic Ocean, and erosion depth estimates. When combined with the coupled ice sheet-climate-sediment physics, these constraints suggest a Pliocene regolith thickness of 40 m or less.

5.1 INTRODUCTION

During the last three million years, the landscape of North America has been heavily influenced by glacial conditions. A confident determination of the amount of glacial erosion that had occured over this time interval would strongly aid in deciphering this influence. However, while there are observationally-based estimates for the total amount of sediment removed from North America during this time interval, it is largely unknown what fraction of this material was sourced from glacial erosion of bedrock versus pre-existing Pliocene regolith. Constraining long term erosion rates is necessary for assessing the likelihood of exhumation of long term nuclear waste repositories by glacial action and thus site selection (McKinley and Chapman, 2009). Capable models of sediment transport history allow for more targeted mineral exploration (Klassen and Gubins, 1997) and potentially lowered environmental impact from such campaigns. From an earth system dynamics perspective, such constraint would permit clearer assessment of the role soft sediment processes may have played in the mid-Pleistocene Transition (the Regolith Hypothesis, P. U. Clark and Pollard, 1998). To address this, herein we use data-constrained large ensemble modelling to determine such constraints.

Below, we start with an overview of the state of ice sheet sediment modelling and the model used in these experiments, identifying newly added couplings. We then present model verification tests and sensitivity analysis of the sediment transport component. Following these, we describe the available model constraints, inputs, and experimental results and terminate with a discussion and conclusions.

5.1.1 *Current Models of Glacial Sedimentary Processes*

Though current paleo ice sheet models can incorporate relevant glaciological processes, climate representation is the largest challenge for long term earth system simulation. For the applicable time scales, full coupling with a general circulation model (GCM) is not feasible. Paleo ice sheet modelling studies therefore make simplifications such as snap shotting output from a GCM, glacial indexing, using lower fidelity earth systems models of intermediate complexity (EMICs), or energy balance models (EBMs).

The challenge of climate representation is further exacerbated by the uncertainty of atmospheric composition extending back to the beginning of the Pleistocene (or earlier in the case of Pollard and DeConto (2020)). Reliable globally averaged estimates of CO_2 extend back to 800 kyr in the Antarctic ice core record (Bereiter et al., 2015). While the boron isotope proxy record is extending inferences of atmospheric pCO_2 back into the Pleistocene (Chalk et al., 2017), early Pleistocene estimates remain sparse and uncertain (Hönisch et al., 2009).

Glacial sedimentary numerical models have been around for decades (Harbor, Hallet, and Raymond, 1988; P. U. Clark and Pollard, 1998; Pollard and Deconto, 2009; Melanson, T. Bell, and Tarasov, 2013; Ugelvig and Egholm, 2018). However, they have not received the same attention as other aspects of the glacial ice/climate/earth system. For example, there has not been a model intercomparison project as there have been for other important ice sheet processes. These sedi-

mentary models are essentially unconstrained owing to the paucity of quantitative constraint available at the continental scale. The majority of subglacial sediment modelling studies have focused on reproducing ice-catchment scale landscape evolution (*e.g.* (Harbor, Hallet, and Raymond, 1988; Braun, Zwartz, and Tomkin, 1999; Ugelvig, Egholm, and Iverson, 2016)). Only a scant subset of models have been applied to the scale of continental ice sheets (shown in tbl. 4).

Continental scale ice sheet numerical models have incorporated subsets of the processes relevant to glacial erosion and at a range of complexities (table 4). At first order, a model must simulate the evolution of ice mass and motion combined with a relationship between motion and sediment transport. Table 4 shows the steady progression of increasing completeness of glacial erosion models over time. Each of these studies must assume initial sediment distribution at simulation start because this quantity is unknown in each case – a further challenge for modelling sedimentary processes.

Simulating removal of regolith along a 1-D flowline profile of the North American ice sheet over the Pleistocene, P. U. Clark and Pollard (1998) started with a uniform thickness 50 m of sediment and modelled transport by deformation. They also assumed the entire base of the ice sheet was warm and that effective pressure was close to zero. P. U. Clark and Pollard (1998) had to cap ice free areas at 100 m sediment thickness to avoid accumulating around 500 m of sediment at the Southern margin, citing missing non-glacial transport as a short-coming.

Pollard and DeConto (2003) use the same transport model as in P. U. Clark and Pollard (1998), supplemented with a sediment production law and applied to a 2-D ice sheet model in Antarctica over 400 kyr during onset glaciation. The ice sheet model is asynchronously coupled to a GCM with slab ocean with sufficient temporal resolution to capture obliquity and eccentricity cycles. The model neglects subglacial hydrologic processes simulating basal water pressure, thereby requiring the same effective pressure assumption as P. U. Clark and Pollard (1998): effective

Model Reference	Production	Transp	Hyd	Therm	IA	Ice Dyn	Slid Cpl	Dim	Scale
Jenson, MacAyeal, et al. (1996)	None	Sub	N	N	ice	SIA	N	1D	1500 km/60 kyr
P. U. Clark and Pollard (1998)	None	Sub	N	N	ice	SIA	N	1D	2500 km/3 Myr
Dowdeswell and Siegert (1999)	Emp	Emp	N	N	N	SIA	N	2D	
Pollard and DeConto (2003)	Emp	Sub	N	Y	ice	SIA	N	2D	4000 km/400 kyr
D. H. Hildes et al. (2004)	Abr/Qr	Eng	N	Y	ice	SIA	N	2D	3500 km/120 kyr
Melanson, T. Bell, and Tarasov (2013)	Abr/Qr/Emp	Eng/Sub	Y	Y	ice	SIA	N	2D	3500 km/120 kyr
Pollard and DeConto (2020)	Emp	Sub	N	Y	ice/sed	Hyb	Sed	2D	4000 km/40 Myr
This work	Abr/Qr	Eng/Sub	Y	Y	ice/sed	Hyb	Sed/Hyd	2D	3500 km/2.5 Myr

Table 4: Summary of processes applied in sediment models in the literature. Production is the type of sediment production, Transp is the mode of sediment transport, Hyd is whether subglacial hydrology is included, Therm is whether thermodynamics is coupled, IA is the component included in the isostatic adjustment loading, Ice Dyn is the ice dynamics used, Slid Cpl is whether the sediment and subglacial hydrology components are coupled into the sliding velocity calculation, Dim is model dimensionality (1D for flowline, 2D for plan view), Scale is the length and spatial scale of the model application. In each case the component complexity is not examined and some components in some models have a more complete treatment than others (e.g. the isostatic adjustment model of Pollard and DeConto (2020) is a local isostatic relaxation model versus the model of Melanson, T. Bell, and Tarasov (2013) and this work which is a gravitationally self-consistent visco-elastic model).

pressure in the sediment layer is only due to sediment weight (water pressure is set = ice sheet overburden). These simulations demonstrate the ability of ice basal action to move tens of metres of sediment from large portions of the Antarctic continent in areas which are repeatedly warm based. Transported sediment yields deposits hundreds of metres thick (up to 900 m) after 400 kyr. Interestingly, the authors show large areas which never yield warm based conditions during the 400 kyr simulation suggesting that pre-glacial sediment may have survived for millions of years.

Pollard and DeConto (2020) extend their effort in Pollard and DeConto (2003) to a continuous simulation over the last 40 Myr. This integration includes improved ice physics and a comparison against seismic observation. Such long model integration requires low spatial resolution at 80/160 km. The results show sediment production amounts varying 3 orders of magnitude with some channels incised down to 7000 m. Thickness of offshore deposits reach 10 km on the shelf and may be limited by the imposed surface slope restriction (0.0075 m/m) simulating slumping. They iteratively model pre-glacial topography and effectively assume 20 m of sediment over the continent and 100 m over marine areas.

D. H. Hildes et al. (2004) model sediment movement and generation over the last glacial cycle with a more comprehensive model (including erosive processes). They assume that the last interglacial sediment distribution is the same as present. Melanson, T. Bell, and Tarasov (2013) uses a similar model, integrating ice sheet evolution and sediment processes over the last glacial cycle as well as assuming present day sediment distribution and topography for last interglacial. Melanson, T. Bell, and Tarasov (2013) used the estimates of total Pleistocene erosion from M. Bell and Laine (1985) as well as transport distances from the Hudson bay.

Here we present a fully coupled model capable of multi-million year integrations which permits long term simulation of sedimentary processes such that the results lend themselves to comparison against both the Quaternary sedimentary record and

the present day distribution of sediment. For the first time, this model incorporates a fully coupled suite of ice dynamics, climate, subglacial hydrology and sediment, where the solid earth model incorporates changes in sediment/bedrock load and the basal velocities depend on the subglacial water pressure and dynamic soft/hard sliding bed mask.

5.2 MODEL OF GLACIAL SEDIMENTATION

The sediment model (Melanson, 2012) applied in the Glacial Systems Model (GSM) is designed after that of D. H. D. Hildes (2001). Both employ separate descriptions of abrasion and quarrying for the sediment production part, although Melanson (2012) provides an optional empirical sediment production as well as a choice between Boulton and Hallet style abrasion whereas D. H. D. Hildes (2001) uses only Hallet. D. H. D. Hildes (2001) tracks relative hardness of substrate and abrasive, abrasion ceases when the latter is less than the former, whereas Melanson (2012) assumes the abrading particle is always harder than the substrate. D. H. D. Hildes (2001) also allows a spatially varying lithology-based calculation of crack growth, and hence of quarrying rates. D. H. Hildes et al. (2004) and Melanson (2012) both use estimates of cavitation (from basal water pressure) in the lee side of basal protrusions to estimate stress regimes and thus quarrying rates. Both models give englacial transport rates through advection, however, D. H. D. Hildes (2001) omits subglacial transport.

The GSM sediment model is detailed in Melanson, T. Bell, and Tarasov (2013) but those details are repeated in apdx. 5.8.2 for convenience. Several aspects of this model have been updated since the publication of Melanson, T. Bell, and Tarasov (2013): performance improvements by shrinking of subgrid arrays (justified by sensitivity analysis) and array vectorization, improved mass conservation through synchronizing all model components in a single time iteration loop, and change to

a generalized Arkawa C grid. The sediment model has now been coupled to the glacio-isostatic adjustment model of the GSM. The coupling accounts for changing surface load from sediment transport. The sediment distribution also dynamically sets the hard/soft bed mask for the basal drag calculation.

5.2.1 *The Glacial Systems Model*

The GSM incorporates a fully coupled system of hybrid SIA/SSA ice physics (Pollard and DeConto, 2012) and 3D ice thermodynamics with local 1D permafrost-resolving bed thermodynamics (Tarasov and W. R. Peltier, 2007). We use the grounding line flux approximation of Schoof (2007), subgrid surface mass-balance and ice flow hypsometry parametrization of Le Morzadec et al. (2015), subshelf melt of Lazeroms et al. (2018), surface drainage solver of (Tarasov and W. Peltier, 2006), and viscoelastic solid earth (Tarasov and W. R. Peltier, 1997).

The coupled climate is an ensemble parameter controlled weighting of temperature and precipitation fields from two components: an EBM with 2D geography, non-linear snow and ice albedo feedbacks, and a slab ocean, and a glacial indexing of a set of empirical orthogonal functions (EOFs) extracted from the PMIP I, II, and III modelling results. These modelling projects used multiple ice sheet boundary conditions – ICE4G, ICE5G, ICE6G, Glac1D, and ANU. Of these, ICE4G did not have a major Keewatin Ice Dome. The glacial indexing (interpolation between present day and last glacial maximum conditions) of the EOFs relies both on the height of the simulated Keewatin ice dome from the ice dynamical model and the temperature of the North Atlantic from the EBM slab ocean model. The basal hydrology model is a linked-cavity drainage system coupled to an efficient drainage tunnel solver (Drew and Tarasov, 2022). A more detailed description of the GSM is forthcoming in Tarasov, Hank, and LeCavalier(in prep.).

5.2.2 *Sediment-Isostasy Coupling*

We incorporated changes in surface sediment load and bed rock erosion into the loading changes of the solid earth. The pre-glaciation to PD bed elevation changes are given by:

$$\text{bed}_{Plio} - \text{bed}_{PD} = \text{reg}_{Plio} - \text{reg}_{PD} - \text{Ero} + \text{IA}\left(\text{Ero}, \text{reg}_{Plio} - \text{reg}_{PD}\right) \tag{90}$$

where bed* are the bed elevations at Pliocene (pre-glaciation) and PD, reg* are the unconsolidated sediment (regolith) distributions, Ero is the total bed erosion from quarrying and abrasion over the Pleistocene, and IA is the long term isostatic adjustment due to all of these terms (neglecting shorter term ice and water distribution changes). This isostatic adjustment is calculated on the basis of load changes from the equilibrated (present day plus residual GIA) bed:

$$L_{\text{sed+eros}} = \left(\text{reg}_{PD} - \text{reg}_{Plio}\right) \frac{\rho_{sed}}{\rho_{ice}} - \text{Ero} \frac{\rho_{rock}}{\rho_{ice}} \tag{91}$$

In fig. 54 we add varying thicknesses of sediment to show the impact on elevation changes of the solid earth surface (not including sediment) due to isostatic adjustment.

5.2.3 *Basal Drag Coupling*

The basal velocity is from either a hard or soft bed sliding rule. For the hard bed the basal sliding rule is a fourth power Weertman sliding law (Cuffey and Paterson, 2010):

$$u_b^{hard} = \frac{c_{hard} f_{Neff} \left|\tau_b\right|^3 \tau_b}{N_{eff}} \tag{92}$$

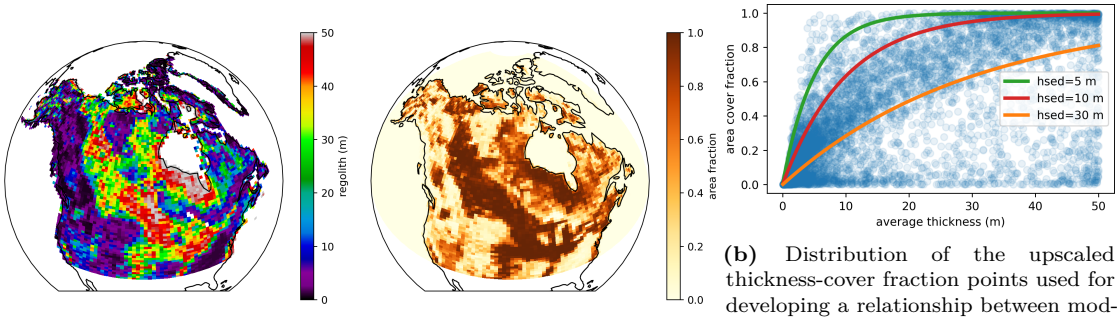

(a) Comparison of present day regolith thickness and area based sediment covered fraction from upscaling the regolith field of Pelletier et al. (2016).

(b) Distribution of the upscaled thickness-cover fraction points used for developing a relationship between modelled sediment thickness and soft bed fraction.

Figure 37

where c_{hard} is a parmeterized sliding coefficient which includes a parameterization for basal roughness, f_{Neff} is the effective pressure normalization factor, N_{eff} is the effective pressure given by the subglacial hydrology model, and τ_b is the basal drag. The basal velocity for soft bedded sliding is similarly a Weertman type sliding law with a parameterized power with integer values between one and seven.

$$u_b^{soft} = \frac{c_{soft} f_{Neff} |\tau_b|^4 \tau_b}{N_{eff}} \tag{93}$$

with separately parametrized soft sliding coefficient c_{soft} (which also includes a parameterization for basal roughness).

For a soft bed fraction greater than one half, the sliding rule is a soft bed rule. Otherwise it is hard. The soft bed fraction is calculated with a parameterized relationship with sediment thickness (h_{sed}). To develop this relationship the high resolution (1 km) sediment dataset of Pelletier et al. (2016) (shown in fig. 39 b)) was upscaled to the GSM North American $1.0 \times 0.5°$ latitude-longitude grid. The distribution of points in fig. 37b was used to derive a parameterized empirical relationship between sediment thickness and soft bed fraction to estimate the shielding factor, h_c:

$$f_{soft} = 1 - e^{h_{sed}/h_c} \tag{94}$$

This shielding factor is also used in the quarrying (eqn. 106), abrasion (eqn.), and englacial sediment mixing coefficient (eqn. 108) relationships.

5.2.4 *Sediment Model Verification Tests*

To verify that the model solves the physical equations in § 5.8.2 as intended, a series of model verification tests were performed. The verification strategy was three-fold: symmetric solution given symmetric boundary conditions, convergence to a continuous solution given increasing grid resolution, and conservation of mass. The test bed used for these model solutions was a square root ice sheet topography with coupled subglacial hydrology, sediment, and dynamically calculated basal sliding velocity (from the effective pressure solution of the subglacial hydrology and the driving stress from the square root ice surface).

5.2.5 *Sediment Transport Sensitivity for a Square Root Ice Sheet*

Symbol	Description	Distribution	Justification
K_{cond}	hydraulic conductivity of cavity network	$[1e-3]$	(Drew and Tarasov, 2022)
h_r	basal protrusion height	$[0.01, 20]m$	(Drew and Tarasov, 2022)
l_r	basal protrusion wavelength	$[10, 20]m$	(Drew and Tarasov, 2022)
T_{crit}	basal freeze point (PMP rel.)	$[-1, 0]$	Ansatz
$f_{N_{eff}}$	N_{eff} basal sliding term	$[1e4, 2.5e7]$	(Drew and Tarasov, 2022)
$HV^{\star}$	Vicker hardness bedrock	$[1.5e9, 7e9]$	(D. H. D. Hildes, 2001)
$\mu^{\star}$	Rock-rock friction coef.	$[0.3, 0.85, 10]$	(Byerlee, 1978)
$R^{\star}_{mean}$	Mean size of grain dist.	$[10^{-4}, 10^{-3}, 10^{-2}]m$	(Boulton, 1979; Haldorsen, 2008; Hubbard and Sharp, 1995)
$h^{\star}_f$	water film thickness	$[10^{-8}, 10^{-6}, 10^{-4}]m$	(Hubbard and Nienow, 1997; Hallet, 1979)
$C^{\star}_{quar}$	quarrying coefficient	$[10^{-11}, 10^{-10}, 10^{-9}]Pa^{-1}$	Ansatz, $\propto k_{abr}/HV^{star}$
$\zeta^{\star}_b$	basal roughness	$[0.01, 0.1, 1]$	$\propto$ size erratics (Krabbendam and Glasser, 2011), obstacle size (Weertman, 1957)
$n^{\star}_p$	quarrying law exponent	$[0.3, 0.5, 1]$	(Cuffey and Paterson, 2010)

$h^\star_{sed}$	shielding factor	$[2, 6, 20]m$	Ansatz
$\phi^\star$	internal friction angle basal sed.	$[20, 22, 24]^\circ$	(Jenson, P. U. Clark, et al., 1995)
$n^\star_s$	rheology exponent of basal sed.	$[1.25, 1.5, 1.75]$	(Jenson, P. U. Clark, et al., 1995)
$\mu^\star_0$	Newtownian reference viscosity basal sed.	$[0.1, 5, 100] \times 10^9 Pas$	(Jenson, P. U. Clark, et al., 1995)
$\phi^\star_p$	sediment porosity	$[0.3, 0.4, 0.5]$	Ansatz
$Z^\star_r$	thermal resistivity of englacial debris	$[0.23, 0.55, 1.1]mK/W$	(D. H. D. Hildes, 2001; Hallet, 1979)
$C^\star_{max}$	upper bound on sed concentration by vol	$[.85, 0.9, 0.95]$	Ansatz
$\tilde{D}^\star$	prefactor diffusion coefficient	$10^{[-11,-10,-9]}m^2/s$	(Alley and MacAyeal, 1994)
$\tilde{z}^\star$	scale factor for exponential coefficient in D	$[3, 5, 7]m$	heuristic
$C^\star_{crit}$	critical debris concentration	$[0.3, 0.4, 0.5]$	(D. H. D. Hildes, 2001)

Table 5: Parameters in the GSM sediment model. Those probed with the transport sensitivity analysis in § 5.2.5 are highlighted in green.

Sensitivity analysis of model behaviour based on uncertainty in the input parameters identifies those parameters which produce the most uncertainty in the model response phase space. Those producing the widest range in model response would most effectively reduce uncertainty in system behaviour if the parameter uncertainty were reduced. The process of identifying the most important parameters in this sense is called "factor prioritization" (Saltelli, Ratto, et al., 2008). Analyzing model sensitivity to parameter uncertainty also allows identifying those parameters which produce the least amount of variability and, due to a scarcity of computational resources, are not worth probing. The process of identifying those parameters which may be held constant when exploring model response in order to capture system behaviour is called "factor fixing" (Saltelli, Ratto, et al., 2008). In this section we aim to identify those parameters the coupled subglacial hydrology-sediment system which may be fixed and those which are the most important controls on sediment transport.

For most systems, conducting grid search for a 15-dimensional parameter space is unfeasible. Though it depends on model response surface rugosity, a grid search is likely not necessary and low discrepancy sampling methods have been demonstrated to capture phase space variability for some non-linear systems (e.g. see Saltelli (2002)). The most commonly applied sensitivity analyses are variance based methods.

We focus here on sediment transport sensitivity, the parameters controlling sediment production rates are known well enough a priori. Here we use both a variance and a distribution based method to capture model sensitivity and assess the relative importance of various parameters. These sensitivities are used for selecting ensemble parameters in the following sections and setting the rest to constant values.

Variance based sensitivity indices (S_i) of model response (y) sensitivity to model input (x_i) are built on conditional variances (Saltelli, Ratto, et al., 2008):

$$S_i = \frac{V_{x_i}\left(E_{x\ i}\left(y|x_i\right)\right)}{V(y)} \tag{95}$$

which Saltelli, Aleksankina, et al. (2019) describes as "the expected fractional reduction in the variance of y that would be achieved if factor x_i could be fixed. $S_i = 1$ implies that all of the variance of y is driven by x_i, and hence that fixing it also uniquely determines y."

Distribution based sensitivity indices are based on a measure of change in the model response distribution from fixing x_i – the difference between the unconditional probability distribution of of y and the distribution conditional on a given value of x_i. The Kolmogorov-Smirnov statistic is commonly used as a non-parametric measure of the discrepancy between two distributions which Pianosi and Wagener (2015) use to measure the conditional-unconditional difference:

$$S_i = \underset{x_i}{median}\left(KS\left(x_i\right)\right), \text{ where } KS\left(x_i\right) = \underset{y}{max}\left|F(y) - F\left(y|x_i\right)\right| \tag{96}$$

where $F(y)$ is the unconditional cumulative distribution function of the model response and $F\left(y|x_i\right)$ is the cumulative distribution function which is conditional on selecting $x = x_i$.

For both sensitivity metrics, the amount of sediment transported is most sensitive to the sediment viscosity (fig. 38). Following this the subglacial hydrology parameters are second most important. We therefore assign the subglacial hydrology parameters, sediment viscosity, and the shielding factor (h_c, ho in fig. 38 to which basal drag and erosion are sensitive) to the ensemble parameter set and assign constant median values to the remaining subglacial sediment model parameters.

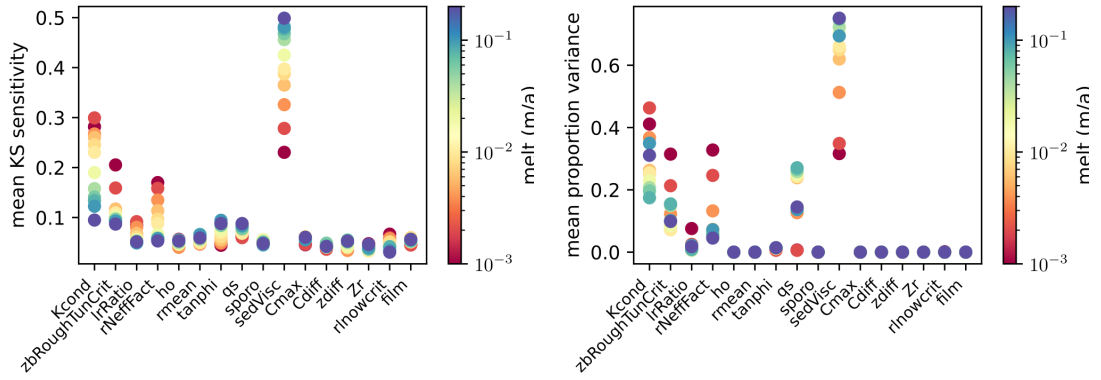

Figure 38: Sediment transport senstivity to parameters. Mean KS sensitivity is the metric of (Pianosi and Wagener, 2015), mean proportion variance is the metric of (Saltelli, Ratto, et al., 2008).

5.3 CONSTRAINTS

5.3.1 *Present Day Sediment Distribution*

To answer what constraint is offered by glaciological constraint and the present day distribution of unconsolidated sediment on pre-glacial sediment thickness, we must first have an estimate for the present day sediment thickness. As uncertain as the Pliocene unconsolidated sediment distribution is, even the present day sediment distribution has large uncertainty. The sediment distribution is most uncertain in Canada where data is sparse. In the United States, relatively dense population gives a wealth of well data whereas broad regions of Canada are sparsely populated. There are some exceptions to this. In Southern Ontario and Quebec, well data, geological surveys and high resolution DEMs give more reliable estimates. Some of the most important areas from a glaciation perspective (*e.g.* Northern Saskatchewan and Manitoba, North West Territories and Nunavut, Northern Quebec-Labrador) have no constraint beyond surficial geology mapping (Fulton, 1995) and digital elevation maps from remote sensing (Porter et al., 2018). As such the sediment thickness estimates in these regions are transform functions of those products. Some seismic data are available for reconstructing sediment thickness off shore.

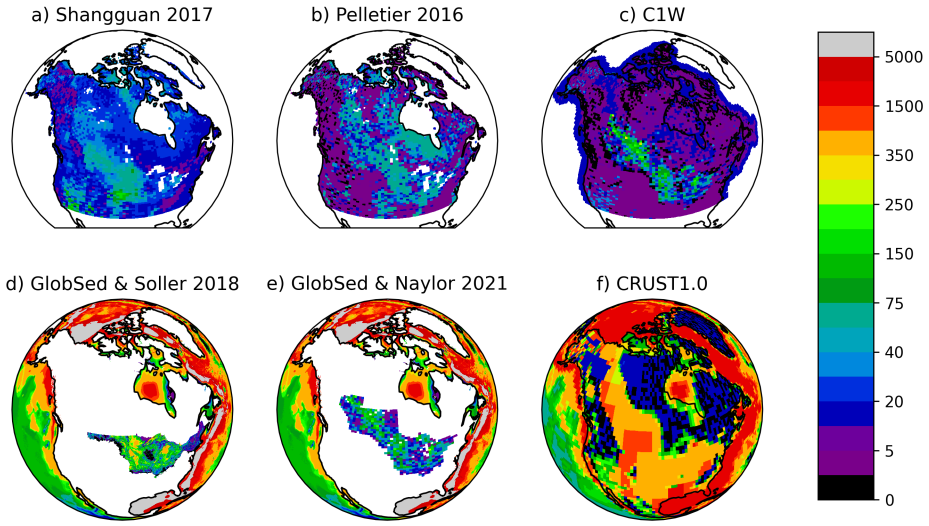

Figure 39: Comparison of various present day unconsolidated surface sediment thicknesses. a) dataset of Shangguan et al. (2017) produced with machine learning methods, b) dataset of Pelletier et al. (2016) produced with empirical relationships from soil profiles and water wells, c) dataset of Taylor (2023) which incorporates many data sources, d) dataset Soller and Garrity (2018) for the onshore and Straume et al. (2019) for the offshore, e) dataset of (Naylor et al., 2021) for the onshore and Straume et al. (2019) for the offshore, and f) dataset of Laske et al. (2013). The three datasets (Pelletier et al., 2016; Shangguan et al., 2017; Taylor, 2023) with the best terrestrial coverage were selected for constraining model results,

However seismic data collection in areas with sea ice cover is difficult and data in the Arctic are sparse (Stashin, 2021).

Soller and Garrity (2018) produced a composite map of sediment thickness and bedrock elevation for the glaciated regions of the Northern United States to the East of the Rocky Mountains from many smaller scale regional maps (in fig. 39 d). Naylor et al. (2021) constructed a bedrock elevation map in order to assess present day sediment thickness and bedrock erosion during the Pleistocene. This product synthesized regional maps from many states and provinces in the United States and Canada, subsequently validating the final result against available well data.

The sediment distribution by the Canada1Water initiative brought together maps by Soller and Garrity (2018), Parent et al. (2021), Russell et al. (2017), and Smith and Lesk-Winfield (2010). Areas outside these maps were assigned

Ref.	Region	Source Data
(Taylor, 2023)	Glaciated N. Am.	Geol
(Soller and Garrity, 2018)	Glaciated US East of Rockies	Mult. USGS Databases
(Pelletier et al., 2016)	Global Terrestrial	Wells, Machine Learning
(Shangguan et al., 2017)	Global Terrestrial	Wells, Machine Learning
(Straume et al., 2019)	Global Marine	Seismic & Borehole
(Laske et al., 2013)	Global Terrestrial & Marine	Seismic

Table 6: A summary of datasets available, their geographical coverage, and data sources.

thicknesses based on surficial geologic units from "Surficial geology of Canada" (2014), Karlstrom (1964), and GIS Team National Park Service (1999) with assumed thicknesses for various geologic units in as laid out in table 7.

The offshore areas of Laske et al. (2013) and Straume et al. (2019) are remarkably similar. Indeed, both datasets use seismic methods to estimate the depth of unconsolidated sediment on the oceans seafloors and provide excellent coverage. The issues with using these data to constrain modelled sediment fields are two fold: it is unclear what proportion of those depths are Quaternary aged sediment and it is unclear whether the reported layers which are based on seismic p-wave thresholds correspond to unconsolidated sediment or other units.

Onshore, there is broad agreement on thick sediment coverage in the southern prairies and north-central US and thin sediment over the Rockies. Interestingly, only (Pelletier et al., 2016) gives thick sediment cover of the Hudson Bay Lowlands (south of Hudson Bay). In the Canadian Arctic Archipelago, (Shangguan et al., 2017) and (Pelletier et al., 2016) both show thick sediment over Banks and Victoria Island and moderate sediment over Baffin while (Taylor, 2023) shows thin sediment over the region north of the Arctic Circle as a whole. In terms of total sediment volume, the three reconstructions vary by more than 100% between the most and least capacious: Pelletier et al. (2016) gives 310000 km^3, Shangguan et al. (2017) gives 460000 km^3, and Taylor (2023) gives 200000 km^3.

Though nearly forty years old, the estimate of Quaternary aged material deposited in the oceans around the domain of the Laurentide ice sheet by M. Bell and Laine (1985) is still the most comprehensive to date. They detail estimates for the Gulf of Mexico, the west Atlantic, and the Canadian Arctic on the basis of drilling and seismic surveys. Due to the harsh and sensitive environment of the Arctic both drilling and seismic are difficult even today. As such their calculation of Quaternary material for this region has large uncertainties and they state they cannot provide a reliable calculation for this region. M. Bell and Laine (1985)

state that the West Atlantic has excellent seismic coverage and, referring to several studies therein, estimate 1.2×10^6 km^3 of Laurentide sourced Quaternary aged sediment in this region. From multiple data sources M. Bell and Laine (1985) calculate 7.4×10^5 km^3 of Quaternary sediment in the Gulf of Mexico. Hay, Shaw, and Wold (1989) rejected the M. Bell and Laine (1985) estimate of Laurentide sourced sediment due to a disagreement on the proportion of Mississippi transported sediment of non-glacial origin. Whereas M. Bell and Laine (1985) estimate this rate on the basis of the Miocene accumulation rate in the Gulf, Hay, Shaw, and Wold (1989) point out that the present day sediment load of the Mississippi river is brought by the Missouri River from the Rockies, not the Laurentide region. Furthermore, because there is no fluvial transport in our model, relating the glacial sediment estimate from (M. Bell and Laine, 1985) to material glacially transported to the southern margin in our simulations is non-trivial. Because of the above uncertainties, we focus on comparing our model results against the Atlantic region estimate.

5.3.2 *Erosion Estimates*

Naylor et al. (2021) estimate 71 metres of bedrock erosion from all sources since the Pliocene in an area encompassing Southern Ontario, Northern US and parts of the Canadian prairies. Ehlers et al. (2006) use apatite (U-Th)/He to estimate hundreds to thousands of metres of bedrock erosion over the Pleistocene. Gulick et al. (2015) use seismic interpretation to reconstruct Pliocene to Pleistocene offshore sedimentation rates. They infer an increase in erosion across the Plio-Pleistocene Transition (PPT) and again during the mid-Pleistocene Transition (MPT). It is not easy to identify the catchment from which these sediments came and so inferring a catchment wide erosion rate is difficult. Though the unstated uncertainties are likely large, the Naylor et al. (2021) erosion estimate is the most useful constraint

for modelling North American glacial erosion over the Pleistocene at a continental scale. The bounds on Cordilleran erosion are wide and likely impose less of a constraint on the processes in such a model, meanwhile it is not clear what the precise source region is for the sediment record interpreted by Gulick et al. (2015).

5.4 UNCERTAINTY IN CO_2 FORCING

Proxy data for atmospheric CO_2 concentration prior to coverage by the ice core record (PD-800 ka, Bereiter et al. (2015)) are sparse with wide uncertainty bounds (Hönisch, 2021). Carbon dioxide is well mixed in the atmosphere and the gas is exchanged quickly on paleo timescales at the sea surface. As such that sea surface carbonate chemistry is sensitive to changes in mean atmospheric CO_2. The ^{11}B isotope proxy is sensitive to changes in pH and as such is used as a proxy for atmospheric carbon dioxide (Hönisch et al., 2009). The benefits of this record are its temporal range, estimates are available back to 2.1 Ma. However, the temporal coverage is sparse and not orbitally well-resolved (Dyez, Hönisch, and Schmidt, 2018, e.g.). As such boron isotope records are not sufficient for developing a CO_2 forcing. Other proxies have poorer coverage and larger uncertainties (Willeit et al., 2015; Hönisch, 2021).

The benthic $\delta^{18}O$ climate proxy record has excellent temporal coverage over the Plio-Pleistocene and is sensitive to changes in global temperature, of which CO_2 forms a part of the signal. We adopt the approach of deriving a CO_2 forcing based on this $\delta^{18}O$-temperature-CO_2 relationship with the boron isotope record as a validation dataset. As a start point we develop an empirical $\delta^{18}O$-CO_2 relationship through regression of the European Project for Ice Coring in Antarctica (EPICA) ice core (Bereiter et al., 2015) and ProbStack (Ahn et al., 2017) records. We use the pymc3 python package for probabilistic programming (Salvatier, Wiecki, and Fonnesbeck, 2016) to develop a generalized linear model through Hamiltonian

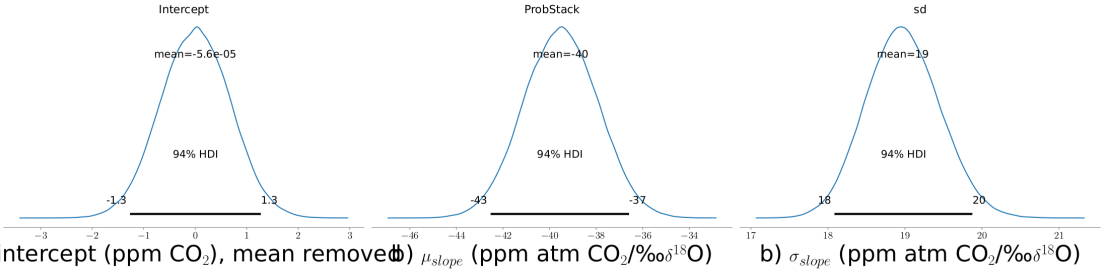

Figure 40: Distribution of the intercept, mean slope, and standard deviation of the slope of a linear fit between ProbStack (Ahn et al., 2017) and EPICA (Bereiter et al., 2015).

Monte Carlo sampling (specifically No U-Turns Sampler) and obtain distributions for the linear regression coefficients. First the mean was subtracted from both datasets, then the sampler was run on 16 chains with 2000 draws. This yielded distributions for intercept ($\approx$ 0, left panel fig. 40), mean slope estimate ($\approx$ 40 ppm/‰, centre panel fig. 40), and standard deviation of the slope estimate ($\approx$ 19 ppm/‰, right panel fig. 40). A comparison of the underlying data and the final chosen linear relationship along with a comparison of the output time series and the boron isotope record from data in (Dyez, Hönisch, and Schmidt, 2018) can be seen in fig. 41. The relationship between oxygen isotopes and carbon dioxide is assumed to change sometime around the MPT and so the slope and intercept coefficients are linearly changed to those of the expected EPICA-ProbStack linear regression over 1300 to 900 ka. This linear fit persists until EPICA coverage begins at 798 ka. The carbon dioxide time series from the oxygen isotope regression were merged with the carbon dioxide measurements from the EPICA record using a linear weighting over 750 to 798 ka. We test multiple CO_2 forcings on the basis of this distribution, finding that a $CO_2/\delta^{18}O$ slope four standard deviations away from the expected slope and a mean CO_2 of 266 ppm versus the mean EPICA CO_2 of 236 ppm were necessary to attain a target sea level amplitude similar to that of Elderfield et al. (2012) and Rohling et al. (2014). This significant departure (four standard deviations) from the expected regression values of EPICA vs ProbStack is in line with the findings of Dyez, Hönisch, and Schmidt (2018) who found that the

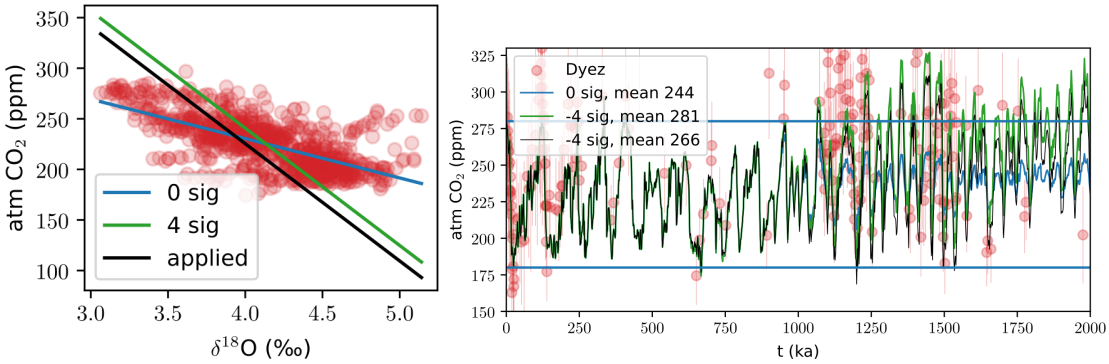

Figure 41: Scatterplot and time series showing the fit of the extracted relationships. Various σ (sig in plot legend) based on HMC results in fig. 40.

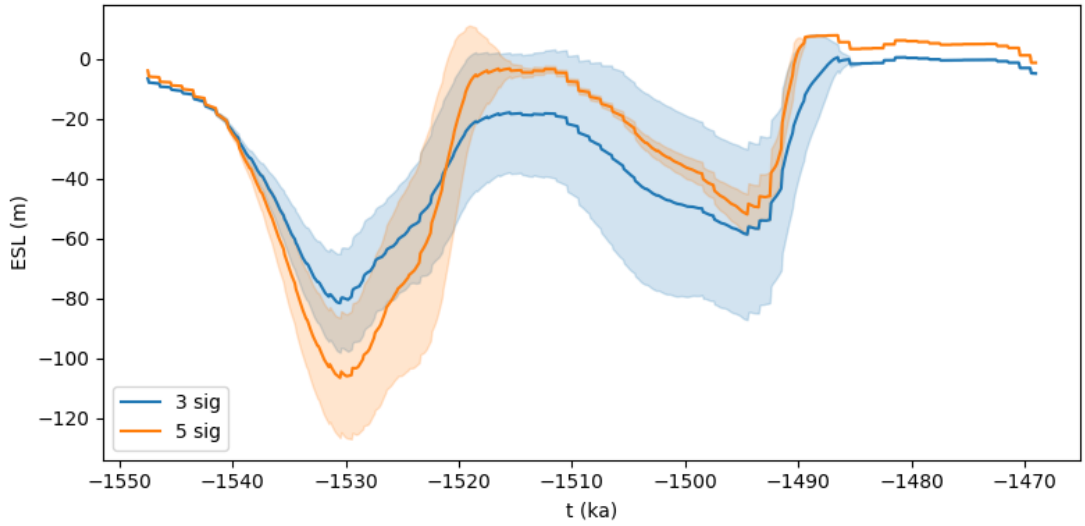

Figure 42: Resulting ensemble mean sea level curves (with one standard deviation shading) for 35 parameter vectors run for CO_2 from ProbStack using a slope three σ and five σ away from the expected value from the distribution shown in fig. 41.

ice volume-carbon dioxide relationship as approximated by the boron and oxygen isotope records changed significantly across the MPT.

5.5 METHODOLOGY

The GSM was run for both the North American Ice Complex (the primary target for our sedimentary study) and the Eurasian Ice Complex (to incorporate a stronger obliquity response). To obtain a set of parameter vectors which reproduce a realistic North American Ice Complex, the model was tuned through several iterations of

Latin hypercube sampling for GSM ensemble parameters, omitting the subglacial hydrology and sediment model components. These sample distributions were then sieved (all runs which lie outside the range for each constraint metric were removed) by bounds on inferred last glacial maximum (LGM) sea level (Spratt and Lisiecki, 2016), deglacial margin chronology (Dyke, 2004), Early Pleistocene sea level amplitude (Rohling et al., 2014; Elderfield et al., 2012), and Early Pleistocene extent (Roy et al., 2004; Balco and Rovey, 2010). These sieved distributions were then fit with a beta distribution and re-sampled with a Latin hypercube for 2 more iterations. This gave a set of basis vectors for the ice dynamic and climate parameters which were then combined with samples for the subglacial hydrology model and re-sieved. This basis vector selection, sampling and combination was done again with the sediment model.

Simulations with the sieved ensemble parameter vectors were then run for the full Pleistocene (2.58 Myr) from several uniform starting sediment distributions of 10, 20, 40, and 60 m thickness over both the North American and Eurasian model domains.

5.6 RESULTS

Here we compare model results with the present day sediment distribution reconstructions by Taylor (2023), Shangguan et al. (2017), and Pelletier et al. (2016). Each data set was interpolated to the GSM model grid for comparison against model results. The data of Pelletier et al. (2016) were extrapolated over missing data in lakes and ocean areas then upscaled. Prior to comparison, all three data sets were masked to the same coverage as Shangguan et al. (2017) (no coverage over ocean areas, great lakes and major lakes in the Canadian Prairies). The max and min across the three data sets for each cell was extracted and used as the bounds for misfit scoring. Modelled thicknesses which lie within these maximum

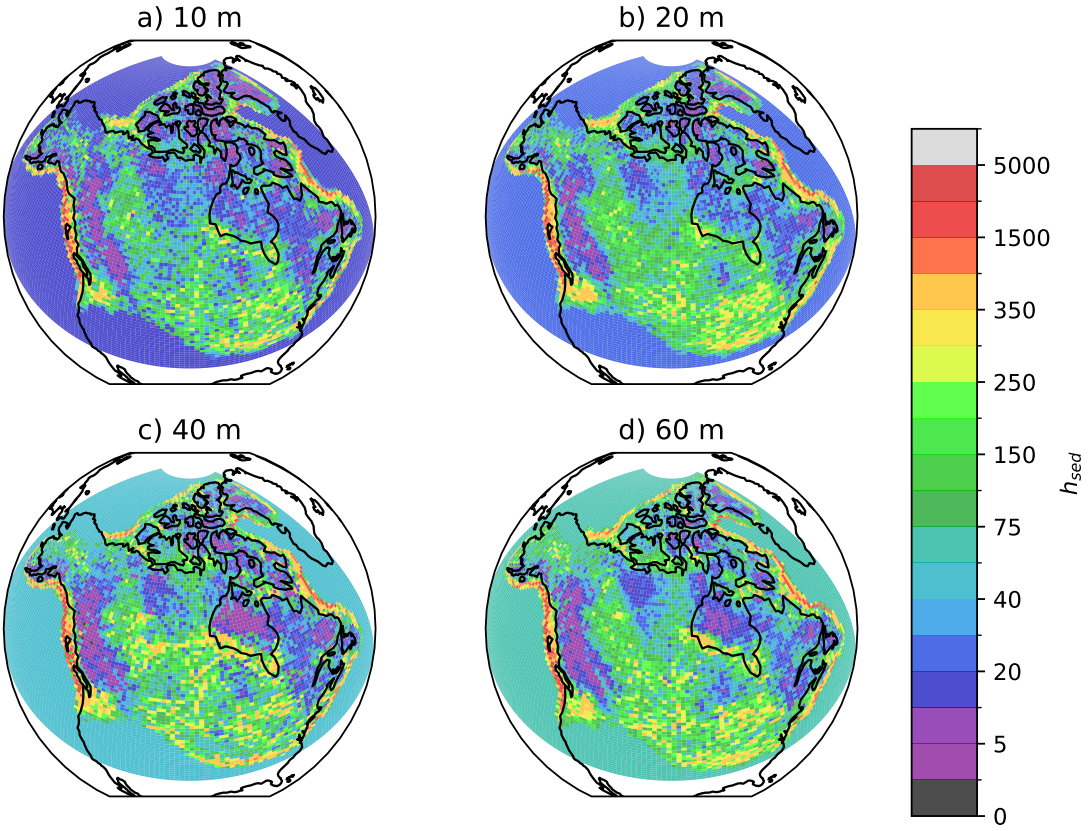

Figure 43: Mean ending sediment distribution by starting sediment thickness

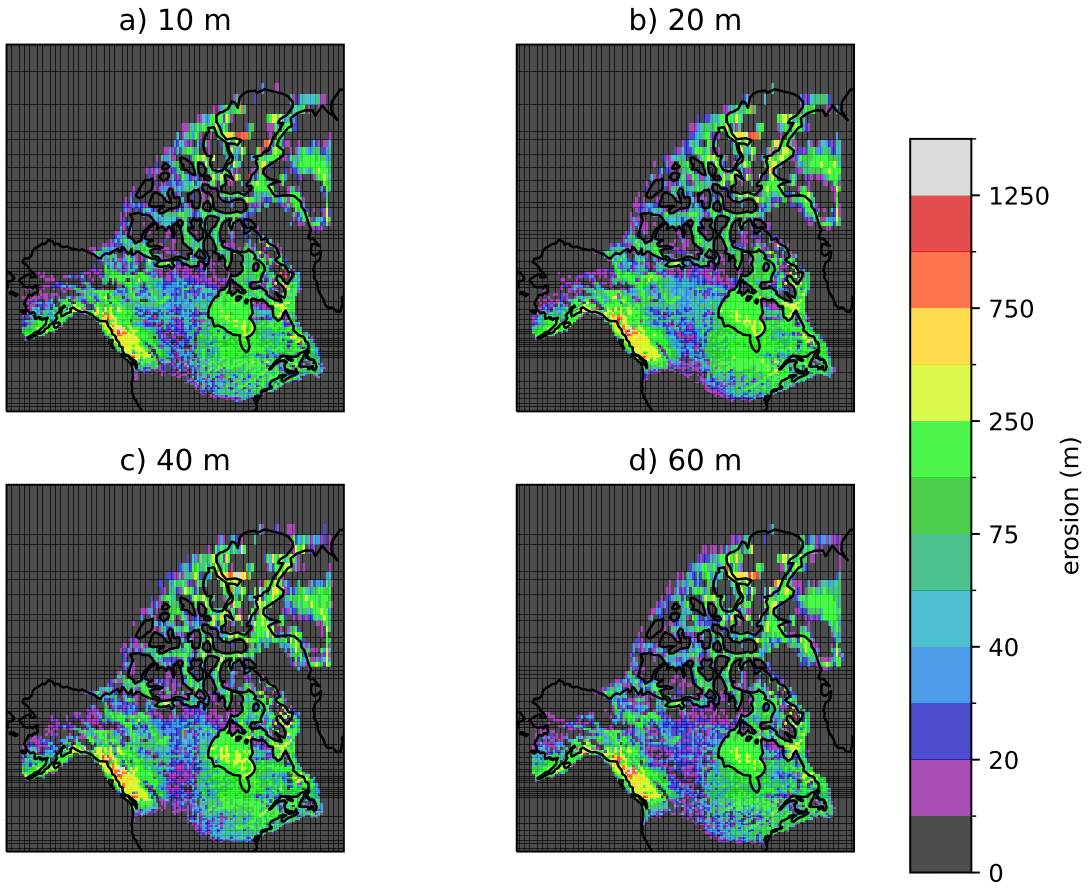

Figure 44: Total glacial sediment production, mean across all parameter vectors for different starting sediment thicknesses

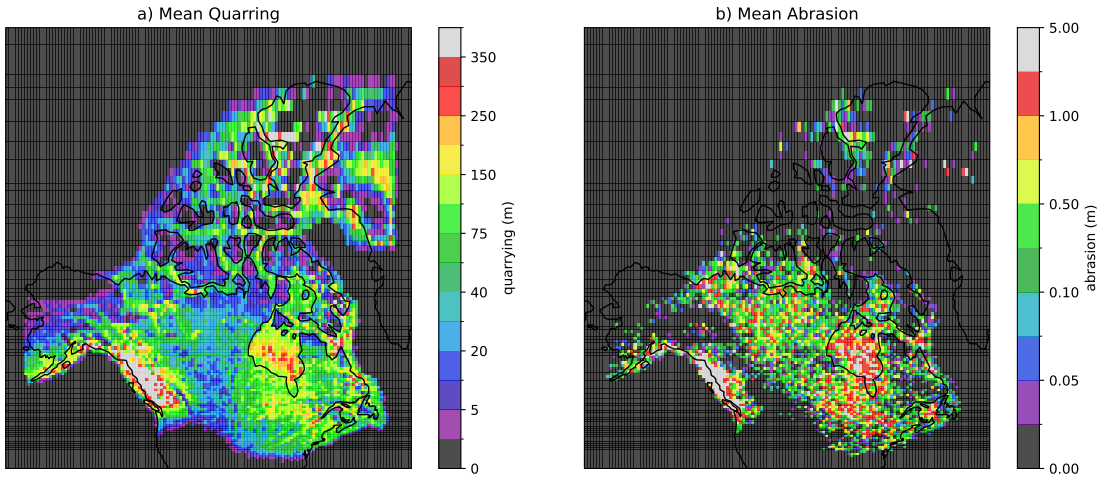

Figure 45: Mean depth of bedrock weathered due to a) quarrying and b) abrasion. Note the colours are differently scaled to highlight the spatial differences.

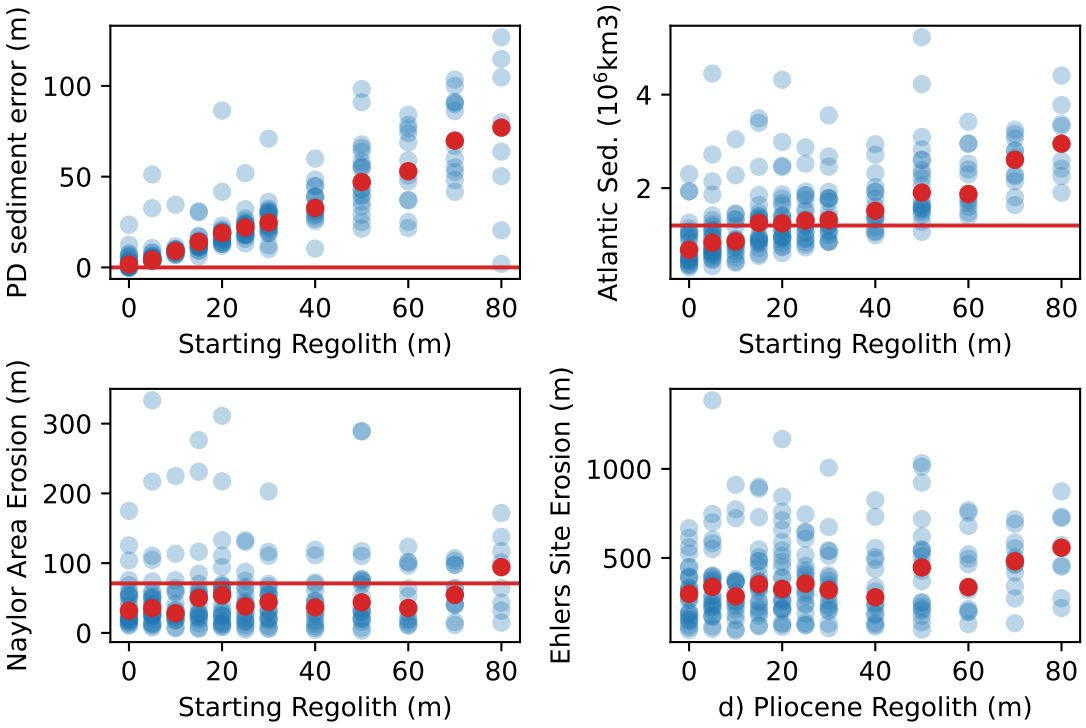

Figure 46: Misfit scores against present day sediment distribution estimates for varying levels of starting sediment thickness. The red dots indicate median for each sediment distribution. In panel b) the M. Bell and Laine (1985) estimate for total Quaternary sediment deposited from North America into the Atlantic is shown by a horizontal red line. In panel c) the Naylor et al. (2021) estimate for mean bedrock erosion depth (71 m) in their study area is shown by a horizontal red line.

and minimum bounds were assigned zero misfit, outside this range the difference with the closest bound was used. Below we examine the mean L1 norm misfit with respect to these bounds.

Fig. 46 shows that the match between simulated and observed present day sediment distribution depends on both the amount of starting sediment. Our results indicate that Pliocene regolith thicknesses were likely less than 60 m. The median estimate for the 20 m ensemble in fig. 46 b) agrees remarkably well with amount of sediment transported to the North American Atlantic sector estimated by M. Bell and Laine (1985). However this estimate carries large and unquantified uncertainty and both the 10 m and 40 m ensemble median values likely lie well within its bounds. The ensemble median Naylor et al. (2021) study area sediment production values shown in panel c)are closest to the inferred value at 20 m Pliocene

regolith thickness. However, there is no strong trend in sediment production for this region with respect to initial regolith thickness and sediment production is largely independent of initial regolith thickness in this area. Furthermore, Naylor et al. (2021) did not assess the uncertainty in their mean ≈ 70 m of eroded bedrock estimate, limiting its interpretability. The most likely 20 m thickness which can be concluded from panels b) and c) departs from the results in panel a) where the thinnest 10 m regolith scores the lowest misfit. This may be because the present day sediment datasets fail to capture the full thickness of the largest terrestrial deposits, e.g. Pelletier et al. (2016) has a 50 m cut off in their dataset. For the 20 m and greater thicknesses all of panels a, b, and c show the same trend in increasing misfit with observation. Ehlers et al. (2006) inferred large erosion bounds in their study area of 100's to 1000's m. The wide distribution within each ensemble also shows this. Whereas the wide bounds on erosion depth inferred by Ehlers et al. (2006) is the result of both methodological uncertainty from thermochronometry and likely wide range in basal thermal regime in rough terrain, the distribution in each ensemble is due to parametric uncertainty.

5.7 DISCUSSION

For those runs where erosion rates agree with the Naylor et al. (2021) bounds, the sediment areal coverage over North America does not decrease much or in some cases actually increases. There are four potential reasons for this: 1. the sediment transport parameters should be tuned for a more transportive ice sheet, 2. the unstated uncertainties in bedrock erosion estimates of (Naylor et al., 2021) are large and lower values may be correct, 3. the missing fluvial, glaciofluvial, and hillslope processes may be more important than assumed, and 4. there was little regolith cover in the Pliocene. The main sediment transport parameter is the sediment viscosity in the soft sediment deformation rheology relationship eq. 110.

While this parameter is largely unconstrained, decreasing the sediment viscosity results in peak sediment velocities which depart from observed sliding velocities in contemporary ice sheets. The uncertainties in the present day bedrock surface depth map of Naylor et al. (2021) are not stated and are likely far less than their Pliocene surface geomorphological reconstruction, the two inputs to their bedrock erosion estimate. It is difficult to assess how large these uncertainties are without an intimate understanding of the inputs and workflow. A detailed uncertainty assessment of these reconstructions would strongly facilitate interpretation and usability.

The fluvial role in North American sediment coverage following 2.58 Myr of Pleistocene glaciation remains to be quantified. Koppes and Montgomery (2009) point out that where sediment is mobilized by recent disturbance, a condition which a recent deglaciation likely satisfies, fluvial transport can increase "dramatically." Furthermore, the large amount of water availability during deglaciation and glacial lake drainage events may also increase this effect. Future work to encapsulate sediment transport due to glacial lake drainage events, glaciofluvial transport, and interglacial fluvial and hill slope transport in a model similar to that presented here would help assess to what degree those processes can increase the amount of sediment transported during the Pleistocene. During interglacials chemical weathering could weaken bedrock and produce more quantities of regolith throughout the Pleistocene requiring even greater transport. Of course it is also possible that there was not enough Pliocene regolith to require an increased transport capacity to match the present day observation. If the change in North American hard bedded area across the Pleistocene was not significant, this would refute the regolith hypothesis for the mid-Pleistocene Transition.

Our understanding of the change in sediment coverage over the Pleistocene can be made more confident by quantifying the amount of Pleistocene aged sediment in significant depositional basins. Large scale geomorphological interpretation of

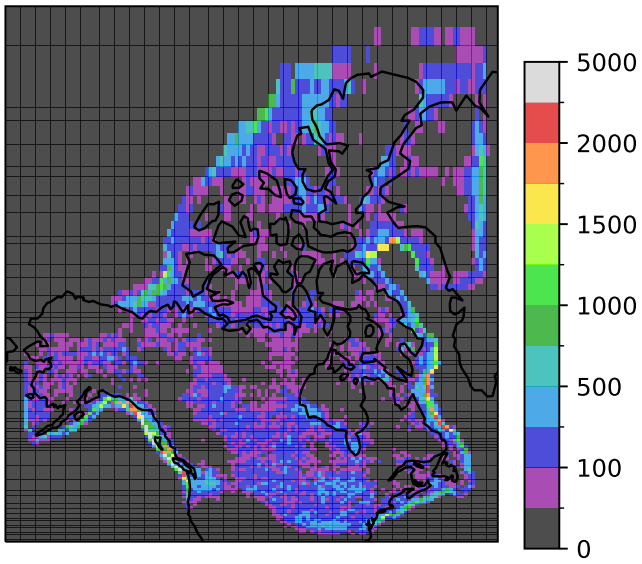

Figure 47: Mean ending sediment distribution across all parameter vectors and initial sediment thicknesses.

large terrestrial deposits could help distinguish between the roles of glacial versus (glacio)fluvial transport. Notable terrestrial depositional basins for glacial sediment simulated by the model are: the area at the southern end of the glaciated Rocky and Coastal Mountains, southern margin tills in north-central USA, Western Canadian Sedimentary Basin, and the Hudson Bay Lowlands. Pelletier et al. (2016) shows a thick sediment package in the Hudson Bay Lowlands whereas Taylor (2023) and (Shangguan et al., 2017) do not.

In this model, most of the sediment is transported to marine areas (see fig. 47) An exploration program (or re-analysis of past programs) over a few offshore basins would provide good constraint to the Quaternary sediment budget. Perhaps the most significant and accessible location for sediment budget constraint is the Saglek Basin area at the mouth of Hudson Strait. The Saglek basin is distal from large present day fluvial systems and its Pleistocene sediment volume is probably dominated by ice stream transport. This area has been of interest for oil & gas exploration in the past and there are several wells and 2D seismic lines in the area (Jauer and Budkewitsch, 2010). This basin would also be the deltaic depocenter for the hypothesized Bell River which is supposed to have carried sediment from

large parts of North America across a terrestrial Hudson Bay prior to glaciation. This far-flung dispersion is support by recent detrital zircon work showing some of the pre-glacial sediment in the Saglek basin came from the Colorado Plateau (Sears and Beranek, 2022). Similarly, the Laurentian Channel and Scotian shelf have been targeted for exploration with existing data coverage. Additional areas include the north end of Baffin Bay and Canada Basin – though exploration in Canada Basin in particular has proved particularly difficult (Stashin, 2021).

Total glacial sediment production is largely insensitive to the amount of starting sediment tested here (fig. 44, 55). Differences do emerge when examining median sediment production amounts as in fig. 46. Fig. 46 shows good agreement between the median value of Atlantic marine sediment in the model and the estimate of M. Bell and Laine (1985) at 20 m initial sediment thickness. 20 and 40 m appear closest to the erosion estimate of Naylor et al. (2021). The Ehlers site erosion results are all in range of the wide bounds by Ehlers et al. (2006). The simulations with less starting sediment score better against the present day distribution of sediment. Additional estimates on the spatial distribution of Pleistocene erosion depth at a catchment scale in more northern areas (e.g. Nunavut) would provide good constraint for the Pleistocene sediment budget and help improve understanding of glacial erosion processes. For example, estimates of erosion from terrestrial cosmogenic nuclide concentrations in till can be used to estimate mean catchment erosion rates at a scale comparable to ice sheet modelling (Staiger et al., 2006).

Due to the parameterization of quarrying and abrasion in the sediment model, it is difficult to use these results to quantify the relative contribution of those processes to historical rates of erosion. The spatial differences, however, do lend themselves to comparison. Abrasion rates diminish over the CAA and are mostly restricted to continental portions of the North American Ice Complex (NAIC) domain, with the highest values over the Cordillera, Hudson Bay, and Ontario. Modelled high abrasion rates also appear to correlate visually with areas of densely

mapped eskers suggesting a common underlying control (Storrar, Stokes, and Evans, 2013). Quarrying is also strongest over the Cordillera, and Hudson bay, but is active at all latitudes. It is also elevated in areas of ice streaming. Quarrying rates are high in the channels dividing the CAA, for example in the vicinity of Amundsen Gulf and McKenzie Corridor, McClintock Channel, Massey Sound, Nansen Sound, Nares Strait, Lancaster Sound, Cumberland Sound, Frobisher Bay, Hudson Strait, the Labrador Marginal Trough, and Gulf of St Lawrence (Margold, Stokes, and C. D. Clark, 2015).

Based on the discussion above, we would single out two desired model inputs to make the basal processes representations more realistic. Rougher terrains will have more bedrock rising above the unconsolidated sediment fill – the hard bedded area calculation should account not only for the mean thickness of sediment but for topographic roughness as well. High resolution (2 m) digital elevation models (DEMs) are available which would allow roughness calculations at the relevant several metre scales (Porter et al., 2018). This would also allow incorporating basal roughness in the sediment and subglacial hydrology models as a field from DEMs than a spatially uniform parameter. It is not clear, however, what measure of basal roughness (e.g. standard deviation, slope, power spectra, etc.) would be most applicable. Bedrock erodability likely varies spatially as well, whereas in the model it is currently treated as a uniform uncertainty parameter. Quarrying has been shown to be controlled by jointing/fracture spacing (Hooyer, Cohen, and Iverson, 2012) and abrasion by rock hardness (Engelder and Scholz, 1976). Incorporating maps of erodability in the respective modes based off lithology and other attributes would be a major improvement.

Taken as a whole, the sedimentological constraints of M. Bell and Laine (1985), Naylor et al. (2021), and Ehlers et al. (2006) on our modelling results suggest that Pliocene regolith thickness was around 20 m. Comparison of our modelling results

with estimates of the present distribution of sediment suggests erosion rates lower than those estimated by (Naylor et al., 2021).

The spatial patterns of sediment production from a Hallet (1979) model of abrasion are significantly different and far more geographically limited than those of Iverson (1991) style quarrying.

5.8 APPENDIX

5.8.1 *Present Day Sediment Estimates*

Unit	Description	Thickness (m)
I	Glacier ice	not used
O	Organic > 2 m	3
E	Eolian	3
Cv	Colluvial veneer	1
C	Colluvial seds, undif	4
A	Alluvial seds, undif	4
Ln	Lacustrine (littoral, nearshore)*below modern lakes	5
Lo	Lacustrine (offshore)*below modern lakes	10
Mn	Marine (littoral, nearshore)*below modern seas	5
Mo	Marine (offshore)*below modern seas	10
GMn	Glaciomarine and marine (littoral, nearshore)	5
GMv	Glaciomarine and marine (veneer)	1
GMo	Glaciomarine and marine (offshore)	10
GLn	Glaciolacustrine and lacustrine (littoral, nearshore)	5
GLo	Glaciolacustrine and lacustrine (offshore)	10
GFp	Glaciofluvial seds (outwash plain)	10
GFc	Glaciofluvial seds (ice-contact)	25
Tv	Glacial seds (till veneer)	1
Tb	Glacial seds (till blanket)	7
Th	Glacial seds (hummocky till)	10
Tm	Glacial seds (moraine complex)	35
Wv	Weathered bedrock (regolith veneer)	1
W	Weathered bedrock (regolith, undiff)	3
V	Bedrock (Quaternary volcanic rocks and deposits)	0
R	Bedrock, undiff (> 75% outcrop)	0

Table 7: Assumed sediment thicknesses by surficial geologic unit used by Taylor (2023) for reconstructing the present day sediment thickness over North America were direct observations were lacking (outside the study areas of Soller and Garrity (2018), Parent et al. (2021), Russell et al. (2017), and Smith and Lesk-Winfield (2010)).

5.8.2 *Description*

Abrasion

$$\dot{A} = \exp\left(-h_{sed}/\tilde{h}^{\star}_{sed}\right)\frac{k_{abr}}{HV^{\star}}\sum_{R} C_b\left(R\right)F_N\left(R\right)\left|v_{par}\left(R\right)\right| \tag{97}$$

$$C^{\star}_{abr} = k_{abr} / HV. \tag{98}$$

$$C_b(R) = \frac{C^1_{eng} \exp\Big\{ - \left(\log_{10}(R) - \log_{10}(\mathrm{E}[R])\right)^2 / (2 \log_{10} \mathrm{Var}[R]) \Big\}}{\pi R^2 \sum \exp\Big\{ - \left(\log_{10}(R) - \log_{10}(\mathrm{E}[R])\right)^2 / (2 \log_{10} \mathrm{Var}[R]) \Big\}} \tag{99}$$

$$F_N = A_e P_e \tag{100}$$

$$v_{par}(R) = |v_s| - 2B^{\star}_g R \left(\frac{\mu^{\star} P_e A_e}{A_r} \right)^3 - \frac{P_m P_e A_e}{2 L_{fus} \rho_i A_r R} \tag{101}$$

$$F_N(R) = f^N_{bed} \frac{4 \pi \eta R^3}{\tilde{R}^2 + R^2} v_n \tag{102}$$

$$v_{par} = |v_s| \left(1 - \frac{\mu^{\star} f^N_{bed} \sin\theta}{f^T_{bed}} \right) - \frac{\mu^{\star} f^N_{bed}}{f^T_{bed}} \dot{b}_{melt} \tag{103}$$

Quarrying

$$P_s = P_{ice} - \frac{\tau_b}{\pi \zeta^{\star}} \tag{104}$$

$$\dot{Q} = \exp\!\left(-h_{sed} / \tilde{h}^{\star}_{sed}\right) C^{\star}_{quar} \left(\frac{P_w - P_s}{\tilde{P}_r} \right)^{n^{\star}_p} \tag{105}$$

Englacial

$$\frac{\partial C}{\partial t} = -\nabla \cdot C \vec{v}_i - \frac{\partial (C \dot{V}_{net})}{\partial z} + V_{mix} \tag{106}$$

$$V_{mix} = \frac{\partial}{\partial z} \left(D \frac{\partial C}{\partial z} \right) \tag{107}$$

$$D = \tilde{D}^{\star} \left(\frac{|v_s|}{\tilde{v}_s} \right) e^{-z / \tilde{z}^{\star}} e^{-h_{sed} / \tilde{h}^{\star}} \tag{108}$$

Subglacial

$$\frac{\partial h_{sed}}{\partial t} = -\nabla \cdot \vec{Q}_s + \dot{E} - V_{net} \tag{109}$$

$$v_i = \frac{\left[\tau_{iz} - (c + N_{eff} \tan\phi^{\star} + \Delta \rho g z \tan\phi^{\star}) \right]^{n_s + 1} / (n_s + 1)}{\left[(2 D_0)^{\frac{n_s - 1}{n_s}} \mu_0 \right]^{n_s} \Delta \rho g \tan\phi^{\star}} + \gamma_1 \tag{110}$$

5.8.3 *Model Verification*

We verify the model in three ways: symmetry of solutions, convergence under increasing resolution, and mass conservation. All model solutions were found to be symmetric. The temporal convergence tests are in § 5.8.3, spatial in § 5.8.3, number of bed dips in the abrasion calculation in § 5.8.3, number of grain sizes in the abrasion calculation in § 5.8.3, and number of vertical levels in the englacial transport grid in § 5.8.3. Mass conservation test is in § 5.8.3.

Temporal convergence test

As a test of convergence under increasing temporal resolution (decreasing time step length) the sediment model was run to steady state under SHMIP scenario A (constant 2.5 mm/a de Fleurian et al., 2018), a sinusoidal melt forcing with constant sliding velocity, and sinusoidal melt forcing with coupled basal velocity. The convergence is shown in fig. 48. Under this scenario quarrying never switched on owing to the low driving stress of the setup, but the quarrying rate is numerically similar to (and simpler than) abrasion. Convergence is shown for the effective pressure N_{eff}, abrasion rate $\dot{E}_{abr}$, subglacial sediment thickness h_{subgl}, and englacial sediment thickness h_{engl}. The effective pressure solution converged most quickly followed by abrasion rate, and lastly the subglacial and englacial convergence were about the same (englacial not captured for highest time step).

Spatial convergence test

Here we show the effect of varying spatial resolution on the model solution. The models are run to steady state with prescribed melt and basal velocity (1.75 m/a ice and 2.0 m/a respectively) in the SHMIP setup (de Fleurian et al., 2018). The square root ice sheet flowline length from divide to toe is 100 km and the number of cells varied between 2,45. The model solution at each resolution is linearly

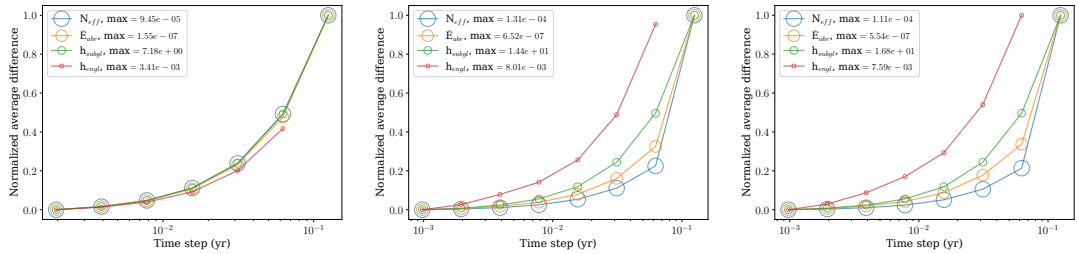

(a) Steady state, constant melt, 2.5 mm/yr

(b) Sinusoidal melt, 50 year period, 0 to 2.5 mm/yr

(c) Same as 48b plus basal sliding feedback and 0 to 3.5 mm/yr

Figure 48: Convergence with decreasing time step. Each metric is normalized such that the scale is consistent across metrics. The normalization factor shown in the legend (max).

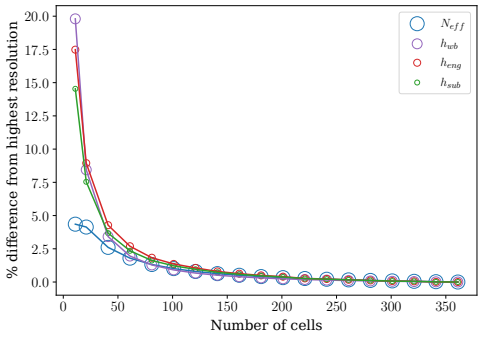

Figure 49: Difference in mean flowline solutions for unsteady SHMIP square root ice sheet topography as a function of increasing spatial resolution, at the end of 10 kyr run.

interpolated to the highest resolution grid and the absolute sum of the difference against the highest resolution solution is used for the error.

Fig. 49 shows the convergence of model solutions (same set as fig. 48) at increasing spatial resolution (shorter cell width).

Number of bed dips convergence test

Here we show convergence under an increasing number of bed dips relevant for calculating normal force and velocities in the abrasion rate calculation. The abrasion rate model solution converges with an increasing number of dips. To optimize model performance, the number of bed dips was chosen at NUMBEDDIP = 10 (see fig. 50). Resolutions tested are $\{5i\}$ for $i \in [1, 18], i \in \mathbb{N}$ for uniform distribution of angles, $\theta_{dip} \epsilon [-34°, +34°]$.

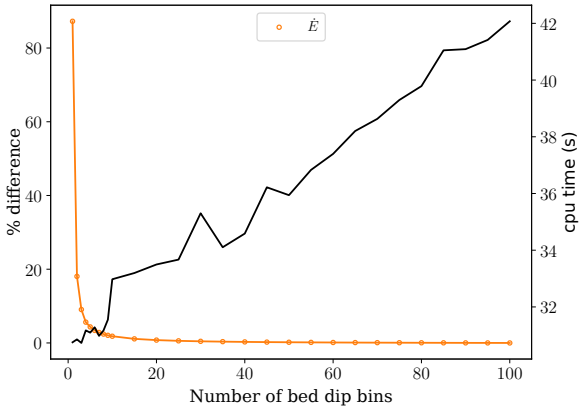

Figure 50: L2 norm between each resolution and the highest resolution run, normalized by highest resolution run.

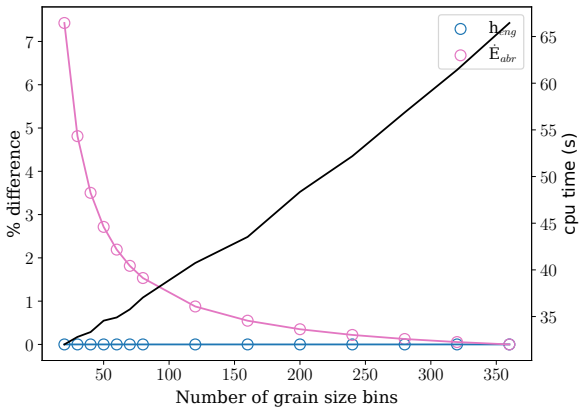

Figure 51: L2 norm between each resolution and the highest resolution run, normalized by highest resolution run.

Number of grains size bins convergence test

The grain size distribution is used to calculate normal force and particle velocity in the abrasion rate. The abrasion rate solution converges with an increasing number of bins in the grains size distribution (fig. 51). Between 5 and 360 bins were tested and showed small error between the lowest and highest number of bins. As such 10 bins was chosen to optimize model performance.

Englacial grid resolution test

The englacial grid is used in the vertical diffusion of sediment during englacial transport. A depiction of the non-linear grid is shown in fig. 52. The number of

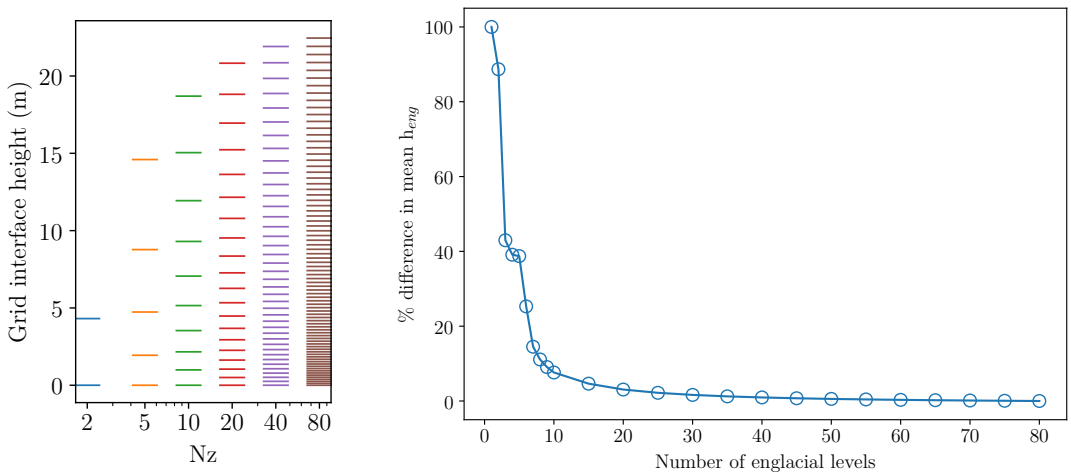

Figure 52: Convergence of englacial sediment thickness with more levels in the exponential englacial sediment grid.

englacial grid levels was tested between 2 and 80, with 10 chosen to optimize model performance (10 bins had $< 10\%$ error relative to highest bin count, see fig. 52).

Mass conservation test

The integral of the total erosion and removal of sediment over the ice sheet extent less the subglacial and englacial fluxes at the margin will give the total sediment within the ice sheet extent (subglacial and englacial). To test mass balance with unsteady input, we applied a sinusoidal meltwater forcing (eqn. 82) to the *SQRT_TOPO* setup with a basal sliding velocity coupled to effective pressure. The sediment mass balance is calculated as the balance of inputs and outputs:

$$net_{sed}^{t_i} = \int_0^{t_i} \left(\int_{\mathcal{A}} \dot{E}_{abr} + \dot{E}_{quar} da - \oint_{\mathcal{S}} \left[\mathbf{Q}_{subgl} + \mathbf{U}_b \int_0^{z_{engmax}} C_{eng} dz \right] \cdot \mathbf{n} dS \right) d\tau - \mathrm{h}_{subgl}^{initial} \tag{111}$$

$$ERR_{sed}^{t_i} = \frac{\left| net_{sed}^{t_i} - V_{sed}^{t_i} \right|}{V_{sed}^{t_i}} \tag{112}$$

where $V_{sed}^{t_i}$ is the total subglacial and englacial sediment within the ice sheet extent at time step t_i.

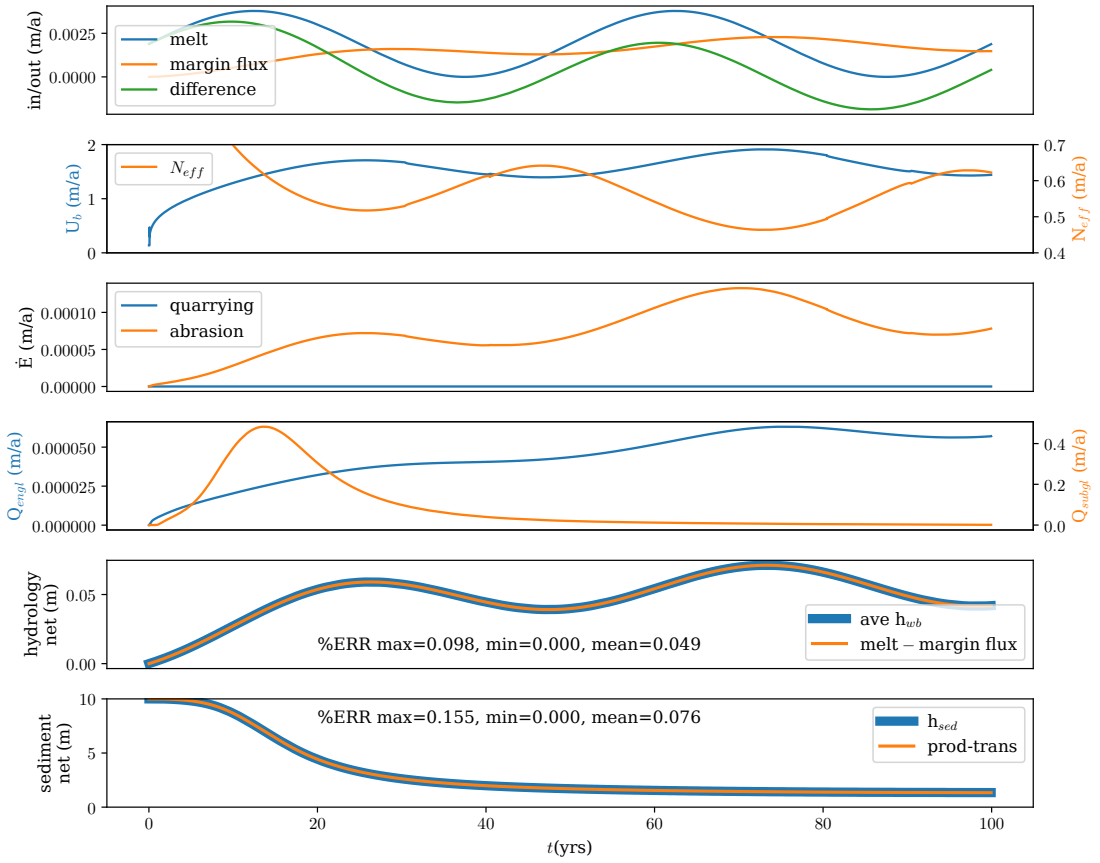

Figure 53: Mass conservation for sinusoidal melt input Mass balance for subglacial hydrology and basal sediment models given square root ice sheet topography and sinusoidal ice sheet basal mass balance (ice thickness, m/a), $Gb = 3.5 \times 10^{-3}/2 \sin 2\pi t/1000 + 3.5 \times^{-3} /2$. Basal sliding velocity calculated from driving stress (equivalent to shear stress in eqn. 79) and effective pressure.

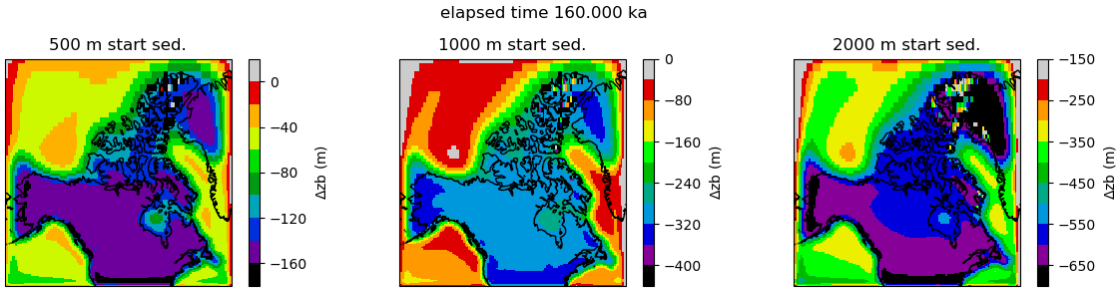

Figure 54: These isostatic adjustment tests show 40 kyr of adjustment (topographic effect of the sediment itself is removed) from increasing sediment loads imposed uniformly over the whole model domain: 20, 500, 1000, and 2000 m.

5.8.4 *Sediment Loading and Isostatic Adjustment Test*

We initialize the bed with the present day isostatic equilibrium, impose the sediment load (increasing from experiment to experiment) and run to near equilibrium over 40 kyr. For these tests the CO_2 was set to 700 ppm to suppress ice growth (no ice developed), this melted ice over Ellesmere and the stub Greenlandic ice sheet. The change in topographic elevation (less sediment thickness) is plotted in fig. 54 and shows increased subsidence with increasing sediment load.

5.8.5 *Produced and pre-existing sediment*

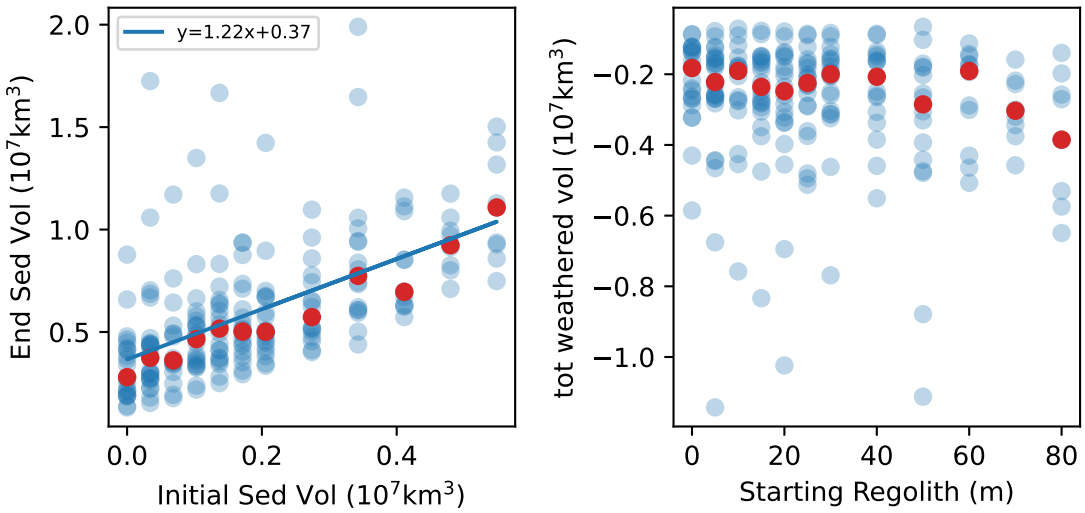

Figure 55: A comparison of the amount of sediment produced during glaciation with the amount of pre-existing regolith. The lefthand panel shows final sediment volume against initial sediment volume with a nearly one to one (1.22) linear slope – the final sediment volume is controlled mostly by input (initial) sediment volume. The righthand panel shows the total weathered (produced) volume of sediment against initial regolith thickness. The bulk volume of sediment produced is largely independent of the starting thickness. Around one to four million km^3 of sediment is produced throughout the Pleistocene – on the same order as the y-intercept in the lefthand plot.

REFERENCES

Ahn, S., D. Khider, L. E. Lisiecki, and C. E. Lawrence (2017). "A probabilistic Pliocene–Pleistocene stack of benthic δ^{18}O using a profile hidden Markov model". In: *Dynamics and Statistics of the Climate System* 2.1. ISSN: 2059-6987. DOI: 10.1093/climsys/dzx002. URL: http://dx.doi.org/10.1093/climsys/dzx002.

Alley, R. B. and D. R. MacAyeal (Aug. 1994). "Ice-rafted debris associated with binge/purge oscillations of the Laurentide Ice Sheet". In: *Paleoceanography* 9.4, pp. 503–511. ISSN: 0883-8305. DOI: 10.1029/94pa01008. URL: http://dx.doi.org/10.1029/94PA01008.

Balco, G. and C. W. Rovey (Sept. 2010). "Absolute chronology for major Pleistocene advances of the Laurentide Ice Sheet". In: *Geology* 38.9, pp. 795–798. ISSN: 0091-7613. DOI: 10.1130/g30946.1. URL: http://dx.doi.org/10.1130/G30946.1.

Bell, M. and E. P. Laine (Mar. 1985). "Erosion of the Laurentide Region of North America by Glacial and Glaciofluvial Processes". In: *Quaternary Research* 23.02, pp. 154–174. ISSN: 1096-0287. DOI: 10.1016/0033-5894(85)90026-2. URL: http://dx.doi.org/10.1016/0033-5894(85)90026-2.

Bereiter, B., S. Eggleston, J. Schmitt, C. Nehrbass-Ahles, T. F. Stocker, H. Fischer, S. Kipfstuhl, and J. Chappellaz (Jan. 2015). "Revision of the EPICA Dome C CO2 record from 800 to 600 kyr before present". In: *Geophysical Research Letters* 42.2, pp. 542–549. ISSN: 0094-8276. DOI: 10.1002/2014gl061957. URL: http://dx.doi.org/10.1002/2014GL061957.

Boulton, G. (1979). "Processes of Glacier Erosion on Different Substrata". In: *Journal of Glaciology* 23.89, pp. 15–38. ISSN: 1727-5652. DOI: 10.3189/s0022143000029713. URL: http://dx.doi.org/10.3189/S0022143000029713.

Braun, J., D. Zwartz, and J. H. Tomkin (1999). "A new surface-processes model combining glacial and fluvial erosion". In: *Annals of Glaciology* 28, pp. 282–290.

ISSN: 1727-5644. DOI: 10.3189/172756499781821797. URL: http://dx.doi.org/10.3189/172756499781821797.

Byerlee, J. (1978). "Friction of rocks". In: *Pure and Applied Geophysics PAGEOPH* 116.4–5, pp. 615–626. ISSN: 1420-9136. DOI: 10.1007/bf00876528. URL: http://dx.doi.org/10.1007/bf00876528.

Chalk, T. B., M. P. Hain, G. L. Foster, E. J. Rohling, P. F. Sexton, M. P. S. Badger, S. G. Cherry, A. P. Hasenfratz, G. H. Haug, S. L. Jaccard, and et al. (Nov. 2017). "Causes of ice age intensification across the Mid-Pleistocene Transition". In: *Proceedings of the National Academy of Sciences* 114.50, pp. 13114–13119. ISSN: 1091-6490. DOI: 10.1073/pnas.1702143114. URL: http://dx.doi.org/10.1073/pnas.1702143114.

Clark, P. U. and D. Pollard (Feb. 1998). "Origin of the Middle Pleistocene Transition by ice sheet erosion of regolith". In: *Paleoceanography* 13.1, pp. 1–9. ISSN: 0883-8305. DOI: 10.1029/97pa02660. URL: http://dx.doi.org/10.1029/97PA02660.

Cuffey, K. and W. S. B. Paterson (2010). *The Physics of Glaciers*. 4th ed. Academic Press.

de Fleurian, B., M. A. Werder, S. Beyer, D. J. Brinkerhoff, I. Delaney, C. F. Dow, J. Downs, O. Gagliardini, M. J. Hoffman, R. L. Hooke, J. Seguinot, and A. N. Sommers (Oct. 2018). "SHMIP The subglacial hydrology model intercomparison Project". In: *Journal of Glaciology* 64.248, pp. 897–916. ISSN: 1727-5652. DOI: 10.1017/jog.2018.78. URL: http://dx.doi.org/10.1017/jog.2018.78.

Dowdeswell, J. A. and M. J. Siegert (July 1999). "Ice-sheet numerical modeling and marine geophysical measurements of glacier-derived sedimentation on the Eurasian Arctic continental margins". In: *Geological Society of America Bulletin* 111.7, pp. 1080–1097. ISSN: 0016-7606. DOI: 10.1130/0016-7606(1999)111<1080:isnmam>2.3.co;2. URL: http://dx.doi.org/10.1130/0016-7606(1999)111%3C1080:ISNMAM%3E2.3.CO;2.

Drew, M. and L. Tarasov (Nov. 2022). "Surging of a Hudson Strait Scale Ice Stream: Subglacial hydrology matters but the process details don't". In: DOI: 10.5194/tc-2022-226. URL: http://dx.doi.org/10.5194/tc-2022-226.

Dyez, K. A., B. Hönisch, and G. A. Schmidt (Nov. 2018). "Early Pleistocene Obliquity-Scale pCO 2 Variability at 1.5 Million Years Ago". In: *Paleoceanography and Paleoclimatology* 33.11, pp. 1270–1291. ISSN: 2572-4525. DOI: 10.1029/2018pa003349. URL: http://dx.doi.org/10.1029/2018PA003349.

Dyke, A. S. (2004). "An outline of North American deglaciation with emphasis on central and northern Canada". In: *Developments in Quaternary Sciences*, pp. 373–424. ISSN: 1571-0866. DOI: 10.1016/s1571-0866(04)80209-4. URL: http://dx.doi.org/10.1016/S1571-0866(04)80209-4.

Ehlers, T. A., K. A. Farley, M. E. Rusmore, and G. J. Woodsworth (2006). "Apatite (U-Th)/He signal of large-magnitude accelerated glacial erosion, southwest British Columbia". In: *Geology* 34.9, p. 765. ISSN: 0091-7613. DOI: 10.1130/g22507.1. URL: http://dx.doi.org/10.1130/G22507.1.

Elderfield, H., P. Ferretti, M. Greaves, S. Crowhurst, I. N. McCave, D. Hodell, and A. M. Piotrowski (Aug. 2012). "Evolution of Ocean Temperature and Ice Volume Through the Mid-Pleistocene Climate Transition". In: *Science* 337.6095, pp. 704–709. ISSN: 1095-9203. DOI: 10.1126/science.1221294. URL: http://dx.doi.org/10.1126/science.1221294.

Engelder, J. and C. Scholz (May 1976). "The role of asperity indentation and ploughing in rock friction—II". In: *International Journal of Rock Mechanics and Mining Sciences & Geomechanics Abstracts* 13.5, pp. 155–163. ISSN: 0148-9062. DOI: 10.1016/0148-9062(76)90820-2. URL: http://dx.doi.org/10.1016/0148-9062(76)90820-2.

Fulton, R. J. (1995). "Surficial materials of Canada". In: DOI: 10.4095/205040. URL: http://dx.doi.org/10.4095/205040.

GIS Team National Park Service, A. R. O. (1999). “State Surficial Geology Map of Alaska”. In.

Gulick, S. P. S., J. M. Jaeger, A. C. Mix, H. Asahi, H. Bahlburg, C. L. Belanger, G. B. B. Berbel, L. Childress, E. Cowan, L. Drab, M. Forwick, A. Fukumura, S. Ge, S. Gupta, A. Kioka, S. Konno, L. J. Levay, C. Maerz, K. M. Matsuzaki, E. L. McClymont, C. Moy, J. Mueller, A. Nakamura, T. Ojima, F. R. Ribeiro, K. D. Ridgway, O. E. Romero, A. L. Slagle, J. S. Stoner, G. St-Onge, I. Suto, M. D. Walczak, L. L. Worthington, I. Bailey, E. Enkelmann, R. Reece, and J. M. Swartz (Dec. 2015). “Mid-Pleistocene Climate Transition Drives Net Mass Loss From Rapidly Uplifting St. Elias Mountains, Alaska”. In: *PNAS* 112.49, pp. 15042–15047.

Haldorsen, S. (Jan. 2008). “Grain-size distribution of subglacial till and its realtion to glacial scrushing and abrasion”. In: *Boreas* 10.1, pp. 91–105. ISSN: 1502-3885. DOI: 10.1111/j.1502-3885.1981.tb00472.x. URL: http://dx.doi.org/10.1111/j.1502-3885.1981.tb00472.x.

Hallet, B. (1979). “Subglacial Regelation Water Film”. In: *Journal of Glaciology* 23.89, pp. 321–334. ISSN: 1727-5652. DOI: 10.1017/s0022143000029932. URL: http://dx.doi.org/10.1017/S0022143000029932.

Harbor, J. M., B. Hallet, and C. F. Raymond (May 1988). “A numerical model of landform development by glacial erosion”. In: *Nature* 333.6171, pp. 347–349. ISSN: 1476-4687. DOI: 10.1038/333347a0. URL: http://dx.doi.org/10.1038/333347a0.

Hay, W. W., C. A. Shaw, and C. N. Wold (July 1989). “Mass-balanced paleogeographic reconstructions”. In: *Geologische Rundschau* 78.1, pp. 207–242. ISSN: 1437-3262. DOI: 10.1007/bf01988362. URL: http://dx.doi.org/10.1007/bf01988362.

Hildes, D. H. D. (Dec. 2001). “Modelling subglacial erosion and englacial sediment transport of the North American ice sheets”. PhD thesis. Department of Earth,

Ocean and Atmospheric Sciences Faculty of Science 2020 – 2207 Main Mall Vancouver, BC Canada V6T 1Z4: University of British Columbia. DOI: 10.14288/1.0052346. URL: http://hdl.handle.net/2429/13111.

Hildes, D. H., G. K. Clarke, G. E. Flowers, and S. J. Marshall (Feb. 2004). "Subglacial erosion and englacial sediment transport modelled for North American ice sheets". In: *Quaternary Science Reviews* 23.3-4, pp. 409–430. ISSN: 0277-3791. DOI: 10.1016/j.quascirev.2003.06.005. URL: http://dx.doi.org/10.1016/j.quascirev.2003.06.005.

Hönisch, B., N. G. Hemming, D. Archer, M. Siddall, and J. F. McManus (June 2009). "Atmospheric Carbon Dioxide Concentration Across the Mid-Pleistocene Transition". In: *Science* 324.5934, pp. 1551–1554. ISSN: 1095-9203. DOI: 10.1126/science.1171477. URL: http://dx.doi.org/10.1126/science.1171477.

Hönisch, B. (2021). "Paleo-CO2 data archive (Version 1)". In: DOI: 10.5281/zenodo.5777278. URL: https://doi.org/10.5281/zenodo.5777278.

Hooyer, T. S., D. Cohen, and N. R. Iverson (June 2012). "Control of glacial quarrying by bedrock joints". In: *Geomorphology* 153–154, pp. 91–101. ISSN: 0169-555X. DOI: 10.1016/j.geomorph.2012.02.012. URL: http://dx.doi.org/10.1016/j.geomorph.2012.02.012.

Hubbard, B. and P. Nienow (Jan. 1997). "Alpine subglacial hydrology". In: *Quaternary Science Reviews* 16.9, pp. 939–955. ISSN: 0277-3791. DOI: 10.1016/s0277-3791(97)00031-0. URL: http://dx.doi.org/10.1016/S0277-3791(97)00031-0.

Hubbard, B. and M. Sharp (1995). "Basal Ice Fades and Their Formation in the Western Alps". In: *Arctic and Alpine Research* 27.4, pp. 301–310. DOI: 10.1080/00040851.1995.12003127. URL: https://www.tandfonline.com/doi/abs/10.1080/00040851.1995.12003127.

Iverson, N. R. (1991). "Potential effects of subglacial water-pressure fluctuations on quarrying". In: *Journal of Glaciology* 37.125, pp. 27–36. ISSN: 1727-5652.

DOI: 10.3189/s0022143000042763. URL: http://dx.doi.org/10.3189/S0022143000042763.

Jauer, C. D. and P. Budkewitsch (Aug. 2010). "Old marine seismic and new satellite radar data: Petroleum exploration of north west Labrador Sea, Canada". In: *Marine and Petroleum Geology* 27.7, pp. 1379–1394. ISSN: 0264-8172. DOI: 10.1016/j.marpetgeo.2010.03.003. URL: http://dx.doi.org/10.1016/j.marpetgeo.2010.03.003.

Jenson, J. W., P. U. Clark, D. R. MacAyeal, C. Ho, and J. C. Vela (Nov. 1995). "Numerical modeling of advective transport of saturated deforming sediment beneath the Lake Michigan Lobe, Laurentide Ice Sheet". In: *Geomorphology* 14.2, pp. 157–166. ISSN: 0169-555X. DOI: 10.1016/0169-555x(95)00056-0. URL: http://dx.doi.org/10.1016/0169-555X(95)00056-0.

Jenson, J. W., D. R. MacAyeal, P. U. Clark, C. L. Ho, and J. C. Vela (Apr. 1996). "Numerical modeling of subglacial sediment deformation: Implications for the behavior of the Lake Michigan Lobe, Laurentide Ice Sheet". In: *Journal of Geophysical Research: Solid Earth* 101.B4, pp. 8717–8728. ISSN: 0148-0227. DOI: 10.1029/96jb00169. URL: http://dx.doi.org/10.1029/96JB00169.

Karlstrom, T. (1964). "Surficial geology of Alaska: U.S. Geological Survey Miscellaneous Geologic Investigations Map 357". In.

Klassen, R. and A. Gubins (1997). "Glacial history and ice flow dynamics applied to drift prospecting and geochemical exploration". In: *Proceedings of Exploration*. Vol. 97, pp. 221–232.

Koppes, M. N. and D. R. Montgomery (Aug. 2009). "The relative efficacy of fluvial and glacial erosion over modern to orogenic timescales". In: *Nature Geoscience* 2.9, pp. 644–647. ISSN: 1752-0908. DOI: 10.1038/ngeo616. URL: http://dx.doi.org/10.1038/NGEO616.

Krabbendam, M. and N. F. Glasser (July 2011). "Glacial erosion and bedrock properties in NW Scotland: Abrasion and plucking, hardness and joint spacing".

In: *Geomorphology* 130.3–4, pp. 374–383. ISSN: 0169-555X. DOI: 10.1016/j.geomorph.2011.04.022. URL: http://dx.doi.org/10.1016/j.geomorph.2011.04.022.

Laske, G., G. Masters, Z. Ma, and M. E. Pasyanos (2013). "Update on CRUST1.0: a 1-degree Global Model of Earth's Crust". In: *Geophysical Research Abstracts*. Vol. 15. European Geosciences Union General Assembly 2013 2658. European Geosciences Union. Vienna,Austria.

Lazeroms, W. M. J., A. Jenkins, G. H. Gudmundsson, and R. S. W. van de Wal (Jan. 2018). "Modelling present-day basal melt rates for Antarctic ice shelves using a parametrization of buoyant meltwater plumes". In: *The Cryosphere* 12.1, pp. 49–70. ISSN: 1994-0424. DOI: 10.5194/tc-12-49-2018. URL: http://dx.doi.org/10.5194/tc-12-49-2018.

Le Morzadec, K., L. Tarasov, M. Morlighem, and H. Seroussi (Oct. 2015). "A new sub-grid surface mass balance and flux model for continental-scale ice sheet modelling: testing and last glacial cycle". In: *Geoscientific Model Development* 8.10, pp. 3199–3213. ISSN: 1991-9603. DOI: 10.5194/gmd-8-3199-2015. URL: http://dx.doi.org/10.5194/gmd-8-3199-2015.

Margold, M., C. R. Stokes, and C. D. Clark (Apr. 2015). "Ice streams in the Laurentide Ice Sheet: Identification, characteristics and comparison to modern ice sheets". In: *Earth-Science Reviews* 143, pp. 117–146. ISSN: 0012-8252. DOI: 10.1016/j.earscirev.2015.01.011. URL: http://dx.doi.org/10.1016/j.earscirev.2015.01.011.

McKinley, I. G. and N. A. Chapman (Aug. 2009). "The impact of subsidence, uplift and erosion on geological repositories for radioactive wastes". In: *Volcanic and Tectonic Hazard Assessment for Nuclear Facilities*, pp. 548–565. DOI: 10.1017/cbo9780511635380.025. URL: http://dx.doi.org/10.1017/CBO9780511635380.025.

Melanson, A. (2012). "Numerical modelling of subglacial erosion and sediment transport and its application to the North American ice sheets over the last glacial cycle". Includes bibliographical references (leaves 76-87). URL: https://research.library.mun.ca/2370/.

Melanson, A., T. Bell, and L. Tarasov (May 2013). "Numerical modelling of subglacial erosion and sediment transport and its application to the North American ice sheets over the Last Glacial cycle". In: *Quaternary Science Reviews* 68, pp. 154–174. ISSN: 0277-3791. DOI: 10.1016/j.quascirev.2013.02.017. URL: http://dx.doi.org/10.1016/j.quascirev.2013.02.017.

Naylor, S., A. D. Wickert, D. A. Edmonds, and B. J. Yanites (Nov. 2021). "Landscape evolution under the southern Laurentide Ice Sheet". In: *Science Advances* 7.48. ISSN: 2375-2548. DOI: 10.1126/sciadv.abj2938. URL: http://dx.doi.org/10.1126/sciadv.abj2938.

Parent, M., M. Ross, D. Howlett, and K. Bédard (2021). "3D model of the Quaternary sediments in the St. Lawrence valley and adjacent regions, southern Quebec and eastern Ontario". In: DOI: 10.4095/329082. URL: http://dx.doi.org/10.4095/329082.

Pelletier, J. D., P. D. Broxton, P. Hazenberg, X. Zeng, P. A. Troch, G.-Y. Niu, Z. Williams, M. A. Brunke, and D. Gochis (Jan. 2016). "A gridded global data set of soil, intact regolith, and sedimentary deposit thicknesses for regional and global land surface modeling". In: *Journal of Advances in Modeling Earth Systems* 8.1, pp. 41–65. ISSN: 1942-2466. DOI: 10.1002/2015ms000526. URL: http://dx.doi.org/10.1002/2015MS000526.

Pianosi, F. and T. Wagener (May 2015). "A simple and efficient method for global sensitivity analysis based on cumulative distribution functions". In: *Environmental Modelling & Software* 67, pp. 1–11. ISSN: 1364-8152. DOI: 10.1016/j.envsoft.2015.01.004. URL: http://dx.doi.org/10.1016/j.envsoft.2015.01.004.

Pollard, D. and R. M. DeConto (Sept. 2012). "A simple inverse method for the distribution of basal sliding coefficients under ice sheets, applied to Antarctica". In: *The Cryosphere* 6.5, pp. 953–971. ISSN: 1994-0424. DOI: 10.5194/tc-6-953-2012. URL: http://dx.doi.org/10.5194/tc-6-953-2012.

Pollard, D. and R. M. DeConto (Sept. 2003). "Antarctic ice and sediment flux in the Oligocene simulated by a climate–ice sheet–sediment model". In: *Palaeogeography, Palaeoclimatology, Palaeoecology* 198.1-2, pp. 53–67. ISSN: 0031-0182. DOI: 10.1016/s0031-0182(03)00394-8. URL: http://dx.doi.org/10.1016/S0031-0182(03)00394-8.

— (Jan. 2020). "Continuous simulations over the last 40 million years with a coupled Antarctic ice sheet-sediment model". In: *Palaeogeography, Palaeoclimatology, Palaeoecology* 537, p. 109374. ISSN: 0031-0182. DOI: 10.1016/j.palaeo.2019.109374. URL: http://dx.doi.org/10.1016/j.palaeo.2019.109374.

Pollard, D. and R. M. Deconto (Mar. 2009). "A Coupled Ice-Sheet/Ice-Shelf/Sediment Model Applied to a Marine-Margin Flowline: Forced and Unforced Variations". In: *Glacial Sedimentary Processes and Products*, pp. 37–52. DOI: 10.1002/9781444304435.ch4. URL: http://dx.doi.org/10.1002/9781444304435.ch4.

Porter, C., P. Morin, I. Howat, M.-J. Noh, B. Bates, K. Peterman, S. Keesey, M. Schlenk, J. Gardiner, K. Tomko, M. Willis, C. Kelleher, M. Cloutier, E. Husby, S. Foga, H. Nakamura, M. Platson, J. Wethington Michael, C. Williamson, G. Bauer, J. Enos, G. Arnold, W. Kramer, P. Becker, A. Doshi, C. D'Souza, P. Cummens, F. Laurier, and M. Bojesen (2018). *ArcticDEM, Version 3*. Version V1. DOI: 10.7910/DVN/OHHUKH. URL: https://doi.org/10.7910/DVN/OHHUKH.

Rohling, E. J., G. L. Foster, K. M. Grant, G. Marino, A. P. Roberts, M. E. Tamisiea, and F. Williams (Apr. 2014). "Sea-level and deep-sea-temperature variability over the past 5.3 million years". In: *Nature* 508.7497, pp. 477–482. ISSN: 1476-

4687. DOI: 10.1038/nature13230. URL: http://dx.doi.org/10.1038/nature13230.

Roy, M., P. U. Clark, G. M. Raisbeck, and F. Yiou (Nov. 2004). "Geochemical constraints on the regolith hypothesis for the middle Pleistocene transition". In: *Earth and Planetary Science Letters* 227.3-4, pp. 281–296. ISSN: 0012-821X. DOI: 10.1016/j.epsl.2004.09.001. URL: http://dx.doi.org/10.1016/j.epsl.2004.09.001.

Russell, H., N. Atkinson, A. Bajc, B. Brodaric, G. Keller, K. Lo, M. Parent, M. Pyne, R. Smith, and B. Todd (2017). "A 3-D framework of surficial geology for Canada". In: *Joint Annual Meeting, Programs with Abstracts* 40. URL: https://geoscan.nrcan.gc.ca/starweb/geoscan/servlet.starweb?path=geoscan/fulle.web&search1=R=327036.

Saltelli, A. (May 2002). "Making best use of model evaluations to compute sensitivity indices". In: *Computer Physics Communications* 145.2, pp. 280–297. ISSN: 0010-4655. DOI: 10.1016/s0010-4655(02)00280-1. URL: http://dx.doi.org/10.1016/S0010-4655(02)00280-1.

Saltelli, A., K. Aleksankina, W. Becker, P. Fennell, F. Ferretti, N. Holst, S. Li, and Q. Wu (Apr. 2019). "Why so many published sensitivity analyses are false: A systematic review of sensitivity analysis practices". In: *Environmental Modelling & Software* 114, pp. 29–39. ISSN: 1364-8152. DOI: 10.1016/j.envsoft.2019.01.012. URL: http://dx.doi.org/10.1016/j.envsoft.2019.01.012.

Saltelli, A., M. Ratto, T. Andres, F. Campolongo, J. Cariboni, D. Gatelli, M. Saisana, and S. Tarantola (2008). *Global Sensitivity Analysis. The Primer*. 1st ed. The Atrium, Southern Gate, Chichester,West Sussex PO19 8SQ, England: John Wiley & Sons, Ltd. ISBN: 978-0-470-05997-5.

Salvatier, J., T. V. Wiecki, and C. Fonnesbeck (Apr. 2016). "Probabilistic programming in Python using PyMC3". In: *PeerJ Computer Science* 2, e55. ISSN: 2376-

5992. DOI: 10.7717/peerj-cs.55. URL: http://dx.doi.org/10.7717/peerj-cs.55.

Schoof, C. (Feb. 2007). "Marine ice-sheet dynamics. Part 1. The case of rapid sliding". In: *Journal of Fluid Mechanics* 573, pp. 27–55. ISSN: 1469-7645. DOI: 10.1017/s0022112006003570. URL: http://dx.doi.org/10.1017/S0022112006003570.

Sears, J. W. and L. P. Beranek (Mar. 2022). "The Great Preglacial "Bell River" of North America: Detrital Zircon Evidence for Oligocene–Miocene Fluvial Connections Between the Colorado Plateau and Labrador Sea". In: *Geoscience Canada* 49.1. ISSN: 0315-0941. DOI: 10.12789/geocanj.2022.49.184. URL: http://dx.doi.org/10.12789/geocanj.2022.49.184.

Shangguan, W., T. Hengl, J. Mendes de Jesus, H. Yuan, and Y. Dai (Jan. 2017). "Mapping the global depth to bedrock for land surface modeling". In: *Journal of Advances in Modeling Earth Systems* 9.1, pp. 65–88. ISSN: 1942-2466. DOI: 10.1002/2016ms000686. URL: http://dx.doi.org/10.1002/2016MS000686.

Smith, I. R. and K. Lesk-Winfield (2010). "Drift isopach, till isopach, and till facies reconstructions for Northwest Territories and northern Yukon". In: DOI: 10.4095/261783. URL: http://dx.doi.org/10.4095/261783.

Soller, D. R. and C. P. Garrity (2018). "Quaternary sediment thickness and bedrock topography of the glaciated United States east of the Rocky Mountains". In: *Scientific Investigations Map*. ISSN: 2329-132X. DOI: 10.3133/sim3392. URL: http://dx.doi.org/10.3133/sim3392.

Spratt, R. M. and L. E. Lisiecki (Apr. 2016). "A Late Pleistocene sea level stack". In: *Climate of the Past* 12.4, pp. 1079–1092. ISSN: 1814-9332. DOI: 10.5194/cp-12-1079-2016. URL: http://dx.doi.org/10.5194/cp-12-1079-2016.

Staiger, J., J. Gosse, E. Little, D. Utting, R. Finkel, J. Johnson, and J. Fastook (Feb. 2006). "Glacial erosion and sediment dispersion from detrital cosmogenic nuclide analyses of till". In: *Quaternary Geochronology* 1.1, pp. 29–42. ISSN:

1871-1014. DOI: 10.1016/j.quageo.2006.06.009. URL: http://dx.doi.org/10.1016/j.quageo.2006.06.009.

Stashin, S. (2021). "Late Cenozoic Basin Evolution of the western Canadian Arctic Archipelago: The Beaufort Formation and Iperk Sequence". Masters Thesis. Dalhousie University. URL: http://hdl.handle.net/10222/80367.

Storrar, R. D., C. R. Stokes, and D. J. Evans (Sept. 2013). "A map of large Canadian eskers from Landsat satellite imagery". In: *Journal of Maps* 9.3, pp. 456–473. ISSN: 1744-5647. DOI: 10.1080/17445647.2013.815591. URL: http://dx.doi.org/10.1080/17445647.2013.815591.

Straume, E. O., C. Gaina, S. Medvedev, K. Hochmuth, K. Gohl, J. M. Whittaker, R. Abdul Fattah, J. C. Doornenbal, and J. R. Hopper (Apr. 2019). "GlobSed: Updated Total Sediment Thickness in the World's Oceans". In: *Geochemistry, Geophysics, Geosystems* 20.4, pp. 1756–1772. ISSN: 1525-2027. DOI: 10.1029/2018gc008115. URL: http://dx.doi.org/10.1029/2018GC008115.

"Surficial geology of Canada" (2014). In: DOI: 10.4095/295462. URL: http://dx.doi.org/10.4095/295462.

Tarasov, L. and W. R. Peltier (1997). "A high-resolution model of the 100 ka ice-age cycle". In: *Annals of Glaciology* 25, pp. 58–65. ISSN: 1727-5644. DOI: 10.3189/s026030550001380x. URL: http://dx.doi.org/10.3189/S026030550001380X.

Tarasov, L. and W. R. Peltier (June 2007). "Coevolution of continental ice cover and permafrost extent over the last glacial-interglacial cycle in North America". In: *Journal of Geophysical Research* 112.F2. ISSN: 0148-0227. DOI: 10.1029/2006jf000661. URL: http://dx.doi.org/10.1029/2006JF000661.

— (Apr. 2006). "A calibrated deglacial drainage chronology for the North American continent: evidence of an Arctic trigger for the Younger Dryas". In: *Quaternary Science Reviews* 25.7–8, pp. 659–688. ISSN: 0277-3791. DOI: 10.1016/j.

quascirev.2005.12.006. URL: http://dx.doi.org/10.1016/j.quascirev.2005.12.006.

Taylor, A. (Mar. 2023). "Sediment thickness map of continental Canada and Canada-U.S. transboundary watersheds". In.

Ugelvig, S. V. and D. L. Egholm (May 2018). "The influence of basal-ice debris on patterns and rates of glacial erosion". In: *Earth and Planetary Science Letters* 490, pp. 110–121. ISSN: 0012-821X. DOI: 10.1016/j.epsl.2018.03.022. URL: http://dx.doi.org/10.1016/j.epsl.2018.03.022.

Ugelvig, S. V., D. L. Egholm, and N. R. Iverson (Nov. 2016). "Glacial landscape evolution by subglacial quarrying: A multiscale computational approach". In: *Journal of Geophysical Research: Earth Surface* 121.11, pp. 2042–2068. ISSN: 2169-9003. DOI: 10.1002/2016jf003960. URL: http://dx.doi.org/10.1002/2016JF003960.

Weertman, J. (1957). "On the Sliding of Glaciers". In: *Journal of Glaciology* 3.21, pp. 33–38. ISSN: 1727-5652. DOI: 10.3189/s0022143000024709. URL: http://dx.doi.org/10.3189/S0022143000024709.

Willeit, M., A. Ganopolski, R. Calov, A. Robinson, and M. Maslin (July 2015). "The role of CO2 decline for the onset of Northern Hemisphere glaciation". In: *Quaternary Science Reviews* 119, pp. 22–34. ISSN: 0277-3791. DOI: 10.1016/j.quascirev.2015.04.015. URL: http://dx.doi.org/10.1016/j.quascirev.2015.04.015.

Preface to Chapter 6, "Self Consistency of the Regolith Hypothesis for the Mid-Pleistocene Transition"

This manuscript is intended for submission to Nature. It satisfies the main research objectives laid out in 1.4.

This chapter assesses the self-consistency of the regolith hypothesis for the mid-Pleistocene Transition (MPT). The MPT is seen as an increase in glacial state resilience of the earth system (Tzedakis et al., 2017). It has been hypothesized that a secular decline in CO_2 could produce this increased resiliency (Berger and Loutre, 2010). The other most prominent mechanism for increased resiliency is the regolith hypothesis (Clark et al., 2006). In this chapter we bring together the model components of previous chapters to examine the self-consistency of the regolith hypothesis with a fully coupled climate-glacial-hydrology-sediment system – to date the most fully coupled and process complete earth systems model applied to a glacial cycle-continental scale.

Chapter 6

Self Consistency of the Regolith Hypothesis for the Mid-Pleistocene Transition

ABSTRACT

The mid-Pleistocene transition (MPT) from small 40 kyr sea level cycles (glacial cycles) to large abruptly terminating 100 kyr cycles is a poorly understood tipping point in the earth system. A leading mechanism for this transition is a stabilization of the North American ice sheet by removing easily deformed regolith to expose the high friction bedrock underneath. The removal of regolith by Pleistocene ice sheets remains poorly constrained and past modelling efforts examining its role have lacked the relevant processes. Furthermore, the dynamical role of regolith in the transition remains unclear.

To properly test this regolith-based mechanism, at least three components are required: a capable model, observational constraints, and appropriate uncertainty estimation. The model used herein incorporates a state-of-the-art fully coupled sediment production/transport model, subglacial hydrology, ice physics, and climate driven only by insolation and atmospheric greenhouse gases. Our simulations are run over the full Pleistocene. The required observational constraints include present-day regolith distribution and Pleistocene ice volume and extent inferred from proxy records. Uncertainty is estimated via several bounding numerical experiments.

Our numerical experiments indicate that the removal of North American regolith was not a straightforward driver of the transition. We find thicker pre-glacial regolith does not simply delay its complete removal and thus delay the transition – it also limits marine based ice in the key areas of the Canadian Arctic Archipelago and Hudson Bay while cooling those locations via the elevation-lapse rate feedback. These latter effects in fact produce larger ice sheets, not smaller ones. When erosion rates are consistent with available observations, we find that the North American Ice Complex reaches a hard bedded area similar to present day by 1.5 Ma, staying largely steady there after. This poses a challenge for the self-consistency of the Regolith Hypothesis.

6.1 AN IMPORTANT CLIMATIC TRANSITION

A key component of the changing climate during the current geologic period is the cyclic growth and melt of polar ice sheets (Westerhold, Marwan, et al., 2020). The largest enduring shift of this period is the MPT from smaller 41 kyr glaciations to larger 100 kyr ones around 1 million years ago (between 650 and 1250 ka (Clark, Archer, et al., 2006)). This transition presents a challenge to the accepted and well evidenced explanation of orbital forcing of glacial cycles termed Milankovitch theory (Hays, Imbrie, and Shackleton, 1976): the MPT occurred in the absence of any change in orbital forcing (Westerhold, Röhl, and Laskar, 2012) and so appears to be the result of internal system dynamics. While the orbital eccentricity does have a 100 kyr period, the power at this mode is too weak to explain a change in dominant mode of the climate from obliquity to eccentricity driven (Berger and Loutre, 2010). This internal mechanism is a major gap in our understanding of the evolution of Pleistocene glacial cycles and by extension, the process of sea level rise in warming worlds.

Hypotheses for the MPT must also explain the transition to asymmetry of the glacial cycles (Tziperman and Gildor, 2003). Prior to the MPT glaciation and deglaciation both took 20 kyr – a symmetric cycle. Following the transition ice build up occurred over ≈90 kyr and the melt phase only ≈10 kyr, still much shorter than early Pleistocene deglaciation while starting from a larger ice volume. Several mechanisms for accumulated instability (Tzedakis et al., 2017) have been proposed to explain this asymmetry. Some include ice sheet processes (*e.g.* glacial isostatic adjustment (GIA) causing a greater area of the ice sheet to be below the equilibrium line altitude and causing more of the ice sheet to be marine based and thus enhancing calving (Clark and Pollard, 1998)) or ocean processes (*e.g.* Tziperman and Gildor (2003)'s sea ice switch).

6.2 TWO HYPOTHESES: REGOLITH VS. CO2

Hypothesized mechanisms for the transition fall into two camps: ice sheet dynamic changes and atmospheric/oceanic changes. Although a downward trend in mean CO_2 from early to mid-Pleistocene would make ice sheets more easily incepted and resilient (*e.g.* Berger and Loutre (2010)), no such trend in interglacial CO_2 values is present in the related boron isotope record (Dyez, Hönisch, and Schmidt, 2018), nor in the European Project for Ice Coring in Antarctica (EPICA) ice core record (800 ka) (Clark, Archer, et al., 2006).

A further hurdle to the CO_2 mechanism for the MPT is in explaining the similar extent between early and late Pleistocene Laurentide ice sheets. Tills deposited at similar latitudes (see fig. 57) in the north-central U.S. date to multiple times both before and after the MPT, as inferred from magnetostratigraphy and tephrochronology (Roy et al., 2004). Similarly, early Cordilleran ice sheets reached as far as those after the transition (Hidy et al., 2013). A gradual lowering of CO_2 would enhance glaciation, making inception easier and deglaciation more difficult, but it does not explain some ice sheets before the MPT reaching the same latitude as those after. This is a curiosity of the MPT: how could inferred smaller early Pleistocene North American ice sheets reach as south as the larger later Pleistocene ones?

This curious similarity in extent while significantly different in ice volume is explainable by a change in basal friction. The regolith hypothesis posits the lengthening and strengthening of glacial cycles resulted from the removal of easily deforming soft sediment by successive glaciations, eventually denuding enough of the underlying hard bed rock to transition to slower sliding velocities (Clark and Pollard, 1998). The basal drag is approximately balanced by the driving stress (Cuffey and Paterson, 2010) so that an increase in basal friction implies a steeper ice sheet surface slope (the determinant of driving stress) and thus thicker ice

sheets. This might explain the similar areal extent seen in the till record and there is geochemical evidence that such a change in substrate character took place. Roy et al. (2004) measured chemical indices of alteration and cosmogenic nuclide concentrations which support a change from removal of chemically weathered sediment which had been exposed to cosmic radiation to the erosion of fresh crystalline bedrock across the MPT. However, this till evidence is sparse and carries much uncertainty. Key questions remain around the regolith hypothesis, chief among them is whether this hypothesis is self consistent.

6.3 A SELF-CONSISTENCY TEST OF THE REGOLITH HYPOTHESIS

To date modelling efforts around the regolith hypothesis have simply forced hard/soft bed difference in the basal drag of the North American ice sheet. While this demonstrates that an increase in basal friction could plausibly affect its stability at large scales, it does not show that the regolith hypothesis was responsible for the mid-Pleistocene transition. What is the full effect of regolith removal on Pleistocene glacial cycles when the removal is treated as a system-internal process?

Model tests of the regolith hypothesis have not incorporated sediment production (e.g. Clark and Pollard, 1998; Willeit et al., 2019). This presents a potential challenge for removal of regolith: as the mantle of regolith is removed, bedrock is exposed and sediment production rates increase. As such, the major question remains: given our understanding of glacial removal of bed surface material, was the Laurentide ice sheet capable of removing sufficient regolith to transition within the timing inferred for the MPT?

We adopt a dose-response strategy for studying the regolith hypothesis: if regolith removal is responsible for the MPT, varying the amount of regolith in a way which is consistent with all other processes at play should hasten (in the case of thinner regolith) or delay (in the case of thicker regolith) the onset of the

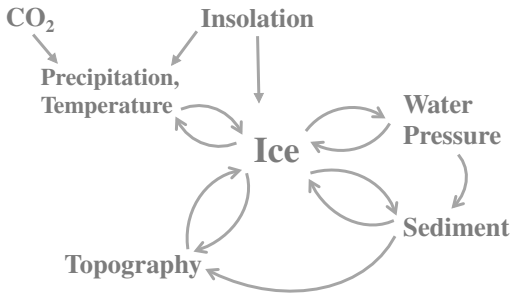

Figure 56: Summary of system interactions needed for modelling the effect from regolith on glacial cycles.

transition within parametric uncertainty. At the onset of this study, we expected to find a correspondence between regolith thickness and timing of the MPT. The actual effect is more interesting and poses a challenge for the regolith hypothesis.

To address the effect of regolith on the system, a model which couples all of the relevant physics is necessary. The Glacial Systems Model (GSM) is the first such model to couple all of these processes together, summarized in fig. 56.

6.4 CONSTRAINT IN AN UNCERTAIN TIME PERIOD

Our inferences of the changing state of the planet become more uncertain the farther back in time. Orbitally-resolved sea level records with quantified uncertainties provide an important constraint for glacial cycle modelling. However, despite community efforts to infer Pleistocene sea level progression, the uncertainties remain too large to constrain any single marine isotope stage ice volume prior to the MPT. Two records extend across the MPT but both carry significant uncertainty in absolute sea level, in part due to long term processes. Elderfield et al. (2012) use the Mg/Ca ratio to isolate the temperature and sea level signals in benthic δ^{18}O at a location where benthic waters are less influenced by hydrography than other records. However, this analysis did not take into account that the Mg/Ca ratio of ocean water likely increased over the Pleistocene (Raymo et al.,

2018). By using a Mediterranean planktic δ^{18}O stack with a basin-box and strait model, Rohling, Foster, Grant, et al. (2014) reconstruct sea level on the basis of salinity changes due to the balance of net evaporation and sea water exchange with the Atlantic through the shallow Strait of Gibraltar. However, sources of fresh water for the Mediterranean basin carry different δ18O concentrations and river input would have changed with the precessionally driven African monsoon and the aridification of the region after 1.5 Ma relative to before (Rohling, Foster, Gernon, et al., 2022).

While the absolute value of these records carry large systematic uncertainties, the relative change in sea level from glacial to interglacial carries little of the secular trend component of uncertainty. The records of Elderfield et al. (2012) and Rohling, Foster, Grant, et al. (2014) agree that the pre MPT (1500-950 ka) amplitude in sea level change is around 85 m and the post MPT (950 ka to PD) is greater than 105 m (5^{th} to 95^{th} sea level percentile difference).

The till record provides constraint on the extent of early and late Pleistocene ice sheets. (Roy et al., 2004) details 15 early Pleistocene tills dated with tephra and paleomagnetism to 800-1300 ka and 1300-2700 ka, all within 39.5 to 42 degrees in the pre-MPT period. This is comparable in southern extent to 13 post-MPT tills (again dated with tephra and paleomagnetism) which range 40.5 to 42.5 degrees latitude.

6.5 RESULTS

Using a set of basis vectors extracted from large ensembles (methods), we conducted two sets of experiments. Pleistocene bedrock erosion rates are uncertain. As such, we first present simulations with negligible sediment production to show the transport capacity of a glacial system and the contribution of regolith removal and the consequent topographic change to the progression of glacial cycles. Following

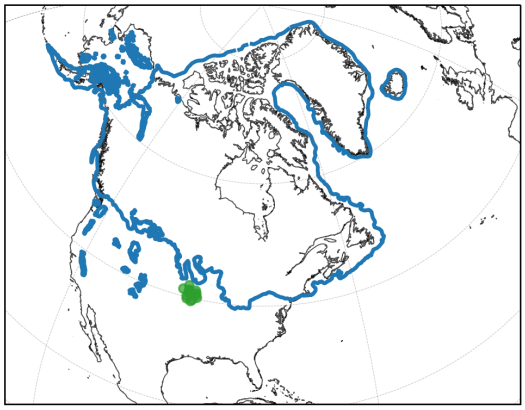

Figure 57: Dalton et al. (2020) last glacial maximum margin and the location of several tills deposited before and after the mid-Pleistocene transition (Roy et al., 2004) showing the similarity in extent across it

these, bedrock erosion was increased and iteratively tuned to the bulk estimate of Naylor et al. (2021) (methods). Each of these used CO_2 from a linear transform of the ProbStack (Ahn et al., 2017) prior to EPICA coverage (Bereiter et al., 2015), shown in fig. 64.

Below we examine the increase in hard bed area relative to the range of estimates of present day hard bed (methods). This change in area is then related to the progression of glacial cycles.

6.5.1 *The transition and regolith removal in absence of sediment production*

To start, we assess the effect of regolith removal alone (without sediment production) on the MPT. We test multiple uniform thicknesses of Pliocene sediment covering the range of bedrock and regolith removal inferred by (M. Bell and Laine, 1985): 20, 65, 110, 155, and 200 m. However, the 20 m results are not shown here as the late Pleistocene hard bedded area was larger than the range of present day estimates. In the ensemble mean, the model removes a significant amount of sediment around the

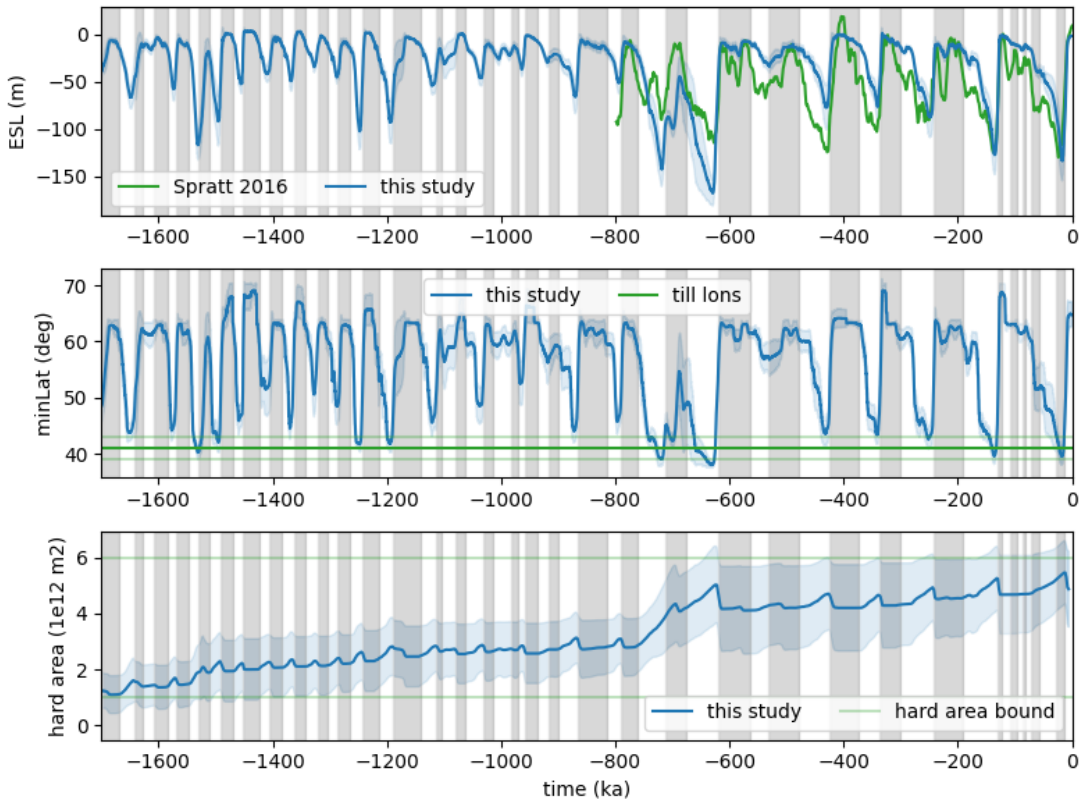

Figure 58: Modelled sea level (blue) overlain on the sea level reconstruction of Spratt and Lisiecki (2016) (green), ice sheet minimum latitude compared with the till evidence for before and after the MPT, and the changing hard bed area under the core glaciated domain due to regolith removal (absent physical weathering due to glacial sediment production). Blue line shows ensemble mean, shaded area shows 2σ range.

time of the MPT becoming increasingly hard bedded and achieves similar Southerly extent before the MPT as after. Fig. 58 shows the ensemble mean sea level changes: sea level amplitude prior to the transition is less than afterward. The simulated sea level time series agrees with the sea level reconstruction of Spratt and Lisiecki (2016) within the large uncertainties at those time scales. The minimum latitude is similar across the transition and agrees well with the evidence from mid-continent tills (Roy et al., 2004). The mean hard bedded area reaches the estimated present day value in advance of timing of the MPT, though some individual runs reach the range of present-day hard bed area estimates closer to the MPT.

Based on these findings it is plausible that the Laurentide could have removed large amounts of regolith and its hard bed area could have increased quickly around

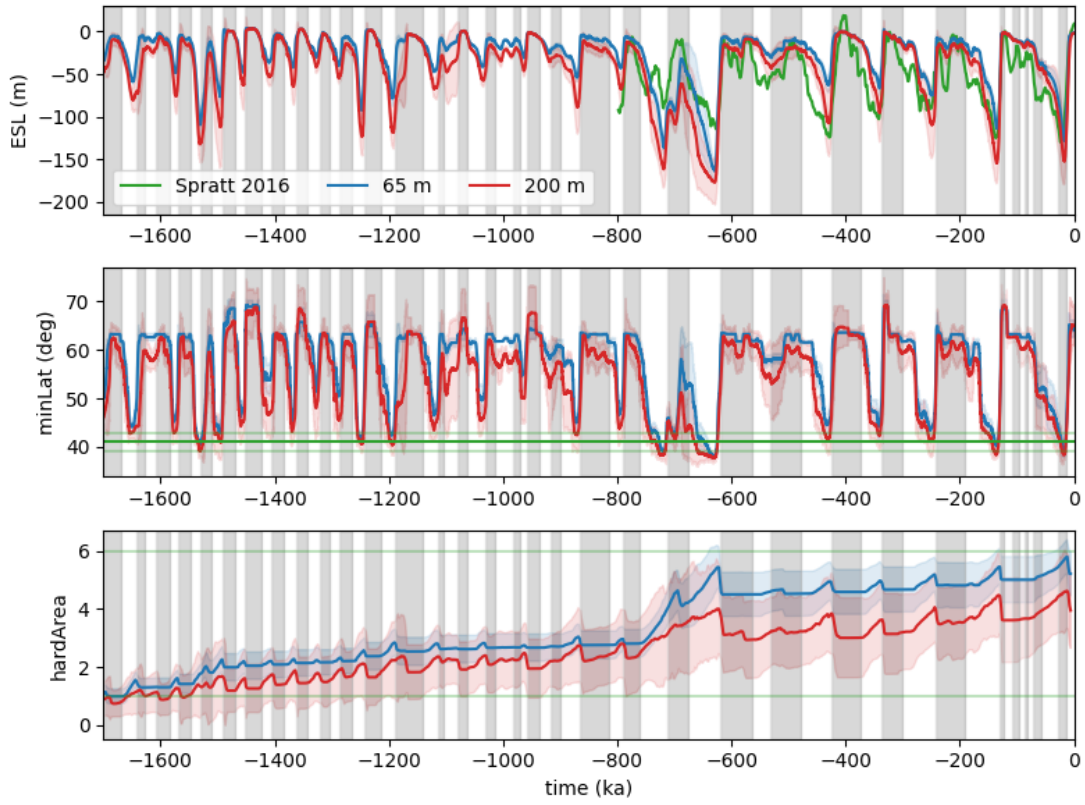

Figure 59: Regolith removal (no sediment production) and glacial cycle progression for the thickest and thinnest starting regolith thicknesses which lie in the range of the present day hard bedded area by the last glacial maximum (LGM) – 65 and 200 m. Blue line shows the mean ESL, most southerly latitude of ice and hard bed area mean across all basis vectors for 65 m starting regolith thickness. Red shows the same for 200 m. Shading shows the 2σ range for each and vertical grey and white regions indicate successive marine isotope stages (Lisiecki and Raymo, 2005). The green curve in the ESL plot is the sea level stack of Spratt and Lisiecki (2016), the horizontal green lines in the minLat plot show the mean and max/min of several early Pleistocene tills studied by Roy et al. (2004), and the horizontal green lines in the hardArea plot show the range of estimated present day hard bed area from the present day sediment thickness reconstructions of Pelletier et al. (2016), Shangguan et al. (2017), and Taylor (2023), shown in chap. 5, fig. 39.

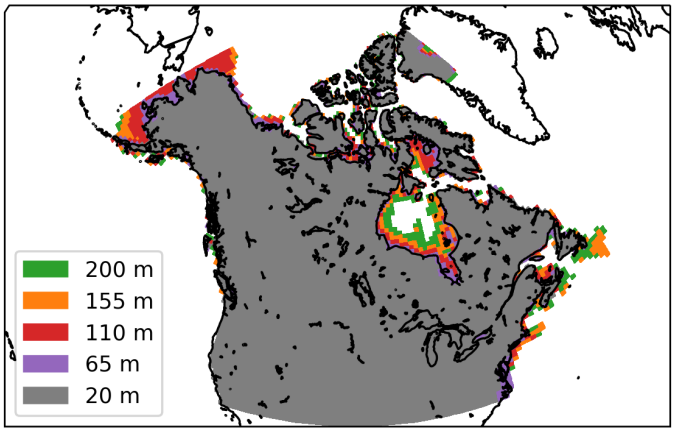

Figure 60: Map of areas above sea level in the initial topography for varying starting sediment thicknesses in the regolith removal only experiments. Coloured areas indicate areas which are above sea level for that sediment thickness and all those thicker. These fields are taken after 60 kyr of subsidence once the sediment was added.

the timing of the MPT. However, the question remains – what is the role of regolith in the timing of the transition itself? To answer this question we conduct a dose response experiment to measure the system response to the dose (thickness) of starting regolith.

The response was not a shift in the timing of the MPT but different sea level curves where increased sediment thickness (200 m versus 65 m) gave stronger glacial cycles – even lengthening some (e.g. just prior to 1600 ka, at 1200 and 1100 ka) as shown in fig. 59. The mechanism of regolith removal is therefore not related to the timing of the MPT in a straightforward way. While a change in basal friction can change how easily ice sheets deglaciate, trying to delay the MPT by adding more regolith and delaying its removal has unexpected consequences. This is because of the accompanying topographic effects from adding a layer of sediment between 20 and 200 m thick. This sediment layer changes the land sea mask as shown in fig. 60, rendering much of the Hudson bay and Foxe Basin terrestrial and making the channels between islands in the Canadian Arctic Archipelago shallower. Additionally, the increase in elevation across the domain will give colder temperatures earlier in a glacial cycle, and thereby quicker inception and a larger ice sheet.

These topographic effects influence the overall mass balance of the North American ice sheet, inducing larger ice sheets (sea level drop is nearly 50% higher in the 200 vs 65 m run shown in fig. 61 b) due to a reduction in negative mass balance contributors. The domain mean melt is lower in the higher elevation 200 m starting regolith scenario and the calving is decreased due to channel and basin infill bringing more of the ice sheet bed above sea level.

6.5.2 *Inclusion of sediment production*

Introducing glacial sediment production to the system brings the system to a new steady state. We loosely tuned bedrock erosion to the level inferred by Naylor et al. (2021) and Ehlers et al. (2006) by iteratively adjusting the quarrying and abrasion rate scalers. With realistic erosion rates, denudation allows for sediment production from the exposed bedrock. This results in a steady state hard bedded area independent of starting regolith distribution. In fig. 62, the hard bedded area time series appear to roughly converge on a narrow range of values for varied Pliocene regolith thicknesses prior to the MPT. The 10 m starting case has a higher interglacial value of hard bedded area before the MPT than after – a hard bedded Pliocene domain would progressively become softer throughout the Pleistocene as a result of glacial sediment production. The 20 m starting Pliocene regolith thickness is the only other case which results in a present day distribution (after a full transient simulation) consistent with that observed. This is also the amount which best agrees with both the amount of bedrock erosion found by Naylor et al. (2021) and the Atlantic Quaternary sediment volume estimated by M. Bell and Laine (1985).

The oscillation in hard bedded area throughout each glacial cycle is due to the large volumes of sediment entrained in progressively larger ice sheets (see changes in entrained sediment volume in fig. 63). Within an individual glacial cycle, the

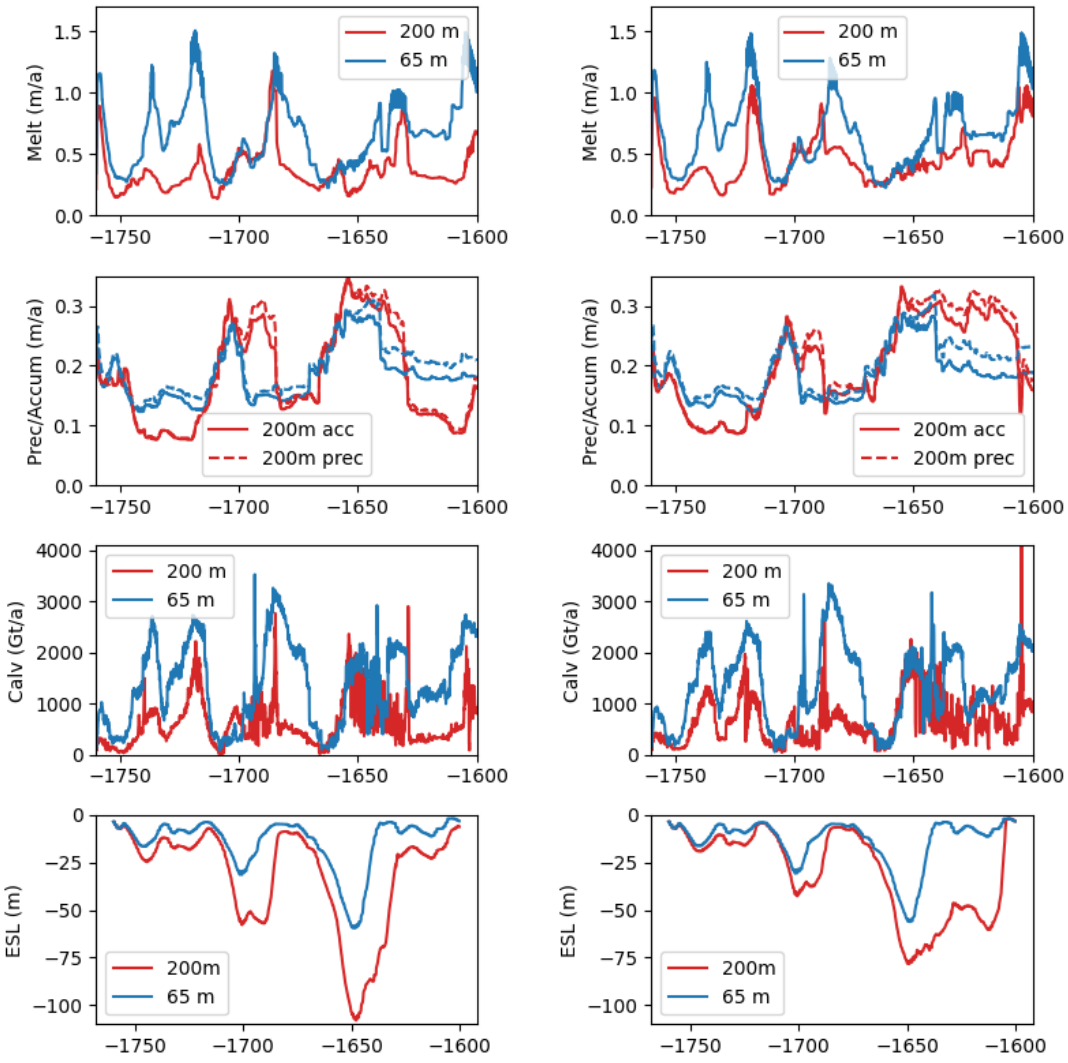

Figure 61: The effect of increased starting sediment thickness in the regolith removal only experiments on whole ice sheet mass balance. Panel a) has isostatic adjustment due to dynamic sediment loading turned off while b) has it on. The difference between the 200 and 65 m starting regolith thickness distributions is less with the isostatic adjustment of sediment load turned on demonstrating the importance of including that process.

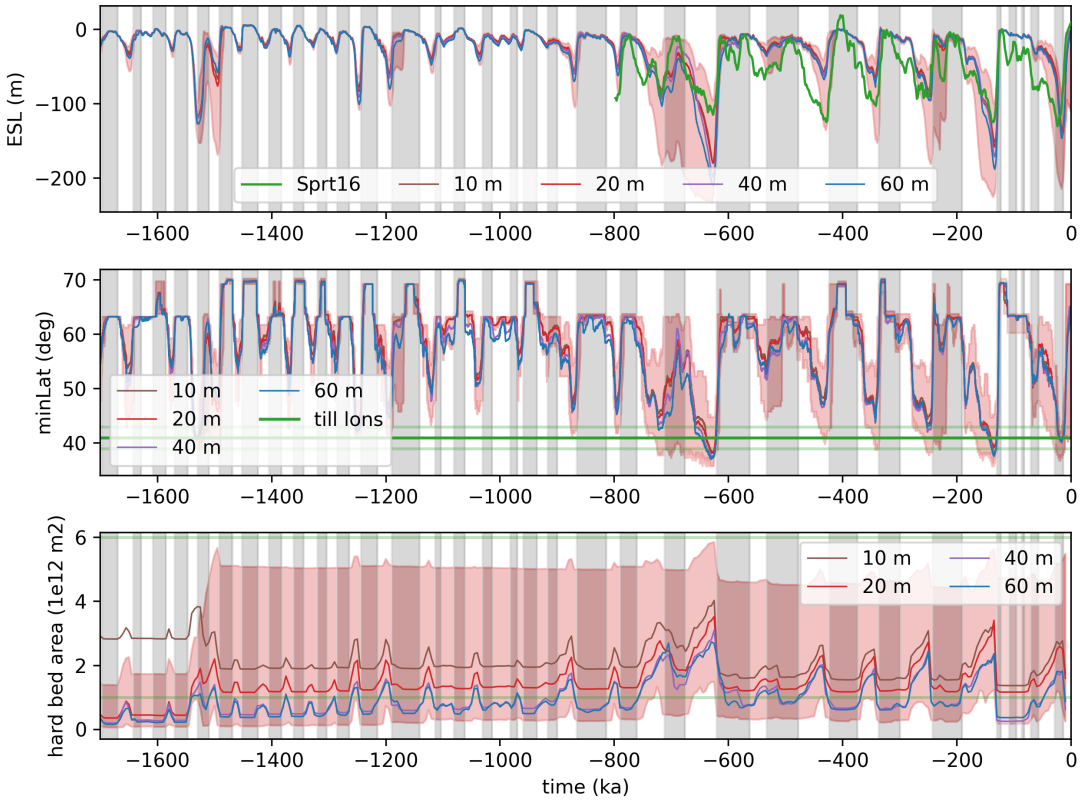

Figure 62: These curves show the progression of glacial cycles for varying levels of Pliocene sediment, including glacial sediment production. The top panel is mean modelled eustatic sea level for each Pliocene sediment thickness compared with the sea level stack of Spratt and Lisiecki (2016) with shaded max/min bounds for the 20 m starting sediment ensemble. The centre panel shows minimum latitude reached by the Laurentide ice sheet compared with the range of latitudes of the tills of Roy et al. (2004), the red shaded region shows the max/min bounds for the 20 m starting sediment ensemble. The bottom panel shows the change in hard bedded area during successive glaciations with the present day estimated range of hard bedded area bounded by the green lines (based on the reconstructions of Pelletier et al. (2016), Shangguan et al. (2017), and Taylor (2023) shown in chap. 5, fig. 39. The red shaded region is max/min bounds on the 20 m ensemble.

hard bedded area grows solely due to this process, a potentially neglected effect in studies of the regolith hypothesis to date. Furthermore, basal debris likely affects the sliding process such that a more hard bedded ice sheet with high basal debris content may slide more slowly than one with little entrained debris (Iverson, Helanow, and Zoet, 2019), a process not currently accounted for in the GSM.

6.6 CONCLUSION

We show that large scale topographic changes from glacial sedimentary processes likely had profound effects on the mass balance of the North American Ice Complex. A more continental ice sheet with reduced marine contact over the Canadian Arctic Archipelago and Hudson Bay and an ice sheet domain at mean higher elevation results in larger North American ice sheets. In some cases, these ice sheets take longer to ablate, giving a prolonged glacial state and even skipping an interglacial (e.g. at 1100 ka). Not accounting for the effect of changing sediment and bedrock load on isostatic adjustment leads to overestimation of the topographically induced changes in the mass balance (e.g. lower calving rates and surface melt).

Physical limits on the rate of glacial denudation further challenges the regolith hypothesis as the North American Ice Complex likely reached its interglacial hard bedded area well in advance of the mid-Pleistocene Transition, given the range of Pliocene regolith thicknesses and erosion rates which agree with inferences from the literature. Regolith may induce a positive feedback whereby larger ice sheets entrain larger volumes of sediment, producing more stabilizing hard bedded areas.

A key caveat to our results is that fluvial transport and hillslope processes are missing from the system studied above. If sediment production and transport in a warm wet Pliocene climate was in an approximate steady state, then glaciation would have significantly perturbed this system. Koppes and Montgomery (2009) finds that fluvial systems in areas undergoing rapid change due to volcanic or

tectonic activity transport more sediment. Likewise, major river systems such as the Mississippi and the MacKenzie could have transported relatively large volumes of sediment during and after rapid change during deglaciation. Currently, the amount of Quaternary sediment in the delta complexes of both rivers is poorly constrained (Hay, Shaw, and Wold, 1989; Stashin, 2021). If the transient climate of Quaternary glacial cycles makes flowing water a more effective transporter of sediment the same way tectonic processes do, this may be an important missing process contributing to regolith hypothesis plausibility. Constraining sediment volumes in major paleo-deltas and basins through subsurface work would reduce uncertainties as to the amount of sediment produced and transported by the North American Ice Complex (NAIC) over the Pleistocene and thereby reduce uncertainty around the landscape evolution contribution to glacial cycle variability. It is also not known whether the tills deposited in the central United States are representative of the majority of early Pleistocene ice sheets or record one off short lived advances. Discovery of additional tills and reduction of the age uncertainty in those deposits would be a major boon to our understanding of Pleistocene glacial cycles.

6.7 METHODS

HARD BEDDED AREA CALCULATION The appropriate criteria for determining the transition from soft bed to hard bed in a coarse model grid cell is not clear and likely depends on the roughness. However, even the relevant roughness is difficult to quantify. Willeit et al. (2019) chose 100 m of sediment as a transition point between hard and soft and uses a dataset for which the proportion of the reported sediment thickness corresponding to unconsolidated sediment is not apparent (seismic p-wave velocity cutoff Laske et al., 2013). Here we use an upscaling from the high resolution (30 arc-second) dataset of Pelletier et al. (2016) to relate mean sediment thickness in a 1x0.5° area to the fraction of area

covered by 0.5 m of regolith or more. Using this relationship, we calculate the area of hard beds by imposing a 0.5 soft bed fraction threshold consistent with the application of hard and soft bedded sliding in the GSM. The present day hard bed area is estimated using the same algorithm applied to three datasets of present day sediment thickness distribution: Pelletier et al. (2016), Shangguan et al. (2017), and Taylor (2023) all upscaled to the same resolution as the 1x0.5° GSM resolution for consistent comparison. This gives a range of estimated North American hard bed areas between 1 and 6 million km^2.

EROSION AND QUATERNARY SEDIMENT CONTROL The best estimate of Quaternary erosion depth at a scale relevant to continental scale ice sheet modelling comes from the reconstruction of Naylor et al. (2021). Therein the authors construct a bedrock digital elevation map (DEM) by assimilating multiple state and provincial bedrock surveys with borehole control. The Pliocene bedrock surface is then reconstructed by interpretation of palimpsest features in the present day bedrock DEM. The Quaternary sediment thickness in this area is then the difference between the surface and bedrock elevations. Naylor et al. (2021) take the difference between the present day and Pliocene DEMs for the bedrock erosion estimate. While this method alleviates the need to calculate mean isostatic adjustment due to removal of regolith and bedrock load, it does not account for any differences in flexure across the domain of reconstruction. As such the error bars for such an estimate are large.

The present day bedrock surface DEM is validated against 938157 boreholes throughout the domain and has a root mean square error of 12.5 m. In light of this, we take 50% as a rough estimate of the uncertainty in the mean erosion thickness estimate for the domain. The erosion parameters were tuned to fall within this uncertainty range.

MODEL TUNING In order to simulate the MPT, the glacial systems model parameter space (climate, ice dynamical, and subglacial hydrological) needed to be adequately probed in order to extract a set of parameter vectors which capture the the following constraints: (1) ice volume of the last glacial maximum (Tarasov et al., 2012), (2) proximity to deglacial margin chronology from LGM (Dyke, 2004), (3) the timing of last deglacial marine limit of Hudson Bay, (4) sea level amplitude in the early and late Pleistocene estimated from Rohling, Foster, Grant, et al. (2014) and Elderfield et al. (2012) for North America and Eurasia (parameterized for other ice masses: Greenland proportional to North America and Eurasia, Antarctica proportional to CO_2), and (5) maximum southerly extent inferred from the mid-western till records (Roy et al., 2004; Balco and Rovey, 2010). This was done through successive iterations of perturbed parameter ensembles of the model, initially with the ice dynamical and climate relevant model components only, then coupling in the subglacial hydrology model and finally the sediment model. This process is further detailed in § 6.10.

6.8 APPENDIX

6.9 MODEL DESCRIPTION

This model is driven only by insolation and atmospheric greenhouse gas concentration. The climate is a weighting between a two dimensional energy balance model (EBM) with non-linear snow/ice albedo feedbacks and slab ocean; and glacially-indexed PMIP fields. The glacial indexing is based on North Atlantic sea surface temperature from the EBM and the height of the Keewatin ice dome, while both PMIP1 and PMIP2 fields are used to incorporate climate fields for different thicknesses of Keewatin ice. The ice sheet dynamics are 3D thermomechanically coupled and use hybrid shallow-ice/ shallow-shelf physics (Pollard and Deconto, 2009). The basal sliding calculation is a function of the basal shear stress, water pressure, and soft sediment mask. The subglacial hydrology component computes the basal water pressure and is fully coupled to the ice dynamics (Drew and Tarasov, 2022). This component includes both inefficient (linked cavity) and efficient (tunnel) subglacial drainage. The sediment model is mass conserving and incorporates the dominant glacial sedimentary processes (Melanson, T. Bell, and Tarasov, 2013; Hildes et al., 2004). Sediment is transported englacially by regelation entrainment and basal melt out deposition or subglacially through soft sediment deformation. Bedrock is quarried (through subglacial water pressure) and abraded (by englacial sediment grains), modifying the topography at higher or lower rates depending on how much sediment cover there is.

The GSM includes a full accounting of the interactions between the North American ice sheet and the surface of the solid earth. In detail, the change in bed elevation from end Pliocene (2.58M Ma) to present day is the sum of the change in regolith cover, bedrock erosion, and the solid earth response (isostatic adjustment, IA) to those changes:

$$\mathrm{bed}_{Plio} - \mathrm{bed}_{PD} = \mathrm{reg}_{Plio} - \mathrm{reg}_{PD} - \mathrm{Ero} + \mathrm{IA}\left(\mathrm{Ero}, \mathrm{reg}_{Plio} - \mathrm{reg}_{PD}\right) \quad (113)$$

Where bed_{Plio} and bed_{PD} are the Pliocene and present day bed elevations respectively, reg_{Plio} and reg_{PD} are the Pliocene and present day regolith thickness distributions, (Ero is the bed erosion from quarrying and abrasion, and IA $(\text{Ero}, \text{reg}_{Plio} - \text{reg}_{PD})$ is the visco-elastic solid earth response to those changes.

6.10 ASSESSING SYSTEM BEHAVIOUR & MAPPING THE PARAMETER SPACE

A set of dynamics coupled to this degree is highly non-linear and the 2.5 Myr length of the Pleistocene is infeasible for performing a parameteric probe for the entire interval. As such we use efficient sampling methods to map the model parameter vector space to system behaviour – iteratively sampling, scoring the model output, and resampling. The first was a Latin-hyper-cube sampling with 1000 members over 10 ice dynamic and climate parameters run during the last glacial interval (120 ka to present). Those with acceptable ice volume at last glacial maximum, deglacial margin reproduction, and well timed Hudson Bay deglaciation were then run for MIS 55 to 45 (1600 to 1400 ka). Ensemble parameter vectors which then also reproduced eustatic sea level amplitude in line with available reconstructions, reached a north-south extent matching the till record within dating uncertainty, and had volumes not surpassing that at LGM were then selected. For this sub-ensemble. each parameter vector component was fitted to a Beta distribution. Three iterations of Latin-hyper-cube sampling from these Beta distributions, scoring, and beta-fitting were performed.

Once a set of ice dynamic and climate parameter vectors which performed well on both pre and post MPT periods was obtained, a sensitivity analysis was conducted to tune the subglacial hydrologic and sediment models. The results of this sensitivity analysis were used to select a representative subset of parameter vectors – 19 vectors for the negligible erosion experiments and 56 for the tuned

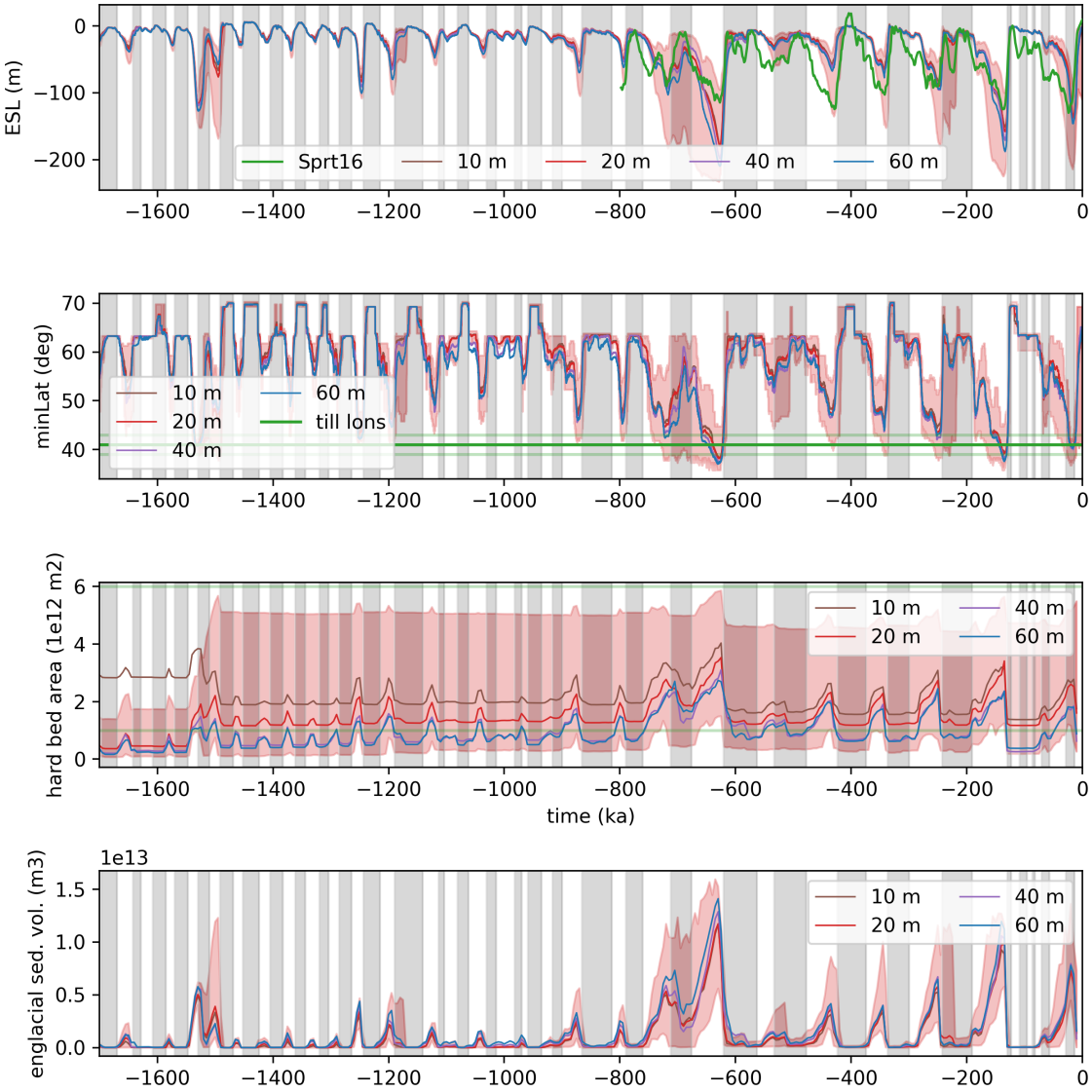

Figure 63: Eustatic sea level, minimum latitude of ice, hard bedded area all shown in relation to the total englacial sediment volume. Large volumes of sediment are entrained – enough to explain nearly 1 million km^2 changes in hard bedded area between glacials and interglacials.

erosion experiments. These sets were used for 2.58 Myr regolith removal simulations.

6.11 ATMOSPHERIC GREENHOUSE GAS

(**Huybers˙2006**; Dyez, Hönisch, and Schmidt, 2018)

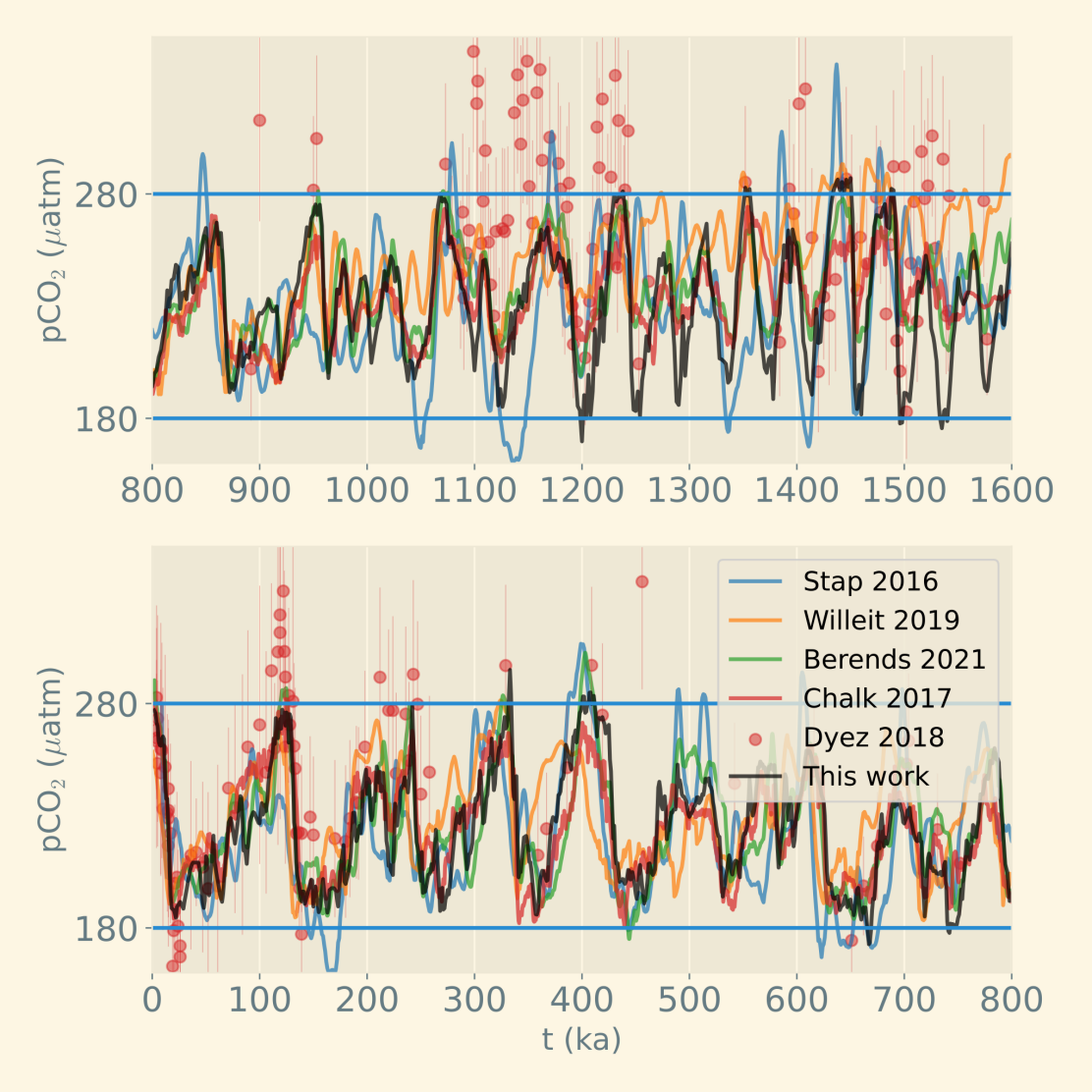

Figure 64: Comparison between multiple CO2 proxy reconstructions and the composite regression and EPICA approach used here.

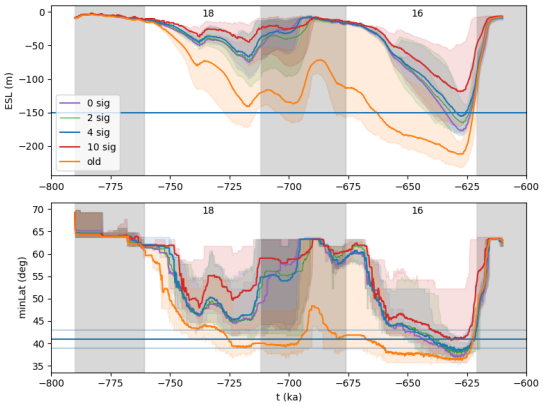

Figure 65: Model results demonstrating the effects of bias and uncertainty in EPICA CO_2 concentrations at the bottom of the core for MIS 18-16 . Old and mean estimates give sea level minima around 200 m.

6.11.1 *EPICA Uncertainty and the update to MIS 18-16 CO2*

Bereiter et al. (2015) found an analytical bias in the EPICA CO_2 at the bottom of the core covering marine isotope stages 18 through 16 from the analysis of Lüthi et al. (2008) and Siegenthaler et al. (2005) . This updated CO_2 decreases the ice volume at glacial maximum during MIS 18-16 – the period of lowest sea level in our ensembles. Though the full magnitude of EPICA CO_2 may be greater, we use the two σ CO_2 time series in fig. 65 in our forcing.

REFERENCES

Ahn, S., D. Khider, L. E. Lisiecki, and C. E. Lawrence (2017). "A probabilistic Pliocene–Pleistocene stack of benthic δ^{18}O using a profile hidden Markov model". In: *Dynamics and Statistics of the Climate System* 2.1. ISSN: 2059-6987. DOI: 10.1093/climsys/dzx002. URL: http://dx.doi.org/10.1093/climsys/dzx002.

Balco, G. and C. W. Rovey (Sept. 2010). "Absolute chronology for major Pleistocene advances of the Laurentide Ice Sheet". In: *Geology* 38.9, pp. 795–798. ISSN: 0091-7613. DOI: 10.1130/g30946.1. URL: http://dx.doi.org/10.1130/G30946.1.

Bell, M. and E. P. Laine (Mar. 1985). "Erosion of the Laurentide Region of North America by Glacial and Glaciofluvial Processes". In: *Quaternary Research* 23.02, pp. 154–174. ISSN: 1096-0287. DOI: 10.1016/0033-5894(85)90026-2. URL: http://dx.doi.org/10.1016/0033-5894(85)90026-2.

Bereiter, B., S. Eggleston, J. Schmitt, C. Nehrbass-Ahles, T. F. Stocker, H. Fischer, S. Kipfstuhl, and J. Chappellaz (Jan. 2015). "Revision of the EPICA Dome C CO2 record from 800 to 600 kyr before present". In: *Geophysical Research Letters* 42.2, pp. 542–549. ISSN: 0094-8276. DOI: 10.1002/2014gl061957. URL: http://dx.doi.org/10.1002/2014GL061957.

Berger, A. and M. Loutre (July 2010). "Modeling the 100-kyr glacial–interglacial cycles". In: *Global and Planetary Change* 72.4, pp. 275–281. ISSN: 0921-8181. DOI: 10.1016/j.gloplacha.2010.01.003. URL: http://dx.doi.org/10.1016/j.gloplacha.2010.01.003.

Clark, P. U., D. Archer, D. Pollard, J. D. Blum, J. A. Rial, V. Brovkin, A. C. Mix, N. G. Pisias, and M. Roy (Dec. 2006). "The middle Pleistocene transition: characteristics, mechanisms, and implications for long-term changes in atmospheric pCO2". In: *Quaternary Science Reviews* 25.23-24, pp. 3150–3184.

ISSN: 0277-3791. DOI: 10.1016/j.quascirev.2006.07.008. URL: http://dx.doi.org/10.1016/j.quascirev.2006.07.008.

Clark, P. U. and D. Pollard (Feb. 1998). "Origin of the Middle Pleistocene Transition by ice sheet erosion of regolith". In: *Paleoceanography* 13.1, pp. 1–9. ISSN: 0883-8305. DOI: 10.1029/97pa02660. URL: http://dx.doi.org/10.1029/97PA02660.

Cuffey, K. and W. S. B. Paterson (2010). *The Physics of Glaciers*. 4th ed. Academic Press.

Dalton, A. S., M. Margold, C. R. Stokes, L. Tarasov, A. S. Dyke, R. S. Adams, S. Allard, H. E. Arends, N. Atkinson, J. W. Attig, P. J. Barnett, R. L. Barnett, M. Batterson, P. Bernatchez, H. W. Borns, A. Breckenridge, J. P. Briner, E. Brouard, J. E. Campbell, A. E. Carlson, J. J. Clague, B. B. Curry, R.-A. Daigneault, H. Dubé-Loubert, D. J. Easterbrook, D. A. Franzi, H. G. Friedrich, S. Funder, M. S. Gauthier, A. S. Gowan, K. L. Harris, B. Hétu, T. S. Hooyer, C. E. Jennings, M. D. Johnson, A. E. Kehew, S. E. Kelley, D. Kerr, E. L. King, K. K. Kjeldsen, A. R. Knaeble, P. Lajeunesse, T. R. Lakeman, M. Lamothe, P. Larson, M. Lavoie, H. M. Loope, T. V. Lowell, B. A. Lusardi, L. Manz, I. McMartin, F. C. Nixon, S. Occhietti, M. A. Parkhill, D. J. Piper, A. G. Pronk, P. J. Richard, J. C. Ridge, M. Ross, M. Roy, A. Seaman, J. Shaw, R. R. Stea, J. T. Teller, W. B. Thompson, L. H. Thorleifson, D. J. Utting, J. J. Veillette, B. C. Ward, T. K. Weddle, and H. E. Wright (Apr. 2020). "An updated radiocarbon-based ice margin chronology for the last deglaciation of the North American Ice Sheet Complex". In: *Quaternary Science Reviews* 234, p. 106223. ISSN: 0277-3791. DOI: 10.1016/j.quascirev.2020.106223. URL: http://dx.doi.org/10.1016/j.quascirev.2020.106223.

Drew, M. and L. Tarasov (Nov. 2022). "Surging of a Hudson Strait Scale Ice Stream: Subglacial hydrology matters but the process details don't". In: DOI: 10.5194/tc-2022-226. URL: http://dx.doi.org/10.5194/tc-2022-226.

Dyez, K. A., B. Hönisch, and G. A. Schmidt (Nov. 2018). "Early Pleistocene Obliquity-Scale pCO 2 Variability at 1.5 Million Years Ago". In: *Paleoceanography and Paleoclimatology* 33.11, pp. 1270–1291. ISSN: 2572-4525. DOI: 10.1029/2018pa003349. URL: http://dx.doi.org/10.1029/2018PA003349.

Dyke, A. S. (2004). "An outline of North American deglaciation with emphasis on central and northern Canada". In: *Developments in Quaternary Sciences*, pp. 373–424. ISSN: 1571-0866. DOI: 10.1016/s1571-0866(04)80209-4. URL: http://dx.doi.org/10.1016/S1571-0866(04)80209-4.

Ehlers, T. A., K. A. Farley, M. E. Rusmore, and G. J. Woodsworth (2006). "Apatite (U-Th)/He signal of large-magnitude accelerated glacial erosion, southwest British Columbia". In: *Geology* 34.9, p. 765. ISSN: 0091-7613. DOI: 10.1130/g22507.1. URL: http://dx.doi.org/10.1130/G22507.1.

Elderfield, H., P. Ferretti, M. Greaves, S. Crowhurst, I. N. McCave, D. Hodell, and A. M. Piotrowski (Aug. 2012). "Evolution of Ocean Temperature and Ice Volume Through the Mid-Pleistocene Climate Transition". In: *Science* 337.6095, pp. 704–709. ISSN: 1095-9203. DOI: 10.1126/science.1221294. URL: http://dx.doi.org/10.1126/science.1221294.

Hay, W. W., C. A. Shaw, and C. N. Wold (July 1989). "Mass-balanced paleogeographic reconstructions". In: *Geologische Rundschau* 78.1, pp. 207–242. ISSN: 1437-3262. DOI: 10.1007/bf01988362. URL: http://dx.doi.org/10.1007/bf01988362.

Hays, J. D., J. Imbrie, and N. J. Shackleton (Dec. 1976). "Variations in the Earth's Orbit: Pacemaker of the Ice Ages". In: *Science* 194.4270, pp. 1121–1132. ISSN: 1095-9203. DOI: 10.1126/science.194.4270.1121. URL: http://dx.doi.org/10.1126/science.194.4270.1121.

Hidy, A. J., J. C. Gosse, D. G. Froese, J. D. Bond, and D. H. Rood (Feb. 2013). "A latest Pliocene age for the earliest and most extensive Cordilleran Ice Sheet in northwestern Canada". In: *Quaternary Science Reviews* 61, pp. 77–84. ISSN:

0277-3791. DOI: 10.1016/j.quascirev.2012.11.009. URL: http://dx.doi.org/10.1016/j.quascirev.2012.11.009.

Hildes, D. H., G. K. Clarke, G. E. Flowers, and S. J. Marshall (Feb. 2004). "Subglacial erosion and englacial sediment transport modelled for North American ice sheets". In: *Quaternary Science Reviews* 23.3-4, pp. 409–430. ISSN: 0277-3791. DOI: 10.1016/j.quascirev.2003.06.005. URL: http://dx.doi.org/10.1016/j.quascirev.2003.06.005.

Iverson, N. R., C. Helanow, and L. K. Zoet (Dec. 2019). "Debris-bed friction during glacier sliding with ice–bed separation". In: *Annals of Glaciology* 60.80, pp. 30–36. ISSN: 1727-5644. DOI: 10.1017/aog.2019.46. URL: http://dx.doi.org/10.1017/aog.2019.46.

Koppes, M. N. and D. R. Montgomery (Aug. 2009). "The relative efficacy of fluvial and glacial erosion over modern to orogenic timescales". In: *Nature Geoscience* 2.9, pp. 644–647. ISSN: 1752-0908. DOI: 10.1038/ngeo616. URL: http://dx.doi.org/10.1038/NGEO616.

Laske, G., G. Masters, Z. Ma, and M. E. Pasyanos (2013). "Update on CRUST1.0: a 1-degree Global Model of Earth's Crust". In: *Geophysical Research Abstracts*. Vol. 15. European Geosciences Union General Assembly 2013 2658. European Geosciences Union. Vienna,Austria.

Lisiecki, L. E. and M. E. Raymo (Jan. 2005). "A Pliocene-Pleistocene stack of 57 globally distributed benthic δ^{18}O records". In: *Paleoceanography* 20.1, n/a–n/a. ISSN: 0883-8305. DOI: 10.1029/2004pa001071. URL: http://dx.doi.org/10.1029/2004PA001071.

Lüthi, D., M. Le Floch, B. Bereiter, T. Blunier, J.-M. Barnola, U. Siegenthaler, D. Raynaud, J. Jouzel, H. Fischer, K. Kawamura, and T. F. Stocker (May 2008). "High-resolution carbon dioxide concentration record 650,000-800,000 years before present". In: *Nature* 453.7193, pp. 379–382. ISSN: 1476-4687. DOI: 10.1038/nature06949. URL: http://dx.doi.org/10.1038/nature06949.

Melanson, A., T. Bell, and L. Tarasov (May 2013). "Numerical modelling of subglacial erosion and sediment transport and its application to the North American ice sheets over the Last Glacial cycle". In: *Quaternary Science Reviews* 68, pp. 154–174. ISSN: 0277-3791. DOI: 10.1016/j.quascirev.2013.02.017. URL: http://dx.doi.org/10.1016/j.quascirev.2013.02.017.

Naylor, S., A. D. Wickert, D. A. Edmonds, and B. J. Yanites (Nov. 2021). "Landscape evolution under the southern Laurentide Ice Sheet". In: *Science Advances* 7.48. ISSN: 2375-2548. DOI: 10.1126/sciadv.abj2938. URL: http://dx.doi.org/10.1126/sciadv.abj2938.

Pelletier, J. D., P. D. Broxton, P. Hazenberg, X. Zeng, P. A. Troch, G.-Y. Niu, Z. Williams, M. A. Brunke, and D. Gochis (Jan. 2016). "A gridded global data set of soil, intact regolith, and sedimentary deposit thicknesses for regional and global land surface modeling". In: *Journal of Advances in Modeling Earth Systems* 8.1, pp. 41–65. ISSN: 1942-2466. DOI: 10.1002/2015ms000526. URL: http://dx.doi.org/10.1002/2015MS000526.

Pollard, D. and R. M. Deconto (Mar. 2009). "A Coupled Ice-Sheet/Ice-Shelf/Sediment Model Applied to a Marine-Margin Flowline: Forced and Unforced Variations". In: *Glacial Sedimentary Processes and Products*, pp. 37–52. DOI: 10.1002/9781444304435.ch4. URL: http://dx.doi.org/10.1002/9781444304435.ch4.

Raymo, M. E., R. Kozdon, D. Evans, L. Lisiecki, and H. L. Ford (Feb. 2018). "The accuracy of mid-Pliocene δ^{18}O-based ice volume and sea level reconstructions". In: *Earth-Science Reviews* 177, pp. 291–302. ISSN: 0012-8252. DOI: 10.1016/j.earscirev.2017.11.022. URL: http://dx.doi.org/10.1016/j.earscirev.2017.11.022.

Rohling, E. J., G. L. Foster, K. M. Grant, G. Marino, A. P. Roberts, M. E. Tamisiea, and F. Williams (Apr. 2014). "Sea-level and deep-sea-temperature variability over the past 5.3 million years". In: *Nature* 508.7497, pp. 477–482. ISSN: 1476-

4687. DOI: 10.1038/nature13230. URL: http://dx.doi.org/10.1038/nature13230.

Rohling, E. J., G. L. Foster, T. M. Gernon, K. M. Grant, D. Heslop, F. D. Hibbert, A. P. Roberts, and J. Yu (Nov. 2022). "Comparison and Synthesis of Sea-Level and Deep-Sea Temperature Variations Over the Past 40 Million Years". In: *Reviews of Geophysics* 60.4. ISSN: 1944-9208. DOI: 10.1029/2022rg000775. URL: http://dx.doi.org/10.1029/2022RG000775.

Roy, M., P. U. Clark, G. M. Raisbeck, and F. Yiou (Nov. 2004). "Geochemical constraints on the regolith hypothesis for the middle Pleistocene transition". In: *Earth and Planetary Science Letters* 227.3-4, pp. 281–296. ISSN: 0012-821X. DOI: 10.1016/j.epsl.2004.09.001. URL: http://dx.doi.org/10.1016/j.epsl.2004.09.001.

Shangguan, W., T. Hengl, J. Mendes de Jesus, H. Yuan, and Y. Dai (Jan. 2017). "Mapping the global depth to bedrock for land surface modeling". In: *Journal of Advances in Modeling Earth Systems* 9.1, pp. 65–88. ISSN: 1942-2466. DOI: 10.1002/2016ms000686. URL: http://dx.doi.org/10.1002/2016MS000686.

Siegenthaler, U., T. F. Stocker, E. Monnin, D. Lüthi, J. Schwander, B. Stauffer, D. Raynaud, J.-M. Barnola, H. Fischer, V. Masson-Delmotte, and J. Jouzel (Nov. 2005). "Stable Carbon Cycle–Climate Relationship During the Late Pleistocene". In: *Science* 310.5752, pp. 1313–1317. ISSN: 1095-9203. DOI: 10.1126/science.1120130. URL: http://dx.doi.org/10.1126/science.1120130.

Spratt, R. M. and L. E. Lisiecki (Apr. 2016). "A Late Pleistocene sea level stack". In: *Climate of the Past* 12.4, pp. 1079–1092. ISSN: 1814-9332. DOI: 10.5194/cp-12-1079-2016. URL: http://dx.doi.org/10.5194/cp-12-1079-2016.

Stashin, S. (2021). "Late Cenozoic Basin Evolution of the western Canadian Arctic Archipelago: The Beaufort Formation and Iperk Sequence". Masters Thesis. Dalhousie University. URL: http://hdl.handle.net/10222/80367.

Tarasov, L., A. S. Dyke, R. M. Neal, and W. Peltier (Jan. 2012). "A data-calibrated distribution of deglacial chronologies for the North American ice complex from glaciological modeling". In: *Earth and Planetary Science Letters* 315-316, pp. 30–40. ISSN: 0012-821X. DOI: 10.1016/j.epsl.2011.09.010. URL: http://dx.doi.org/10.1016/j.epsl.2011.09.010.

Taylor, A. (Mar. 2023). "Sediment thickness map of continental Canada and Canada-U.S. transboundary watersheds". In.

Tzedakis, P. C., M. Crucifix, T. Mitsui, and E. W. Wolff (Feb. 2017). "A simple rule to determine which insolation cycles lead to interglacials". In: *Nature* 542.7642, pp. 427–432. ISSN: 1476-4687. DOI: 10.1038/nature21364. URL: http://dx.doi.org/10.1038/nature21364.

Tziperman, E. and H. Gildor (Jan. 2003). "On the mid-Pleistocene transition to 100-kyr glacial cycles and the asymmetry between glaciation and deglaciation times". In: *Paleoceanography* 18.1, pp. 1–8. ISSN: 0883-8305. DOI: 10.1029/2001pa000627. URL: http://dx.doi.org/10.1029/2001PA000627.

Westerhold, T., N. Marwan, A. J. Drury, D. Liebrand, C. Agnini, E. Anagnostou, J. S. K. Barnet, S. M. Bohaty, D. De Vleeschouwer, F. Florindo, T. Frederichs, D. A. Hodell, A. E. Holbourn, D. Kroon, V. Lauretano, K. Littler, L. J. Lourens, M. Lyle, H. Pälike, U. Röhl, J. Tian, R. H. Wilkens, P. A. Wilson, and J. C. Zachos (Sept. 2020). "An astronomically dated record of Earth's climate and its predictability over the last 66 million years". In: *Science* 369.6509, pp. 1383–1387. ISSN: 1095-9203. DOI: 10.1126/science.aba6853. URL: http://dx.doi.org/10.1126/science.aba6853.

Westerhold, T., U. Röhl, and J. Laskar (June 2012). "Time scale controversy: Accurate orbital calibration of the early Paleogene". In: *Geochemistry, Geophysics, Geosystems* 13.6, n/a–n/a. ISSN: 1525-2027. DOI: 10.1029/2012gc004096. URL: http://dx.doi.org/10.1029/2012GC004096.

Willeit, M., A. Ganopolski, R. Calov, and V. Brovkin (Apr. 2019). “Mid-Pleistocene transition in glacial cycles explained by declining CO2 and regolith removal”. In: *Science Advances* 5.4, eaav7337. ISSN: 2375-2548. DOI: 10.1126/sciadv.aav7337. URL: http://dx.doi.org/10.1126/sciadv.aav7337.

Chapter 7

Conclusions

In this project, a model which incorporates all of the relevant processes for simulating multi-million year glacial cycle and landscape evolution, permitting study of their contribution to ice sheet variability over the last geologic period is laid out. In particular, this work builds to a test of the self-consistency of the Regolith Hypothesis for the MPT. In order to model the contribution from the regolith mechanism to the MPT, basal processes are needed to simulate glacial sedimentation and the interactions between basal processes and the broader earth system. In chap. 2 and 3 the conceptual framework and model building for the relevant basal processes is presented before examing the contribution from subglacial hydrology to ice stream variability in the subsequent chapter.

7.1 SUBGLACIAL HYDROLOGY

In order to study the subglacial hydrologic contribution to large scale ice stream variability, several subglacial hydrologic systems have been incorporated in the the 3D thermomechanically coupled Glacial Systems Model (GSM). These are: poro-elastic, linked-cavity, and leaky-bucket. Two of these are mass conserving – flux in the poro-elastic system follows Darcy's Law for laminar flow and linked-cavity flux follows the Darcy-Weisbach equation for turbulent flow. The other system – leaky-bucket – is not mass conserving and simply integrates the basal mass balance in a subglacial reservoir with a constant leak (removal) rate.

In this work, value ranges are justified for parameters which have little justification elsewhere in the literature. This modelling work demonstrates that subglacial hydrology is an important influence on ice sheet geometry (given a crude climate representation) for all three subglacial hydrologic systems.

Three aspects of ice stream surging are examined for a Hudson Strait scale ice stream: number of surges in a 50 kyr period (periodicity), size of the velocity increase (amplitude), and duration of the surge. Sensitivity analysis shows that

the effective pressure normalization term used in the basal velocity calculation is the most important parameter for determining ice streams prone to surging – significantly more than other parameters responsible for hard and soft bedded sliding.

The contribution from each subglacial hydrologic system to the surge characteristics is not different except in the case of duration. Each produces roughly the same distribution of surge periodicity and amplitude. However the linked-cavity hydrology produces longer duration surges than the other two. This is likely due to a negative feedback on basal velocity in the linked-cavity system. Whereby higher velocities give faster cavity opening rates which give higher effective pressures and higher effective pressures slow basal sliding velocities. While the poro-elastic and leaky-bucket hydrologies quickly go to zero effective pressure, the linked-cavity system can sustain more intermediate values of effective pressure maintaining melt-water generation due to frictional heating throughout the surge.

This subglacial hydrology system forms an important system inductance which makes the transition from cold-based to a warm based sliding patch of ice more continuous. The experiments demonstrate that inclusion of this inductance is necessary for producing surge type behaviour in large ice streams at time scales longer than centennial but the specific form of the system is less important.

These processes have yet to gain widespread adoption in ice sheet modelling. Building upon this examination, this subglacial hydrology is coupled to a model of glacial sedimentary processes in order to establish bounds on the Pliocene regolith thickness.

7.2 GLACIAL SEDIMENTARY PROCESSES, CONSTRAINTS, AND THE PLIOCENE REGOLITH

This work tightens the previously wide bounds on Pliocene regolith thickness through the constraints of present day distribution of sediment, sparse estimates of Pleistocene erosion, and bulk estimates of off-shore sediment.

Sensitivity tests with a square root ice sheet with dynamically determined sliding velocities show that subglacial hydrology and regolith effective viscosity are the two basal process parameters which most greatly affect the rate of regolith removal. Furthermore, the rate of basal meltwater production affects sediment transport sensitivity to all hydrology and sediment parameters.

In full Pleistocene transient numerical experiments of the North American Ice Complex with varied initial Pliocene regolith thicknesses, 20 m and below results in the best fits with the inferred present day distribution. However, this present day distribution is highly uncertain with large variance in sediment thickness between the three datasets examined. Owing to this large variance, the inference of present day hard bedded area over the previous glaciated regions of North America has a broad range – between one and six million km^2. When applied to the modelling, the available erosion constraints and bulk estimates of Quaternary sediment in the North American region of the Atlantic Ocean gives a Pliocene regolith thickness less than 60 m. The 20 m Pliocene regolith thickness ensemble has the least misfit to these constraints. With established bounds on Pliocene regolith, tested model of glacial sedimentation, and fully coupled earth system, a test of the self-consistency of the Regolith Hypothesis is now feasible.

7.3 REGOLITH REMOVAL AND THE MPT

With the tools and findings developed in the rest of this project, the GSM was applied to the simulation of Pleistocene regolith removal and its holistic effect on Pleistocene glacial cycles. Two sets of experiments were conducted, the first without sediment production and the second with.

In the no sediment production set of ensembles, a large range of Pliocene regolith thicknesses bound the range inferred from observation for mean material removal from North America. These experiments demonstrate the effect of topographic uncertainty on the intensity and duration of glaciation across the MPT. When larger Pliocene regolith thicknesses are imposed, some glaciations grow large enough continental ice volumes to survive orbital interglacials and thereby enable a longer glacial cycle. This is due to the changes in mass balance due to reduced marine feedbacks (i.e. lower calving rates) and reduced negative surface mass balance from a higher elevation domain. This effect is slightly reduced when isostatic adjustment of the changing bed is included. Changing amounts of regolith thickness do not affect the MPT in a way which the classical regolith hypothesis would predict: increasing amounts of regolith does not simply delay the onset of the MPT, but through the topographic effects on the rest of the system can produce longer and stronger early Pleistocene glaciations.

Experiments incorporating sediment production do not show the North American Ice Complex removing an appropriate amount of regolith around the time of the MPT. Instead, the ensemble which most closely matches the erosional and transport constraints reaches a hard bedded area within the present day bounds well in advance of the MPT (1500 kyr), with little mean change thereafter. Interestingly, the transient simulations produce a common amount of hard bedded area for all Pliocene regolith ensembles. Sediment cover inhibits sediment production – thus

encouraging denudation, while bedrock exposure allows generating sediment – thus increasing sediment cover.

These results pose a challenge to the classical Regolith Hypothesis for the MPT. Regolith removal appears more likely to be part of a set of processes non-linearly contributing to the MPT.

7.4 FUTURE DIRECTIONS

Basal processes form a critical part of the earth system. Interactions between processes at the ice-bed interface and the adjacent systems can produce behaviours which are difficult to predict until properly encoded in a coupled model. Footprints left on the Earth's surface by these processes can provide important information about its history. This work is a step toward using numerical models of basal processes to incorporate information from the sedimentary record into our understanding of past earth system dynamics in a quantitative way.

A critical need is to constrain the sediment budget through observation and relate the processes herein to the formation of landforms at large scale. Subsurface work which constrains the amount of Quaternary aged sediment in important off-shore basins will greatly reduce uncertainties in Pliocene regolith thickness. Estimates of eroded bedrock depth from (e.g.) cosmogenic isotopes and thermochronometry at large scale will be important for constraining the supply side of the Quaternary sediment budget. Furthermore, it may be possible to relate particular landforms to basal process regimes. For example, eskers are thought to be deposited in Röthlisberger channels (R-channels) and may be relatable to efficient drainage regimes in subglacial hydrology models. Drumlins and megascale lineations may be relatable to particular sliding and soft sediment deformation regimes. An understanding of the relationship between tunnel valleys and glacio-fluvial systems

may help constrain the action of subglacial hydrology and subglacial lake drainage events.

Sediment volumes stored in the layers of ice rafted debris which define Heinrich Events may be useful for establishing rates of glacial entrainment and transport of sediment. Modelling the englacial transport will lead to a deeper understanding of the inferred relationship between the Heinrich Event record and surging of the Laurentide ice sheet. Incorporating these constraints will push our understanding of earth system dynamics futher back in time and strengthen our prediction of the changes yet to come.

Chapter 8

Appendix A

8.1 DISCRETIZATIONS

8.1.1 *Hydrology Model Discretization*

Discretization of a General Transport Equation

Calculation of mass balance is done through finite volume discretization of the transport equation, eqn. 114. Here I show this discretization for one dimension, after Patankar (1980) and Norris (2000).

$$\frac{\partial(\rho\phi)}{\partial t} + \frac{\partial(\rho u\phi)}{\partial x} = S_\phi \tag{114}$$

The density is held constant

$$\rho(x,t) = \rho. \tag{115}$$

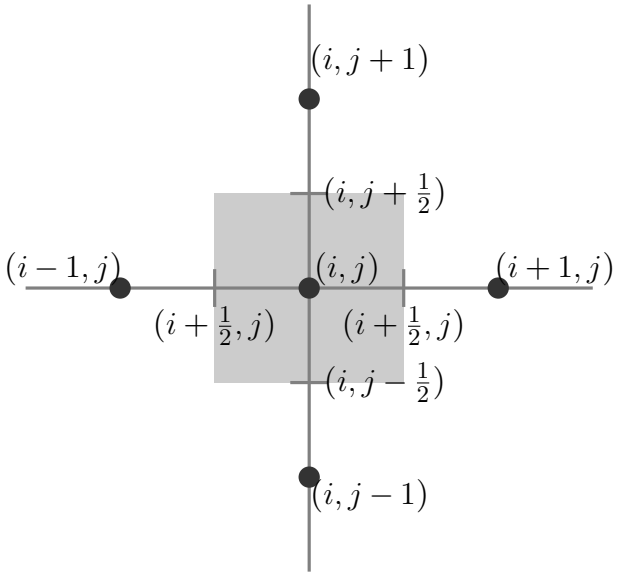

Figure 66: Staggered grid and labelled indices used in the the hydrology discretization. The control volume used for finite volume discretization is shaded in grey.

The general transported property in 114, ϕ, will be replaced later by basal water thickness and transport is treated as pure advection. Integration over the control volume and time step gives:

$$\int_t^{t+\Delta t} \int_{x_{i-\frac{1}{2}}}^{x_{i+\frac{1}{2}}} \frac{\partial(\rho\phi)}{\partial t} dx dt + \int_t^{t+\Delta t} \int_{x_{i-\frac{1}{2}}}^{x_{i+\frac{1}{2}}} \frac{\partial(\rho u\phi)}{\partial x} dx dt = \int_t^{t+\Delta t} \int_{x_{i-\frac{1}{2}}}^{x_{i+\frac{1}{2}}} S_\phi dx dt \tag{116}$$

$$\rho\left[\phi_i^{n+1} - \phi_i^n\right]\Delta x + \int_t^{t+\Delta t} \rho\left[u_{i+\frac{1}{2}}\left(\phi_{i+\frac{1}{2}}\right)\phi_{i+\frac{1}{2}} - u_{i-\frac{1}{2}}\left(\phi_{i-\frac{1}{2}}\right)\phi_{i-\frac{1}{2}}\right] dt = S_\phi \Delta x \Delta t \tag{117}$$

where ϕ^n is the current value and ϕ^{n+1} is the value at start of the next iteration. This presents two problems:

1. ϕ is not defined between time steps

2. nor on the $i \pm \frac{1}{2}$ interfaces

To address the first problem, assume the time integral is a weighted average at the start of current time step and at the start of the next time step:

$$\int_t^{t+\Delta t} u\phi dt = \left[(f)u^{n+1}\phi^{n+1} + (1-f)u^n\phi^n\right]\Delta t. \tag{118}$$

Varied values of f gives a range of numerical schemes, *e.g.* :

- $f = 0$ gives an explicit scheme
- $f = 0.5$ gives a semi-implicit Crank Nicholson scheme
- $f = 1$ gives a fully-implicit scheme

Here we will use the explicit scheme:

$$\Delta x\left[\phi_i^{n+1} - \phi_i^n\right] + \left[u_{i+\frac{1}{2}}^n \phi_{i+\frac{1}{2}}^n - u_{i-\frac{1}{2}}^n \phi_{i-\frac{1}{2}}^n\right] = S_\phi \Delta x \Delta t \tag{119}$$

To address the second problem, (Patankar, 1980) uses the upwind formulation of advection coefficient:

$$\phi_{i+\frac{1}{2}} u_{i+\frac{1}{2}} = \begin{cases} \rho\phi_i u_{i+\frac{1}{2}}\left(\phi_i\right) & u_{i+\frac{1}{2}} > 0 \\ \rho\phi_{i+1} u_{i+\frac{1}{2}}\left(\phi_{i+1}\right) & u_{i+\frac{1}{2}} \leq 0 \end{cases} \tag{120}$$

This can be written with the max operator, $\left[\!\left[a, b\right]\!\right]$, which yields which ever argument is most positive.

$$\rho\phi_{i+\frac{1}{2}} \cdot u_{i+\frac{1}{2}}\left(\phi_{i+\frac{1}{2}}\right) = \rho\phi_i \cdot \left[\!\left[u_{i+\frac{1}{2}}\left(\phi_i\right), 0\right]\!\right] - \rho\phi_{i+1} \cdot \left[\!\left[-u_{i+\frac{1}{2}}\left(\phi_{i+1}\right), 0\right]\!\right] \tag{121a}$$

$$\rho\phi_{i-\frac{1}{2}} \cdot u_{i-\frac{1}{2}}\left(\phi_{i-\frac{1}{2}}\right) = \rho\phi_{i-1} \cdot \left[\!\left[u_{i-\frac{1}{2}}\left(\phi_{i-1}\right), 0\right]\!\right] - \rho\phi_i \cdot \left[\!\left[-u_{i-\frac{1}{2}}\left(\phi_i\right), 0\right]\!\right] \tag{121b}$$

Combining eqn. 119 with 121 gives:

$$\frac{\Delta x}{\Delta t}\left[\phi_i^{n+1}-\phi_i^n\right]+\phi_i^n\left[\!\left[u_{i+\frac{1}{2}}^n\left(\phi_i^n\right),0\right]\!\right]-\phi_{i+1}^n\left[\!\left[-u_{i+\frac{1}{2}}^n\left(\phi_{i+1}^n\right),0\right]\!\right]-\phi_{i-1}^n\left[\!\left[u_{i-\frac{1}{2}}^n\left(\phi_{i-1}^n\right),0\right]\!\right]+\phi_i^n\left[\!\left[-u_{i-\frac{1}{2}}^n\left(\phi_i^n\right),0\right]\!\right] = S_\phi\Delta x/\rho \tag{122}$$

Which can be rearranged to show grid point coefficients to check for potential stability violations:

$$\frac{\Delta x}{\Delta t}\phi_i^{n+1}+\phi_i^n\left\{\left[\!\left[u_{i+\frac{1}{2}}^n\left(\phi_i^n\right),0\right]\!\right]+\left[\!\left[-u_{i-\frac{1}{2}}^n\left(\phi_i^n\right),0\right]\!\right]+\frac{\Delta x}{\Delta t}\right\}-\phi_{i+1}^n\left\{\left[\!\left[-u_{i+\frac{1}{2}}^n\left(\phi_{i+1}^n\right),0\right]\!\right]\right\} -\phi_{i-1}^n\left\{\left[\!\left[u_{i-\frac{1}{2}}^n\left(\phi_{i-1}^n\right),0\right]\!\right]\right\} = S_\phi\Delta x/\rho \tag{123}$$

Which is rewritten with coefficients:

$$\tilde{a}_i\phi_i^{n+1} = -a_i\phi_i^n+a_{i+1}\phi_{i+1}^n+a_{i-1}\phi_{i-1}^n+S_\phi\Delta x/\rho \tag{124}$$

And the coefficients are written as:

$$a_{i+1} = \left[\!\left[-u_{i+\frac{1}{2}}\left(\phi_{i+1}\right),0\right]\!\right] \tag{125a}$$

$$a_{i-1} = \left[\!\left[u_{i-\frac{1}{2}}\left(\phi_{i-1}\right),0\right]\!\right] \tag{125b}$$

$$\tilde{a}_i = \frac{\Delta x}{\Delta t} \tag{125c}$$

$$
\begin{aligned}
a_i =& \llbracket u_{i+\frac{1}{2}}\left(\phi_i\right), 0 \rrbracket + \llbracket -u_{i-\frac{1}{2}}\left(\phi_i\right), 0 \rrbracket + \tilde{a_i} \\
=& \llbracket u_{i+\frac{1}{2}}\left(\phi_i\right), 0 \rrbracket - \llbracket -u_{i+\frac{1}{2}}\left(\phi_{i+1}\right), 0 \rrbracket + \llbracket -u_{i+\frac{1}{2}}\left(\phi_{i+1}\right), 0 \rrbracket \\
& + \llbracket -u_{i-\frac{1}{2}}\left(\phi_i\right), 0 \rrbracket - \llbracket u_{i-\frac{1}{2}}\left(\phi_{i-1}\right), 0 \rrbracket + \llbracket u_{i-\frac{1}{2}}\left(\phi_{i-1}\right), 0 \rrbracket + \tilde{a_i} \\
=& u_{i+\frac{1}{2}}\left(\phi_{i+\frac{1}{2}}\right) + a_{i+1} - u_{i-\frac{1}{2}}\left(\phi_{i-\frac{1}{2}}\right) + a_{i-1} + \tilde{a_i}
\end{aligned} \tag{125d}
$$

A Priori Stability Evaluation of the Spatial Discretization

Patankar (1980) outlines his *four basic rules* for stability:

1. Consistency at Control Volume Faces (Patankar, 1980, pp. 36): This is equivalent to the conservativeness property of discretisation schemes described in Versteeg and Malalasekera (2007)

    - flux expression from left control volume:

$$
\phi_{1+1/2} \cdot u_{1+1/2} = \phi_1 \llbracket u_{3/2}, 0 \rrbracket - \phi_2 \llbracket -u_{3/2}, 0 \rrbracket
$$

- flux expression from right control volume:

$$\phi_{2-1/2} \cdot u_{2-1/2} = \phi_1 \llbracket u_{3/2}, 0 \rrbracket - \phi_2 \llbracket -u_{3/2}, 0 \rrbracket$$

$\therefore$ Rule 1 satisfied

2. Positive Coefficients (Patankar, 1980, pp. 37):

- $a_{i+1} = \llbracket -u_{i+\frac{1}{2}} \left(\phi_{i+1} \right), 0 \rrbracket \geq 0$
- $a_{i-1} = \llbracket u_{i-\frac{1}{2}} \left(\phi_{i-1} \right), 0 \rrbracket \geq 0$
- $a_i = \llbracket u_{i+\frac{1}{2}} \left(\phi_i \right), 0 \rrbracket + \llbracket -u_{i-\frac{1}{2}} \left(\phi_i \right), 0 \rrbracket \geq 0$

$\therefore$ Rule 2 satisfied

3. Negative Slope Linearization (Patankar, 1980, pp.38):

$$S_h = S_{melt} - S_{aquifer} h$$

$\therefore$ Rule 3 satisfied

4. Sum of the Neighbour Coefficients (Patankar, 1980, eqn. 3.19): Patankar states this rule holds when "differential equations contain only the derivatives of the dependent variable" (Patankar, 1980, pp. 38). For transport of a conservative tracer the transport equation has advective terms of the form[1]:

$$\frac{\partial u_j \phi}{\partial x_j} = u_j \frac{\partial \phi}{\partial x_j} + \phi \frac{\partial u_j}{\partial x_j}. \tag{126}$$

In the examples presented in this chapter of Patankar, he is able to apply a second conservation law, the continuity equation. Assuming constant density:

$$\frac{\partial \cancelto{0}{\rho}}{\partial t} + \rho \frac{\partial u_j}{\partial x_j} = 0 \tag{127}$$

yielding a differential equation composed solely of derivative of the dependent variable ϕ. In the case of this hydrology model however, our conservative tracer is mass (by way of water thickness, scaled volume at constant density) and so the transport equation is the continuity equation. This rule does not therefore apply to our advective scheme.

More concretely, consider a higher hydraulic potential imposed on the system as a result of heavier ice sheet overburden (boundary condition) at the central point. It would be unexpected for the central water thickness to be the average of its neighbours in the absence of some compensating source term.

[1] Here, repeated indices indicate summation.

The **C**ourant-**F**riedrich-**L**ewis (CFL) condition states the maximum velocity cannot exceed the ratio of spatial to temporal resolution:

$$\max\left(v\right) \leq \frac{\Delta x}{\Delta t}. \tag{128}$$

If the above inequality does not hold then velocities may get large enough to pass over a grid cell within a single time step. In this case, an erroneously large flux will be attributed to the passed-over cell. This can result in sharp, self perpetuating solution gradients which generate increasingly nonmonotonic solutions which ring like feedback in a microphone. Typically, a dynamic time step is used to ensure the CFL condition is met, as is the case in this model:

$$\Delta t = \text{FCFL} \lceil\!\lceil \min\left(\Delta x / v\right), \Delta t_{min} \rceil\!\rceil \tag{129}$$

where FCFL is a "safety factor" and Δt_{min} is a lower bound on the time step which will give an error and end the model run.

A more general statement of Patankar (1980)'s fourth rule is the Scarborough condition (Scarborough, 1930, pp. 186), shown here as formulated by Golub, Silvester, and Wathen (1996) and Versteeg and Malalasekera (2007, pp. 143),

$$\frac{\sum\limits_{nb} |a_{nb}|}{|a_p|} \leq 1. \tag{130}$$

Showing again the upwind formulation for the advective transport equation (replacing ϕ with h, the sought quantity in the hydrology model, $\tilde{h}$ the value at the next time step, source m, and velocity (u, v)):

$$
\begin{aligned}
&\rho\tfrac{\partial h}{\partial t} + \rho\tfrac{\partial hu}{\partial x} + \rho\tfrac{\partial hv}{\partial y} = m \\
&\Rightarrow \rho\Delta x\Delta y\left[\tilde{h}_i - h_i\right] + \rho\Delta y\Delta t\left[h_{i+\frac{1}{2}j}u_{i+\frac{1}{2}j} - h_{i-\frac{1}{2}j}u_{i-\frac{1}{2}j}\right] \\
&+ \rho\Delta x\Delta t\left[h_{ij+\frac{1}{2}}u_{ij+\frac{1}{2}} - h_{ij-\frac{1}{2}}u_{ij-\frac{1}{2}}\right] = m\Delta x\Delta y\Delta t \\
&\Rightarrow \left[\tilde{h}_{ij} - h_{ij}\right] + \tfrac{\Delta t}{\Delta x}\left[h_{i+\frac{1}{1}j}u_{i+\frac{1}{2}} - h_{i-\frac{1}{2}}u_{i-\frac{1}{2}}\right] + \tfrac{\Delta t}{\Delta y}\left[h_{ij+\frac{1}{2}}u_{ij+\frac{1}{2}} - h_{ij-\frac{1}{2}}\right] = \tfrac{m\Delta t}{\rho}
\end{aligned}
$$

with the usual upwinding:

$$h_{k+\frac{1}{2}}u_{k+\frac{1}{2}} = \left\lceil u_{k+\frac{1}{2}}\left(h_k\right)h_k, 0\right\rceil - \left\lceil -u_{k+\frac{1}{2}}\left(h_{k+1}\right)h_{k+1}, 0\right\rceil,$$

$$
\begin{aligned}
&* \left[\tilde{h}_{ij} - h_{ij}\right] + \tfrac{\Delta t}{\Delta x}\left\{\left\lceil h_{ij}u_{i+\frac{1}{2}}\left(h_{ij}\right), 0\right\rceil - \left\lceil -h_{i+1j}u_{i+\frac{1}{2}j}\left(h_{i+1j}\right), 0\right\rceil - \left\lceil h_{i-1j}u_{i-\frac{1}{2}j}\left(h_{i-1j}\right), 0\right\rceil + \left\lceil -h_{ij}h_{i-\frac{1}{2}j}\left(h_{ij}\right), 0\right\rceil\right\} \\
&+ \tfrac{\Delta t}{\Delta y}\left\{\left\lceil h_{ij}u_{ij+\frac{1}{2}}\left(h_{ij}\right), 0\right\rceil - \left\lceil -h_{ij+1}u_{ij+\frac{1}{2}}\left(h_{ij+1}\right), 0\right\rceil - \left\lceil h_{ij-1}u_{ij-\frac{1}{2}}\left(h_{ij-1}\right), 0\right\rceil + \left\lceil -h_{ij}u_{ij-\frac{1}{2}}, 0\right\rceil\right\} = \tfrac{m\Delta t}{\rho}
\end{aligned}
$$

Discretization of the Water Transport

$$\frac{\partial h_{wb}}{\partial =} - \nabla \cdot \mathbf{Q} + \frac{m}{\rho_w} \tag{131}$$

$$\iiint \frac{\partial h_{wb}}{\partial t} dxdydt = -\iiint \nabla \cdot \mathbf{Q} dxdydt + \iiint \frac{m}{\rho_w} dxdydt$$

where the limits of integration are $x \in [x, x + \Delta x]$, $y \in [y, y + \Delta y]$, $z \in [z, z + \Delta z]$.

$$\left(\tilde{h}_{wb} - h_{wb}\right) \Delta x \Delta y = \left[Q_{i+\frac{1}{2}j} - Q_{i-\frac{1}{2}j}\right] \Delta y \Delta t + \left[Q_{ij+\frac{1}{2}} - Q_{ij-\frac{1}{2}}\right] \Delta x \Delta t + \frac{m}{\rho_w} \Delta x \Delta y \Delta t$$

$$\tilde{h}_{wb} = h_{wb} - \left[\frac{Q_{i+\frac{1}{2}j} - Q_{i-\frac{1}{2}j}}{\Delta x} + \frac{Q_{ij+\frac{1}{2}} - Q_{ij-\frac{1}{2}}}{\Delta y}\right] \Delta t + \frac{m}{\rho_w} \Delta t \tag{132}$$

Discretization of the Pressure Closure

The pressure relation of eqn. 65 is reformulated below in terms of effective pressure:

$$\frac{\phi_{eng}}{\rho_w g} \frac{\partial P_{ice} - N_{eff}}{\partial t} = -\nabla \cdot \mathbf{Q} + \frac{m}{\rho_w} + c_2 h_{wb} {N_{eff}}^n - |u_b| \left(h_r - h_{wb}\right).$$

At hydrology time scales the change in ice sheet overburden pressure is negligible:

$$\Rightarrow \frac{\phi_{eng}}{\rho_w g} \frac{\partial N_{eff}}{\partial t} = \nabla \cdot \mathbf{Q} - \frac{m}{\rho_w} - c_2 h_{wb} {N_{eff}}^n + |u_b| \left(h_r - h_{wb}\right). \tag{133}$$

The finite volume discretization then proceeds as:

$$\iiint \frac{\phi_{eng}}{\rho_w g}\frac{\partial N_{eff}}{\partial t}dxdydt = \iiint \nabla \cdot \mathbf{Q}dxdydt - \iiint \frac{m}{\rho_w}dxdydt - \iiint c_2 h_{wb} {N_{eff}}^n dxdydt + \iiint |u_b|\left(h_r - h_{wb}\right)dxdydt$$

where the limits of integration are $x \in [x, x+\Delta x]$, $y \in [y, y+\Delta y]$, $z \in [z, z+\Delta z]$.

$$\left(\tilde{N}_{eff} - N_{eff}\right)\Delta x \Delta y = \frac{\rho_w g}{\phi_{eng}}\left[Q_{i+\frac{1}{2}j} - Q_{i-\frac{1}{2}j}\right]\Delta y \Delta t + \frac{\rho_w g}{\phi_{eng}}\left[Q_{ij+\frac{1}{2}} - Q_{ij-\frac{1}{2}}\right]\Delta x \Delta t - \frac{g}{\phi_{eng}}\left[\rho_w c_2 h_{wb} {N_{eff}}^n - \rho_w |u_b|\left(h_r - h_{wb}\right) + m\right]\Delta x \Delta y \Delta t$$

$$\tilde{N}_{eff} = N_{eff} + \frac{\rho_w g}{\phi_{eng}}\left[\frac{Q_{i+\frac{1}{2}j} - Q_{i-\frac{1}{2}j}}{\Delta x} + \frac{Q_{ij+\frac{1}{2}} - Q_{ij-\frac{1}{2}}}{\Delta y}\right]\Delta t - \frac{g\rho_w}{\phi_{eng}}\left[c_2 h_{wb} {N_{eff}}^n - |u_b|\left(h_r - h_{wb}\right) + \frac{m}{\rho_w}\right]\Delta t \tag{134}$$

PDEs 132 and 134 are coupled and solved at the same time.

Heun's Method

Combination of Euler step predictor and trapezoidal step corrector can be used to solve equations of the form:

$$\frac{\partial \phi}{\partial t} = f(t, \phi(t)) \tag{135}$$

The predicted value (ϕ^*) for the next time step ($t + \Delta t$) is:

$$\phi^* = \phi + \Delta t f(t, \phi) \tag{136}$$

$$\tilde{\phi} = \phi + \frac{\Delta t}{2}(f(t, \phi) + f(t + \Delta t, \phi^*)) \tag{137}$$

If the predictor-corrector change is still larger than convergence, the corrected value is taken as the predicted value:

$$\texttt{if } \left(\left|\tilde{\phi} - \phi^*\right| \geq \varepsilon\right) \quad \texttt{then } \phi^* \leftarrow \tilde{\phi} \tag{138}$$

for some $\varepsilon \in \mathbb{R}_+$ and eqn. 137 is recalculated.

From eqns. 114 and 135, the matrix form of the Heun predictor is:

$$\phi^* = \phi + \frac{\mathbf{A}\phi + S_\phi \Delta x/\rho}{\tilde{a_p}} \tag{139}$$

where $\mathbf{A}$ is the tri-diagonal matrix of coefficients from eqns. 125:, ϕ is a vector of are cell-centred values and

$$A_{i,j} = -\delta_{i,j}\left(a_i\right) + \delta_{i,j-1}\left(a_{i+1}\right) + \delta_{i,j+1}\left(a_{i-1}\right) \tag{140a}$$

$$\begin{aligned} A_{i,j} = -\delta_{i,j}\left(\left[\!\left[u_{i+\frac{1}{2}}\left(\phi_i\right), 0\right]\!\right] + \left[\!\left[-u_{i-\frac{1}{2}}\left(\phi_i\right), 0\right]\!\right]\right) + \delta_{i,j-1}\left(\left[\!\left[-u_{i+\frac{1}{2}}\left(\phi_{i+1}\right), 0\right]\!\right]\right) \\ + \delta_{i,j+1}\left(\left[\!\left[-u_{i-\frac{1}{2}}\left(\phi_{i-1}\right), 0\right]\!\right]\right) \end{aligned} \tag{140b}$$

where $\delta_{i,j}$ is the Kroenecker-delta. The trapezoidal corrector becomes:

$$\phi^* = \phi + \frac{\left[\left(\mathbf{A}\phi + S_\phi \Delta x/\rho\right) + \left(\mathbf{A}^*\phi^* + S_\phi \Delta x/\rho\right)\right]}{2\tilde{a_p}}. \tag{141}$$

Leapfrog Trapezoidal Method

Once an initial time step is computed in sec. 8.1.1, leap-frogging helps stability. In this method the predictor update from the current value (ϕ) is applied to the previous time step (ϕ^{prev}), leap-frogging over the current time step, and then the current value is used with the predictor (ϕ^*) for the trapezoidal step (eqn. 137). The longer time integration helps to smooth instabilities.

$$\phi^* = \phi^{prev} + \Delta t f\left(t, \phi\right) \tag{142}$$

Applied to the discretized transport equation, the previous values are used to update the current value to get the predictor:

$$\phi^* = \phi^{prev} + 2\frac{\mathbf{A}\phi + S_\phi \Delta x / \rho}{\tilde{a_p}} \tag{143}$$

Then the trapezoidal step in eqn. 141 is iterated to convergence

Application to Hydrology Equations

For the hydrology model, the sought quantity is water thickness:

$$\phi = h \tag{144}$$

and the advection velocity at interface k is:

$$u_k = \frac{Q_k}{h_k} \tag{145}$$

where $Q_k = -Kh_k^{\alpha}|\psi_k|^{\beta-2}\psi_k$ as in 58.

$$\begin{aligned} u_{i+\frac{1}{2}}\left(\phi_{i+\frac{1}{2}}\right) &= Q_{i+\frac{1}{2}}\left(h_{i+\frac{1}{2}}\right)/h_{i+\frac{1}{2}} \\ &= -Kh_{i+\frac{1}{2}}^{\alpha-1}\left|\psi_{i+\frac{1}{2}}\right|^{\beta-2}\psi_{i+\frac{1}{2}} \end{aligned} \tag{146}$$

Hydraulic gradient (ψ) is calculated from topography (z_b), water in supraglacial lakes (h_{fill}), ice overburden (P_{ice}), and effective pressure N_{eff} (limited to between 0 and overburden pressure):

$$N_{eff} = min\left\{\left[\left[\frac{1}{c_2 h}\left(u_b\frac{h_r - h}{l_r} - \frac{\partial h}{\partial t}\right)\right]^{1/3}, 0\right], P_{ice}\right\}$$

The discretized version with boundary conditions:

$$N_{eff_i} = \begin{cases} min\left\{ \left[\!\left[\frac{1}{c_2 h_i} \left(u_b \frac{h_r - h_i}{l_r} - \frac{h_i - h_i^{prev}}{\Delta t} \right) \right]\!\right]^{1/3}, 0 \right]\!\!\right], P_{ice_i} \right\} & \iff \begin{pmatrix} \texttt{LINKED\_CAVITY} \wedge (P_{ice_i} \geq \rho_{sw} g z_{sl_i}) \\ \wedge \left[(0 < h_i < h_r) \vee (ixp_i \neq 0) \right] \end{pmatrix} \\ P_{ice_i} \cdot \left[1 - min\left\{ \frac{h_i}{h_c}^{7/2}, 1 \right\} \right] & \iff \begin{pmatrix} \texttt{POROELASTIC} \wedge (P_{ice_i} \geq \rho_{sw} g z_{sl_i}) \\ \wedge \left[(0 < h_i) \vee (ixp_i \neq 0) \right] \end{pmatrix} \\ 0. & \iff \begin{pmatrix} (\texttt{LINKED\_CAVITY} \wedge (h_r < h_i)) \\ \vee (P_{ice_i} \leq \rho_{sw} g z_{sl_i}) \end{pmatrix} \\ P_{ice_i} & \iff (h_i \leq 0) \end{cases} \tag{147}$$

Where `LINKED_CAVITY` and `PORELASTIC` are boolean values representing a choice of drainage system, ρ_{sw} is the density of seawater, z_{sl} is sea water thickness, ixp is non zero in cells where tunnels are present and T_{bp} is the basal temperature. Discretized potential with boundary conditions

$$\varphi_i = \begin{cases} \rho_w g z_{b_i} + \rho_w g h_{fill_i} + (P_{ice_i} - N_{eff_i}) & \\ \quad + \rho_{ice} g H_i \left[2^{min\left\{0.0, \lceil T_{froz}, T_{bp_i} \rceil\right\}/T_{froz}} - 1 \right] & \iff \begin{pmatrix} (P_{ice_i} \geq \rho_{sw} g z_{sl_i}) \\ \wedge \left[(h_i > 0) \vee (ixp_i \neq 0) \right] \end{pmatrix} \\ \rho_{sw} g \left(z_{sl_i} + z_{b_i} \right) & \iff (P_{ice} < \rho_{sw} g z_{sl_i}) \\ 1.0e7 & \iff ((h_i \leq 0) \wedge (ixp_i = 0)) \end{cases} \tag{148}$$

T_{froz} is the temperature at which an entire grid cell freezes. Cases for this last term are:

$$\rho_{ice} g H \left[2^{\frac{min\left\{0.0, \lceil T_{froz}, T_{bp} \rceil\right\}}{T_{froz}}} - 1 \right] = \begin{cases} \rho_{ice} g H & T_{bp} \leq T_{froz} \\ 0 & T_{bp} \geq 0 \\ \rho_{ice} g H \left(2^{T_{bp}/T_{froz}} - 1 \right) & 0 < T_{bp}/T_{froz} < 1 \end{cases} \tag{149}$$

And the gradient is the derivative in the direction of flow of the potential

$$\psi_{i+\frac{1}{2}} = \frac{\varphi_{i+1} - \varphi_i}{\Delta x} \tag{150}$$

Taking eqn. 146 together with eqn. 140

$$\begin{aligned} A_{i,j} =& \delta_{i,j} \left(-K h_{i+1}^{\alpha-1} \llbracket \left| \psi_{i+\frac{1}{2}} \right|^{\beta-2} \psi_{i+\frac{1}{2}}, 0 \rrbracket - K h_i^{\alpha-1} \llbracket - \left| \psi_{i-\frac{1}{2}} \right|^{\beta-2} \psi_{i-\frac{1}{2}}, 0 \rrbracket \right) \\ &+ \delta_{i,j-1} \left(-K h_{i+1}^{\alpha-1} \llbracket - \left| \psi_{i+\frac{1}{2}} \right|^{\beta-2} \psi_{i+\frac{1}{2}}, 0 \rrbracket \right) + \delta_{i,j+1} \left(-K h_{i-1}^{\alpha-1} \llbracket - \left| \psi_{i-\frac{1}{2}} \right|^{\beta-2} \psi_{i-\frac{1}{2}}, 0 \rrbracket \right) \end{aligned} \tag{151}$$

and from eqn. 122, the discretization of hydrologic flux is:

$$\frac{\Delta x}{\Delta t} \left[\tilde{h}_i - h_i \right] = - \left(Q_{i+\frac{1}{2}} - Q_{i-\frac{1}{2}} \right) + S_h \Delta x / \rho \tag{152}$$

with

$$Q_{i+\frac{1}{2}} = \begin{cases} -K_{i+\frac{1}{2}} \left[-h_i^{\alpha} \llbracket - \left| \psi_{i+\frac{1}{2}} \right|^{\beta-2} \psi_{i+\frac{1}{2}}, 0 \rrbracket + h_{i+1}^{\alpha} \llbracket \left| \psi_{i+\frac{1}{2}} \right|^{\beta-2} \psi_{i+\frac{1}{2}}, 0 \rrbracket \right] & \iff h_i > 0 \\ 0 & \iff h_i \leq 0 \end{cases} \tag{153a}$$

$$Q_{i-\frac{1}{2}} = \begin{cases} -K_{i-\frac{1}{2}} \left[-h_{i-1}^{\alpha} \left[-\left| \psi_{i-\frac{1}{2}} \right|^{\beta-2} \psi_{i-\frac{1}{2}}, 0 \right] + h_i^{\alpha} \left[\left| \psi_{i-\frac{1}{2}} \right|^{\beta-2} \psi_{i-\frac{1}{2}}, 0 \right] \right] & \iff h_i > 0 \\ 0 & \iff h_i \leq 0 \end{cases} \tag{153b}$$

The element-wise time integration is as follows. Heun step:

$$h_i^* = \begin{cases} h_i + \frac{-Q_{i+\frac{1}{2}} + Q_{i-\frac{1}{2}} + S_h \Delta x}{\tilde{a_p}} & \iff H > 0 \\ 0 & \iff H \leq 0 \end{cases} \tag{154}$$

the leap-frogging becomes:

$$h_i^* = \begin{cases} h_i^{prev} + 2\frac{-Q_{i+\frac{1}{2}} + Q_{i-\frac{1}{2}} + S_h \Delta x}{\tilde{a_p}} & \iff H > 0 \\ 0 & \iff H \leq 0 \end{cases} \tag{155}$$

and the trapezoidal step is:

$$\tilde{h} = \begin{cases} h + \frac{\left[\left(-Q_{i+\frac{1}{2}} + Q_{i-\frac{1}{2}} + S_h \Delta x \right) + \left(-Q_{i+\frac{1}{2}}^* + Q_{i-\frac{1}{2}}^* + S_h \Delta x \right) \right]}{2\tilde{a_p}} & \iff H > 0 \\ 0 & \iff H \leq 0 \end{cases} \tag{156}$$

$$\texttt{if } \left(\left| \tilde{h} - h^* \right| \geq \varepsilon \right) \quad \texttt{then } h^* \leftarrow \tilde{h} \tag{157}$$

for some $\varepsilon \in \mathbb{R}_+$.

Elliptical or Parabolic

$$\frac{\partial h}{\partial t} + \frac{\partial Q}{\partial x} = m \tag{158}$$

$$\frac{\partial h}{\partial t} + \frac{\partial \left(-kh^{\alpha} \frac{\partial \phi}{\partial x}^{\beta-2} \right)}{\partial x} = m \tag{159}$$

$$\phi_0 = P_{ice} - N_{eff} + \rho_w g z_b \tag{160}$$

$$\frac{\partial h}{\partial t} - k \frac{\partial h^{\alpha}}{\partial x} \frac{\partial \left(\phi_0 + \rho_w g h \right)^{\beta-2}}{\partial x} - kh^{\alpha} \frac{\partial^2 \left(\phi_0 + \rho_w g h \right)^{\beta-2}}{\partial x^2} = m \tag{161}$$

$$\frac{\partial h}{\partial t} - k \frac{\partial h^{\alpha}}{\partial x} \frac{\partial \left(\phi_0 + \rho_w g h \right)^{\beta-2}}{\partial x} - kh^{\alpha} \frac{\partial^2 \left(\phi_0 + \rho_w g h \right)^{\beta-2}}{\partial x^2} = m \tag{162}$$

$$\frac{\partial h}{\partial t} - kh^{\alpha-1} \left[(\beta - 2) \left(\phi_0 + \rho_w g h \right)^{\beta-2} \right] \left[\frac{\partial \phi_0}{\partial x} + \phi_w g \frac{\partial h}{\partial x} \right] \frac{\partial h}{\partial x} \tag{163}$$

$$- kh^{\alpha} (\beta - 2)(\beta - 3) \left(\phi_0 + \rho_w g h \right)^{\beta-4} \frac{\partial \left(\phi_0 + \rho_w g h \right)}{\partial x} \left(\frac{\partial \phi_0}{\partial x} + \rho_w g \frac{\partial h}{\partial x} \right) \tag{164}$$

$$- kh^{\alpha} (\beta - 2) \left(\phi_0 + \rho_w g h \right)^{\beta-3} \left(\frac{\partial^2 \phi_0}{\partial x^2} + \rho_w g \frac{\partial^2 h}{\partial x^2} \right) = m \tag{165}$$

Number of characteristics in a second order partial differential equation depends on evaluating the following expression relative to 0:

$$B^2 - 4AC \gtreqless 0 \tag{166}$$

where A, B, and C are the coefficients of the second order derivatives. Here there are no mixed derivatives ($B = 0$) and so the evaluated expression is $-4AC \gtreqless 0$:

$$-4\left(-kh^{\alpha}(\beta-2)\left(\phi_0+\rho_w g h\right)^{\beta-3}\rho_w g\right)\left(-kh^{\alpha}\left(\beta-2\right)\left(\phi_0+\rho_w g h\right)^{\beta-3}\rho_w g\right) \gtreqless 0 \tag{167}$$

$$-h^{2\alpha}\left(\phi_0+\rho_w g h\right)^{2\beta-6} \gtreqless 0 \tag{168}$$

in the trivial case that $h = 0$ or $\phi_0 = -\rho_w g h$, the PDE is parabolic, however in general this equation is elliptic.

8.1.2 *Sediment Discretization*

The subglacial transport equation is

$$\frac{\partial h_{sed}}{\partial t} = -\vec{\nabla}\cdot\vec{Q}_s + \dot{E} - V_{net} \tag{169}$$

$$
\begin{aligned}
\iiint \frac{\partial h_{sed}}{\partial t} dtdxdy &= -\iiint \vec{\nabla} \cdot \vec{Q}_s dtdxdy + \iiint \dot{E} dtdxdy - \iiint V_{net} dtdxdy \\
\iint \tilde{h}_{sed} - h_{sed} dxdy &= -\iint \vec{\nabla} \cdot \vec{Q}_s \Delta t dxdy + \iint \dot{E} \Delta dxdy - \iint V_{net} \Delta dxdy \\
\left(\tilde{h}_{sed_p} - h_{sed_p}\right) \Delta x \Delta y &= -\left(Q_{se} - Q_{sw}\right) \Delta y \Delta t - \left(Q_{ss} - Q_{sn}\right) \Delta x \Delta t + \dot{E}_p \Delta t \Delta x \Delta y - V_{net_p} \Delta t \Delta x \Delta y \\
\tilde{h}_{sed_p} &= h_{sed_p} - \frac{\left(Q_{se} - Q_{sw}\right)}{\Delta x} \Delta t - \frac{\left(Q_{ss} - Q_{sn}\right)}{\Delta y} \Delta t + \dot{E}_p \Delta t - V_{net_p} \Delta t
\end{aligned} \tag{170}
$$

REFERENCES

Golub, G., D. Silvester, and A. Wathen (May 1996). "Diagonal Dominance And Positive Definiteness Of Upwind Approximations For Advection Diffusion Problems". In: *Numerical Analysis*, pp. 125–131. DOI: 10.1142/9789812812872_0009. URL: http://dx.doi.org/10.1142/9789812812872_0009.

Norris, S. E. (Sept. 2000). *A Parallel Navier-Stokes Solver for Natural Convection and Free Surface Flow*. Department of Mechanical Engineering. URL: https://ses.library.usyd.edu.au/handle/2123/376.

Patankar, S. V. (1980). *Numerical Heat Transfer and Fluid Flow*. 1st ed. 1221 Avenue of the Americas, New York, New York, USA: McGraw-Hill Book Company.

Scarborough, J. B. (1930). *Numerical Mathematical Analysis*. 1st ed. Baltimore, MD, United States: The Johns Hopkins Press.

Versteeg, H. K. and W. Malalasekera (2007). *An Introduction to Computational Fluid Dynamics: The Finite Volume Method*. 2nd ed. Edinburgh Gate, Harlow, Essex CM20 2JE, England: Pearson Education Limited.